EX LIBRIS
UNIVERSITATIS
ALBERTÆNSIS

The Bruce Peel
Special Collections
Library

Digitized by the Internet Archive
in 2025 with funding from
University of Alberta Library

https://archive.org/details/0162010432837

UNIVERSITY OF ALBERTA

Library Release Form

Name of Author: Stéphane M. Gagné

Title of Thesis: Structures, Dynamics and Energetics of Troponin C. The Tale of a Muscular Calcium-Binding Protein.

Degree: Doctor of Philosophy

Year this Degree Granted: 1999

Permission is hereby granted to the University of Alberta Library to reproduce single copies of this thesis and to lend or sell such copies for private, scholarly, or scientific research purposes only.

The author reserves all other publication and other rights in association with the copyright in the thesis, and except as hereinbefore provided, neither the thesis nor any substantial portion thereof may be printed or otherwise reproduced in any material form whatever without the author's prior written permission.

UNIVERSITY OF ALBERTA

Structures, Dynamics and Energetics of Troponin C. The Tale of a Muscular Calcium-Binding Protein.

by

Stéphane M. Gagné ©

A thesis submitted to the Faculty of Graduate Studies and Research
in partial fulfillment of the requirements for the degree of
Doctor of Philosophy.

Department of Biochemistry

Edmonton, Alberta

Spring 1999

UNIVERSITY OF ALBERTA

Faculty of Graduate Studies and Research

The undersigned certify that they have read, and recommend to the Faculty of Graduate Studies and Research for acceptance, a thesis entitled ***Structures, dynamics and energetics of troponin C. The tale of a muscular calcium-binding protein.*** submitted by Stéphane M. Gagné in partial fulfillment of the requirements for the degree of Doctor of Philosophy.

Cette thèse est dédiée à

Nicolas et Céleste

ABSTRACT

Regulation of contraction in skeletal and cardiac muscle occurs through calcium binding to the protein troponin C (TnC). The N-terminal domain of TnC (NTnC) carries the regulatory role through the binding of calcium ions; two calcium in skeletal muscle and one in cardiac muscle. This thesis characterizes several structural, dynamic and thermodynamic properties of the regulatory domain of TnC, some of which are listed below.

1. The NMR solution structures of skeletal NTnC in the presence and absence of calcium were solved, and the resultant calcium-induced structural change is presented. The calcium-induced structural transition in skeletal NTnC involves an opening of the structure. This leads to the exposure of an extensive hydrophobic patch (~500 Å^2), an event believed to be necessary for skeletal muscle contraction.
2. The NMR solution structure of a mutant (E41A) of skeletal NTnC was solved. In this mutant, one bidentate ligand to the calcium in site I is missing. The E41A-NTnC structure remains closed upon calcium binding, indicating that the linkage between calcium binding and the induced conformation change has been broken. This provides a snapshot of skeletal TnC between the relaxed and contracted state, and thereby valuable insight into the mechanism of regulation within skeletal TnC.
3. The NMR solution structure of cardiac NTnC in the presence and absence of calcium were solved. Cardiac NTnC does not open upon binding of calcium. This indicates differences in the way skeletal and cardiac TnC regulate muscle contraction.
4. The backbone and side-chain dynamics of apo skeletal NTnC were characterized by NMR relaxation methods. The backbone dynamics of cardiac NTnC were also studied in the apo and calcium-bound state. Based on these dynamic characteristics of NTnC, conformational entropy of sites I and II was calculated. I show that the calcium affinity is fine-tuned by the amount of conformational entropy present in the loops of the apo form of NTnC. In addition to the direct role of binding loop dynamics, the side-chain methyl group dynamics play an indirect role through the energetics of the calcium-induced structural change.

The implication of these results for the function of skeletal and cardiac TnC is discussed.

ACKNOWLEDGMENTS

I first want to thank my supervisor and friend, Dr. Brian D. Sykes, for the guidance and stimulating discussions he has provided. I am also thankful for the freedom he has granted me throughout my research work. I really appreciate the support and trust Brian has given me even though, in some aspects, I have been the most troublesome graduate student he has ever had.

Thanks to my closest 'lab-mate', Dr. Leo Spyracopoulos. In addition to a great friendship, Leo has provided a high level of scientific stimulation which has considerably influenced me. Thanks Leo for the many discussions and arguments, for the intellectual challenges, for the laughs, for the ski trips, for the many beers, ...

Thanks to Dr. Sakae Tsuda, my good friend and collaborator, for all the collaboration and fun we have shared. Thanks to Dr. Monica Li for her help regarding protein expression, sample preparation, and titration work. Thanks to Dr. Larry Smillie and Joyce Pearlstone for providing most of the constructs used for protein expression. Thanks to Gerry McQuaid for upkeep of the spectrometers, and for all the cookies.

Thanks to Mission Control and its members, Leigh Willard, Tim Jellard and Robert Boyko for their computer programs and all the help related to computers.

Thanks to Dr. Lewis E. Kay for his collaboration in the relaxation studies, and for the pulse sequences and programs he has provided.

Thanks to these lab members and friends who helped me in many ways: Dave Corson, Matthew Crump, Sue Henry, Bruce Lix, Krishna Rajarathnam, Linda Saltibus, and Sue Smith.

Merci à mes parents, Bernadette Boutin et Georges Gagné, pour leur aide, leur support, et pour avoir créé tout ce qu'il y a de bon en moi. Sans eux, je serais probablement encore 'dans la rue'.

Finalement, merci à ma femme, Leigh, pour son support, sa patience et son aide. Merci mon amour.

TABLE OF CONTENTS

Section One: Introduction 1

1. Thesis Overview 2

2. From Muscle Tissues to Troponin C: Organization 4
    The organization of muscle 5
        The thick filament 9
        The thin filament 10
        The troponin complex 12
        Troponin C 13

3. From Calcium Binding to Contraction 15
    The sliding filament mechanism 15
    Calcium release and binding to TnC 17
    The binding of calcium induces a conformation change in TnC 17
    Calcium dependant TnC-TnI interactions 18
    Release of actomyosin ATPase inhibition and power stroke 19

4. Characteristics of Troponin C 22
    The sequences 22
    The binding of calcium to sTnC 24
    Previously known structures of TnC 27
        X-ray structures of sTnC in the Ca_2 state 27
        NMR structures of sTnC peptides 28
        NMR structure of the proteolytic fragment TR_1C in the apo state 31
    Calcium induced conformational changes 32
        Early evidences of conformational changes 32
        HMJ model for the calcium-induced structural change 33
        Preliminary NMR structures of apo and calcium saturated sNTnC 35

Section Two: Structural Aspects of TnC . . . 36

5. Refined Characterization of the Calcium-Induced Structural Change in sTnC . . . 37
Refined NMR structures . . . 37
Relevance of structures. . . . 37
Description of structures . . . 38
Calcium-induced structural change . . . 53
Remarks on the NMR structures of sNTnC•apo and sNTnC•Ca$_2$ . . . 57
Methods for the NMR structural study of sNTnC•apo and sNTnC•Ca$_2$ . . . 58
Sample preparation . . . 58
Structure determination . . . 59
NMR structure of sTnC in the Ca$_4$ state . . . 60
X-ray structure of sNTnC in the Ca$_2$ state . . . 62
X-ray structures of skeletal rabbit TnC in the Ca$_4$ state . . . 64
Cohen et al. structures . . . 64
Phillips et al. structure . . . 64
Which one is correct? Is there an incorrect one? . . . 65

6. Structure of E41A-sNTnC•Ca$_2$ . . . 66
Description and choice of the E41A mutant . . . 66
Calcium titration of E41A-sNTnC . . . 68
Structure of E41A-sNTnC•Ca$_2$ . . . 69
Comparison with the wild type structures . . . 77
Experimental procedures . . . 80
Sample preparation . . . 80
NMR experiments . . . 81
Structure determination . . . 81

7. Mechanism of the calcium-induced structural change in sNTnC . . . 83

8. Cardiac TnC . . . 88
NMR structure of cardiac TnC in the Ca$_3$ state . . . 88
NMR structure of cNTnC in the apo and Ca$_1$ state . . . 91
Implications for the regulation of cardiac muscle . . . 94

9. Structural Comparison with Other Calcium Binding Proteins 96
  Calmodulin 96
    Function and sequence 96
    Structures of calmodulin 97
  Calbindin-D_{9k} 100
    Function and sequence 100
    Structures of calbindin-D_{9k} 101
  S100B 102
    Function and sequence 102
    Structures of S100B 103

Section Three: Dynamics and Thermodynamics Aspects of TnC 106

10. Backbone dynamics analysis of sNTnC•apo 107
    - Theory 108
        - T_1, T_2 and NOE 108
        - Isotropic models 109
            - S^2-τ_e model 109
            - S^2-τ_e-R_{ex} model 109
            - Two-time-scale model 110
            - Determination of the parameters 110
        - Anisotropic models 111
            - Fully anisotropic model 111
            - Axially symmetric model 112
            - Determination of the parameters 113
    - Results 115
        - Influence of sample heating on ^{15}N-T_2 measurements 115
        - ^{15}N-T_1, -T_2, and -NOE data. 117
        - Determination of the overall correlation time (τ_m). 123
        - Backbone analysis under the assumption of isotropic rotational diffusion. 125
            - S^2-τ_e model 125
            - S^2-τ_e-R_{ex} model 127
            - Two-time-scale model 128
            - Summary of isotropic fits 129
        - Rotational diffusion anisotropy. 129
    - Summary of the ^{15}N relaxation results 135
        - Consistency between the 500 and 600 MHz data 136
        - Rotational correlation time and rotational diffusion anisotropy. 138
    - Materials and Methods 139
        - Sample preparation. 139
        - Data acquisition: ^{15}N relaxation experiments. 140
        - Data processing 142

11. Analysis of Methyl Group Dynamics for sNTnC•apo 144
  Theory 144
  Results 145
  Materials and Methods 150
    Sample preparation. 150
    Data acquisition: ^{2}H relaxation experiments. 150
    Data processing 151

12. Contribution of Dynamics to the Function of sNTnC 153
  Comparison with structural data 153
    Backbone dynamics 153
    Methyl group dynamics 155
  Correlation between flexibility and calcium-binding affinity 157

13. Dynamics and thermodynamics of cNTnC•apo and cNTnC•Ca$_1$ 164
  Results 164
    ^{15}N-T$_1$, T$_2$, and NOE data. 164
      cNTnC•apo 164
      cNTnC•Ca$_1$ 166
    Determination of the overall correlation time 169
      cNTnC•apo 169
      cNTnC•Ca$_1$ 170
    Analysis of backbone dynamics 171
  Summary 176
    Rotational correlation time and rotational diffusion anisotropy 177
    Relevance of backbone amide dynamics to solution structures 179
    Comparison of site I and site II dynamics in apo-cNTnC 180
    Comparison to site I and site II dynamics and thermodynamics in apo-sNTnC 185
    Calcium induced changes in dynamics and thermodynamics 187
  Materials and methods 190
    Sample Preparation 190
    NMR Spectroscopy 190
    Data processing and analysis 192

Section Four: Discussion 194

14. To open or not to open? That was the question! 195

15. To be flexible or not to be flexible? That is the question! 201
    Backbone and side-chain dynamics 201
    A flexible open state? 202

16. Future Studies 205
    Structural studies 205
    Dynamics studies 209

17. And the Morale of this Tale is 210

References 211

Curriculum Vitae 222

LIST OF TABLES

Table 1. Characteristics of some thin filament components in skeletal and cardiac muscle. 5

Table 2. Amino acid content of sNTnC. 23

Table 3. Properties of some EF-hand calcium-binding proteins. 26

Table 4. Interhelical angle differences between the N-domain of sTnC and other calcium-binding proteins. 28

Table 5. Characteristics of the solution NMR structures of apo and calcium-loaded sNTnC. 40

Table 6. Interhelical angles in the N-domain of sTnC and CaM. 56

Table 7. Structural statistics of the 40 structures of E41A-sNTnC•Ca_2. 71

Table 8. Inter-helical angles in sTnC and CaM as a function of calcium 78

Table 9. Backbone dihedral angle at the hinge positions as a function of calcium. 85

Table 10. Structural statistics of the 40 structures of cTnC 90

Table 11. Interhelical angles in cTnC compared to sTnC and CaM 91

Table 12. Structural statistics for the 40 structures of cNTnC•apo and cNTnC•Ca_1 . . . 92

Table 13. Summary of overall correlation time (τ_m) determination with the isotropic model 125

Table 14. Experimental diffusion parameters for sNTnC•apo 132

Table 15. T_1/T_2 ratio of the five helices of sNTnC•apo and orientation of N–H vectors relative to the axially symmetric diffusion tensor 134

Table 16. Conformational entropy difference between site I and site II 163

Table 17. Rotational diffusion anisotropy of cNTnC 170

Table 18. Calcium-induced conformational entropy changes in sites I and II of cNTnC 172

LIST OF FIGURES

Figure 1. Skeletal muscle organization 4

Figure 2. The levels of organization in striated muscle 6

Figure 3. Comparison of skeletal and cardiac muscle cells of a mammal 7

Figure 4. An electron micrograph of skeletal muscle showing that the myofibrils in muscle are in register. 8

Figure 5. An electron micrograph of parts of three myofibrils in longitudinal section . . 8

Figure 6. Electron micrograph of a longitudinal section of an insect flight muscle 8

Figure 7. The thick filament of striated muscle 9

Figure 8. The X-ray structure of chicken muscle myosin subfragment-1 (S1) 10

Figure 9. A stereoview ribbon diagram of the 3-D structure of actin. 11

Figure 10. Molecular model of a helical actin filament (F-actin) 11

Figure 11. Arrangement of actin, tropomyosin and troponin components in thin filaments of striated muscle 12

Figure 12. G-actin, F-actin, troponin, and tropomyosin (on scale) 12

Figure 13. Schematic representation and effects of calcium on interactions among thin filament proteins 13

Figure 14. Stereoview ribbon representation of the X-ray structure of turkey skeletal muscle TnC 14

Figure 15. The sliding filament model of muscle contraction 15

Figure 16. The proposed mechanism of force generation in muscle 16

Figure 17. Model of TnC-TnI interactions. 18

Figure 18. Model of the troponin-tropomyosin-actin organization in relaxed and contracted muscle 20

Figure 19. Schematic representation summarizing the various steps involved in muscle contraction 21

Figure 20. Sequence of chicken skeletal TnC 23

Figure 21. Sequence comparison between some of the N-domains in skeletal and cardiac TnC 24

Figure 22. The EF-hand calcium-binding motif 24

Figure 23. Stereoview representation of the oxygen atom ligands 25

Figure 24. Alignment of the four EF-hands in chicken sTnC 27

Figure 25. Structures of sTnC peptides 30

Figure 26. Plot of backbone rmsd in 20 structures of TR_1C 31

Figure 27. Far-UV CD spectra of recombinant sNTnC 33

Figure 28. Sequence comparison between the two domains in sTnC 34

Figure 29. Diagrammatic representation of the proposed calcium-induced conformational change in the N-domain of sTnC 34
Figure 30. Structures of sNTnC 41
Figure 31. Ramachandran plots for sNTnC•apo and sNTnC•Ca_2 NMR structures 42
Figure 32. Rmsd plot for the family of NMR structures 43
Figure 33. Per-residue Ramachandran plots of the NMR structure of sNTnC•apo 43
Figure 33. (part 1 of 5) 44
Figure 33. (Part 2 of 5) 45
Figure 33. (Part 3 of 5) 46
Figure 33. (Part 4 of 5) 47
Figure 33. (Part 5 of 5) 48
Figure 34. Per-residue Ramachandran plots of the NMR structure of sNTnC•Ca_2 48
Figure 34. (Part 1 of 5) 49
Figure 34. (Part 2 of 5) 50
Figure 34. (Part 3 of 5) 51
Figure 34. (Part 4 of 5) 52
Figure 34. (Part 5 of 5) 53
Figure 35. Superimposition of the average structures of sNTnC•apo and sNTnC•Ca_2 showing the calcium induced structural change 55
Figure 36. Exposition of an hydrophobic patch in the N-domain of sTnC upon calcium binding. 57
Figure 37. sTnC•Ca_4 family of NMR structures 61
Figure 38. Superimposition of the NMR structure of sNTnC•Ca_2 with the N-domain of the NMR structure of sTnC•Ca_4. 62
Figure 39. Comparison of the NMR structure of sNTnC•Ca_2, the X-ray structure of sNTnC•Ca_2, and the HMJ model 63
Figure 40. Calcium titration plots for G35 and G71 of E41A-sNTnC 68
Figure 41. Stereoview of the solution structure of E41A-sNTnC•Ca_2 69
Figure 42. Ramachandran plot for the NMR structure of E41A-sNTnC•Ca_2 72
Figure 43. Per-residue Ramachandran plots of the NMR structure of E41A-sNTnC•Ca_2. 72
Figure 43. *(Part 1 of 5).* 73
Figure 43. *(Part 2 of 5).* 74
Figure 43. *(Part 3 of 5).* 75
Figure 43. *(Part 4 of 5).* 76
Figure 43. *(Part 5 of 5).* 77

Figure 44. Comparison of the E41A-sNTnC•Ca_2 structure with sNTnC•apo and sNTnC•Ca_2 79
Figure 45. Superimposition of site I in sNTnC•Ca_2 and E41A-sNTnC-Ca_2 80
Figure 46. Glu41 cannot coordinate calcium when the domain is in the closed form . . 84
Figure 47. Structure of calcium-saturated cTnC 89
Figure 48. Structure of the regulatory domain of cNTnC in apo and calcium-saturated states 93
Figure 49. Calcium-induced structural change in cNTnC 94
Figure 50. Comparison of the cNTnC•Ca_1 structure with the E41A-sNTnC•Ca_2 structures 95
Figure 51. Sequence comparison between chicken sTnC and human CaM 97
Figure 52. Calcium-induced structural change in the N-domain of CaM 98
Figure 53. Structure of CaM bound to MLCK peptide 99
Figure 54. Superimposition of the N-domains of CaM and sNTnC•Ca_2 (NMR structure) in the calcium-bound form. 100
Figure 55. Comparison of the calbindin-D_{9k} sequence with the sequence of the N-domain of sTnC 101
Figure 56. Structure of calcium saturated calbindin-D_{9k} compared to the apo structure of the N-domain of sTnC. 102
Figure 57. Comparison of the S100β sequence with the sequence of the N-domain of sTnC 103
Figure 58. Comparison of the calcium saturated S100β structure with the structure of E41A-sNTnC•Ca_2 105
Figure 59. Effect of sample heating and length of the relaxation delay on the precision and accuracy of the measured ^{15}N-T_2 117
Figure 60. 2D ^{1}H–^{15}N HSQC correlation spectra of sNTnC•apo 118
Figure 61. Representative ^{15}N-T_1 and ^{15}N-T_2 relaxation decays 119
Figure 62. Sequential plots of the measured ^{15}N-T_1, ^{15}N-T_2, and {^{1}H}-^{15}N-NOE 120
Figure 63. Sequential plots of various ratios. 123
Figure 64. Sequential plots summarizing the various fits made under the assumption of isotropic tumbling. 126
Figure 65. Comparison between oblate ($D_\parallel < D_\perp$) and prolate ($D_\parallel > D_\perp$) 132
Figure 66. Representation of the structure of sNTnC•apo relative to the axially symmetric diffusion tensor 134
Figure 67. ^{1}H-^{13}C constant-time HSQC spectra of sNTnC-apo 146
Figure 68. $I_zC_zD_z$, $I_zC_zD_y$, and I_zC_z decay curves 147
Figure 69. Plots of the measured methyl CH_2D ^{2}H-T_1 and ^{2}H-$T_{1\rho}$. 147

Figure 70. Comparison between the nitrogen B-factor of the X-ray structure, the backbone RMSD of the NMR structure, and the backbone order parameters 154
Figure 71. Crystallographic and NMR data showing the lack of flexibility in the calcium binding loops when calcium is bound 158
Figure 72. Comparison of the backbone order parameters between calcium binding site I and II 162
Figure 73. Plots of ^{15}N-T$_1$, ^{15}N-T$_2$, and {^{1}H}^{15}N NOE for cNTnC•apo 167
Figure 74. Plots of ^{15}N-T$_1$, ^{15}N-T$_2$, and {^{1}H}^{15}N NOE for cNTnC•Ca$_1$ 168
Figure 75. Order parameters (S^2) and internal correlation times (τ_e) for cNTnC•apo derived from the S^2-τ_e model 173
Figure 76. S^2 and τ_e for cNTnC•Ca$_1$ derived from the S^2-τ_e model 174
Figure 77. Structures of cNTnC•apo, cNTnC•Ca$_1$, and sNTnC•Ca$_2$ oriented with respect to the long axis of the rotational diffusion tensor ($D_\parallel$) 178
Figure 78. Comparison of the S^2 for site I and site II in sNTnC•apo and cNTnC•apo 182
Figure 79. Backbone atoms for site II in cNTnC•apo and cNTnC•Ca$_1$ 183
Figure 80. Backbone atoms of the central β-sheet in cNTnC•apo 185
Figure 81. Comparison of S^2 for site I and site II in cNTnC•apo and cNTnC•Ca$_2$ . . . 188
Figure 82. Distribution of the C-D inter-helical angle for the various structures of the N-domain of sTnC 203
Figure 83. Representation of the troponin ‘core’ complex 205
Figure 84. sTnC•Ca$_4$:sTnI$_{1\text{-}47,\text{reg}}$ complex 206
Figure 85. Structure of cNTnC•Ca$_1$ complexed with cTnI$_{147\text{-}163}$ 207
Figure 86. 1D ^{1}H NMR spectra of a 43kD troponin complex 208

ABBREVIATIONS

The 20 amino acids:

Ala	Alanine
Arg	Arginine
Asn	Asparagine
Asp	Apsartic acid
Cys	Cysteine
Gln	Glutamine
Glu	Glutamic acid
Gly	Glycine
His	Histidine
Ile	Isoleucine
Leu	Leucine
Lys	Lysine
Met	Methionine
Phe	Phenylalanine
Pro	Proline
Ser	Serine
Thr	Threonine
Trp	Tryptophan
Tyr	Tyrosine
Val	Valine

Troponins:

TnC	troponin C
TnI	troponin I
TnT	troponin T
sTnC	skeletal TnC
cTnC	cardiac TnC
sNTnC	N-domain of sTnC
cNTnC	N-domain of cTnC
TR_1C	residues 12-89 of sTnC

Others:

CaM	calmodulin
CD	circular dichroism
HLH	helix-loop-helix
HMJ	Herzberg-Moult-James model
NMR	nuclear magnetic resonance
NOE	nuclear Overhauser effect
ns	nanosecond
ps	picosecond
rmsd	root mean square deviation
Å	10^{-10} meter

SECTION ONE: INTRODUCTION

1. Thesis Overview 2
2. From Muscle Tissues to Troponin C: Organization 4
3. From Calcium Release to Contraction 15
4. Characteristics of Troponin C 22

Coordinate movement is essential to life. All animals use the same basic mechanism for motor control: the contraction of muscle. A large number of protein structural changes and protein-protein interactions are involved in the process of muscle contraction. Regulation of this process in skeletal and cardiac muscle occurs through the binding of calcium to one of these proteins: troponin C.

1. THESIS OVERVIEW

An obvious question is *why study TnC?* There are two major objectives which justify the research efforts and money which were invested here.

The first objective was to provide a better understanding of TnC as a muscle contraction regulator. All animals rely on muscle contraction for survival, and TnC regulates muscle contraction through the binding of calcium. This thesis provides a new understanding for one of life's basic requirements, muscle contraction, at the atomic level.

The second objective was to provide a better understanding of TnC as a calcium-binding protein. TnC shares the EF-hand structural motif with more than 250 other calcium-binding proteins [1] ¶. Calcium-binding proteins are responsible for many functions within the cell and are of importance in many areas of biology. This thesis provides new understandings applicable to several calcium-binding proteins, and to the mechanism by which they decode calcium signals.

Using primarily NMR, these objectives have been achieved by studying the structural, dynamic and energetic properties of TnC. In my Master's thesis [2], I presented a preliminary description of the calcium-induced structural change in the regulatory domain of skeletal TnC (sNTnC). Although this thesis includes a refined description of the structural changes in TnC which regulate contraction, it goes beyond the "what happens" and focuses on the "how does it happen".

¶ The list of references is located after the discussion, pages [211-221].

This thesis is separated in five sections:

Section One: Introduction	chapters 1-4.
Section Two: Structural aspects of TnC	chapters 5-9.
Section Three: Dynamics and thermodynamics aspects of TnC	chapters 10-13.
Section Four: Discussion	chapters 14-17.
Section Five: Appendices.	

The remainder of the introduction is separated in three chapters. Chapter 2 describes the organization of striated muscle, starting with muscle tissues and ending with TnC. In chapter 3, the current understanding of the various processes involved in muscle contraction is presented, and some of the characteristics of TnC will be outlined in chapter 4.

2. FROM MUSCLE TISSUES TO TROPONIN C: ORGANIZATION

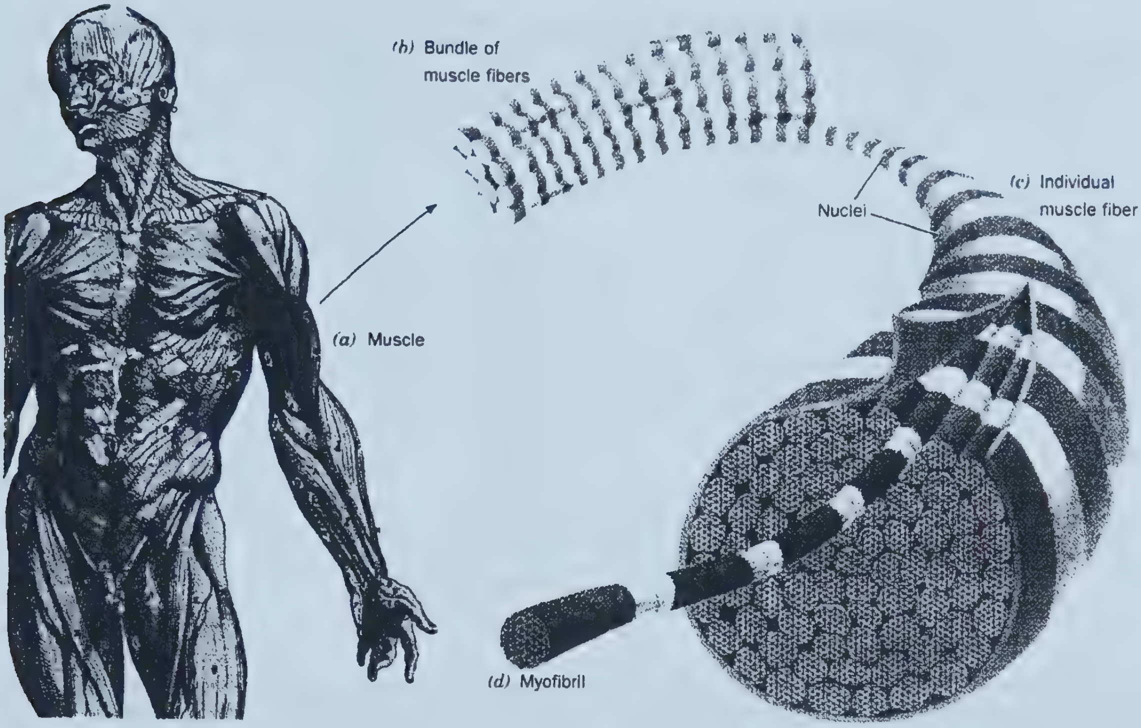

Figure 1. Skeletal muscle organization. A muscle (*a*), consists of bundles of muscle fiber (*b*), each of which is a long thin multi-nucleated cell (*c*), that may run the length of the muscle. Muscle fibers contain bundles of laterally aligned myofibrils (*d*), which consist of bundles of alternating thick and thin filaments. [Adapted from *Biochemistry* 2nd edition, Voet & Voet]

This chapter presents an overview of striated muscle architecture and of its components. Although there is a large number of proteins involved in muscle architecture, I will mainly discuss the ones which are of direct relevance to TnC. Those include the proteins TnC, TnI, TnT, tropomyosin, actin, and myosin. Emphasis is given to the skeletal muscle system, since most of this thesis work was done on skeletal TnC. However, the cardiac muscle system is also discussed to highlight some of the differences between skeletal

and cardiac muscle. Table 1 lists the characteristics of these thin filament proteins for skeletal and cardiac muscle.

Table 1. Characteristics of some thin filament components in skeletal and cardiac muscle.

	protein	# res.	M.W.	pI [a]	structure [b]	helix % [c]	sheet % [c]
skeletal	NTnC [d]	90	9977.47	4.0	yes	53-56	7
	CTnC [e]	75	8600.67	4.3	yes	56-67	8
	TnC [f]	162	18244.85	4.2	yes	62-68	7
	TnI [g]	182	21339.26	8.2	no	85	0
	TnT [h]	258	30597.30	5.7	no	83	0
	tropomyosin [i]	284	32709.58	4.7	yes	97	0
	actin [j]	377	42052.54	5.2	yes	33	23
	calcium	1	40.08	—	—	—	—
cardiac	NTnC [k]	89	10062.69	4.3	yes	55-57	6-7
	CTnC [l]	75	8675.72	4.2	yes	53	8
	TnC [m]	161	18403.15	4.2	yes	57	7
	TnI [n]	210	24008.29	9.8	no	79	0
	TnT [o]	298	35924.72	4.9	no	76	0
	tropomyosin [i]	284	32709.58	4.7	yes	97	0
	actin [p]	377	42020.47	5.2	yes	33	23

[a] Theoretical pI obtained from the program SEQSEE. [b] Whether or not the structure has been solved by X-ray or NMR. [c] Secondary structure profile obtained using VADAR for proteins with structures, and from SEQSEE for proteins without. [d] Residues 1-90 of skeletal TnC (fragment). [e] Residues 88-162 of skeletal TnC (fragment). [f] PIR # TPCHCS. [g] PIR # TPHUIS. [h] PIR # I53021. [i] PIR # A25825. [j] PIR # ATHU. [k] Residues 1-89 of cardiac TnC (fragment). [l] Residues 90-161 of cardiac TnC (fragment). [m] PIR # TPHUCC. [n] PIR # TPHUIC. [o] PIR # TPHUTC. [p] PIR # ATHUC.

The organization of muscle

Figures 1 and 2 show a typical vertebrate striated muscle at successive levels of organization. Striated skeletal muscles are composed of multi-nucleated cylindrical fibers, or myofibers, 10 to 100 μm in diameter and up to several centimeters long. A major difference between skeletal and cardiac muscle is at the cellular level; heart muscle cells are

more conventional, having only a single nucleus (figure 3). Each myofiber contains a bundle of myofibrils, each about 1 μm in diameter. Finally, a myofibril is made up of a long chain of contracting units called sarcomeres, which repeat every 2.3 μm along the fibril axis (figure 2). The periodic structure of the myofibril can be clearly observed by electron microscopy (figure 4 and 5). The electron micrographs show two bands, the A band (dark) and the I band (light), which alternate. A sarcomere is limited by the Z-lines, located in the center of the I band. The striations of the myofibrils are the result of periodic variations in concentration of two kinds of interacting filaments, the thick filament and the thin filament (figure 6). Thick filaments are about 1.5 μm long and 150 Å wide and are separated by 400 Å. Thin filaments are about 1 μm long and 100 Å in diameter. In vertebrate muscle each thick filament is surrounded by six thin filaments, and each thin filament lies symmetrically among three thick filaments (figure 5). As a consequence of this geometry, there are twice as many thin filaments as thick filaments.

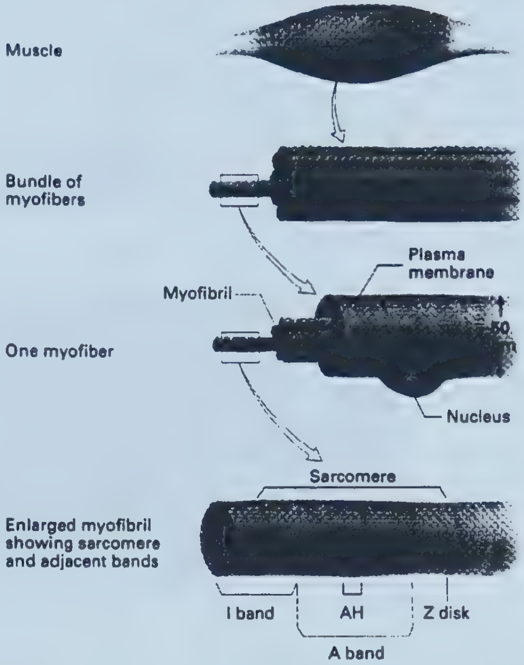
Muscle
Bundle of myofibers
Plasma membrane
Myofibril
One myofiber
50
Nucleus
Sarcomere
Enlarged myofibril showing sarcomere and adjacent bands
I band
AH
Z disk
A band

Figure 2. The levels of organization in striated muscle. Each muscle cell, or myofiber, contains many myofibrils. The sarcomere is the functional unit of contraction; it is about 2 μm long in resting muscle. [Adapted from *Molecular Cell Biology* 2nd edition; Darnel, Lodish & Baltimore]

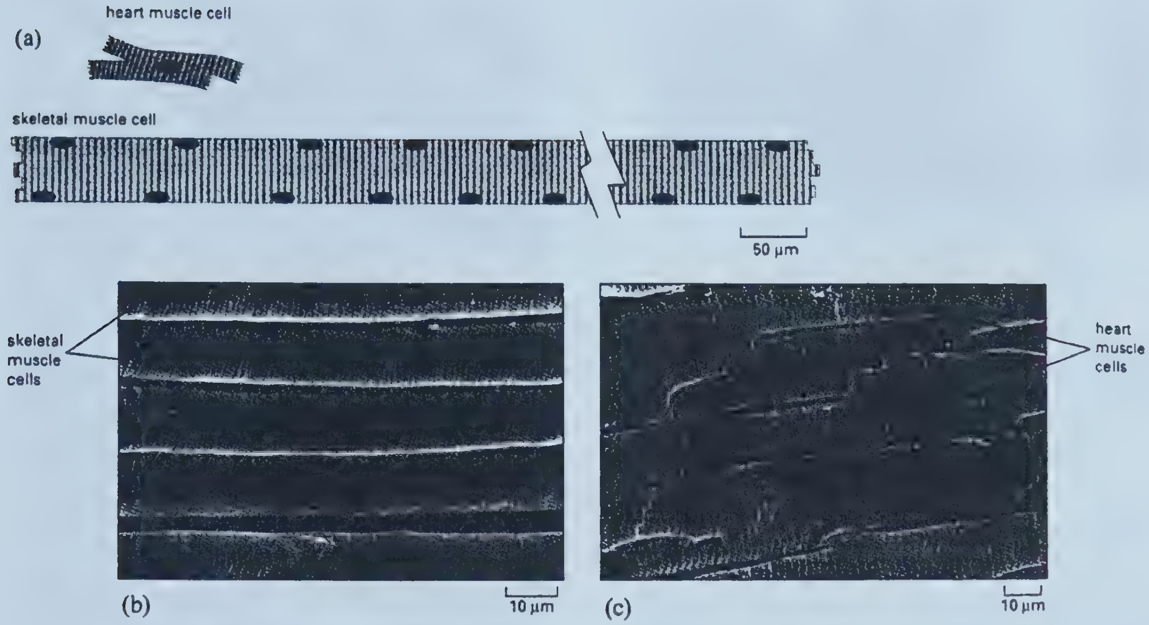
(a)
heart muscle cell
skeletal muscle cell
50 µm
skeletal muscle cells
heart muscle cells
(b)
10 µm
(c)
10 µm

Figure 3. Comparison of skeletal and cardiac muscle cells of a mammal. (*a*) Schematic drawings to scale. (*b-c*) Scanning electron micrographs, showing (*b*) skeletal muscle from the neck of a hamster, and (*c*) heart muscle from a rat. The arrows in (*c*) point to junctions between the heart muscle cells. [Adapted from *Molecular Biology of the Cell* 3rd edition; Alberts *et al.*]

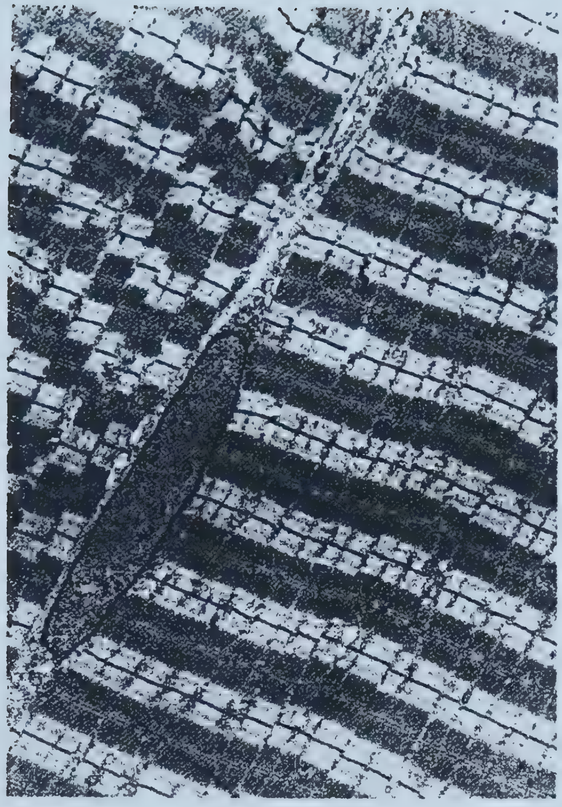

Figure 4. An electron micrograph of skeletal muscle showing that the myofibrils in muscle are in register. The ovoid object near the center is a nucleus. [Adapted from *Biochemistry* 2nd edition; Voet & Voet]

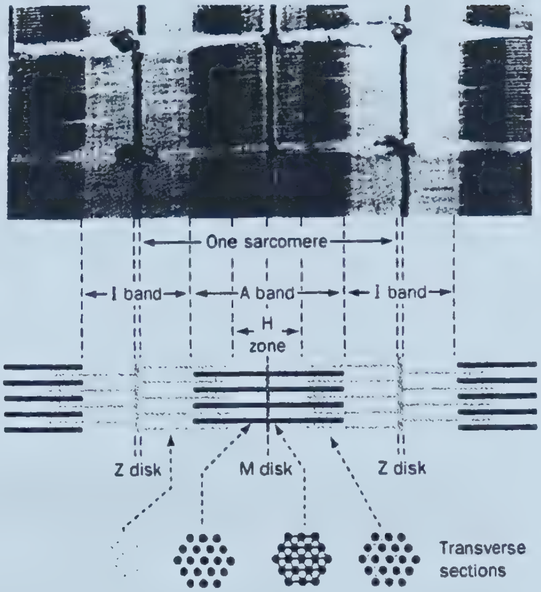
One sarcomere
I band
A band
I band
H zone
Z disk
M disk
Z disk
Transverse sections

Figure 5. An electron micrograph of parts of three myofibrils in longitudinal section. The myofibrils are separated by horizontal gaps. A myofibril's major features, as indicated in the accompanying interpretive drawings, are the light I band, which contains only hexagonally arranged thin filaments; the A band, whose dark H zone contains only hexagonally packed thick filaments, and whose even darker outer segments contain overlapping thick and thin filaments; the Z disk, to which the thin filaments are anchored; and the M disk, which arises from a bulge at the center of each thick filament. The myofibril's functional unit, the sarcomere, is the region between two successive Z disks. [Adapted from *Biochemistry* 2nd edition; Voet & Voet]

Figure 6. Electron micrograph of a longitudinal section of an insect flight muscle. This very thin section shows clearly the alternating myosin and actin filaments and the cross-bridges that link the two. [Adapted from *Molecular Biology of the Cell* 3rd edition; Alberts *et al.*]

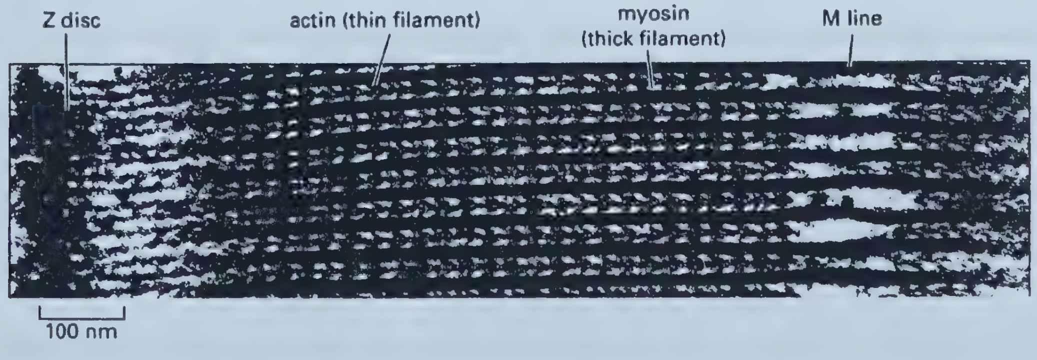
Z disc
actin (thin filament)
myosin
(thick filament)
M line
100 nm

The thick filament

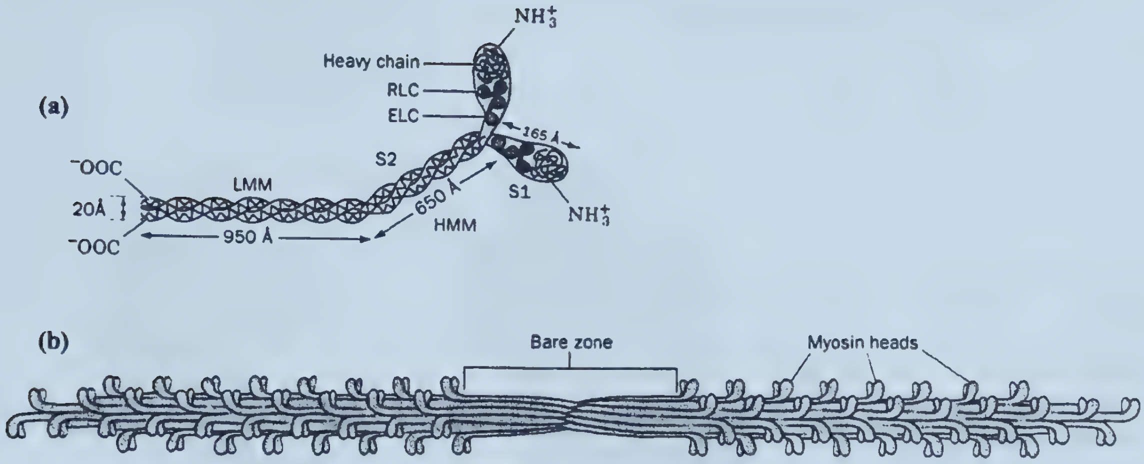

Figure 7. The thick filament of striated muscle. (*a*) The myosin molecule; its rod-shaped tail is formed by the two extended α-helices, one from each of its two identical heavy chains, that wrap around each other to form a parallel coiled-coil. One of each type of myosin light chain, an essential light chain (ELC) and a regulatory light chain (RLC), is associated with each of myosin's identical globular heads. (*b*) A thick filament typically contains several hundred myosin molecules organized in a repeating staggered array such that the myosin molecules are oriented with their globular heads pointing away from the filament's center. [Adapted from *Biochemistry* 2nd edition; Voet & Voet]

The major constituent of the thick filament is myosin, a very large protein molecule (~ 520 kDa) that looks like a two-headed snake (figure 7). Myosin is made of six polypeptide chains: two 220 kDa heavy chains and two pairs of light chains (each approximately 20 kDa). The two heavy chains associate to form a two stranded α-helical coiled coil (~ 1300 Å long) with two globular "head" regions at one extremity. Each head is complexed with two different light chains (often referred to as the regulatory (RLC) and the essential light chains (ELC)). The coiled coil accounts for the self-association of myosin and the formation of the thick filament backbone (figure 7). The heads of myosin may be enzymatically cleaved to isolate what are called S1 fragments, consisting of the globular region of the heavy chain and the two associated light chains (~ 130 kDa). The crystal

structure of myosin S1 has been solved [3], revealing a highly asymmetric molecule with a length of 165 Å, a width of 65 Å, and a thickness of approximately 40 Å (figure 8).

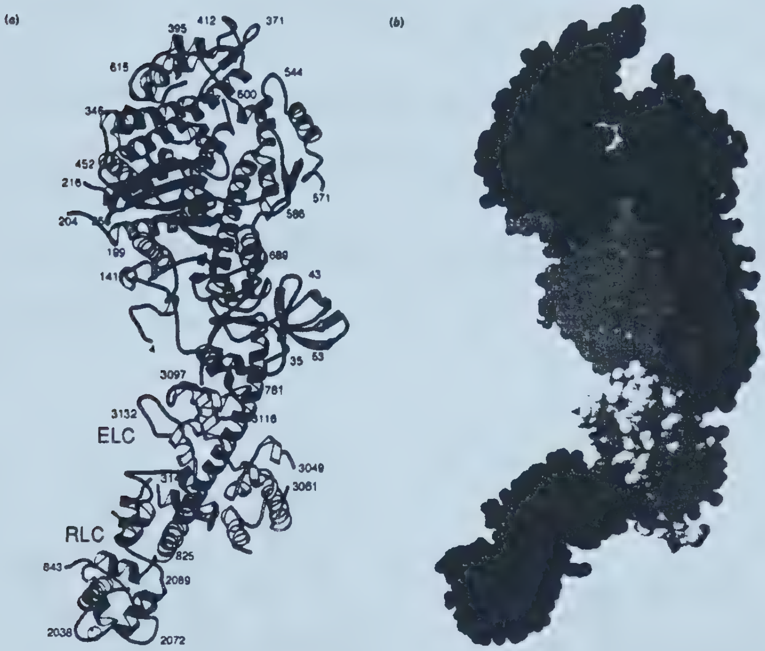

Figure 8. The X-ray structure of chicken muscle myosin subfragment-1 (S1). (*a*) A ribbon diagram of S1. Residue numbers are indicated at various positions, with 2000 and 3000 being added to those of the RLC and ELC to distinguish them from the heavy chain. (*b*) A space-filling representation of S1, oriented similarly to (*a*). [Adapted from *Biochemistry* 2nd edition; Voet & Voet]

The thin filament

The thin filament is a more complex structure containing several proteins of which actin is the major building block. The globular monomeric form of actin, G-actin, is a protein arranged into four domains surrounding a deep cleft (figure 9) [4]. Under physiological conditions, actin polymerizes to form a long, helical fiber (F-actin). The helical stacking of the globular monomers gives F-actin the appearance of two strings of beads wound around one another (figure 10). Although actin is the main constituent of the thin filament, other proteins are essential to the contractile function of striated muscle. One of these is tropomyosin which exists as a dimer of two polypeptide subunits that associate

in a coiled-coil fashion. Electron micrographs and X-ray diffraction have localized tropomyosin along the actin fiber. Elongated tropomyosin polymerizes by a head-to-tail overlap of 8-11 amino acid residues, such that one tropomyosin molecule spans seven actin monomers. At about one third of the distance from the carboxy-terminal end of each tropomyosin molecule resides a troponin complex. This troponin complex is formed of three subunits: TnT, TnI, and TnC. The proposed arrangement of actin, tropomyosin and the troponins in the thin filament is shown in figure 11; an 'on-scale' representation of these proteins is shown in figure 12.

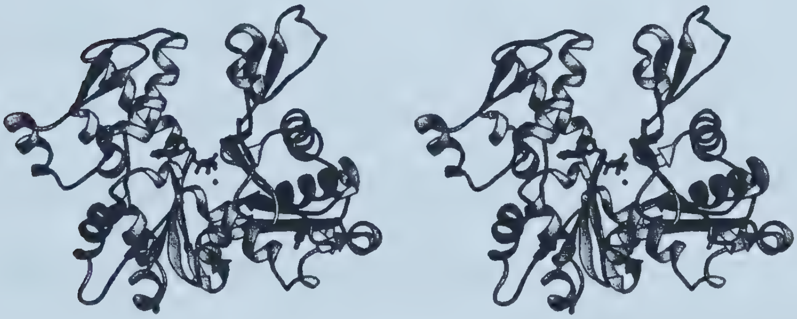

Figure 9. A stereoview ribbon diagram of the 3-D structure of actin viewed roughly perpendicular to the flat face of the molecule. The molecule is thought to have similar orientation in a filament with its long axis vertical. The right side of the molecule is thought to be exposed on the outer surface of the filament.

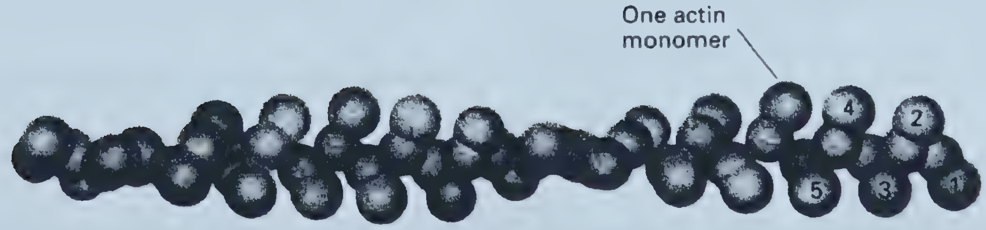

Figure 10. Molecular model of a helical actin filament (F-actin). The globular actin monomer is shown here as two domains. [Adapted from *Molecular Cell Biology* 2nd edition; Darnell, Lodish & Baltimore]

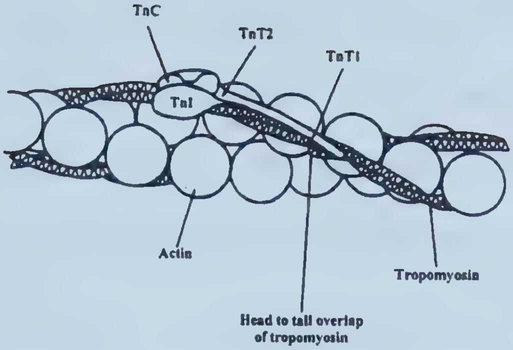

Figure 11. Arrangement of actin, tropomyosin and troponin components in thin filaments of striated muscle. [Adapted from *Guidebook to the Cytoskeletal and Motor Proteins*; Kreis & Vale]

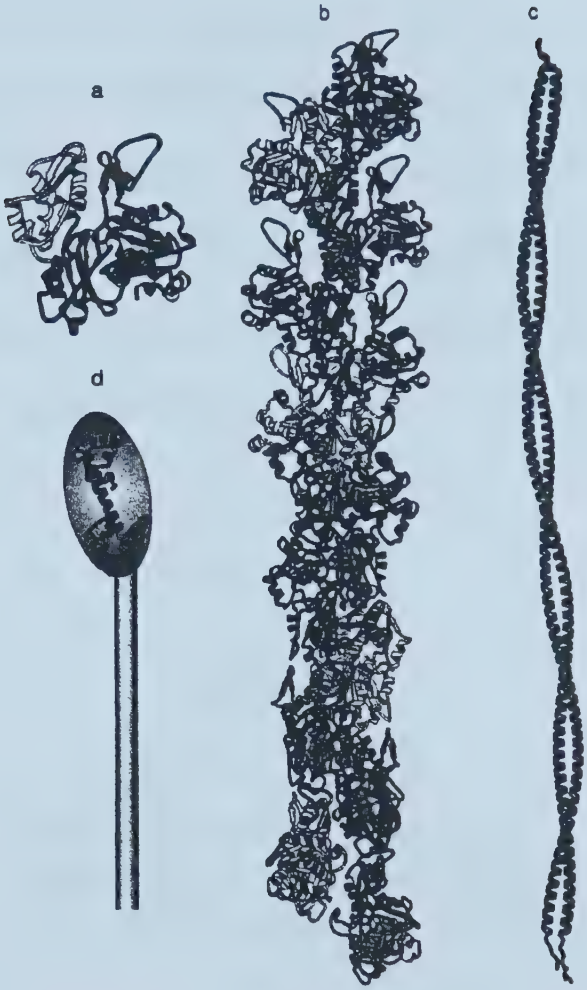

Figure 12. (*a*) Ribbon diagram of the actin monomer structure. (*b*) Ribbon diagram of the actin monomer in panel *a* placed into a 13/6 helix to model the X-ray fiber diffraction data from gels of oriented actin filaments. (*c*) Ribbon diagram of the two-chain, coiled-coil α-helical structure of tropomyosin. (*d*) Schematic illustration of the troponin complex, drawn to the same scale as panels *a-c*, shows TnC as a ribbon diagram and TnT as a rod and part of the oval, which also contains TnI.

The troponin complex

TnT is the largest of the troponin subunits and makes contact with tropomyosin, TnI and TnC; it therefore anchors the troponin complex to the thin filament. Electron micrographs have shown the troponin complex to be globular with a long rod-shaped tail identified as TnT [5]. The asymmetric TnT component, represented by its fragments TnT1 (1-158) and TnT2 (159-259), interacts with tropomyosin both at the head-to-tail overlap (TnT1) and in a region about 13-15 nm from its C-terminal end (TnT2) (figure 13) [6, 7]. The second troponin subunit, TnI, binds to the N-terminal end of TnT2 (figure 13) [8]. In the relaxed state, TnI also interacts with actin and probably

tropomyosin. No tertiary structure of TnI has yet been determined, although the structure of some fragments have been solved recently [9]. The third troponin subunit, TnC, interacts with both TnT and TnI. The interaction between TnC and TnT is uncertain, but some studies show that TnC may interact with the C-terminal end of TnT2 [8]. The interactions between TnC and TnI are better characterized [10], and are found to be calcium-dependent. A schematic representation of the interactions amongst thin filament proteins is shown in figure 13.

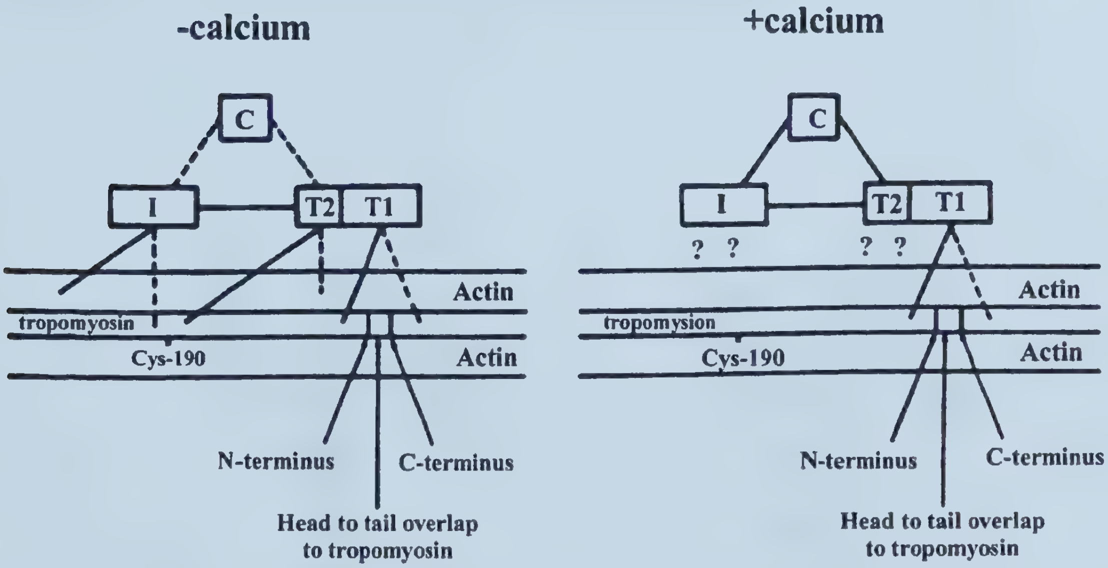
-calcium
C
I
T2
T1
Actin
tropomyosin
Cys-190
Actin
N-terminus
C-terminus
Head to tail overlap
to tropomyosin
+calcium
C
I
T2
T1
? ?
? ?
Actin
tropomysion
Cys-190
Actin
N-terminus
C-terminus
Head to tail overlap
to tropomyosin

Figure 13. Schematic representation and effects of calcium on interactions among thin filament proteins. [Adapted from *Guidebook to the Cytoskeletal and Motor Proteins*; Kreis & Vale]

Troponin C

Skeletal TnC has four calcium-binding sites; two high affinity (sites III and IV) and two low affinity (sites I and II). In cardiac muscle, there is only one low affinity site (site II), as site I is defunct [11]. The high affinity sites are believed to be always occupied by either calcium or magnesium under physiological conditions, and have primarily a structural role.

The low affinity sites are calcium specific and assume a regulatory role in muscle contraction. The crystal structures of turkey skeletal TnC [12] and chicken skeletal TnC [13] reveal a protein consisting of two globular domains, each containing two calcium binding sites, connected by an extended α-helix (figure 14). In these structures, sites III and IV in the C-domain are occupied by calcium, whereas the regulatory sites (I and II) in the N-domain are in the apo state. All four calcium binding sites show the helix-loop-helix motif termed the EF-hand [14]. The helix packing in these half-saturated structures is, however, different between the apo N-domain and the calcium-bound C-domain [15].

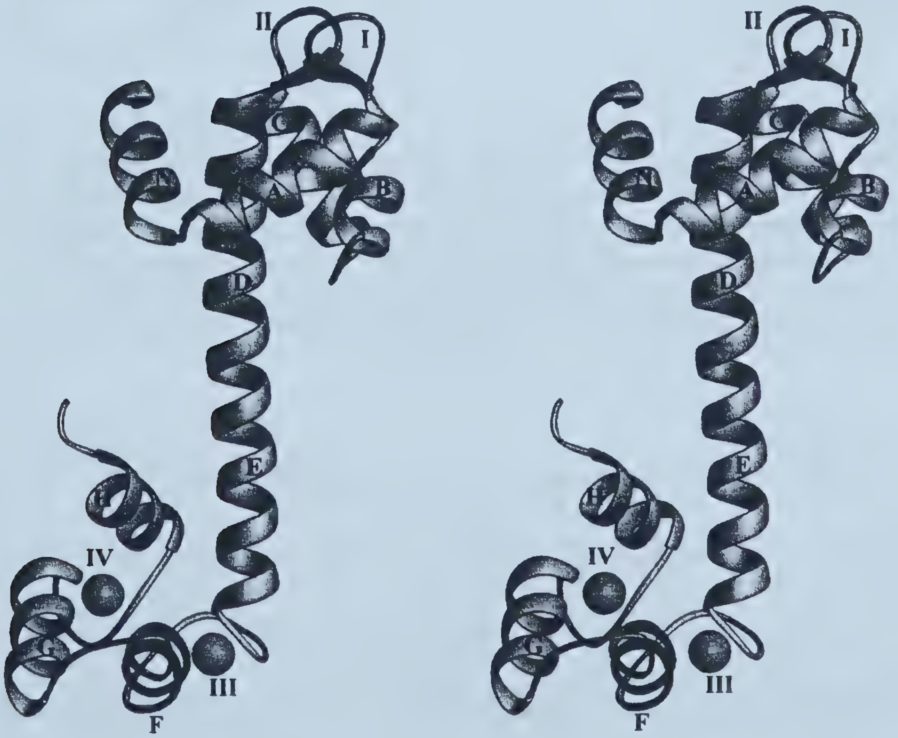

Figure 14. Stereoview ribbon representation of the X-ray structure of turkey skeletal muscle TnC. Helices are labeled N, A-H; calcium binding sites are labeled I through IV. Sites III and IV are filled with calcium, whereas sites I and II are apo.

[illegible]

[illegible]

3. FROM CALCIUM BINDING TO CONTRACTION

The sliding filament mechanism

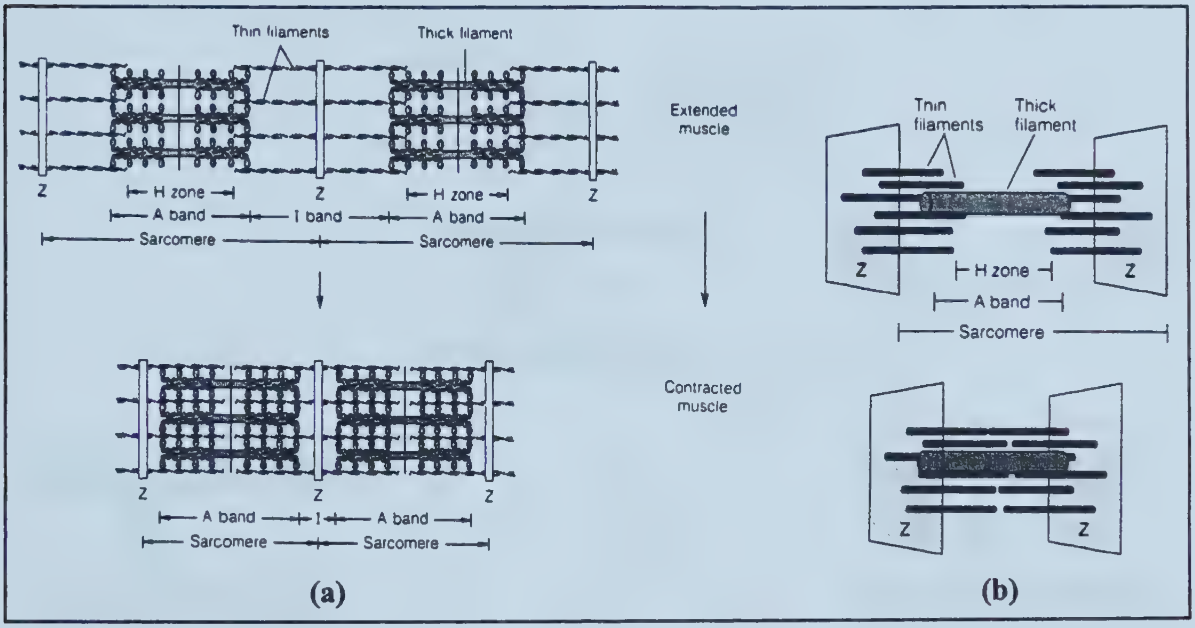
Thin filaments
Thick filament
Z
H zone
Z
H zone
Z
A band
I band
A band
Sarcomere
Sarcomere
Z
Z
Z
A band
I
A band
Sarcomere
Sarcomere
(a)
Extended muscle
Contracted muscle
Thin filaments
Thick filament
Z
Z
H zone
A band
Sarcomere
Z
Z
(b)

Figure 15. The sliding filament model of muscle contraction. (*a*) Two sarcomeres, schematically shown extended and contracted. (*b*) A three-dimensional model of the same. The interaction of actin thin filaments and myosin thick filaments in striated muscle. The heads on the two ends of the myosin filament are oriented in opposite directions, so that the two ends 'walk' along the actin filaments in opposite direction, pulling the actin filaments and their attached α-actinin (Z-lines) toward the center of the sarcomere. The result is contraction. [Adapted from *Biochemistry* 1st edition; Mathews & van Holde]

The sliding filament mechanism of muscle contraction postulates that the thin filament is displaced relative to the thick filament. For sliding to occur, the S1 portion of myosin attaches to a binding-site on actin to form the actomyosin complex. A conformational change then pulls it toward the center of the sarcomere (figure 15). S1 has ATPase activity, and it is the hydrolysis of ATP by S1 that provides the free energy necessary to drive muscle contraction. A schematic representation of the proposed mechanism of force

production is shown in figure 16. For the power stroke to occur, myosin must first properly bind actin, an event which is regulated by calcium.

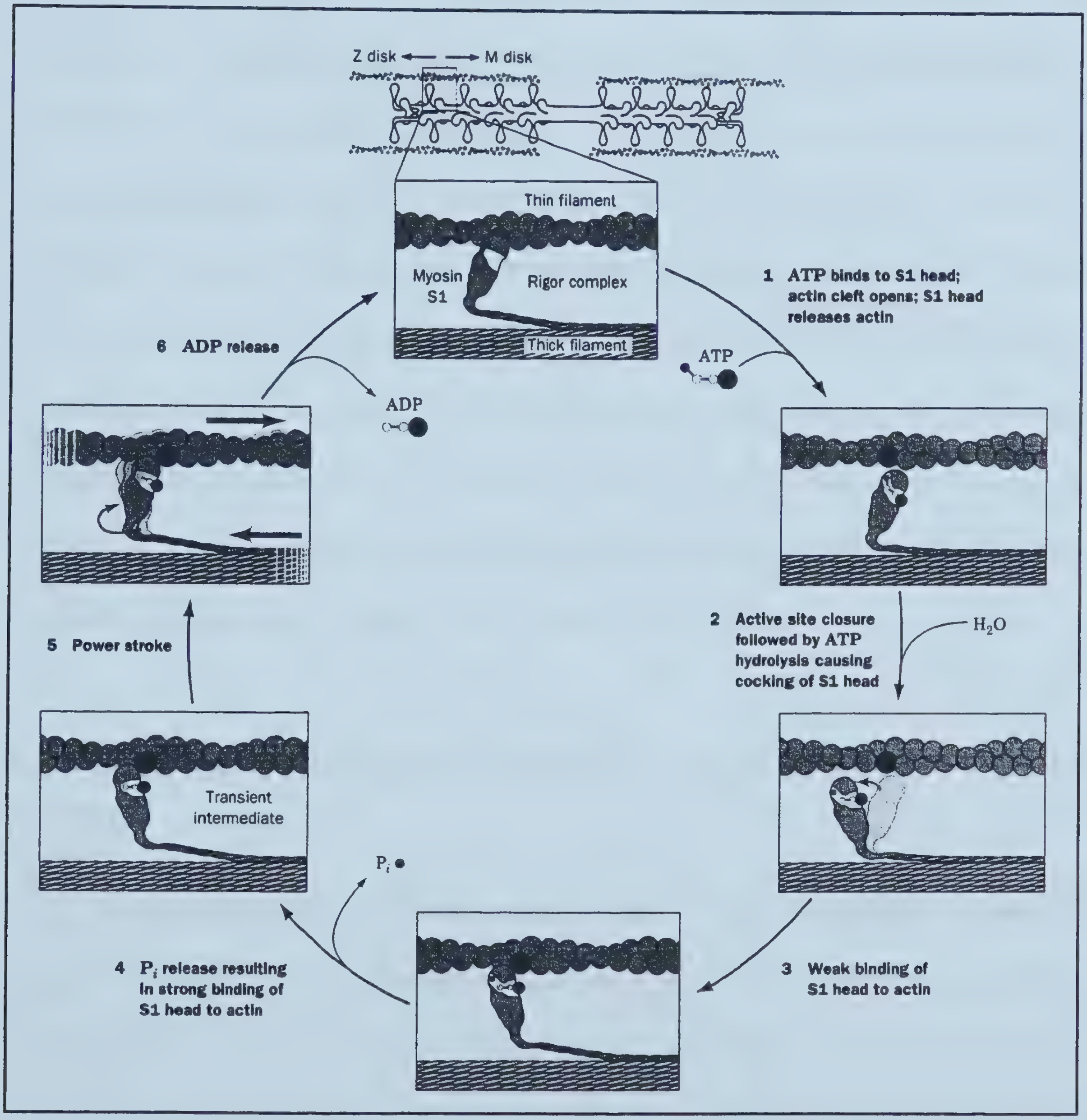
Z disk
M disk
Thin filament
Myosin S1
Rigor complex
Thick filament
1 ATP binds to S1 head; actin cleft opens; S1 head releases actin
ATP
2 Active site closure followed by ATP hydrolysis causing cocking of S1 head
H_2O
3 Weak binding of S1 head to actin
4 P_i release resulting in strong binding of S1 head to actin
P_i
Transient intermediate
5 Power stroke
6 ADP release
ADP

Figure 16. The proposed mechanism of force generation in muscle. The myosin head 'walks' up the actin thin filament through a cyclic vectorial process that is driven by ATP hydrolysis. Only one of myosin's two independent S1 heads is shown. The actin monomer to which S1 was bound at the beginning of the cycle is shown darker for reference. [Adapted from *Biochemistry* 2nd edition; Voet & Voet]

Calcium release and binding to TnC

In resting muscle, calcium ions are actively pumped out of muscle fibers, concentrating the calcium ions within the spaces of the sarcoplasmic reticulum. The concentration of free calcium in muscle fiber in the resting state is in the neighborhood of 10^{-7} M, and the concentration of magnesium is about 10^{-3} M. Consequently, in the resting state, the high affinity sites in the C-domain of TnC are filled with magnesium ions, and the low affinity sites in the N-domain are in the apo state. The crystal structure shown in figure 14 is therefore related to the conformation of TnC in relaxed muscle. Upon neural stimulation, calcium is released from the sarcoplasmic reticulum to the cytoplasm (sarcoplasm) of the muscle fiber. This calcium influx ($> 10^{-6}$ M) causes the binding of calcium to the regulatory domain of TnC, inducing a conformational change, and triggering a sequence of events that ultimately lead to muscle contraction.

The binding of calcium induces a conformation change in TnC

The calcium-induced conformational change in TnC has been studied extensively using various spectroscopic techniques including NMR, CD, fluorescence and Raman spectroscopy (reviewed in chapter 4). These studies have indicated that the C-domain of TnC is mostly unstructured in the apo state, and that the binding of calcium to sites III and IV induces folding. Unlike the C-domain, the N-domain is folded in the apo form. As will be shown later, the calcium-induced structural transition in the N-domain of skeletal TnC

involves an opening of the domain through a large change in interhelical angles. This leads to the increased exposure of an extensive hydrophobic patch.

Calcium dependant TnC-TnI interactions

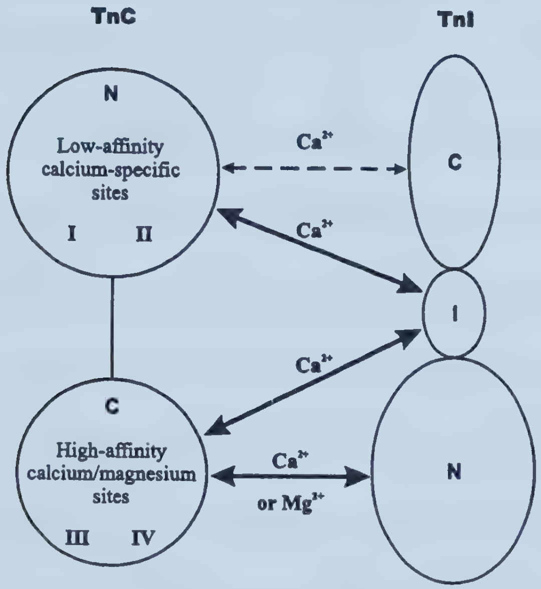
TnC
TnI
N
Low-affinity calcium-specific sites
I
II
C
High-affinity calcium/magnesium sites
III
IV
Ca^{2+}
Ca^{2+}
Ca^{2+}
Ca^{2+} or Mg^{2+}
C
I
N

Figure 17. Model of TnC-TnI interactions. N and C represent the N-terminal and C-terminal domains, respectively, of TnC and TnI. The inhibitory region of TnI is represented by I. Some of the interactions are dependent on the presence of calcium and occur only when sites I and II of TnC are filled during muscle activation. These calcium dependent interactions are found between the inhibitory region of TnI and both N- and C-terminal domains of TnC. The interactions between the N-terminal region of TnI and the C-domain of TnC are calcium/magnesium-dependent, and are believed to be present in both the relaxed and the activated state of muscle.

TnI is composed of three regions: N-domain, C-domain, and inhibitory region. The inhibitory region is the portion of TnI required to inhibit the actomyosin magnesium-ATPase (see below). Recent studies on these regions, in conjunction with TnC mutants, have shown relationships between TnI regions and TnC mutants [10]. Binding studies have revealed that the N-terminal region of TnI interacts with the C-domain of TnC in the relaxed state, and that the inhibitory and C-terminal region of TnI interacts with the N-domain of TnC in a calcium dependent manner [10]. These results are summarized in figure 17. This model suggests that

TnC and TnI are always anchored in an antiparallel fashion via the N-terminal region of TnI and the C-domain of TnC. Upon the calcium induced structural change in the N-domain of TnC, several interactions are created or affected, as indicated in figure 17.

Release of actomyosin ATPase inhibition and power stroke

The primary role of TnI is to inhibit the formation of the actomyosin complex. When muscle is relaxed, TnI interacts with actin and physically prevents myosin from binding actin. As the N-domain of TnC binds calcium and the TnC-TnI interactions change, the interaction between TnI and actin weakens. The troponin-tropomyosin complex is believed to be relocated following the calcium-induced structural change in TnC, allowing the formation of the actomyosin complex and ultimately leading to the power stroke as described in figures 15 and 16. A model for this scenario is shown graphically in figure 18. Finally, the various steps involved in muscle contraction are summarized in figure 19.

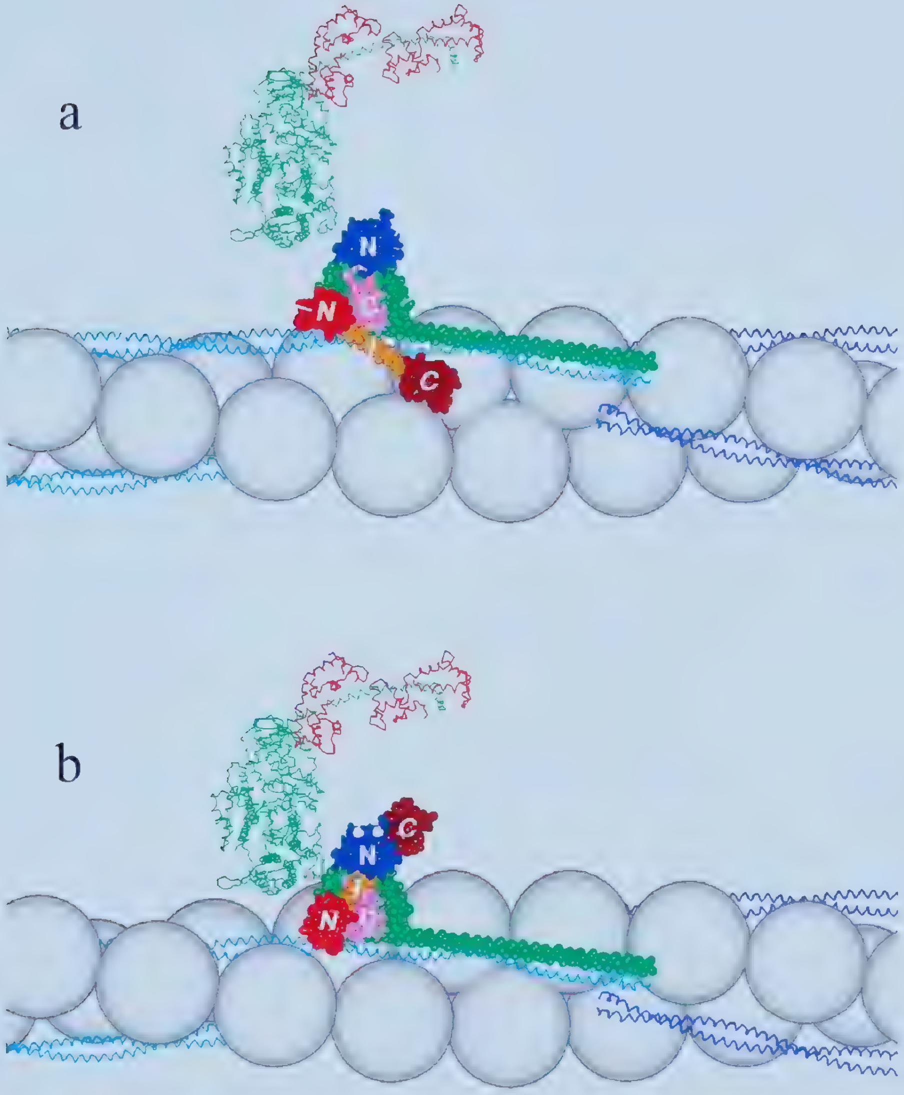

Figure 18. Model of the troponin-tropomyosin-actin organization in relaxed and contracted muscle. TnC is shown in blue for the N-domain, and pink for the C-domain. TnI is shown in red (N-domain), brown (C-domain) and yellow (inhibitory region). TnT is shown in green. Myosin is shown in green (myosin-S1), red (essential light chain) and yellow (regulatory light chain) in stick representation. Tropomyosin is shown in light and dark blue stick representation. Note that only TnC, myosin, actin, and tropomyosin have known structures. TnT and TnI structures are modeled. Actin monomers are represented by 56 Å white spheres which form a filament having 13 actin monomers per turn and a pitch of 720 Å. (*a*) Relaxed state of muscle. The C-domain of TnC is filled with magnesium. The N-terminal domain of TnI is anchored on the C-domain of TnC, whereas the inhibitory region of TnI makes contact with actin and tropomyosin. This organization keeps the thin filament in a conformation that prevents myosin from properly interacting with actin. (*b*) After two calcium ions bind to the N-domain of TnC, which in turn interacts with TnI. The inhibitory region is then released from actin. This leads to a conformation of the thin filament that allows the proper formation of the actomyosin complex.

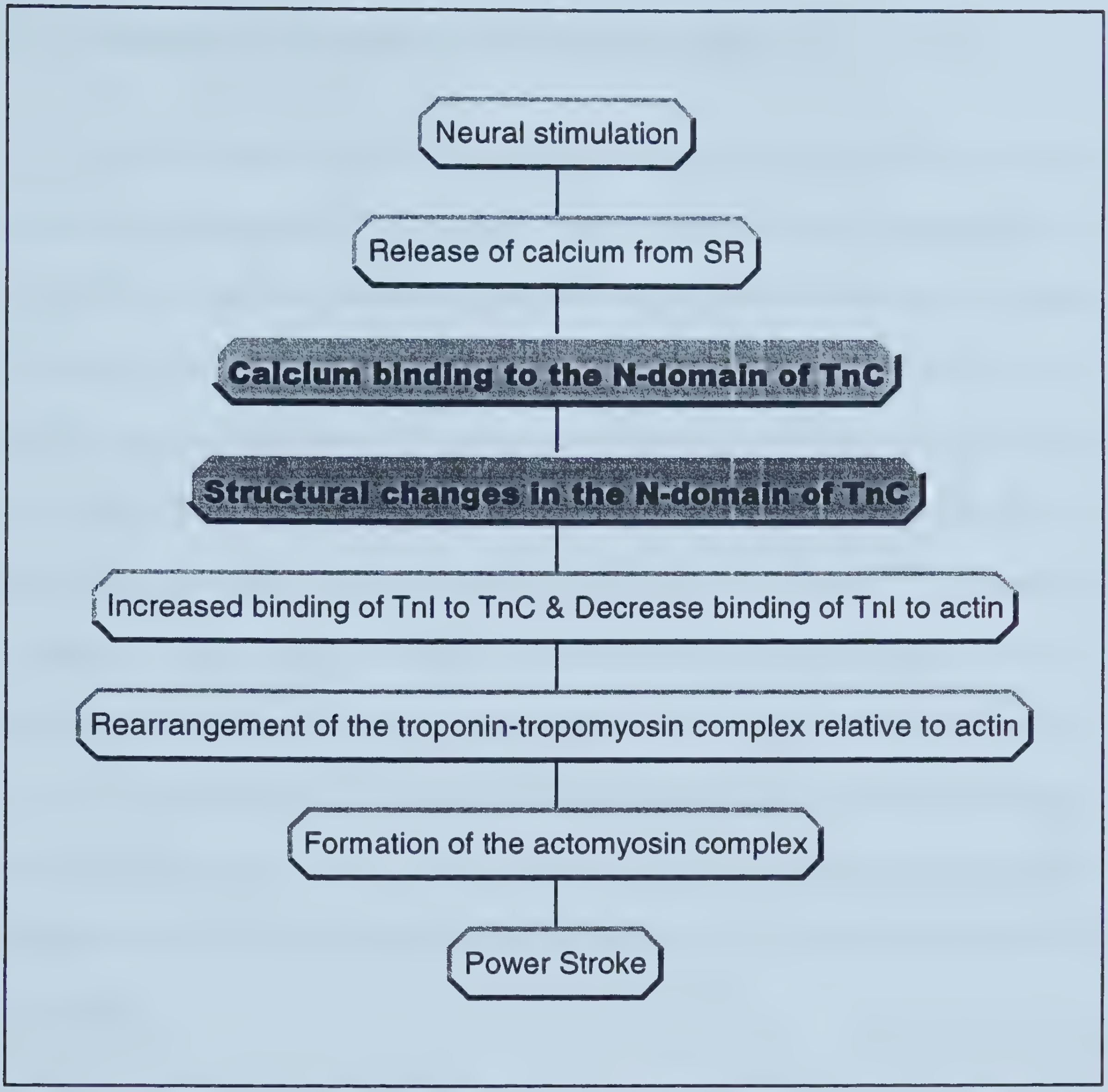
Neural stimulation
Release of calcium from SR
Calcium binding to the N-domain of TnC
Structural changes in the N-domain of TnC
Increased binding of TnI to TnC & Decrease binding of TnI to actin
Rearrangement of the troponin-tropomyosin complex relative to actin
Formation of the actomyosin complex
Power Stroke

Figure 19. Schematic representation summarizing the various steps involved in muscle contraction. The characterization of the calcium-binding and concurrent calcium-induced changes in the regulatory domain of TnC (dark box) is the theme of this thesis.

4. CHARACTERISTICS OF TROPONIN C

In 1963, Ebashi discovered a new protein factor that was necessary for the calcium sensitivity of actomyosin [16, 17]. This protein system was called 'native tropomyosin', but it was soon found that this system was a complex of tropomyosin and a new globular protein, which was named troponin [18]. Hartshorne and Mueller [19] were the first to observe that troponin was made of subunits. They obtained two fractions, which they named troponin A and troponin B. Troponin A, which also carried the name "EGTA sensitizing factor", was found to be required for calcium control of ATP hydrolysis by myosin [20, 21]. Greaser and Gergely [22, 23] later resolved troponin into three subunits and named them troponin T, troponin I and troponin C, the latter corresponding to the troponin A observed previously. In 1972, Murray and Kay [24] reported for the first time that calcium was inducing a conformational change in TnC. There are now well over 1000 [¶] publications which have reported data on TnC. This chapter summarizes some of the data relevant to the course of my research.

The sequences

Thirty-one sequences of TnC have been determined so far, going from human skeletal muscle TnC to sea squirt smooth muscle TnC. The sequence of the protein used in most of the present study, chicken sTnC, is listed in figure 20. The work presented here relates

---

[¶] The number of publication is based on search on MEDLINE

primarily to the N-domain of sTnC (sNTnC, see table 1), and the amino acid composition of sNTnC is listed in table 2. sNTnC is acidic, with 23 Asp/Glu and only 7 Arg/Lys. The various TnC isoforms which will be discussed in this thesis are highly homologous to the sequence of chicken sTnC, as illustrated in figure 21. It is worth noting that the majority of the differences between cardiac and skeletal TnC are located around site I.

Table 2. Amino acid content of sNTnC.

Amino acid	Number	Proportion
A	10	11.1
C	0	0.0
D	10	11.1
E	13	14.4
F	6	6.7
G	7	7.8
H	0	0.0
I	5	5.6
K	4	4.4
L	5	5.6
M	8	8.9
N	1	1.1
P	1	1.1
Q	4	4.4
R	3	3.3
S	4	4.4
T	5	5.6
V	4	4.4
W	0	0.0
Y	0	0.0

1 **ASMTDQQAEA RAFLSEEMIA EFKAAFDMFD ADGGGDIST K**

41 **ELGTVMRMLG QNPTKEELDA IIEEVDEDGS GTIDFEEFL V**

81 **MMVRQMKEDA** KGKSEEELAN CFRIFDKNAD GFIDIEELG E

121 ILRATGEHVT EEDIEDLMKD SDKNNDGRID FDEFLKMME G

161 VQ

Figure 20. Sequence of chicken skeletal TnC. The first 90 residues corresponding to sNTnC are shown in **bold**.

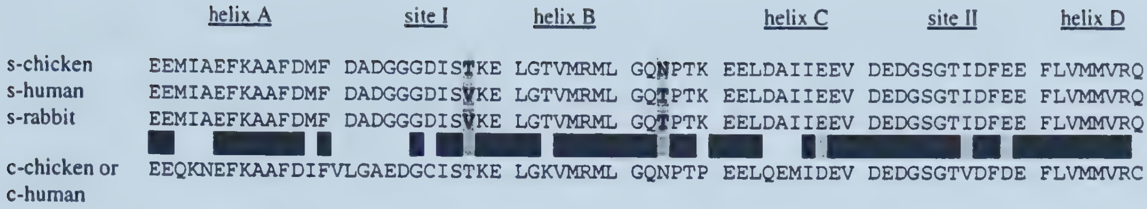

```
                helix A           site I       helix B              helix C         site II      helix D

s-chicken     EEMIAEFKAAFDMF DADGGGDISTKE LGTVMRML GQNPTK EELDAIIEEV DEDGSGTIDFEE FLVMMVRQ
s-human       EEMIAEFKAAFDMF DADGGGDISVKE LGTVMRML GQTPTK EELDAIIEEV DEDGSGTIDFEE FLVMMVRQ
s-rabbit      EEMIAEFKAAFDMF DADGGGDISVKE LGTVMRML GQTPTK EELDAIIEEV DEDGSGTIDFEE FLVMMVRQ

c-chicken or  EEQKNEFKAAFDIFVLGAEDGCISTKE LGKVMRML GQNPTP EELQEMIDEV DEDGSGTVDFDE FLVMMVRC
c-human
```

Figure 21. Sequence comparison between some of the N-domains in skeletal (s-) and cardiac (c-) TnC. (X) indicates sequence variation between different skeletal species; (▮) and (▯) indicates sequence identity and sequence similarity, respectively, between skeletal and cardiac N-domain. Note that helix N is not shown.

The binding of calcium to sTnC

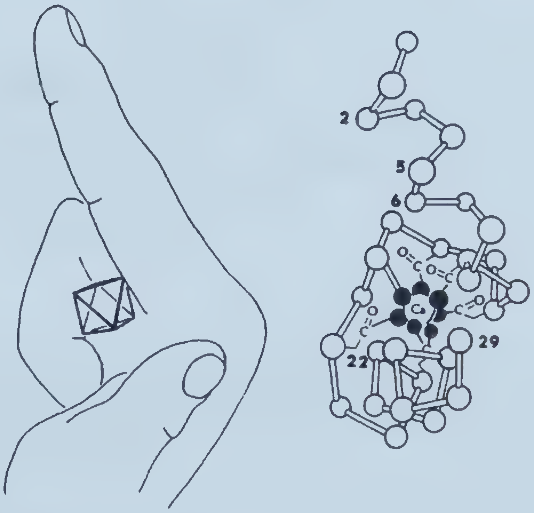

Figure 22. The EF-hand calcium-binding motif. The three-dimensional structure of the EF-hand site can be simulated by the right hand, with the extended thumb and index finger representing the α-helices and the middle finger indicating the calcium-binding loop. [Adapted from *Protein Profile, Calcium-binding Proteins 1: EF-hands*; Kawasaki & Kretsinger]

The family of EF-hand calcium-binding proteins is the largest class of calcium-binding proteins, and includes more than 250 proteins [1]. All EF-hand calcium-binding proteins share a common structural motif: a calcium-binding loop flanked by two α-helices. The designation 'EF-hand' derives from a description of a calcium-binding site in parvalbumin which is formed by helix E, a loop, and helix F. The three-dimensional structure of this calcium binding site can be simulated by the right hand, with the extended thumb and index finger representing the α-helices and the bent middle finger

indicating the calcium-binding loop (figure 22). This motif is often referred as the helix-loop-helix motif (HLH). A typical EF-hand consists of an α-helix (residues 1-10), a 12 residues site which binds calcium (residues 10-21), and a second α-helix (residues 19-21). Calcium ions are coordinated by seven oxygens which are furnished by side-chains, peptide backbone carbonyls, and bridging water molecules. The coordination geometry is a pentagonal bipyramid, as illustrated in figure 23. EF-hands are typically paired and connected in space through a short antiparallel β-sheet.

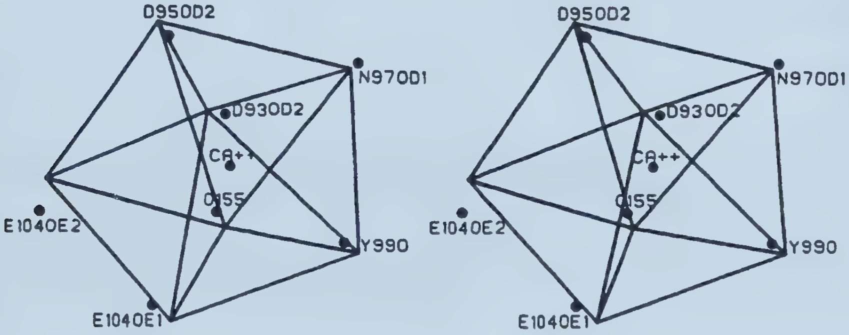

Figure 23. Stereoview representation of the oxygen atom ligands of calcium-binding site III in calmodulin superimposed onto an ideal pentagonal bipyramid. [Adapted from *Annu. Rev. Biochem.* 1989, 58:951-98; Strynadka & James]

EF-hand calcium-binding proteins are found in all living organism, from prokaryotes to eukaryotes. Most are localized within the cell, although some can be found in the blood stream (e.g. S100β). Some EF-hand proteins are restricted to specific cells, such as TnC (muscle cells), whereas others are present ubiquitously, such as calmodulin (present in all eukaryotic cells). There are three main functional aspects which can be assigned to EF-hand calcium binding proteins: mediation of calcium signals (e.g. TnC and calmodulin), direct

calcium-dependent enzymatic activity (e.g. calpain), and buffering of the cytosolic calcium concentration (e.g. parvalbumin and calbindin-D_{9k}). Table 3 lists some of the properties of the EF-hand proteins which will be discussed later.

Table 3. Properties of some EF-hand calcium-binding proteins.

Name	**# of residues**	**Number of calcium-binding sites** [a]				**domain**	**structure** [b]		**calcium-induced structural change** [c]
		1	2	3	4		apo	Ca^{2+}	
troponin C	162	±	+	+	+	N:	Y	Y	opening
						C:	U	Y	folding
calmodulin	148	+	+	+	±	N:	Y	Y	opening
						C:	Y	Y	opening
calbindin-D_{9k}	89	+	+				Y	Y	minor
S100β	91	+	+				Y	Y	minor

[a] (+) indicates a calcium-binding site; (±) indicates a calcium-binding site depending on the species or tissue. [b] (Y) indicates that the structure is solved; (U) indicates unfolded. [c] (opening) indicates a large calcium-induced structural change involving the opening of the structure; (folding) indicates calcium-induced folding of structure; (minor) indicates a small calcium-induced structural change, meaning that the calcium-bound structure stays in the closed conformation.

sTnC possesses 4 of these calcium-binding motifs, and their respective sequence is shown in figure 24. Sites III and IV have relatively high affinity for calcium ($K_{Ca} \approx 2\times10^7$ M^{-1}) and also bind magnesium ($K_{Mg} \approx 2\times10^3$ M^{-1}). The two binding sites of the N-domain (sites I and II) are specific to calcium and are of lower affinity. In the literature, controversial results may be found regarding the binding affinity and the cooperativity of the low affinity sites. Some groups report cooperative coupling between sites I and II, while others propose that the binding process is sequential. The determined published binding affinity varies between 10^4 and 10^5. However, a recent detailed NMR study on sNTnC has quantitatively determined the binding constants in sites I and II [25]. A calcium titration which was

monitored by 2D ^{15}N,^{1}H-HMQC experiments has revealed a stepwise binding for sNTnC with affinities (K_{Ca}) of 6.3×10^{4} and 5.9×10^{5} M^{-1}.

site I	AEFKAAFDMF	**D**A**D**GGG**D**I**S**TK**E**	LGTVMRMLG
site II	EELDAIIEEV	**D**E**D**G**S**G**T**I**D**FE**E**	FLVMMVRQM
site III	EELANCFRIF	**D**K**N**A**D**G**F**I**D**IE**E**	LGEILRATG
site IV	EDIEDLMKDS	**D**K**N**N**D**G**R**I**D**FD**E**	FLKMMEGVQ
consensus	EE--------	**D**----G-I**D**--**E**	----M----

Figure 24. Alignment of the four EF-hands in chicken sTnC. The calcium binding sites are in the middle segments, with residues involved in calcium coordination shown in bold.

Previously known structures of TnC

This section presents an overview of TnC structures which were known prior to the beginning of this thesis work.

X-ray structures of sTnC in the Ca_2 state

The crystal structures of both chicken and turkey sTnC were solved in 1985 [26,27] and refined to 2.0 Å in 1988 [12, 28]. As shown in figure 14, these 65% α-helical structures have two globular domains connected by a single 31 residue long central helix. The N-domain has five helices (N, A, B, C, and D), whereas the C-domain has four helices (E, F, G, and H). The two calcium binding loops of each domain are coupled via a short β-sheet. As noted earlier, in these structures only sites III and IV in the C-terminal domain are occupied by calcium, whereas the regulatory sites I and II in the N-domain are in the apo state. This

structure will therefore be referred as sTnC•Ca$_2$ [¶]. Although both domains are highly homologous, the helix packing is different in the two domains. The structure of the calcium-bound C-domain was found to be very similar to other homologous calcium-binding proteins [15]. However, the apo N-domain was considerably different, mainly in terms of interhelical angles [15]. Table 4 compares the interhelical angles of the N-domain of TnC with a few calcium-bound protein structures, and clearly indicates that the A/B and C/D interhelical angles vary considerably.

Table 4. Interhelical angle differences between the N-domain of sTnC and other calcium-binding proteins.

Helix pair	**others (range)** [a]	**N-domain TnC**	**Δ** [b]
A/B or E/F	96-109	134	**32**
B/C or F/G	111-124	122	5
C/D/ or G/H	84-108	146	**49**
A/D or E/H	110-123	115	2

[a] includes sTnC (C-domain only), calmodulin (2 pairs) and parvalbumin.

[b] difference between the N-domain of sTnC and the average of the four related pairs.

NMR structures of sTnC peptides

The first TnC structures to be solved by NMR were of peptides corresponding to the calcium-binding sites of the C-domain of sTnC [29]. In 1991, the structure of a 39 amino acid proteolytic fragment of rabbit sTnC was solved by the Kay family (Lewis E. Kay, Julie D. Forman-Kay and Cyril M. Kay) [30]. This fragment includes residues 121-159 of rabbit sTnC, corresponding to residues 124-162 of avian sTnC. The helix-loop-helix motif corresponds to the fourth calcium-binding site in sTnC, and dimerizes upon calcium-binding. The global fold of this IV-IV homodimer is remarkably similar to the global fold of the C-domain in the

---

[¶] The abbreviated nomenclature for the several structures used in this thesis is described in the abbreviation section.

sTnC•Ca_2 structure [30]. However, the interhelical angle of the G/H helices in the IV-IV homodimer is about 20° more open than the G/H helices in the crystal structure.

In 1992, Shaw et al. [31] solved the structure of a 34 amino acid synthetic peptide corresponding to the third calcium-binding site of chicken sTnC (residues 93-126). As for the IV-IV homodimer, calcium-binding induces dimerization of this peptide to form the so-called III-III homodimer. The global fold of the III-III homodimer is similar to the wild-type (figure 25). The interhelical angle of this dimer of E-F helices is more closed by about 10° compared to the wild-type, and therefore by about 30° compared to the IV-IV homodimer. More recently, Shaw and Sykes [32] solved the solution structure of another calcium-bound synthetic dimer; this one is of a synthetic III-IV heterodimer (residues 93-126 and 129-162 of chicken sTnC). The III-IV heterodimer is identical in sequence to the C-domain of sTnC with a break of two residues between helix-F and helix-G. Structurally, the III-IV heterodimer is very like the wild-type (figure 25). Unlike the homodimers which have differences in interhelical angle of +10° (III-III) or -20°(IV-IV) with wild-type, the III-IV heterodimer has an identical degree of opening compared to the crystal structure of the wild-type.

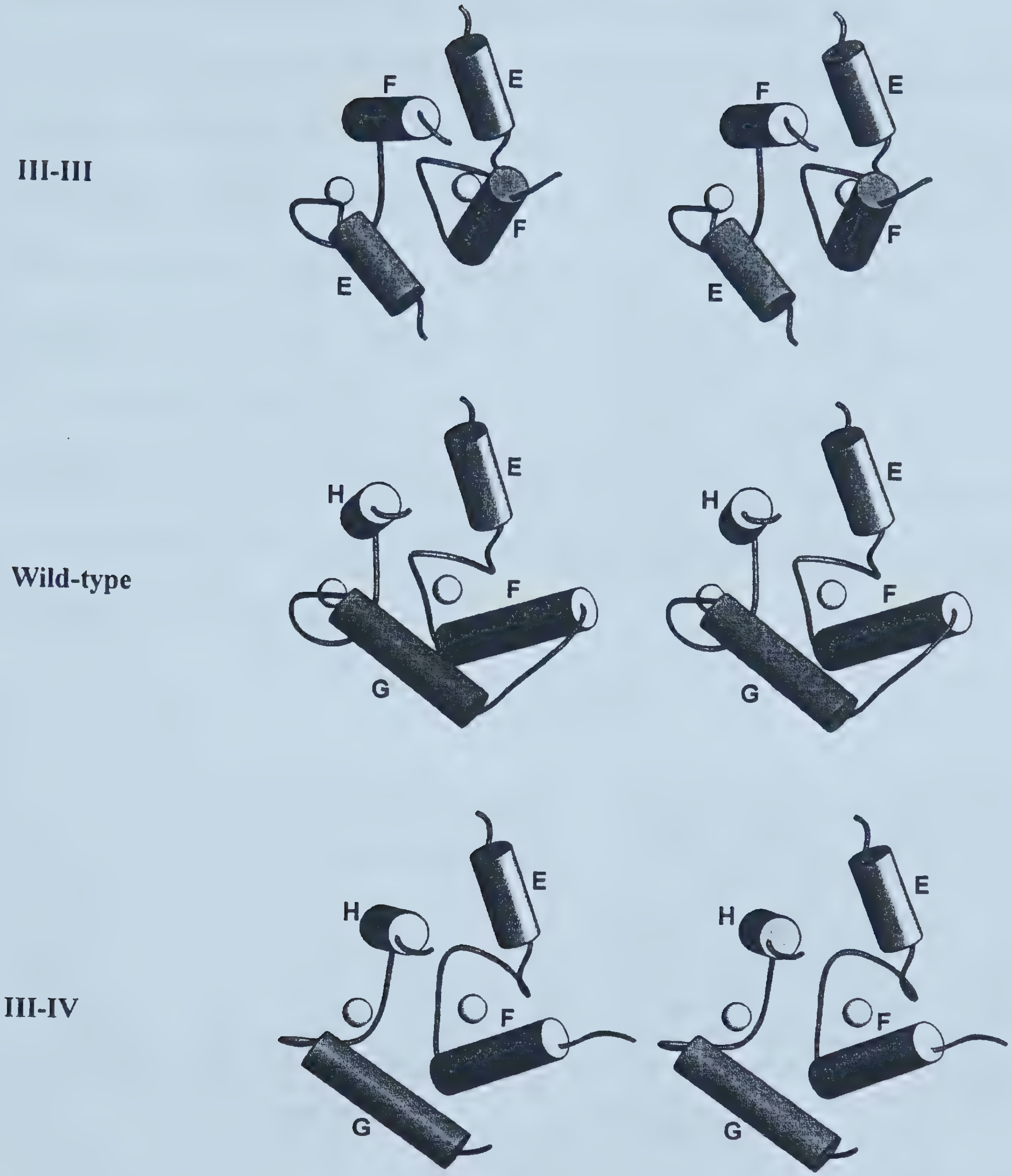
III-III
F
E
F
E
F
E
F
E
Wild-type
H
E
F
G
H
E
F
G
III-IV
H
E
F
G
H
E
F
G

Figure 25. Structures of sTnC peptides. The NMR structures of the III-III homodimer (top) and III-IV heterodimer (bottom) are compared with the X-ray structure of the C-domain of sTnC. All three structure were solved in the calcium-bound state. Structures are shown with helices E/H in similar orientation. Helical segments are represented by cylinders, and calcium ions are shown as spheres.

NMR structure of the proteolytic fragment TR$_1$C in the apo state

In 1994, Findlay et al. [33] published the solution structure of TR$_1$C•apo, a proteolytic fragment of turkey skeletal TnC (residues 12-87). The fragment corresponds to the N-domain of sTnC minus the N-terminal helix. Although helix C is well-defined by itself in the TR$_1$C•apo structure (figure 26), its orientation relative to the other helices is not. It was not clear at the time if helix C really possessed structural heterogeneity in solution. Based on a more recent analysis of the NOE data (B.D. Sykes, unpublished data) and on information presented later in this thesis, it is now believed that the lack of definition of helix C was a consequence of overlapping NOE peaks which could not be unambiguously assigned from homonuclear NMR spectra.

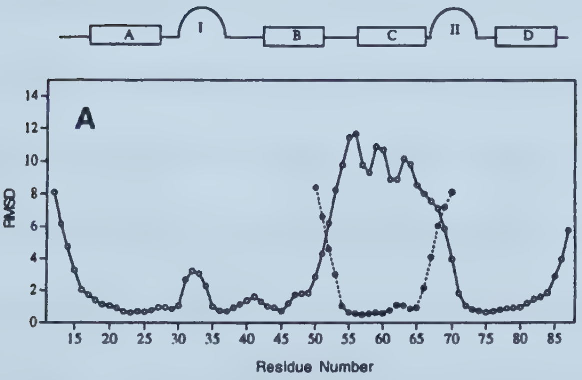

Figure 26. Plot of backbone rmsd in 20 structures of TR$_1$C. The open circles correspond to where helices A, B, and D were superimposed, the closed circles correspond to where helix C was superimposed. This plot clearly indicates that although helix C is well-structured in this NMR structure, its position relative to the rest of the molecule is not defined. As explained in the text, this is now believed to be an artifact due to incomplete experimental data.

Calcium induced conformational changes

Early evidences of conformational changes

Evidence of the calcium induced conformational changes in sTnC was first observed more than 25 years ago in this department (Biochemistry, University of Alberta). In 1972, Murray and Kay [24] used CD spectroscopy to demonstrate that the binding of calcium induced a conformational change in sTnC (or more accurately the ancestor of troponin C, troponin A). Over the years, ^{1}H NMR spectroscopy has been used extensively to characterize the structural changes of the two domains of sTnC. These studies have shown that binding of calcium to the high affinity sites (C-domain) induces changes in the protein fold, and that binding to the low affinity sites (N-domain) leads mainly to changes among hydrophobic side-chains [34-39]. Laser Raman spectroscopy was used, and revealed a large increase in α-helical content due to calcium-binding to the C-domain sites, and none associated to the N-domain [40]. Other studies, using CD and fluorescence, reported large spectroscopic changes associated with calcium binding to the C-domain, and small changes when the low affinity sites were filled [41-45]. These studies reported a large increase of negative ellipticity when sites III and IV are filled, consistent with the NMR results. The estimates of the magnitude of the calcium induced far-UV CD ellipticity changes attributable to the N-domain transition were more subtle, less clearly defined, and somewhat contradictory. A more recent characterization of the calcium induced spectroscopic changes of the recombinant sNTnC clearly indicated a significant increase in the negative far-UV CD ellipticity [46] (figure 27). These data suggested that the binding of calcium to the N-domain induced a significant

increase in α-helix content. However, one of the outcomes of my previous work [2, 47] is that binding of calcium to sNTnC does not affect the secondary structure content, and that the spectral changes seen by CD are most likely due to the reorientation of the α-helices relative to each other [2, 47].

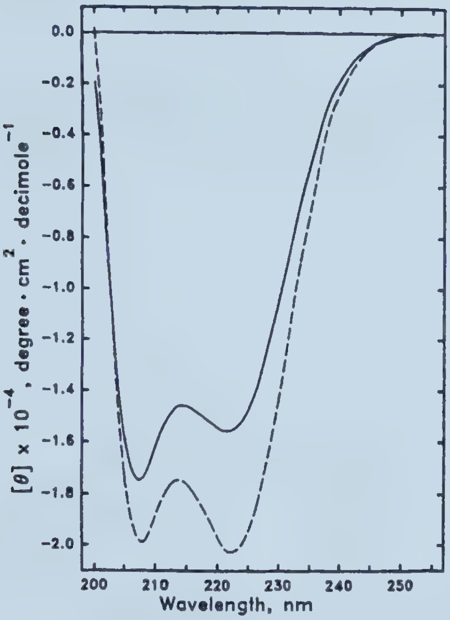

Figure 27. Far-UV CD spectra of recombinant sNTnC in the absence (—) and presence (----) of calcium. The binding of calcium induces a significant increase (~23%) in the negative values of $[\theta]_{221nm}$.

HMJ model for the calcium-induced structural change

By comparing the crystal structure of the apo N-domain of sTnC•Ca_2 with its homologous calcium-bound C-domain (see figure 28), Herzberg et al. proposed the HMJ-model for the conformational change which occurs in the N-domain of TnC upon calcium-binding [48]. Using molecular modeling and the assumption that the calcium-filled N-domain would adopt a conformation similar to the calcium-filled C-domain, they deduced a model structure of sTnC in the Ca_4 state (sTnC^{HMJ}•Ca_4). The major conformational change in their model is the movement of the B/C pair of helices away from the A/D pair, therefore exposing

a hydrophobic patch (figure 29). This model was to be the only structural representation of the calcium-saturated form of the regulatory domain of sTnC for nearly 10 years.

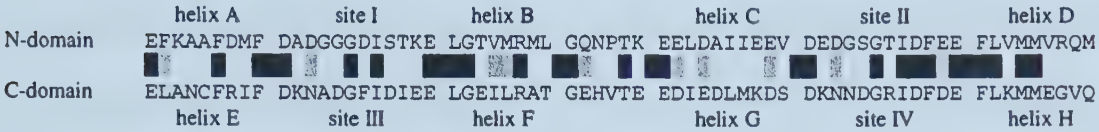
helix A
site I
helix B
helix C
site II
helix D
N-domain
EFKAAFDMF DADGGGDISTKE LGTVMRML GQNPTK EELDAIIEEV DEDGSGTIDFEE FLVMMVRQM
C-domain
ELANCFRIF DKNADGFIDIEE LGEILRAT GEHVTE EDIEDLMKDS DKNNDGRIDFDE FLKMMEGVQ
helix E
site III
helix F
helix G
site IV
helix H

Figure 28. Sequence comparison between the two domains in sTnC. (▮) and (▨) indicates sequence identity and sequence similarity, respectively. Note that helix N is not shown here for the N-domain.

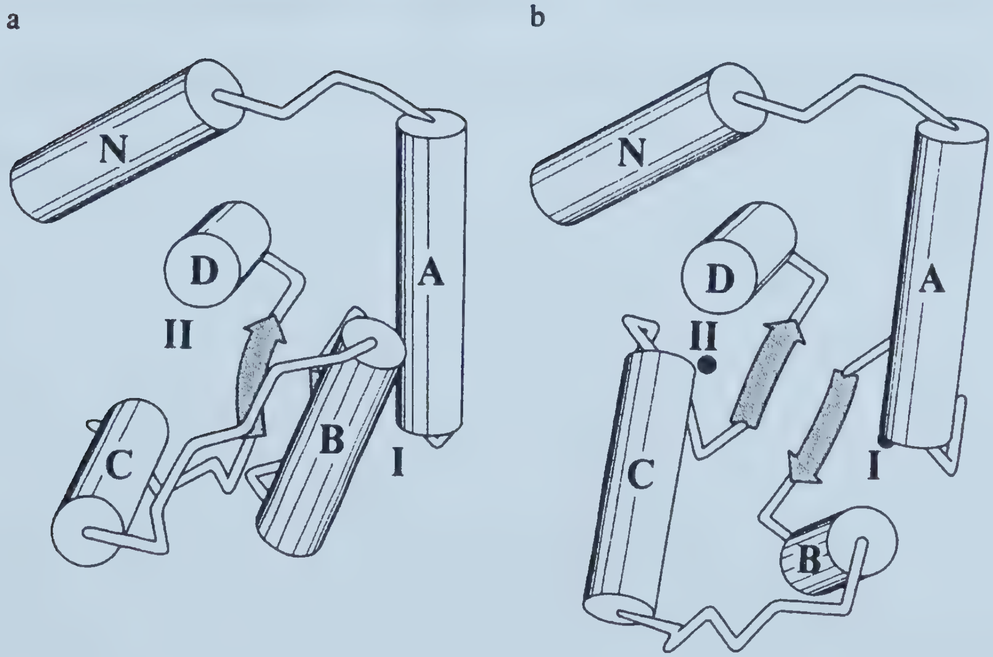
a
b
N
A
D
II
C
B
I
N
A
D
II
C
I
B

Figure 29. Diagrammatic representation of the proposed calcium-induced conformational change in the N-domain of sTnC. In this model helices N, A, and D retain their relative dispositions. Helices B and C and the BC linker peptide move by up to 14 Å when calcium binds. The relative dispositions of helices B and C also remain constant. (a) Calcium-free conformation of the N-domain of sTnC. (b) HMJ model proposed for the calcium-bound conformation of this domain. [Adapted from *Annu. Rev. Biochem.* 1989, 58:951-98; Strynadka & James]

Preliminary NMR structures of apo and calcium saturated sNTnC

In my 1994 Master's thesis [2], I presented preliminary solution structures of apo and calcium saturated sNTnC. This was the first experimental characterization of the calcium-induced structural change in the regulatory domain of sTnC. The calcium-induced opening which was derived from these low resolution structures was similar to the HMJ model described above. Although there were some differences with respect to the HMJ model, the NMR structures needed to be refined before conclusions could be made. As noted in my previous thesis, these results were preliminary and needed more refinement, and therefore the low resolution solution structures were included only as "Note added in proof" [2].

These structures have been refined since, and will be described in detail in the next chapter.

SECTION TWO: STRUCTURAL ASPECTS OF TNC

5. Refined characterization of the calcium-induced structural change in sTnC 37
6. Structure of E41A-sNTnC•Ca_2 66
7. Mechanism of the calcium-induced structural change in sNTnC 83
8. Cardiac TnC 88
9. Structural comparison with other calcium-binding proteins 96

5. REFINED CHARACTERIZATION OF THE CALCIUM-INDUCED STRUCTURAL CHANGE IN STNC

Refined NMR structures

I have solved by NMR spectroscopy the structure of the regulatory domain of sTnC (residues 1-90) in the calcium form (sNTnC•Ca_2). Additionally, in collaboration with Dr. Sakae Tsuda, I have obtained a low resolution solution structure of the apo form of sNTnC (sNTnC•apo). I present here what was, at the time, the only experimental structural description of this skeletal muscle contraction switch.

Relevance of structures.

An obvious question is whether the calcium-induced structural change in sNTnC, as presented here, represents what occurs during muscle contraction before drawing any conclusions. The first concern is whether or not the isolated regulatory domain behaves as in whole sTnC. This question has been addressed previously with every indication that the properties of isolated sNTnC are the same as those of the N-domain in the intact protein [46]. A second concern is that a fraction of sNTnC•Ca_2 exists as a dimer in solution under the conditions used [49]. In the experimental data used for structure calculation, intra and inter molecular NOE's were not distinguishable. I therefore performed a 2D-$^{12}C/^{13}C$ doubly filtered NOESY experiment [50] on a sample containing a 1:1 ratio of unlabeled:$^{15}N/^{13}C$-labeled sNTnC•Ca_2 in order to identify and exclude the small number of possible inter molecular NOEs from the calculations. Also, the small and localized chemical shift changes

(^{1}H, ^{13}C, ^{15}N) observed when going from a dimeric form of sTnC to a monomeric form (in the presence of TFE) [49] indicate that dimerization does not significantly affect the structure of sTnC. I am therefore confident that the structures reported herein provide a valid representation of the calcium-induced structural transition in the regulatory domain of sTnC.

Description of structures

The structures of sNTnC•apo and sNTnC•Ca$_2$ were solved based on the NMR experimental restraints which are summarized in table 5; the approach used is described in the Methods section (page 58). The resulting structures, superimposed on their average, are shown in figure 30a and 30b, respectively. Both structures consist of five helices (N, A, B, C, and D), and two calcium binding loops (site I and II) connected by a short β-strand, as was determined in the NMR study of secondary structure [2,47] and in the crystal structures of the apo N-domain [12,28]. The number of NOE violations (> 0.2 Å) per structure is 0.30 and 0.07 and reflects the agreement between the structures generated and the experimental data. The Ramachandran plots (figure 31 and table 5) indicate that the structures have a good backbone geometry. The rmsd statistics are summarized in table 5 and plotted in figure 32. Additionally, the per-residue distribution of the φ/ψ dihedral angles in the family of structures is shown in detail in figure 33 and 34 for sNTnC•apo and sNTnC•Ca$_2$, respectively. The analysis of the rmsd statistics indicates the following: 1) the five helices are individually well defined (rmsd < 0.3 Å), and their relative orientations are also well defined but to a lesser extent (overall rmsd ~0.7 Å); 2) the calcium-binding sites are better defined in sNTnC•Ca$_2$, mostly due to the inclusion of restraints to the calcium ligands. It is

interesting to note that although there is a two-fold difference in distance restraints for the two states of sNTnC (table 5), the rmsd numbers are similar. One potential explanation for this observation is that most of the additional information in the sNTnC•Ca_2 data comes from intra-residue and short range NOEs (table 5). These NOEs are mainly useful to define helices in the present case, and since helices are already well defined in the apo structure with less NOEs, the gain is not expected to be that significant. Also, it is likely that an open structure, like sNTnC•Ca_2, requires more NOEs than a more compact structure, like sNTnC•apo, to achieve the same definition.

Table 5. Characteristics of the solution NMR structures of apo and calcium-loaded sNTnC.

Characteristic	**sNTnC•apo**	**sNTnC•Ca$_2$**
Distance restraints		
Total	788	1549
Intra-residue (i=j)	352	775
Sequential ($\lvert i-j \rvert=1$)	191	332
Medium range ($1<\lvert i-j \rvert<5$)	119	245
Long range ($\lvert i-j \rvert \geq 5$)	126	186
To calcium [a]	0	11
Dihedral restraints	64 φ, 54 ψ	58 φ, 60 ψ
Restraints violation		
Distance > 0.2 Å	12 (0.30 / str.)	3 (0.07 / str.)
Dihedral > 1°	2 (0.05 / str.)	2 (0.05 / str.)
RMSD [b] (Å)		
Well-defined regions (backbone)	0.65±0.14	0.70±0.11
Well-defined regions (heavy)	1.21±0.14	1.24±0.15
Helix [c]	0.25±0.08	0.27±0.08
Site I (res. 30-41)	0.83±0.20	0.62±0.15
Site II (res. 66-77)	0.80±0.25	0.45±0.13
φ/ψ in most favored region [d] (%)	90.5	83.8

[a] The distance restraints (five in site I, six in site II) to calcium ions were based on the coordination of calcium in the crystal structures of sTnC and other homologous proteins. [b] rmsd are root mean square deviations to the average structure. Well-defined regions include residues 6-30, 35-66, 72-87 for sNTnC•apo, and residues 6-32, 35-48, 54-86 for sNTnC•Ca$_2$. [c] The average of the five rmsd's obtained when each helix is superimposed separately to its average. [d] Percentage of the residues in average structure which are in the most favored region of the Ramachandran plot, as determined by the program PROCHECK.

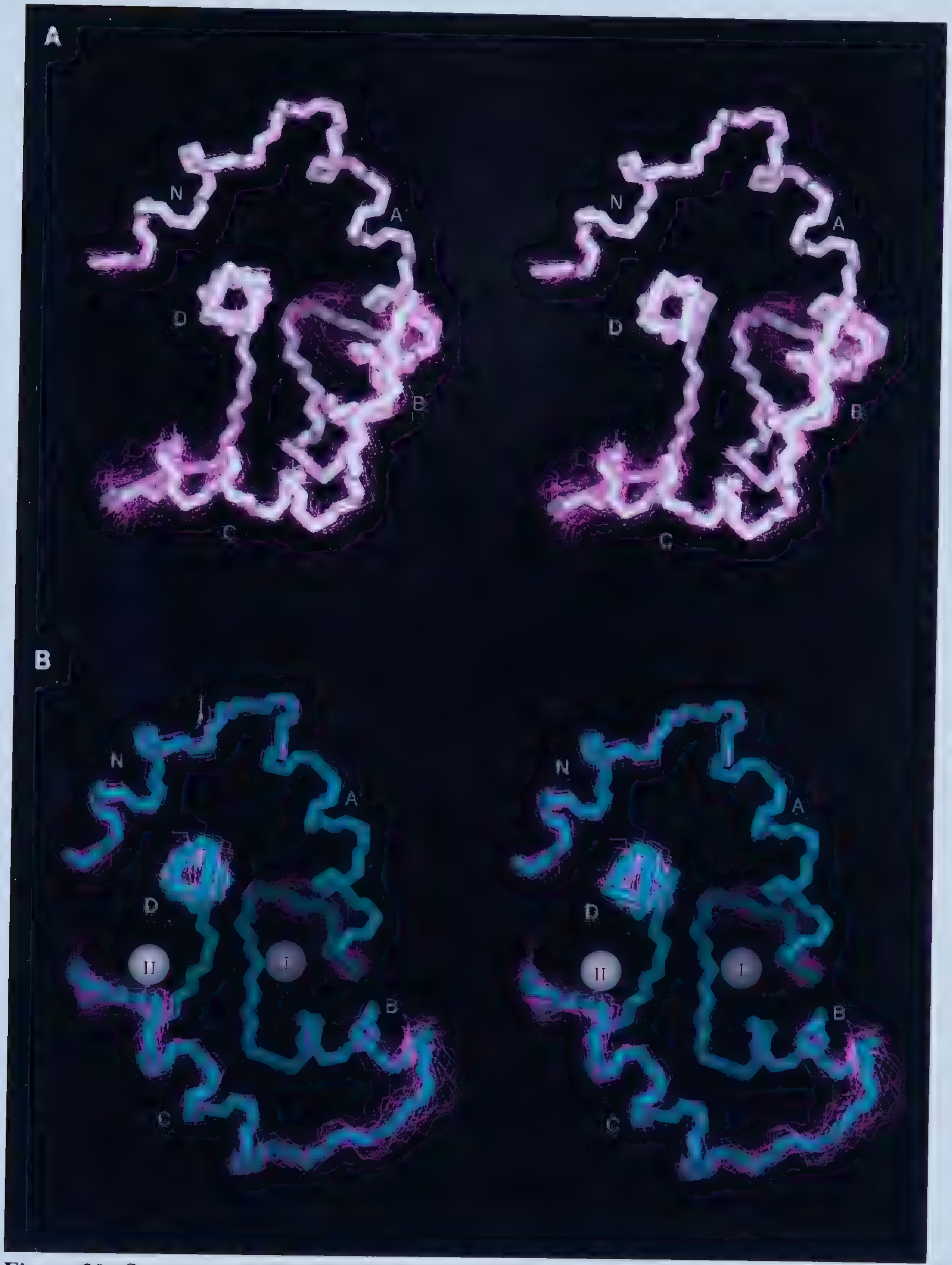

Figure 30. Structure of sNTnC. (*a*) backbone representation (residues 6-86) of the 40 *DGII* NMR structures of sNTnC•apo superimposed on their average. Helices N, A, B, C, and D are very well defined, whereas the calcium binding loop are not, especially site I which has three consecutive glycines. (*b*) backbone representation (residues 6-86) of 40 *DGII* NMR structure of sNTnC•Ca_2 superimposed on their average. As for sNTnC•apo, helices N, A, B, C, and D are well defined. Unlike sNTnC•apo, the binding loops are relatively well defined, as shown by a smaller distribution of the backbone around the average structure. The position of the calcium ions in the average structure are shown as CPK.

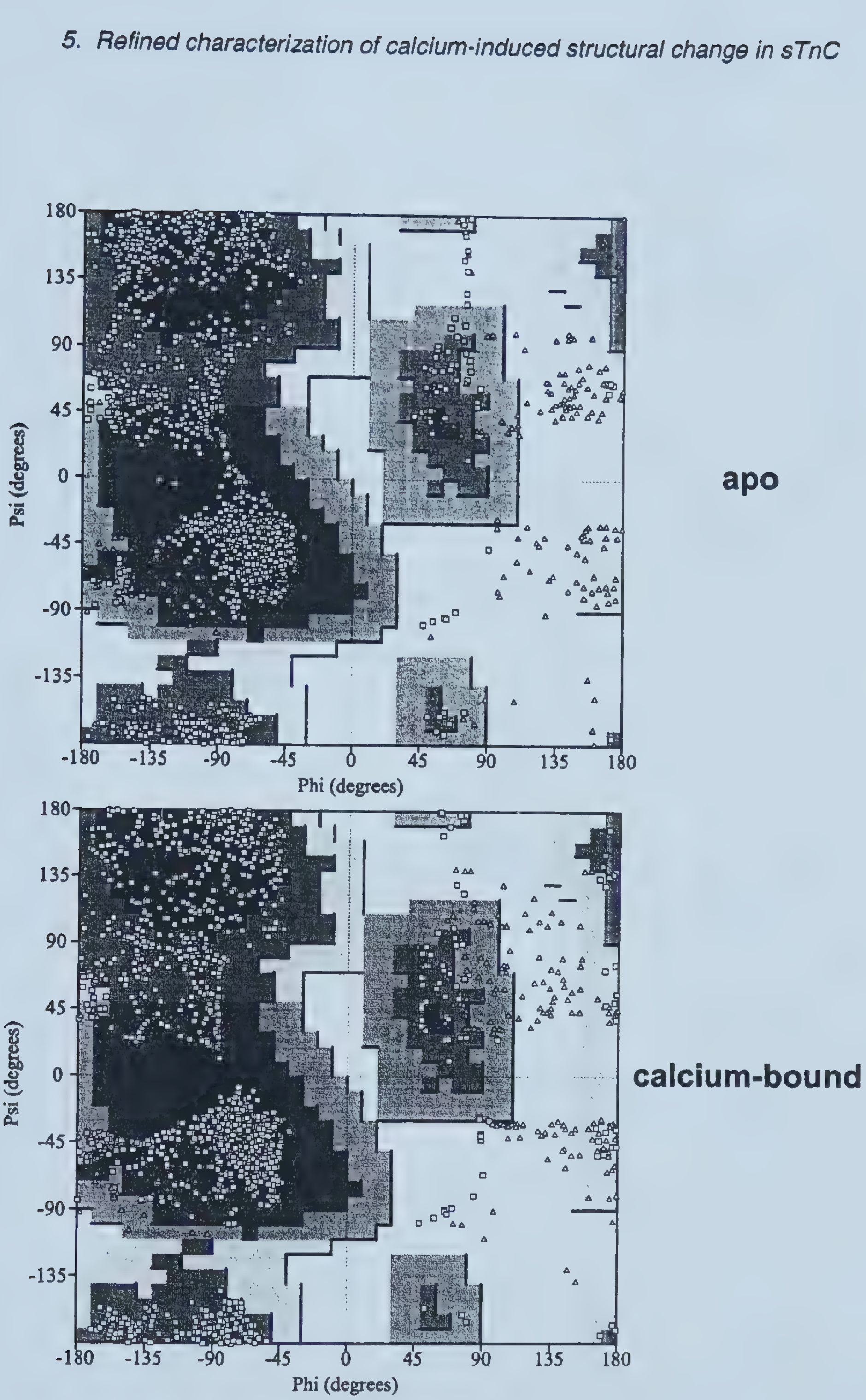

Figure 31. Ramachandran plots for the 40 sNTnC•apo (top) and 40 sNTnC•Ca$_2$ (bottom) NMR structures. Triangles represent glycine residues. The shading is as follows: most favored regions (two darkest regions); additional allowed regions (medium gray); generously allowed regions (light gray)

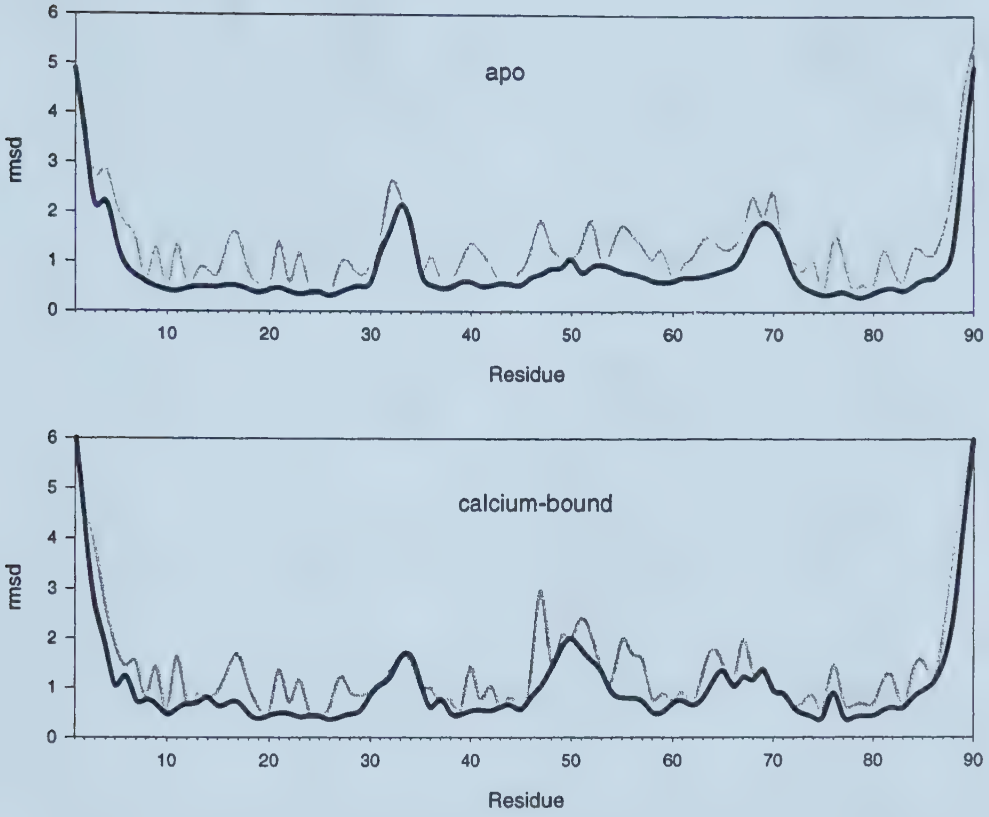

Figure 32. Rmsd plot for the family of NMR structures of sNTnC•apo (top) and sNTnC•Ca_2 (bottom). The dark lines correspond to backbone rmsd, and the gray lines correspond to heavy atom rmsd.

Figure 33. *(shown on the next five pages)* Per-residue Ramachandran plots of the NMR structure of sNTnC•apo. Each square in each Ramachandran plot represents one of the forty structures generated. These plots clearly indicates which regions are well-defined in NMR structures. The secondary structure elements are: helix N (6-13), helix A (16-29), helix B (39-48), helix C (55-64), helix D (75-86), β-sheet (36-38 & 72-74). The calcium-binding sites are residues 30-41 and 66-77.

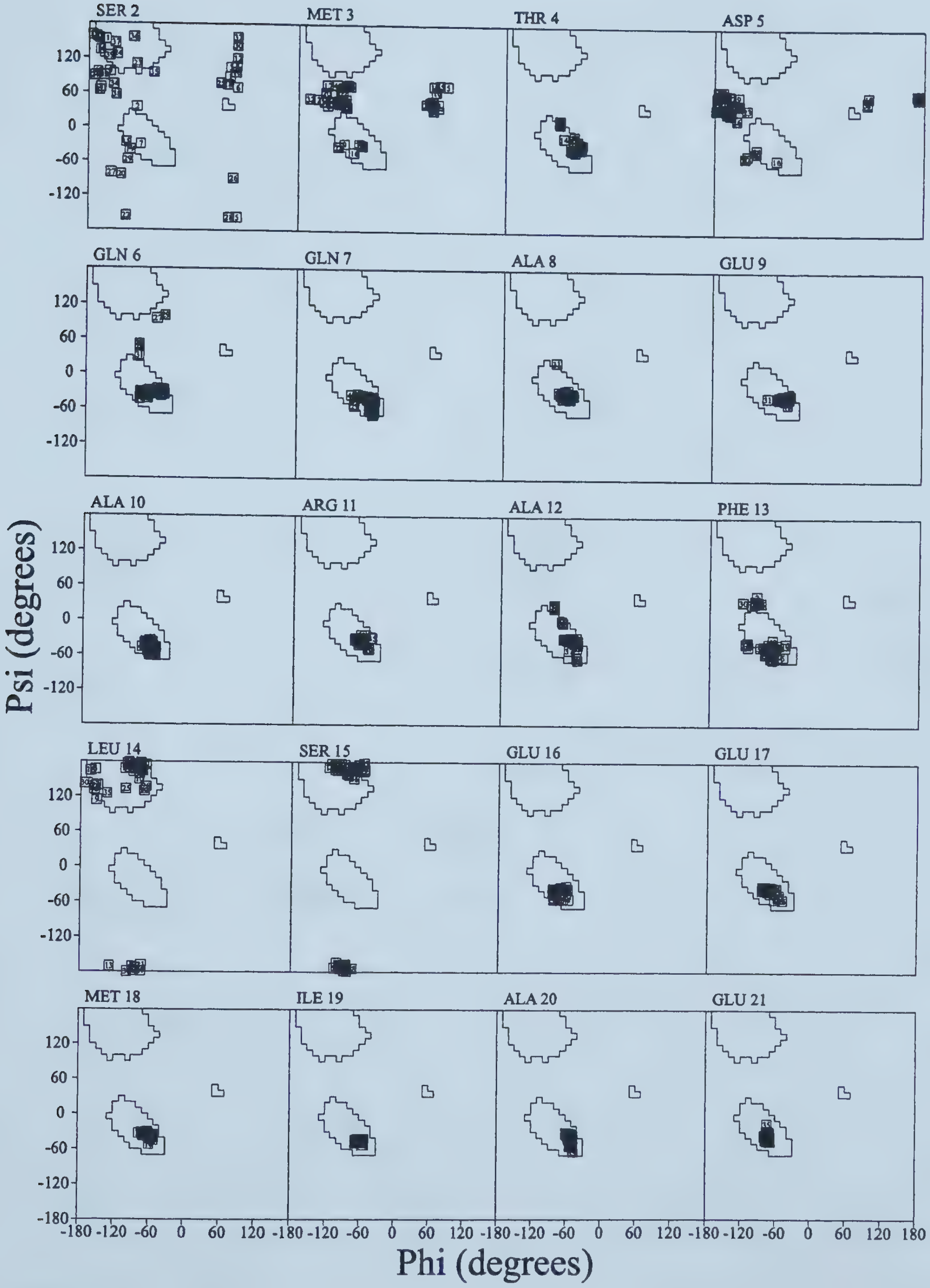

Figure 33. (part 1 of 5)

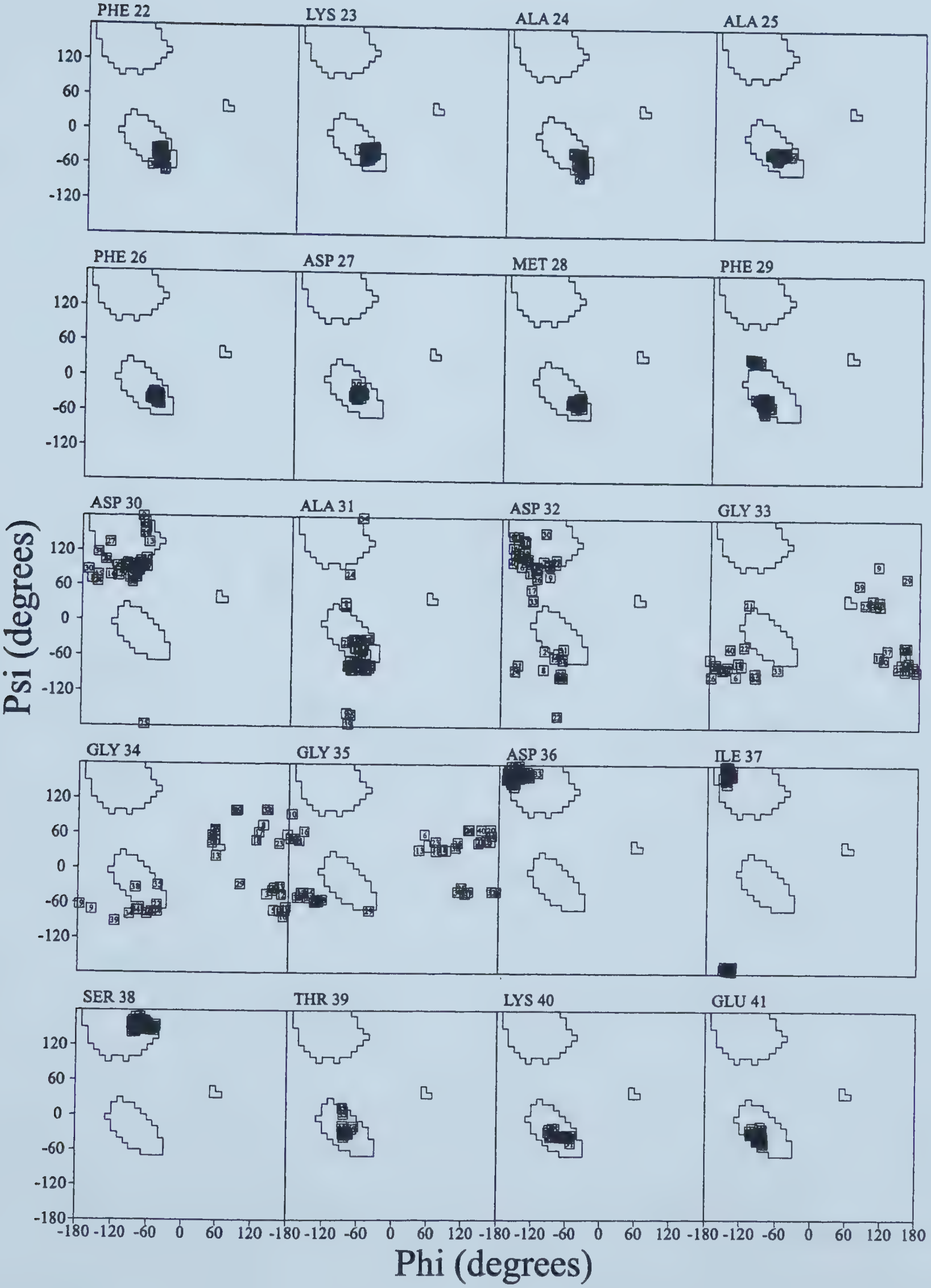

Figure 33. (Part 2 of 5)

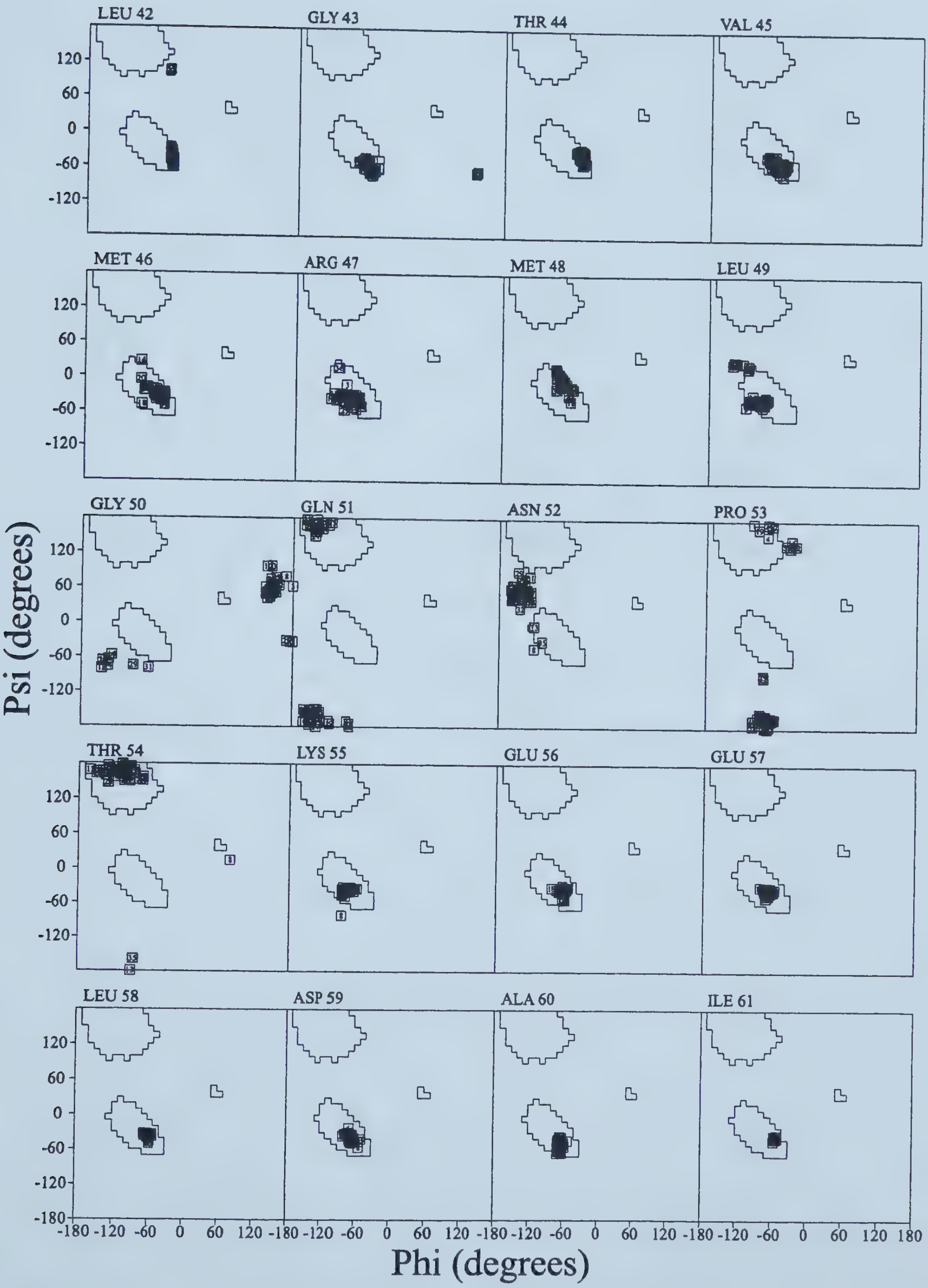

Figure 33. (Part 3 of 5)

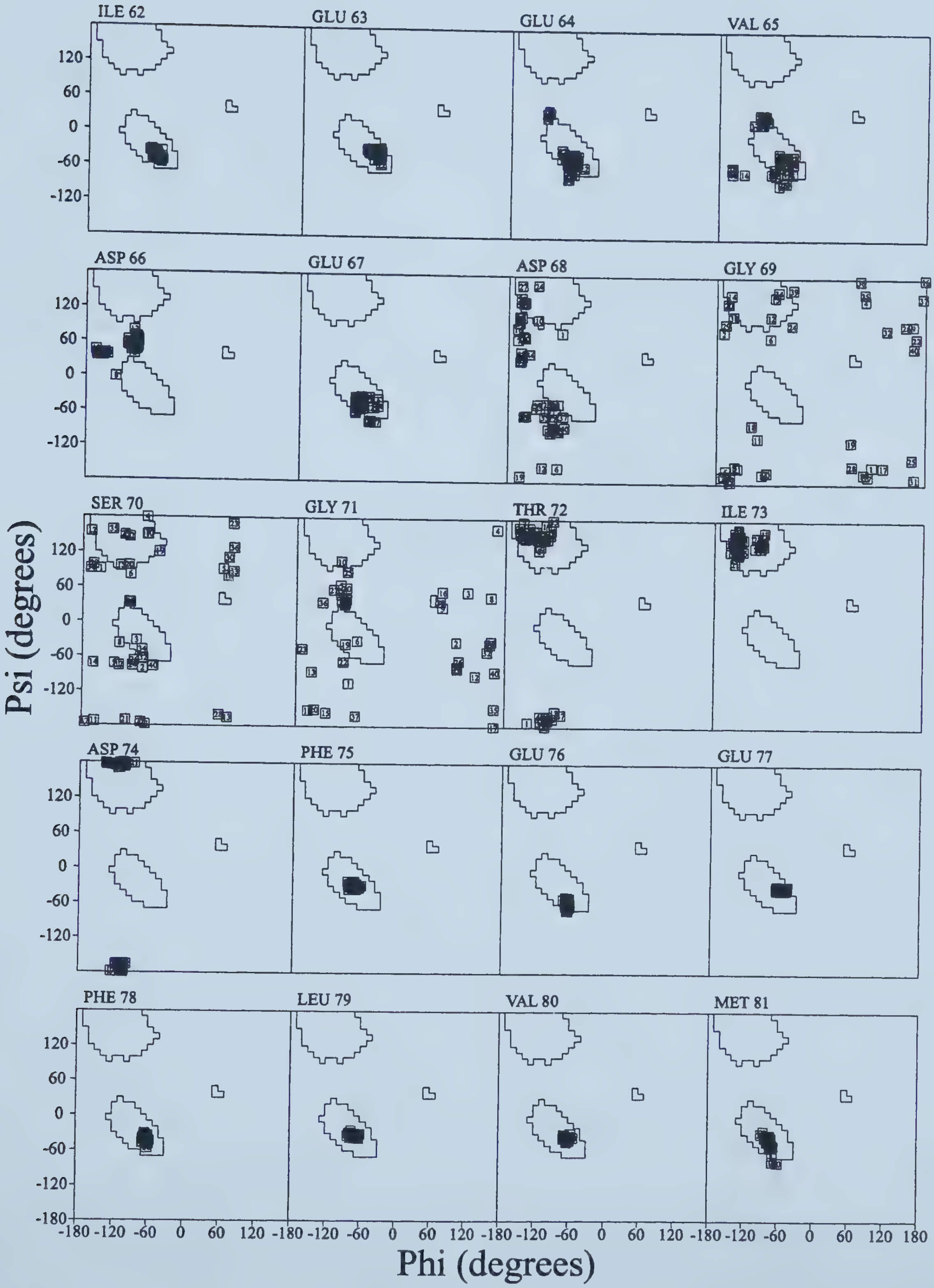

Figure 33. (Part 4 of 5)

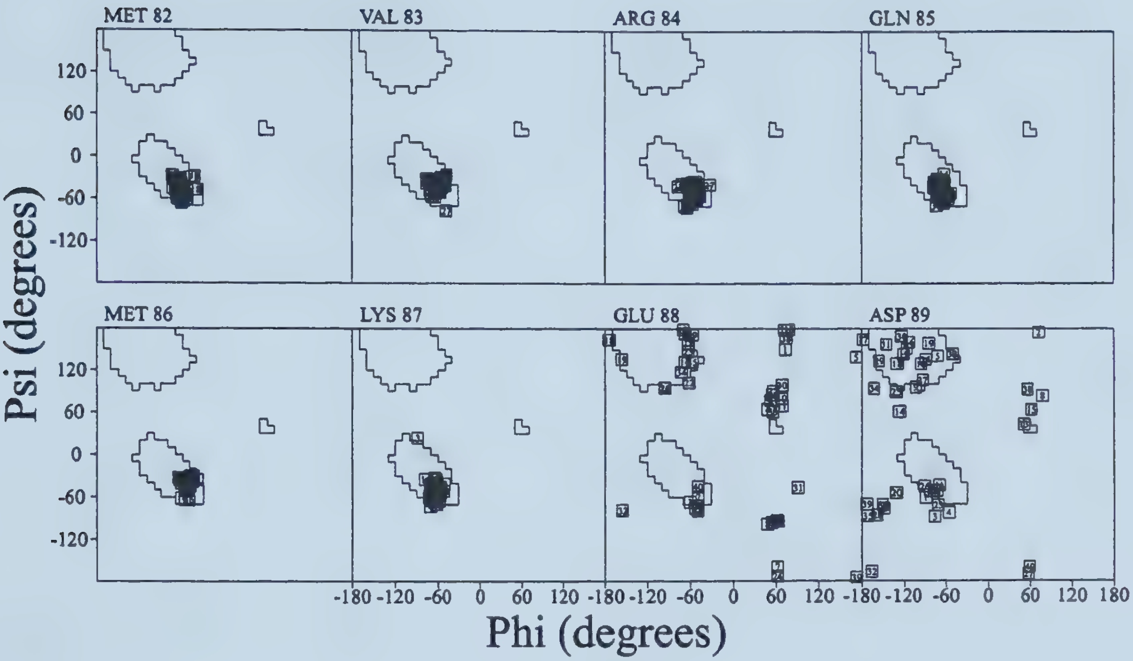

Figure 33. (Part 5 of 5)

Figure 34. *(shown on the next five pages)* Per-residue Ramachandran plots of the NMR structure of sNTnC•Ca$_2$. Each square in each Ramachandran plot represents one of the forty structures generated. These plots clearly indicates which regions are well-defined in NMR structures. The secondary structure elements are: helix N (6-13), helix A (16-29), helix B (39-48), helix C (55-64), helix D (75-86), β-sheet (36-38 & 72-74). The calcium-binding sites are residues 30-41 and 66-77.

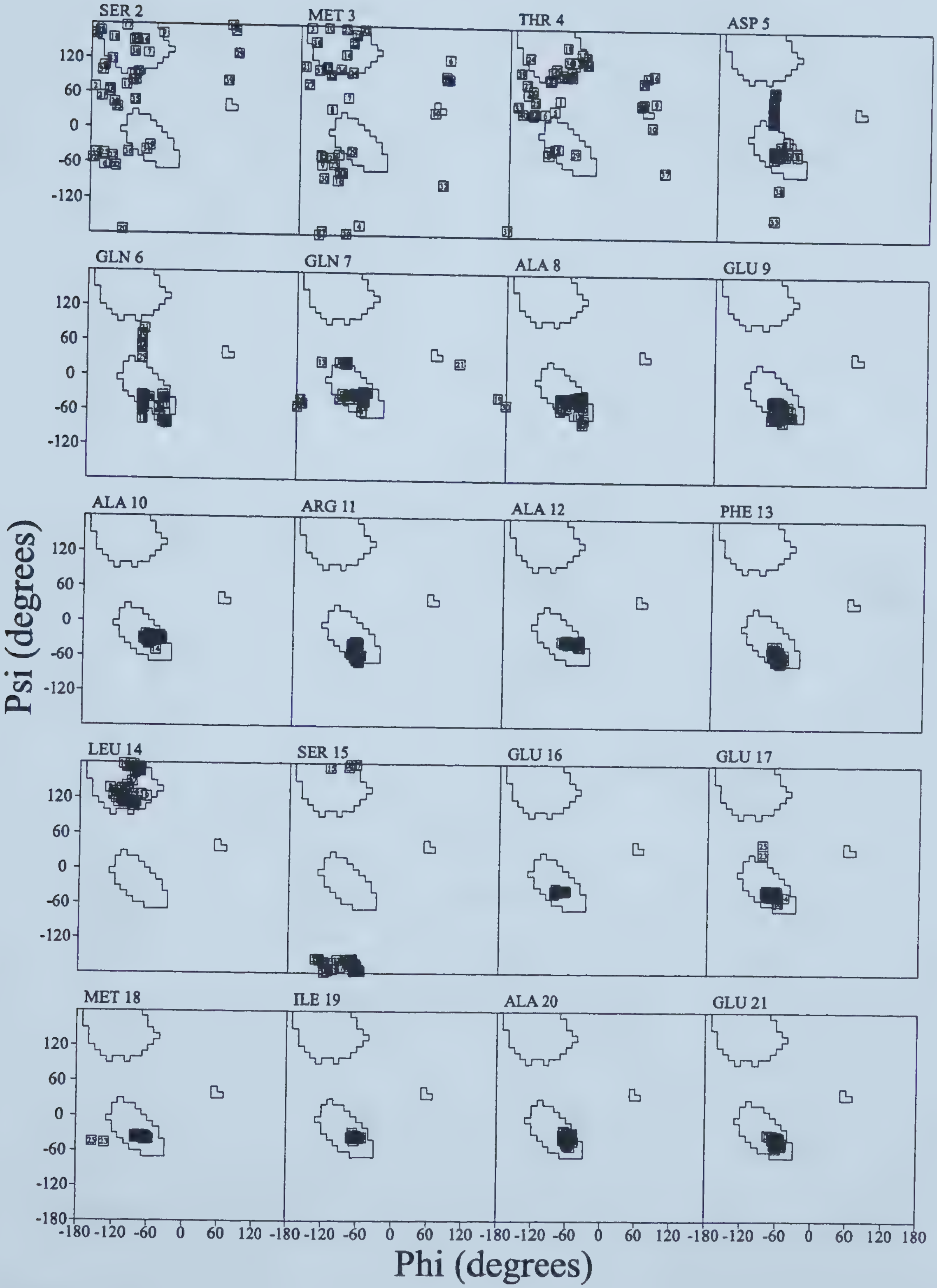

Figure 34. (Part 1 of 5)

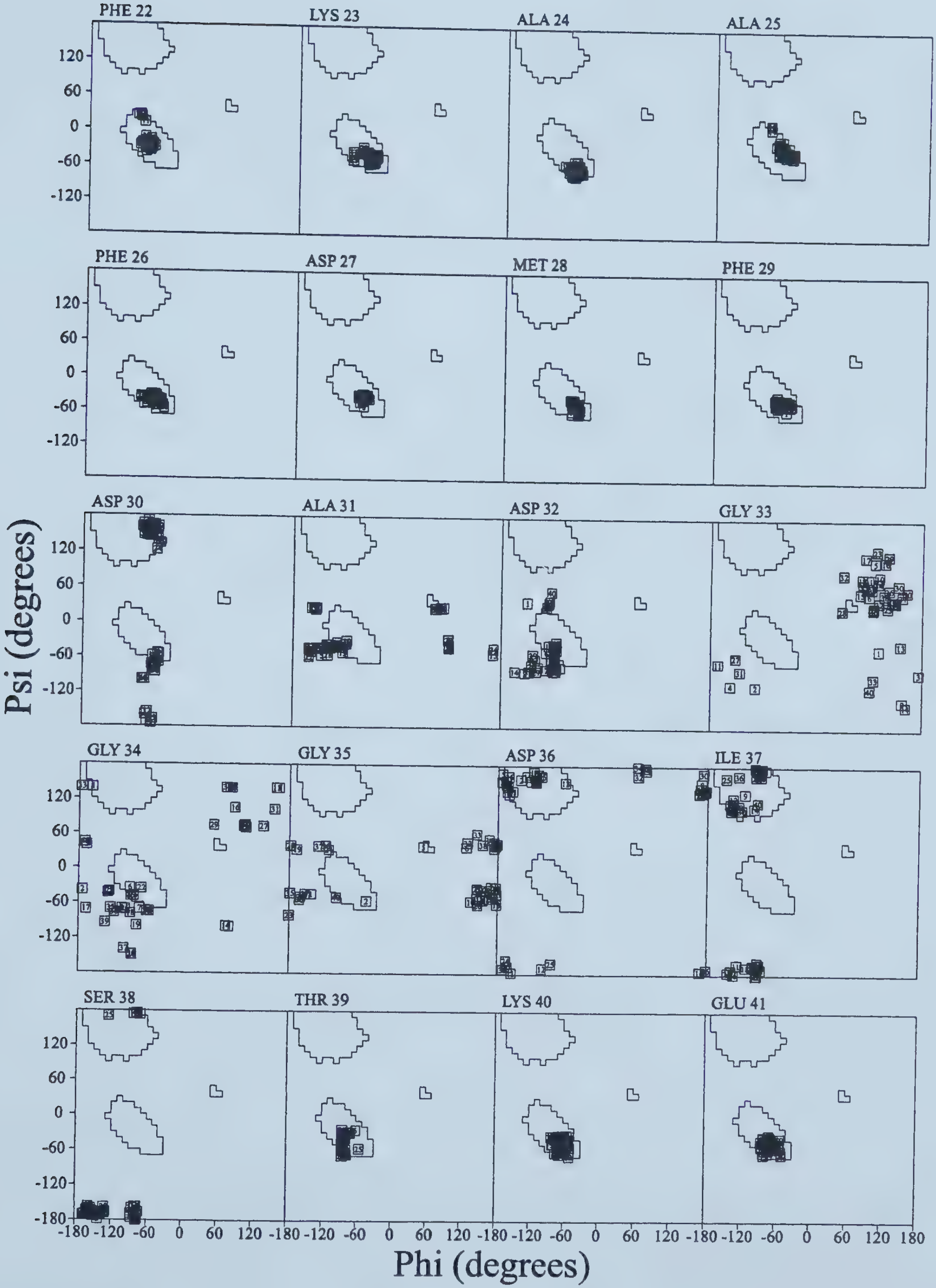

Figure 34. (Part 2 of 5)

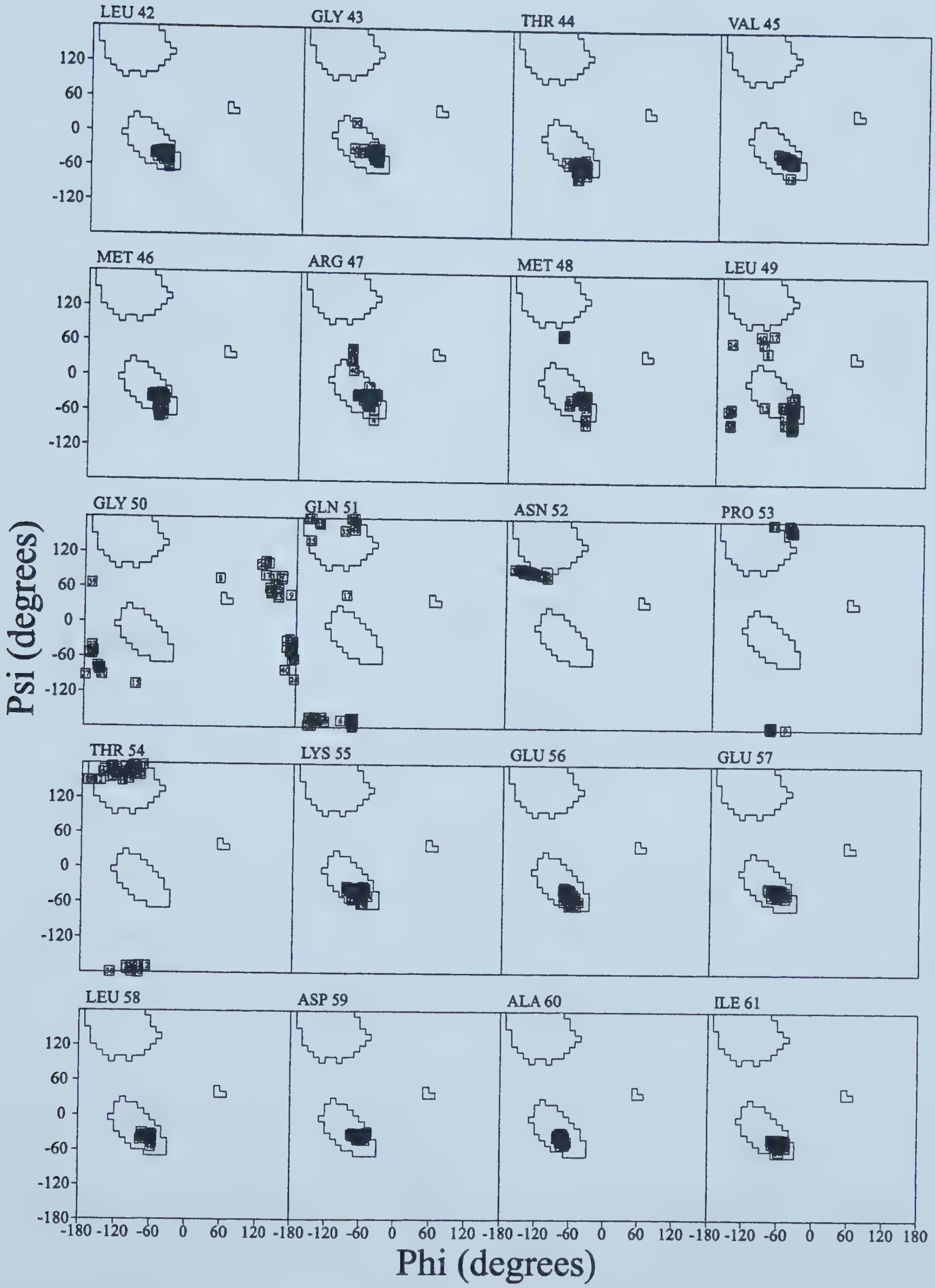

Figure 34. (Part 3 of 5)

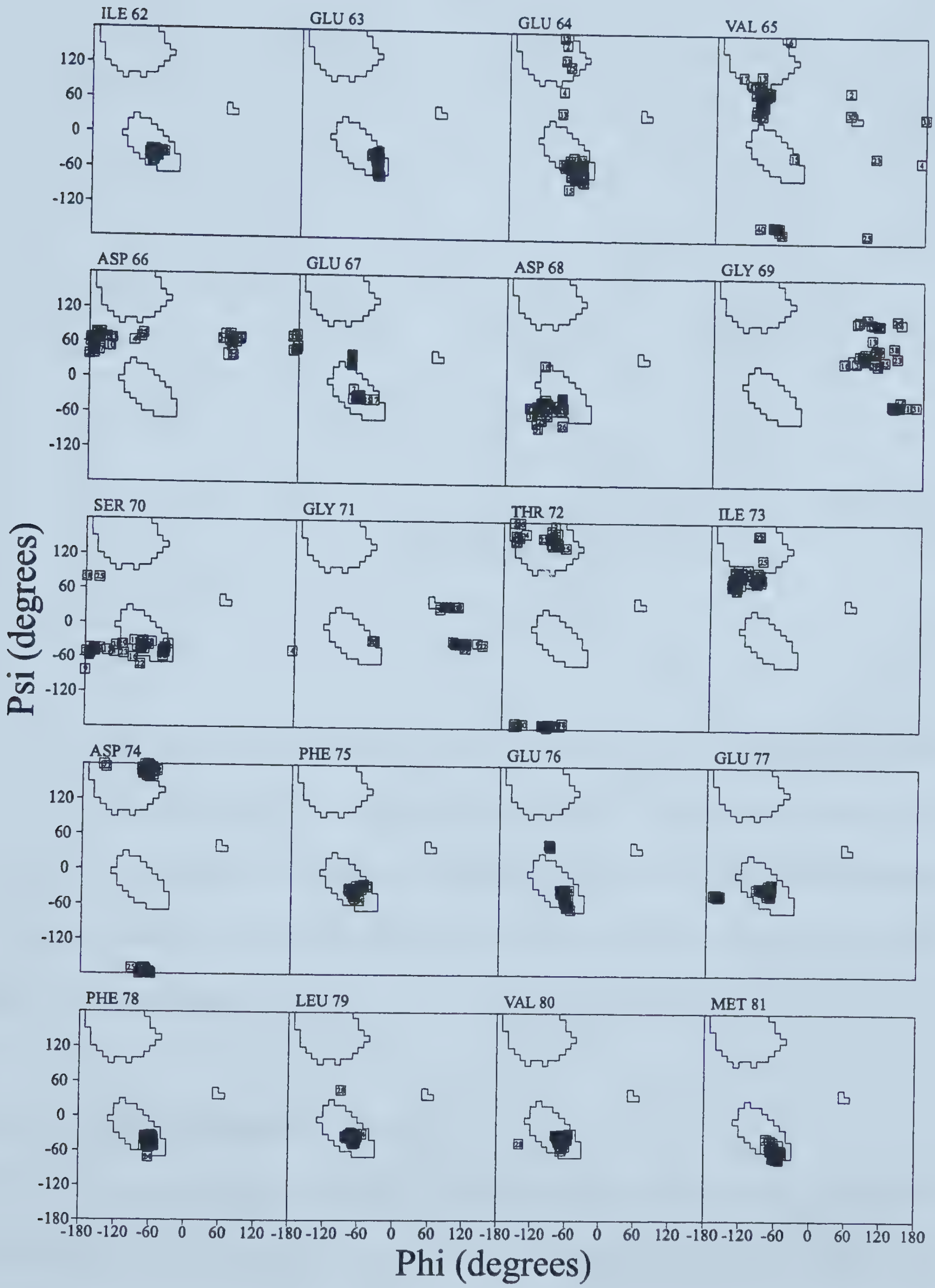

Figure 34. (Part 4 of 5)

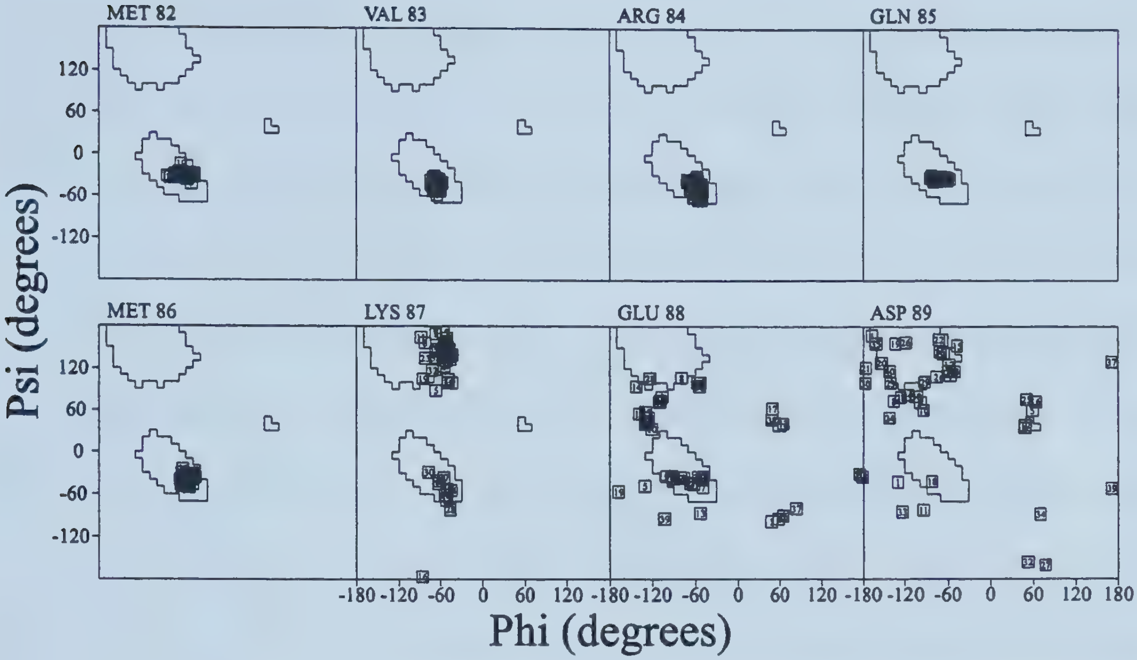

Figure 34. (Part 5 of 5)

The distribution of the φ/ψ dihedral angles in the Ramachandran plot (85-90% in the most favored regions defined by the program PROCHECK [51] shows the good geometry of the structures presented here. Together, these numbers show that the quality of the structures of sNTnC in the apo and calcium forms is adequate to provide an understanding of calcium-induced structural change.

Calcium-induced structural change

As was concluded previously [2, 47], no change in regular secondary structure is observed upon calcium-binding. Except for the straightening of helix B [2, 47], there is no increase in α-helical content upon calcium-binding, therefore reinforcing the fact that the

increase in negative ellipticity observed by circular dichroism is not due to a change in secondary structure, but to a change in tertiary structure [2, 47]. This change is depicted in figure 35, where helices N, A, and D of the apo and calcium saturated forms of sNTnC are superimposed, thus showing the movement of helices B and C when calcium is bound. This opening of the structure is quantified by measuring the difference in interhelical angle between the apo and the Ca_2 structure (table 6). The interhelical angles from sNTnC•apo are in agreement with the N-domain in the crystal structure, except for the C/D angle. In the NMR structure, the C/D angle is more open by over 20° compared to the X-ray angle (table 6). The C/D angle of sNTnC•apo is however identical, within experimental error, to the highly homologous N-domain of apo-calmodulin (table 6). Note that helix C did not have its position defined relative to the rest of the helices in TR_1C•apo structure. A flexible helix C in the apo form could explain the difference between the crystallographic structure and the two NMR structures (TR_1C•apo and sNTnC•apo) if the X-ray structure showed helix C in its most packed conformation, and the NMR structure showed helix C in its averaged conformation. However, recent relaxation data do not support a flexible helix C, at least on the ns-ps timescale (chapter 10). Also, a recent high-resolution, low-temperature NMR structure of sNTnC•apo indicates that helix C is not flexible and is well-packed onto helix D, at least at 4°C (Sakae Tsuda, personal communication). It is therefore likely that helix C is ill-defined in TR_1C•apo and sNTnC•apo due to a lack a long range restraints to helix C, as was suggested in chapter 4. It should be noted that the TR_1C•apo and sNTnC•apo structures were solved using conventional homonuclear 2D-NMR techniques.

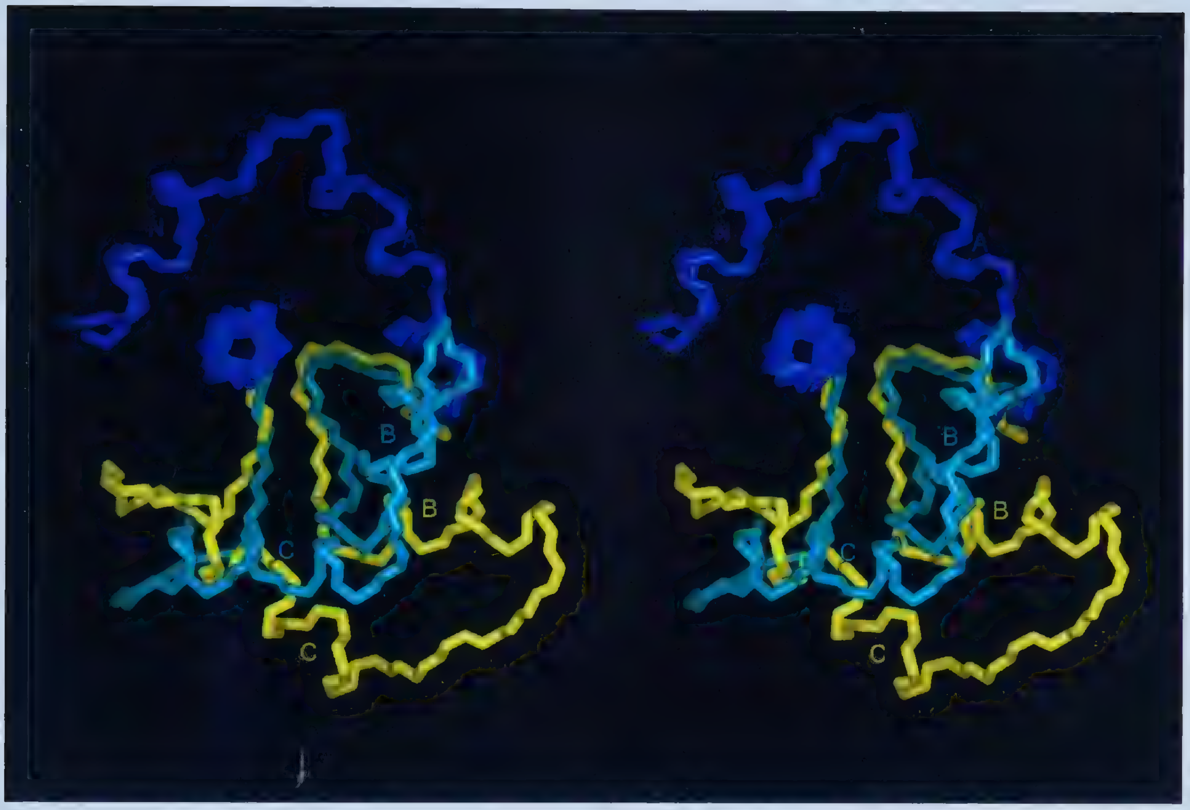

Figure 35. Superimposition of the average structures of sNTnC•apo and sNTnC•Ca$_2$ showing the calcium induced structural change. Helices N, A and D (residues 6-29, 75-86) were superimposed [blue]. Residues of sNTnC not superimposed are shown in [white] for sNTnC•apo and in [green] for sNTnC•Ca$_2$. The magnitude of the movement of helices B and C is large; up to 20Å for some atoms in the B-C linker.

The relative orientation of helices N, A, and D is not affected by calcium binding, whereas the A-B and C-D interhelical angles show significant changes. The concept of a calcium-induced opening of the structure has similarities with the HMJ-model that was predicted in 1986 [48], but is significantly larger than was expected (table 6). The magnitude of the movement of helices B and C is characterized by a large change in interhelical distance, resulting in displacements of 12 Å for the C-terminal end of helix B, 16 Å for the N-terminal end of helix C, and 19 Å for the center of the B-C linker.

Table 6. Interhelical angles in the N-domain of sTnC and CaM.

Protein	Interhelical angle (°) [a]	
	A/B	C/D
sNTnC•apo, present study	127 ± 3 (120-135)	124 ± 4 (115-132)
sNTnC•Ca$_2$, present study	85 ± 4 (74-92)	68 ± 5 (58-81)
apo N-domain of sTnC•Ca$_2$, X-ray	139	146
N-domain of sTnC, HMJ (Ca$_2$)	101	112
N-domain of sTnC•Ca$_4$, NMR	81 ± 5 (74-92)	78 ± 7 (67-89)
sNTnC•Ca$_2$, X-ray	97	83
N-domain of sTnC•Ca$_4$, X-ray (Cohen et al.)	104	97
N-domain of sTnC•Ca$_4$, X-ray (Phillips et al.)	95	89
N-domain of CaM (apo)	128 ± 3	130 ± 4
N-domain of CaM (Ca$_2$)	94	96
N-domain of CaM-MLCK (Ca$_2$)	78	82

[a] The axis orientation for an α-helix was defined by two points, where the first point is the average of the first 11 backbone atoms and the second point is the average of the last 11 backbone atoms. The program used to calculate the angle was IHA (S.M. Gagné). For NMR structures, the average with standard deviation and the range of interhelical angles are shown.

Although the changes in interhelical angle quantify the opening of the structure, it is also of interest to ask what is actually opened. The entity that is opened can be appreciated by looking at figure 36. The changes in interhelical angles result in the exposure of an extensive hydrophobic patch that is partially buried in the apo form. The calcium-induced change in ASA for the hydrophobic residues is +500 Å^2. Hydrophobic residues that undergo a significant increase in accessible surface area are: Leu49 (+73 Å^2), Met82 (+63 Å^2), Met46 (+53 Å^2), Met81 (+48 Å^2), Phe78 (+23 Å^2), Val45 (+23 Å^2), and Ala25 (+22 Å^2).

Additionally, two Gln are significantly exposed upon calcium-binding: Gln85 (+69 Å^2) and Gln51 (+60 Å^2). The binding of calcium to the regulatory domain can therefore be viewed as a switch that turns on a 'sticky' patch.

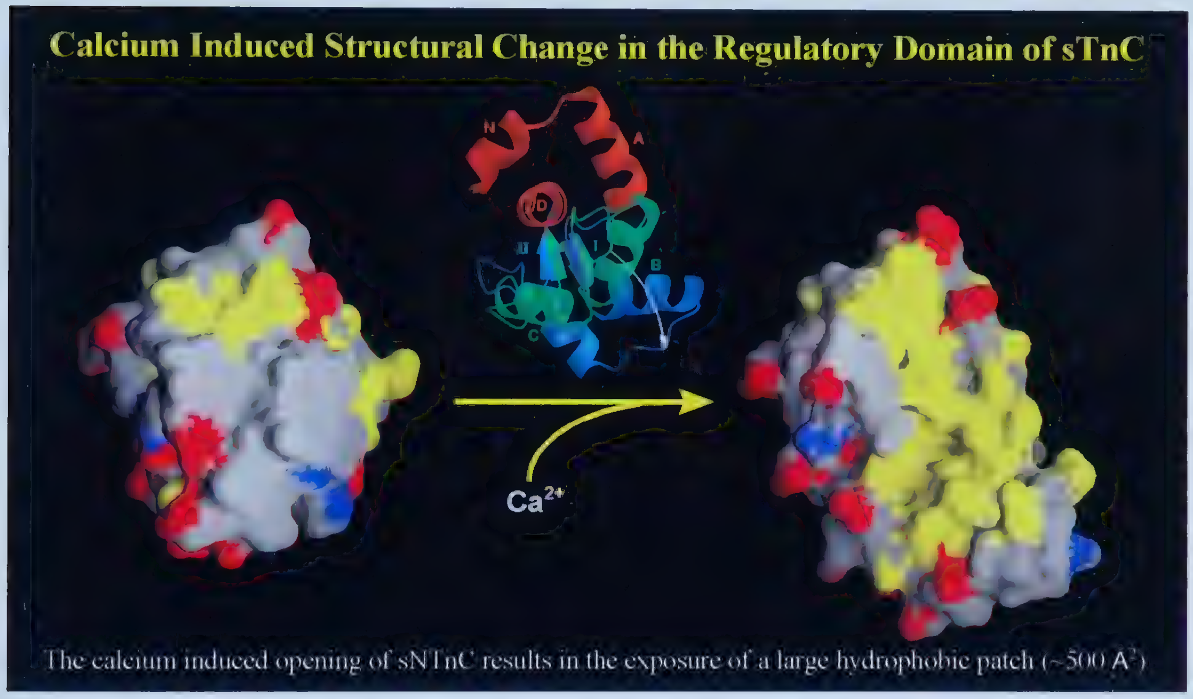
Calcium Induced Structural Change in the Regulatory Domain of sTnC
N
A
D
II
I
B
C
Ca^{2+}
The calcium induced opening of sNTnC results in the exposure of a large hydrophobic patch (~500 Å^2)

Figure 36. Exposition of an hydrophobic patch in the N-domain of sTnC upon calcium binding. Hydrophobic residues are shown in yellow, positive charges in blue, negative charges in red, and others in gray. The apo form is shown on the left and the calcium form on the right. The movement of helices B and C induced by calcium is shown in the middle.

Remarks on the NMR structures of sNTnC•apo and sNTnC•Ca$_2$

When I look at the two structures which are described above, I immediately appreciate how much the field has improved over the last few years. Most of the NMR data for that project was acquired between 1991 and 1994. Since then, significant improvements

have been made in pulse sequences and NMR hardware. It is clear that better structures could now be obtained on the same samples. This will become obvious in the next chapter, where I present the structure of a sNTnC mutant using more 'modern' NMR experiments and spectrometer hardware. For this reason, I will not refer to the NMR structure of sNTnC•apo for comparison, and I will use instead the apo N-domain in the X-ray structure of sTnC. The reason for this choice is the low number of NOEs used for the NMR structure determination of sNTnC•apo, and some of the flexibility features in this structure which were not confirmed by the relaxation data (see Section 3 of this thesis).

However, the NMR structure of sNTnC•Ca_2 will be used for further comparisons. Although there is inevitably some minor flaws in this 'old' NMR structure, the general features which it reveals will be shown to be relevant and essential to the analysis.

Methods for the NMR structural study of sNTnC•apo and sNTnC•Ca_2

Sample preparation

Cloning, expression, and uniform labeling with either ^{15}N or $^{15}N/^{13}C$ the N-terminal domain of sTnC (sNTnC) was performed by M. Li and L. Smillie as described previously [47]. The experimental data were obtained under near-physiological conditions (30°C, pH 6.7, 100 mM KCl) at protein concentration of 1.5 - 2.0 mM as described previously [47].

Structure determination

Chemical shift assignments ($^1H/^{15}N$ for sNTnC•apo, $^1H/^{15}N/^{13}C$ for sNTnC•Ca_2) were performed using conventional multidimensional homonuclear and heteronuclear techniques [47]. Inter-proton distance information was derived from 2D homonuclear NOESY [52, 53] and 3D ^{15}N-edited NOESY [54] NMR experiments. Additionally, 3D ^{13}C-edited NOESY [55] experiments were used for sNTnC•Ca_2. Distance restraints were approximated from the NOE data obtained at mixing times varying between 75 and 150 ms. The 2D-NOESYs were calibrated based on NOEs corresponding to known distances. The 3D-NOESYs were calibrated using an NOE corresponding to a known distance, located on the same ^{15}N or ^{13}C trace (therefore each trace had a different calibration). In cases where direct calibration was not possible, the distance constraints were overestimated. The calcium-ligand distance restraints were set to 2.0-2.8 Å between the calcium ions and the oxygen of the carbonyls involved in coordinating calcium [15]. Only 5 calcium restraints were used in site I (as opposed to 6 in site II) because position 5 in regular EF-hand site has a side-chain coordinating calcium [15], but in site I of sNTnC this residue is a glycine (G34). Dihedral restraints for the φ angle were obtained from HMQC-J experiments [56], and restraints for the ψ angle were obtained from the $d_{N\alpha}/d_{\alpha N}$ ratio as previously proposed [47, 57]. Restraints used for the structure calculation are summarized in table 5. Based on this set of restraints, 60 structures were calculated for each form of sNTnC using the distance geometry protocol *DGII* software [58] included in the *InsightII* package (*Biosym*, San Diego, California). The following parameters were set for the calculations: tetrangle smoothing (groups pairs), metrization (prospective), 4 dimension embedding, majorize weighting scheme (range and

average), 40 Guttman transformations, error function form (sparse matrix), 20 000 (sNTnC•apo) and 25 000 (NTnC•Ca_2) steps in simulated annealing (*DGII* version of simulated annealing), initial energy = 2000 (sNTnC•apo) and 2400 (sNTnC•Ca_2). The remainder of parameters correspond to the default settings in the *InsightII v2.3* package. Structures that converged properly had a *DGII* final error function of 0.04-0.11 (sNTnC•apo) and 0.02-0.07 (sNTnC•Ca_2), whereas structures which did not converge had final error functions of 0.13-5.80 (sNTnC•apo) and 0.09-1.07 (sNTnC•Ca_2). Final structures from *DGII* were not energy minimized. The 40 structures with the lowest error function were selected for the structure analysis.

NMR structure of sTnC in the Ca_4 state

The solution structure of whole sTnC•Ca_4 was published shortly after my structures of the N-domain [59]. This structure was done in the presence of TFE in order to eliminate calcium-induced dimerization [49]. One of the major conclusions of this structure determination was the confirmation that the central helix is flexible and thus the relative orientation of the two domains is not fixed in solution (figure 37). This feature had also been previously observed for calmodulin [60]. Comparison of the NMR structure of the C-domain of sTnC•Ca_4 with the corresponding domain in the crystal structure of sTnC•Ca_2 reveals that the NMR structure is slightly more open. Although the G/H interhelical angle is the same in both structures, the angle between helix E and helix F is more open by 16° in the NMR

structure. Comparison of the NMR structure of the N-domain of sTnC•Ca_4 with the NMR structure of sNTnC•Ca_2 shows a near identical level of opening (figure 38).

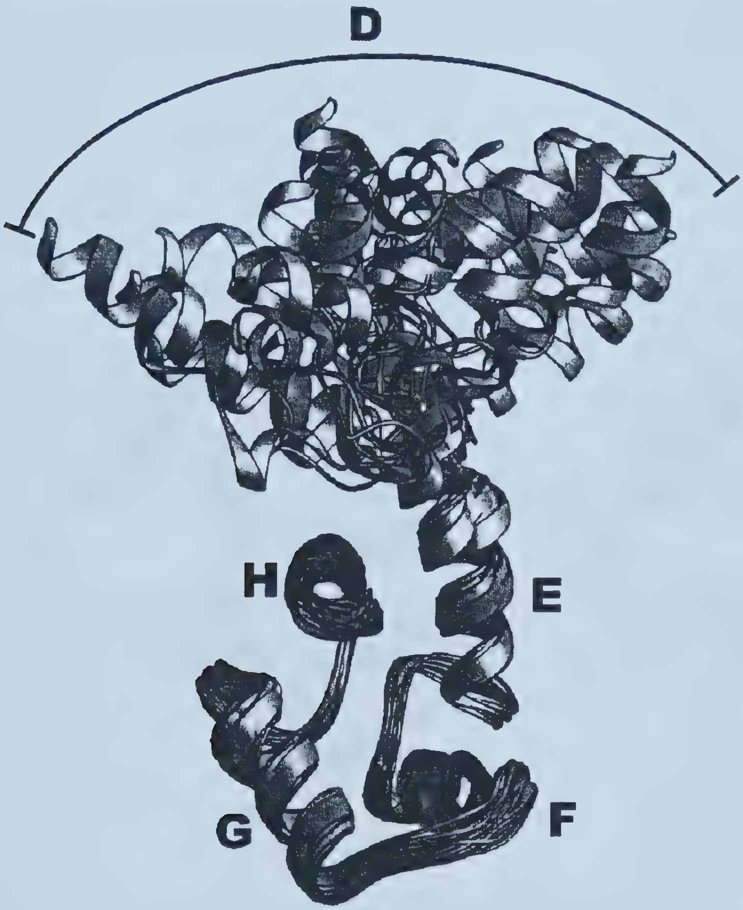

Figure 37. sTnC•Ca_4 family of NMR structures showing the flexibility in the inter-domain linker. The C-domain was superimposed for all structures. For clarity, only helix D is shown for the N-domain.

The A/B and C/D interhelical angles are the same within experimental error, although the average C/D angle is more open by 10° in the structure of sNTnC•Ca_2 (table 6). This structural similarity confirms that the N-domain behaves the same structurally in sNTnC as in intact sTnC, and that structural studies of the isolated domain are valid. The similarity also suggests that neither partial dimerization, nor TFE affects the level of opening.

However, there is the possibility that both conditions actually affect the conformation of the N-domain in a similar fashion.

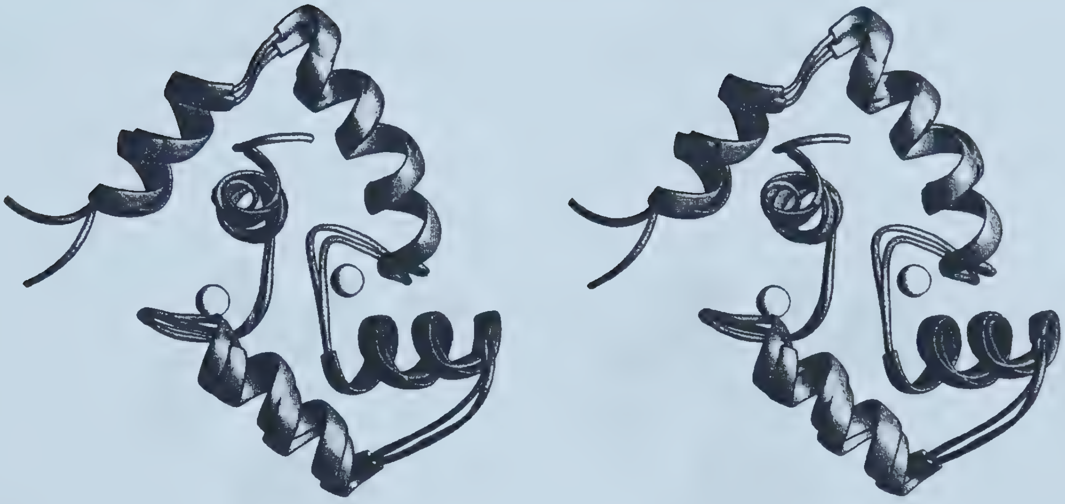

Figure 38. Superimposition of the NMR structure of sNTnC•Ca_2 with the N-domain of the NMR structure of sTnC•Ca_4. Residues 5-85 were used in the superimposition. The backbone rmsd is 1.4 Å when superimposing residues 5-85, and 1.1 Å when superimposing residues 5-29, 36-47, 54-85. This figure, like most other structural figures in this thesis, is shown in stereo.

X-ray structure of sNTnC in the Ca_2 state

Recently, the crystal structure of chicken sNTnC•Ca_2 was reported by Strynadka et al. [61]. The paper reported very detailed features of the calcium-binding loops which were not as well defined in the NMR structures. The X-ray structure of sNTnC•Ca_2 (figure 39)

is compared here with the NMR structures and the HMJ model. The X-ray structure of sNTnC•Ca$_2$ is somewhat less open than the average sNTnC•Ca$_2$ and sTnC•Ca$_4$ NMR structures, although the crystal structure is at one end of the range of interhelical angles covered by the NMR structures (table 6). Compared to HMJ model, the A/B angle is the same, whereas the C/D angle is significantly more open in the X-ray structure of sNTnC•Ca$_2$ (by 29°). Overall, in terms of opening of the structure, the crystal structure of sNTnC•Ca$_2$ and the solution structures of sNTnC•Ca$_2$ and sTnC•Ca$_4$ agree well.

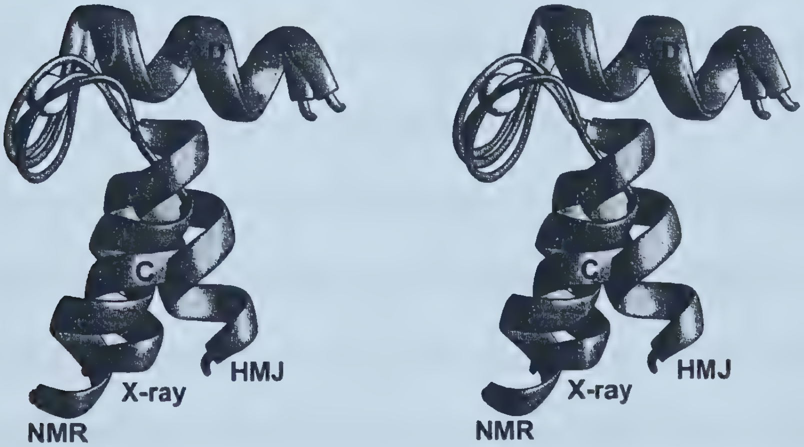

Figure 39. Comparison of the NMR structure of sNTnC•Ca$_2$, the X-ray structure of sNTnC•Ca$_2$, and the HMJ model. Structures were superimposed using residues 75-85 (helix D). Residues 55-85 (helix C, site II, helix D) are shown.

X-ray structures of skeletal rabbit TnC in the Ca_4 state

Cohen et al. structures

Less than a year ago, the crystal structure of rabbit sTnC•Ca_4 was solved by Cohen and coworkers [62]. The structure of rabbit sTnC•Ca_4 was solved in two different crystal forms [62]. A very interesting result is that the two crystal forms gave a significantly different level of opening in the structure of the calcium-bound C-domain.

As shown in table 6, the N-domain in these crystal structures of rabbit sTnC•Ca_4 is more closed than the other structures of sTnC in the calcium-bound state (NMR structure of sNTnC•Ca_2, NMR structure of sTnC•Ca_4, and X-ray structure of sNTnC•Ca_2). At the time, it was not clear why this was so. One possibility was that this was simply a result of sequence differences between skeletal rabbit and skeletal avian TnC.

Cohen and coworkers associated the difference in opening of the C-domain between the two crystal forms to flexibility in the domain. Interestingly, the difference in the opening of the N-domain between their structures and the NMR structures (sNTnC•Ca_2 and sTnC•Ca_4) was attributed to 'the limited resolution of the NMR spectroscopic data' [62]. It should be noted the X-ray structure of sNTnC•Ca_2 was not available to the Cohen group at the time of publication.

Phillips et al. structure

Just a few months ago, the group of Phillips et al. solved the X-ray structure of rabbit sTnC•Ca_4 (G. Phillips, personal communication), the same protein that was solved by Cohen

et al. (above). Following a familiar trend, this structure, in terms of opening, was different from others solved to date. The Phillips structure is more open than the Cohen structures, and more closed than the X-ray and NMR structures of sNTnC•Ca_2 (table 6).

Which one is correct? Is there an incorrect one?

It is interesting that the more there are structures solved, the less it seems like we have an answer. My NMR structure of sNTnC•Ca_2 was the first structure of the regulatory domain of sTnC in the calcium-bound state and suggested that calcium-bound sNTnC was more open than originally predicted by the HMJ model. This 'more-open-than-expected' aspect was later supported by the X-ray structure of sNTnC•Ca_2, although the x-ray structure was slightly less open than the NMR structure. At the time when there were only two structures for the calcium-bound state of the N-domain of sTnC, it could have been argued that the difference was due to one of the structures being incorrect. However, now that there are two additional structures for the N-domain, and that all four structures show a different level of opening, the question has switched from "which one is correct?" to "what is going on?".

6. STRUCTURE OF E41A-SNTNC•CA_2

As shown in the previous chapter, the structural transition in sTnC induced by the binding of two calcium ions involves an 'opening' of the structure, an event that triggers skeletal muscle contraction. Although these structures provided an understanding of the calcium-induced conformational change, the detailed mechanism of the linkage between calcium-binding and this calcium-induced structural change was still unclear.

In this chapter, I present the 3D solution structure of a calcium-bound mutant of the N-domain of sTnC (E41A-sNTnC•Ca_2) in which one of the ligands to the calcium in site I is missing. This structure is a snapshot of sTnC between the off (-calcium) and on (+calcium) state, and therefore provides valuable insight into the mechanism of regulation within sTnC; that is, the coupling between ligand binding and subsequent structural changes. Additionally, insights into the structure of cardiac TnC can be derived from this skeletal mutant.

Description and choice of the E41A mutant

As presented in the Introduction, calcium-binding sites in sTnC involve a pair of helix-loop-helix (HLH) motifs in each domain, which coordinate calcium ions. On the basis of crystal structures of HLH calcium-binding proteins [15], the six amino acid residues involved in calcium-coordination were defined; five are in the loop region (X, Y, Z, -Y, -X positions) and the sixth one (-Z) is in the second helix of the HLH motif. In all regular HLH motifs, the residue at -Z is a glutamate and it contributes both of its side-chain oxygens to the

calcium coordination [15]. The bidentate coordination residue in site I, Glu41, was found to have irregular backbone dihedral angles when sNTnC is in the apo-form, therefore leading to a kink in helix B [12, 15, 28, 47, 63]. In the apo-form, Glu41 forms a salt-bridge with Lys40, which could potentially contribute to stabilization of the kink. I showed that this kink was straightened upon calcium-binding [47, 63], and postulated that this straightening was critical to the function of the N-domain [47]. The behavior of the -Z position in site II is different, and there is no kink in helix D of sNTnC•apo. It has also been shown that site I and II have different calcium-binding affinities [25] and that calcium binding to sNTnC is stepwise. Although it was not possible to unambiguously determine the order of binding, it was suggested that site II has the strongest calcium affinity [25].

My initial goal was to explore the contribution of site I to the calcium induced structural change by making site I defunct. Removal of the bidentate ligand (Glu41) appeared to be the perfect choice since it meant removing two out of seven coordinating oxygens. In addition to the suppression of calcium binding to site I, mutation of Glu41 to Ala41 was attractive for the following reasons. First, the mutant will be lacking the salt bridge (Glu41-Lys40) present in the apo form which potentially stabilizes the kink. Second, alanine is an amino acid having some helix propensity. The Glu41 to Ala41 mutant might therefore be expected to favor the straightening of helix B and the opening of the structure. A 'closed' structure of this mutant in the calcium-saturated state would therefore indicate that binding of calcium to site I is essential to the structural opening.

Calcium titration of E41A-sNTnC

The calcium titration of E41A-sNTnC followed by NMR revealed an unexpected result; despite removal of the bidentate ligand, site I was still able to bind calcium (figure 40). Using an approach similar to one used previously [25], the dissociation constants were determined to be 20-50μM and 1-2mM for site II and site I, respectively [64]. The weak binding was unambiguously assigned to site I, as opposed to non-specific binding, based on local chemical shift changes which were observed during the calcium titration. The large chemical shift changes which occur between one and five equivalents of calcium are localized in site I and are consistent with the ones observed in wild-type sNTnC [47]. The calcium binding constant for site I was reduced by approximately 100-fold relative to wild-type [25], and at the calcium concentration used in this study, site I is 80% filled. This brought a completely new focus to the study; monitoring the critical role of a single residue,

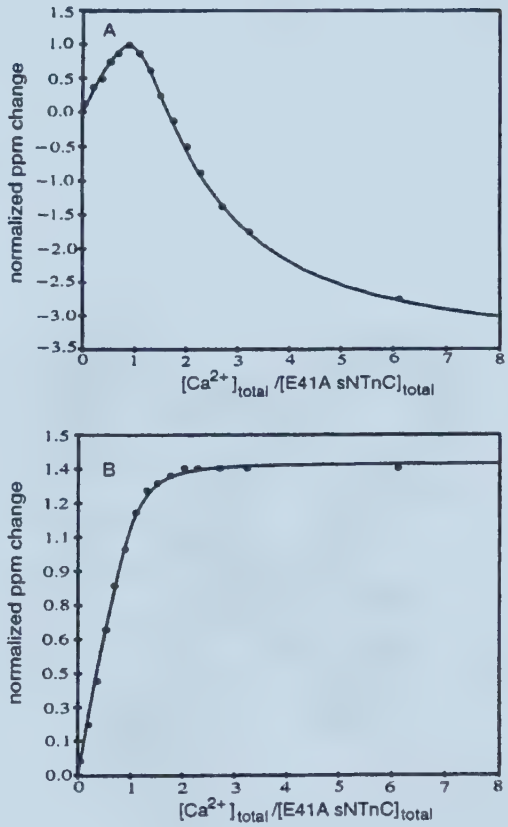

Figure 40. Calcium titration plots for G35 (a) and G71 (b) of E41A-sNTnC derived from a series of NMR spectra acquired at various calcium concentration. The curves which best fit the data points are shown by solid lines. Note that the first calcium affects primarily G71 (site II) and the second calcium affects primarily G35 (site I).

Glu41, to the function of sTnC and elucidating the mechanism of the calcium induced structural change in this protein.

Structure of E41A-sNTnC•Ca_2

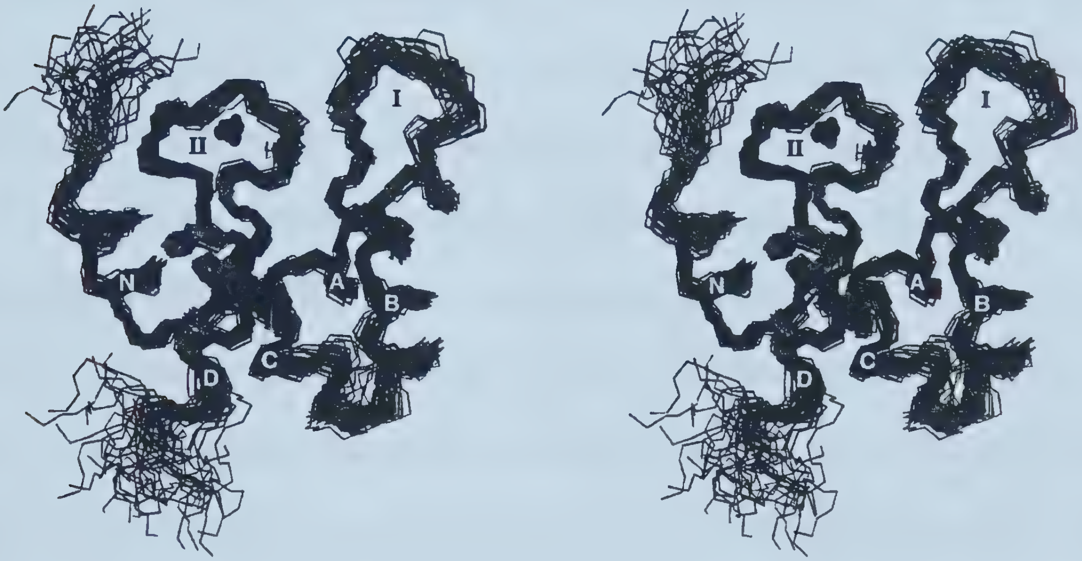

Figure 41. Stereoview of the solution structure of E41A-sNTnC•Ca_2. The backbone (N, Cα, C′) of the family of 40 structures is shown in "rods" representation, and the site II calcium position in each of these structures is shown by a small sphere. Although calcium is present in solution in site I, there is no calcium shown here because none was used in the calculations, as the coordination state of site I was not known *a priori*. The five helices are labeled N, A, B, C, and D. The two calcium binding loops are labeled I and II.

The 3D structure of E41A-sNTnC•Ca_2 has been determined using 1439 experimental restraints (table 7) derived from NMR spectroscopy. Figure 41 shows a stereo view of the best-fit superimposition of the backbone atoms. On the basis of restraint violations, rmsd values and Ramachandran plots (table 7 and figure 42 and 43), this structure is of high

quality. The structure consists of five helices (N: residues 5-13, A: 16-28, B: 42-49, C: 55-64 and D: 75-84), and two calcium-binding sites (I: 30-41, and II: 66-77) connected by a short β-sheet (36-38, 72-74). There is no significant difference in the secondary structure of E41A-sNTnC•Ca_2 compared with wild-type sNTnC•apo and sNTnC•Ca_2. The five helices are very well defined, having individual backbone rmsd around 0.23±0.07Å (table 7). The β-sheet and site II are also well defined, having backbone rmsd of 0.25±0.08Å and 0.24±0.06Å, respectively. The good definition found in site II is not due to the calcium restraints used for the final structure calculation. Structural calculations were made without the calcium restraints and yielded a similar definition for site II. Although the calcium restraints provide better definition for the side-chains involved in coordination of the ion, the backbone conformation of site II is a result of the experimental NMR data. Unlike site II, site I is not as well defined (backbone rmsd of 0.60±0.22Å). The poorer definition of site I relative to site II is partially due to the smaller number of experimental restraints. Other poorly defined regions include the N- and C-termini residues, and the B-C linker. Backbone amide ^{15}N relaxation studies (chapter 10) show that these residues have lower order parameters (S^2), indicating that the poor definition is due, at least in part, to flexibility, and not only to a lack of structural restraints.

Table 7. Structural statistics of the 40 structures of E41A-sNTnC•Ca_2 [a].

rmsd from exptl distance restraints (Å)	
all (1367)	0.006 ± 0.001
inter-residue sequential ($\lvert i-j \rvert = 1$) (332)	0.006 ± 0.002
inter-residue medium range ($1 < \lvert i-j \rvert \leq 5$) (347)	0.005 ± 0.002
inter-residue long range ($\lvert i-j \rvert > 5$) (209)	0.004 ± 0.001
intra-residue (479)	0.006 ± 0.002
rmsd from experimental dihedral restraints (°) (72)	0.17 ± 0.05
rmsd from calcium coordination restraints (Å) (6) [b]	0.0003 ± 0.0009
rmsd from idealized covalent geometry	
bonds (Å)	0.0012 ± 0.0001
angles (°)	0.291 ± 0.006
impropers (°)	0.211 ± 0.004
energies (kcal mol^{-1})	
F_{NOE} [c]	2.2 ± 0.9
F_{cdih} [c]	0.14 ± 0.08
F_{repel} [d]	4.4 ± 1.3
E_{L-J} [e]	-413 ± 30

	backbone atoms	heavy atoms
atomic rmsd (Å) [f]		
residues 1-90	1.08 ± 0.20	1.44 ± 0.14
residues 6-84	0.60 ± 0.11	1.06 ± 0.08
well-defined residues [g]	0.49 ± 0.08	0.88 ± 0.07
helices [h]	0.23 ± 0.07	0.86 ± 0.14
φ/ψ in most favored region (%) [i]	91.6	
φ/ψ in additionally allowed region (%) [i]	8.4	

[a] The number of each type of restraints used in the structure calculation is given in parenthesis. None of the structures exhibits distance violations greater than 0.24 Å or dihedral violations greater than 1.6°. Standard deviations are given when applicable. [b] The distance restraints to the calcium ion in site II were based on the coordination of calcium in the crystal structures of sTnC and homologous proteins. [c] F_{NOE} and F_{cdih} were calculated using force constants of 50 kcal mol^{-1} and 200 kcal mol^{-1} rad^{-2}, respectively. [d] F_{repel} was calculated using a force constant of 4.0 kcal mol^{-1} Å^{-4} with the van der Waals hard sphere raddi set to 0.75 times those in the parameter set PARALLHSA supplied with XPLOR. [e] E_{L-J} is the Lennard-Jones van der Waals energy calculated with the CHARMM empirical energy function and is not included in the target function for simulated annealing calculation. [f] root mean square deviations to the average structure. The average structure was obtained by averaging the coordinates of the individual structures, best fitted to each other, including every residues. [g] Well-defined back-bone atoms were found for 67 residues (74%) and included residues 6-29, 36-49, and 56-84. Of the residues having well-defined back-bone atoms, 55 residues (82%) had a χ_1 and/or χ_2 circular variance smaller than 0.4 and were selected as having well-defined side-chain heavy-atoms. Those 55 residues are 6-14, 18-20, 22-26, 29, 36, 37, 39, 41-47, 49, 56-66, 68-73, 75-77, 79-84. [h] Average of the individual helical rms deviations. N(5-13): 0.22±0.07 / 0.84±0.15 ; A(16-28): 0.27±0.07 / 0.87±0.10 ; B(42-49): 0.27±0.09 / 0.82±0.16 ; C(55-64): 0.22±0.07 / 1.00±0.17 ; D(75-84): 0.18±0.05 / 0.77±0.11. [i] As determined by the program PROCHECK; only residues 5-84 were considered.

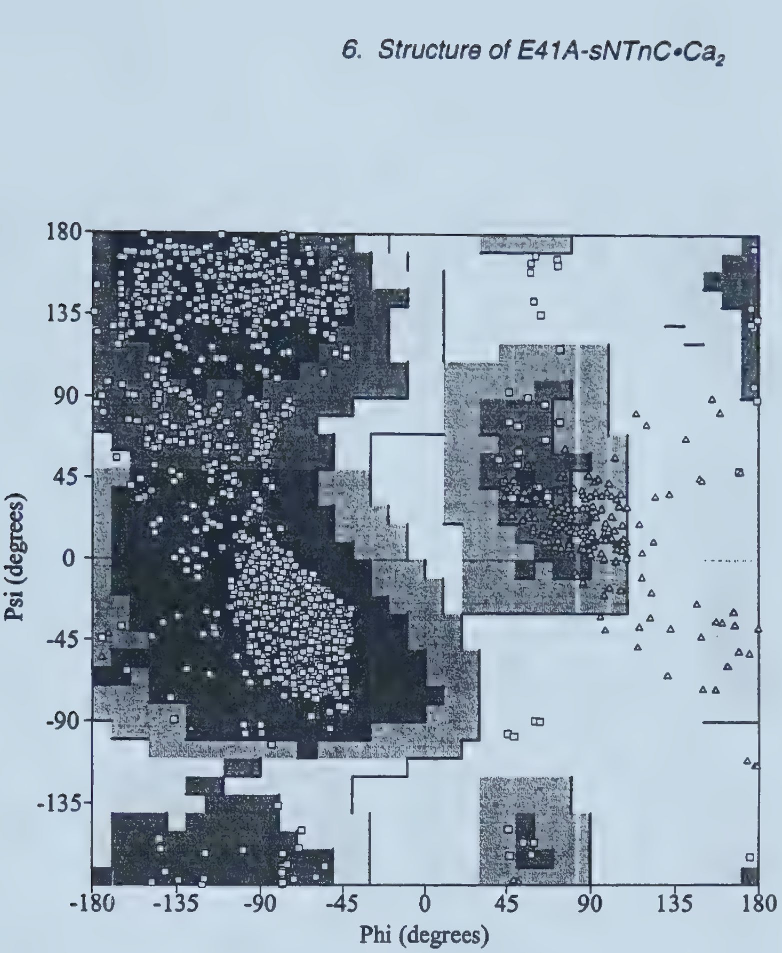

Figure 42. Ramachandran plot for the NMR structure of E41A-sNTnC•Ca$_2$. All 40 calculated structures are shown. Glycine residues are represented by triangles. Shaded regions are as defined in figure 31.

Figure 43. *(shown on the next five pages)* Per-residue Ramachandran plots of the NMR structure of E41A-sNTnC•Ca$_2$. Each square in each Ramachandran plot represents one of the forty structures generated. These plots clearly indicate which regions are well-defined in this family of NMR structures. The secondary structure elements are: helix N (6-13), helix A (16-29), helix B (39-48), helix C (55-64), helix D (75-86), β-sheet (36-38 & 72-74). The calcium-binding sites are residues 30-41 and 66-77.

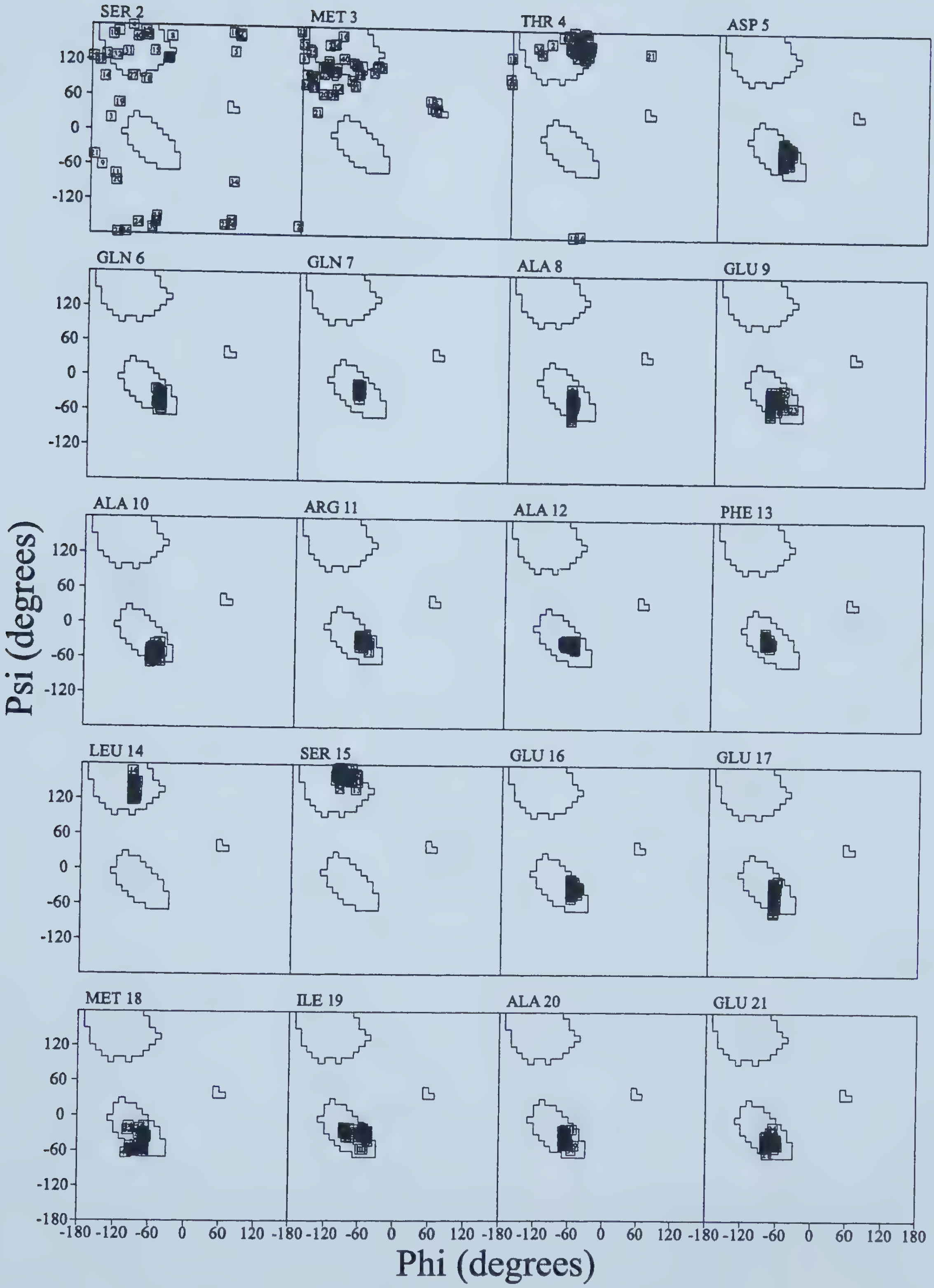

Figure 43. *(Part 1 of 5).*

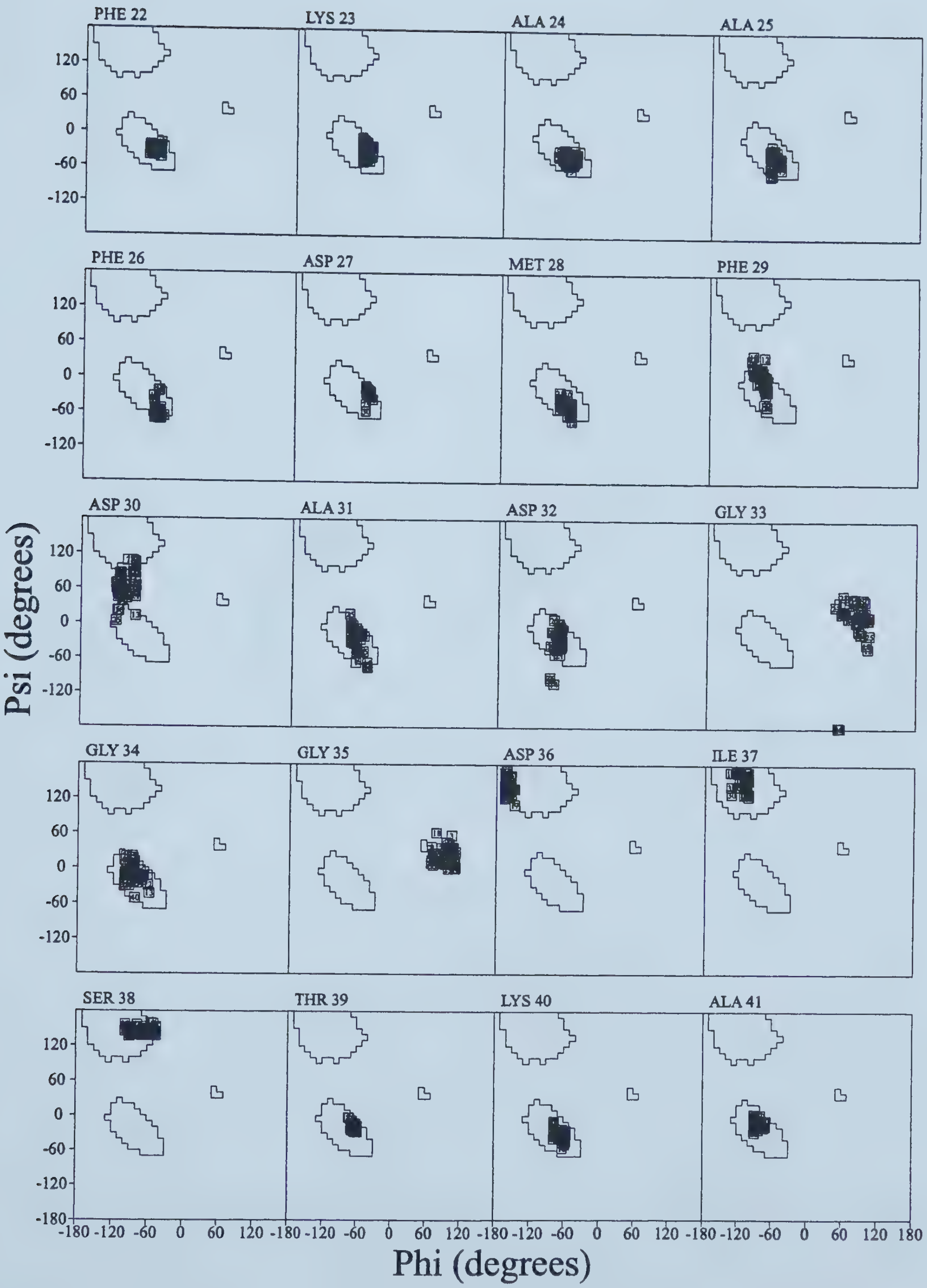

Figure 43. *(Part 2 of 5).*

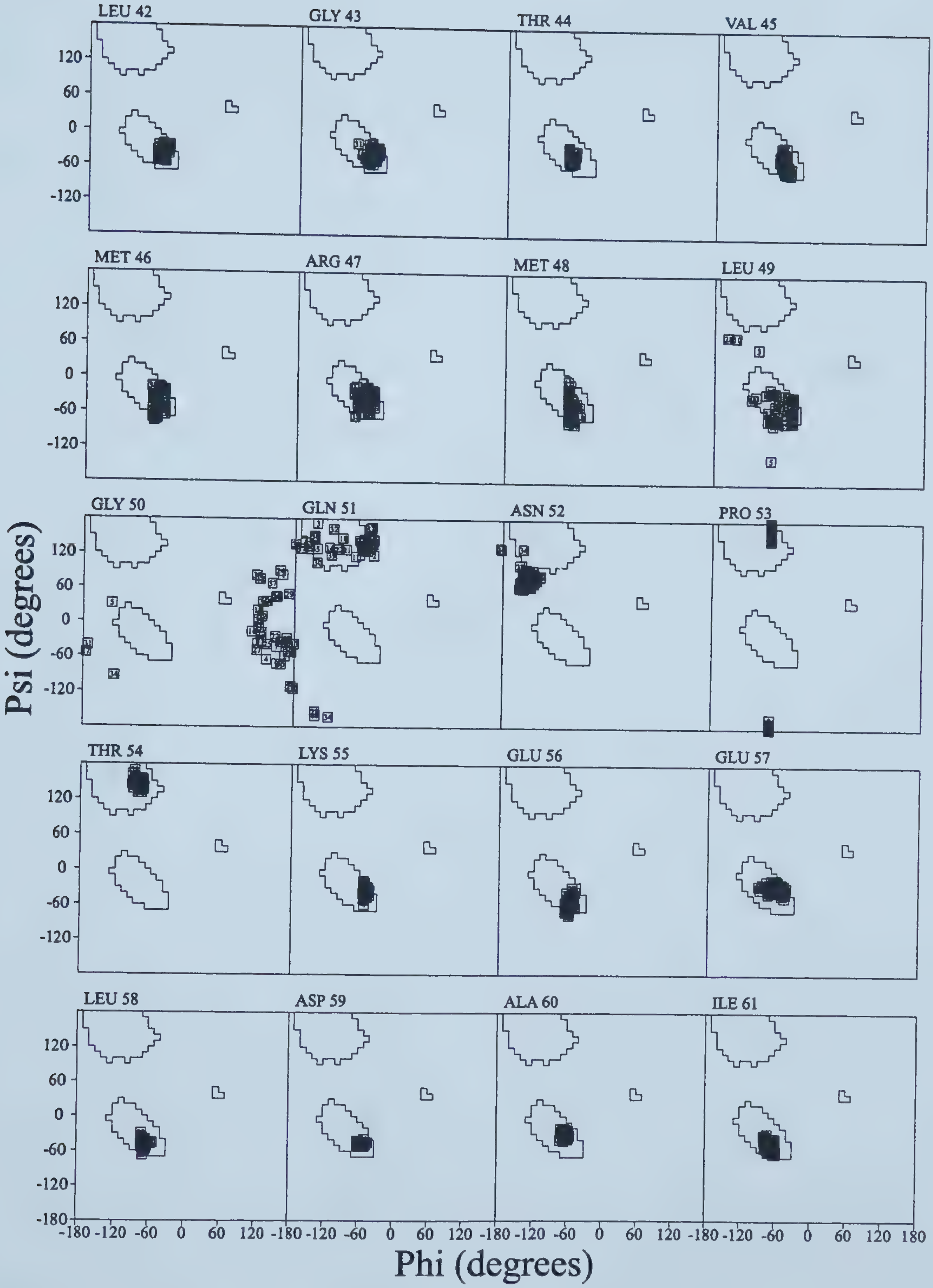

Figure 43. *(Part 3 of 5).*

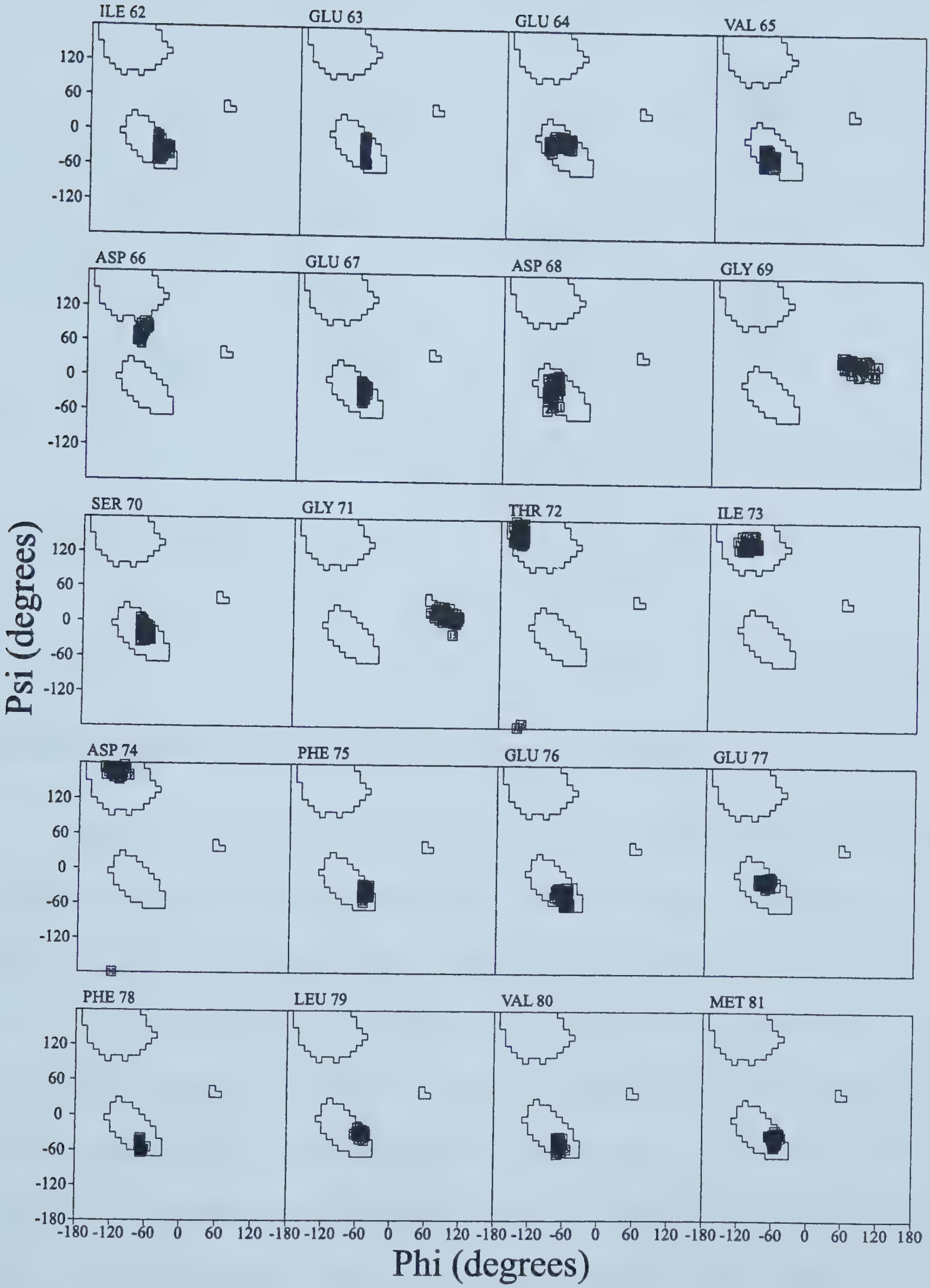

Figure 43. *(Part 4 of 5).*

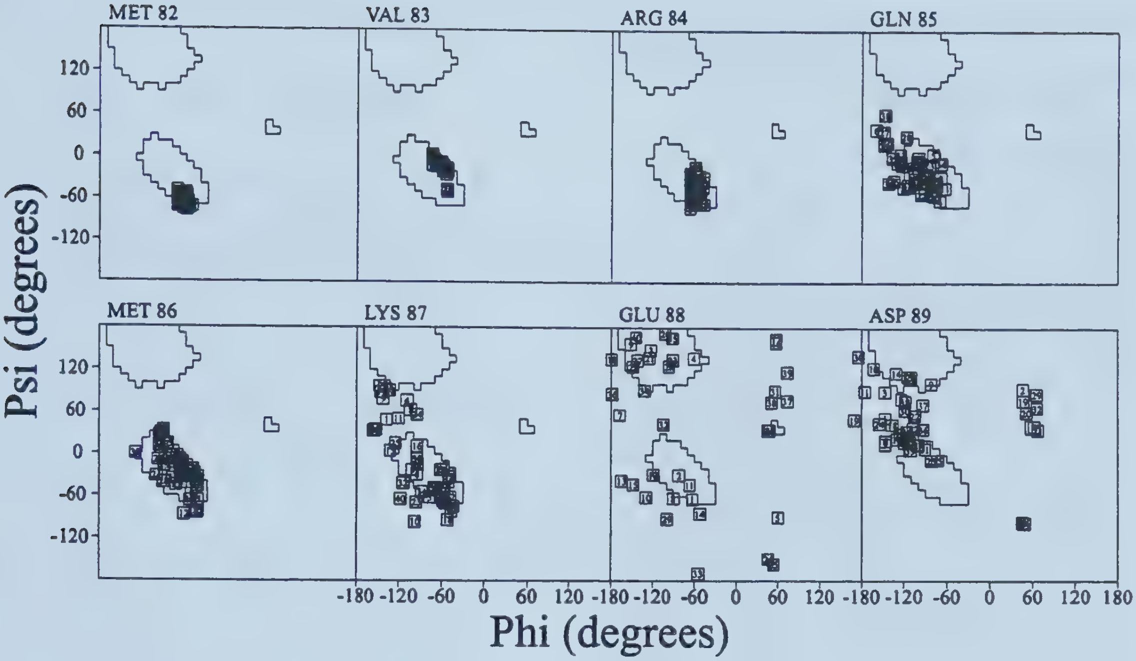

Figure 43. *(Part 5 of 5).*

Comparison with the wild type structures

Figure 44 compares the average NMR structure of E41A-sNTnC•Ca$_2$ with the X-ray structure of the apo N-domain of sTnC•Ca$_2$ and the X-ray structure of sNTnC•Ca$_2$. The quality of the structure presented here is significantly better than the NMR structure of sNTnC•Ca$_2$ (chapter 5), due to a larger number of medium and long range NOEs, to the absence of dimerization problem which was present in sNTnC•Ca$_2$ [49], and to improvements in the techniques used. For this particular case, I used the recent crystal structure of sNTnC•Ca$_2$ as opposed to the NMR structure I previously published (chapter 5), since it is of high resolution (1.78Å). Comparison of the helix packing in E41A-sNTnC•Ca$_2$ with

sNTnC•apo and sNTnC•Ca$_2$ reveals similarities and differences. The arrangement of helices N, A and D are virtually identical in all three structures; the backbone rmsd for these residues (5-28, 75-84) with sNTnC•apo and sNTnC•Ca$_2$ is 0.73Å and 0.76Å, respectively. Since these three helices are not significantly affected by the calcium state, this superimposition will be used frequently and will be referred as NAD. The packing of helix B is similar to sNTnC•apo (NAD: rmsd of 1.3Å), and therefore has major differences with sNTnC•Ca$_2$ (9.2Å). Helix C is positioned between sNTnC•apo (NAD: rmsd of 2.5Å) and sNTnC•Ca$_2$ (8.8Å), closer to sNTnC•apo. The state of the helix packing of E41A-sNTnC is clearly represented by the measure of its inter-helical angles. When compared with the apo or Ca$_2$ form of sTnC and CaM, the inter-helical angles of E41A-sNTnC•Ca$_2$ are like the apo forms, rather then the Ca$_2$ forms (table 8). I have also looked at the accessible surface area of the non-polar groups, which is a measure of the exposure of the hydrophobic patch. Using the Shrake definitions [65] and considering only residues 4-88, the following values were observed: 2872±74 Å^2 for E41A-sNTnC•Ca$_2$, 2866 Å^2 for sNTnC•apo, and 3386 Å^2 for sNTnC•Ca$_2$. These values show that the hydrophobic patch is not exposed in E41A-sNTnC•Ca$_2$.

Table 8. Inter-helical angles in sTnC and CaM as a function of calcium

	Inter-helical angle (°) [a]	
	first site [b]	second site [b]
avg of apo forms [c]	135 ± 5	134 ± 9
avg of Ca$_2$ forms [d]	95 ± 9	91 ± 11
E41A-sNTnC•Ca$_2$	130 ± 3	130 ± 5

[a] Calculated using the program IHA. [b] First site corresponds to the A-B helix pair for N-domains and to the E-F helix pair for C-domains. Similarly, second site corresponds to the C-D and G-H helix pair for N-domains and C-domains, respectively. [c] Average of nine apo domains found in the PDB data bank. PDB accession codes: 1TNP, 5TNC, 4TNC, 1TOP, 1DMO, 1CFC, and 1CMF. [d] Average of 27 calcium saturated domains found in the PDB data bank. PDB accession codes: 1TNQ, 1TNW, 1OSA, 1CLL, 3CLN, 4CLN, 1LIN, 1CTR, 1CDM, 1CDL, 2BBN, 5TNC, 4TNC, 1TOP, 1PON, 1CMG, and 1AVS.

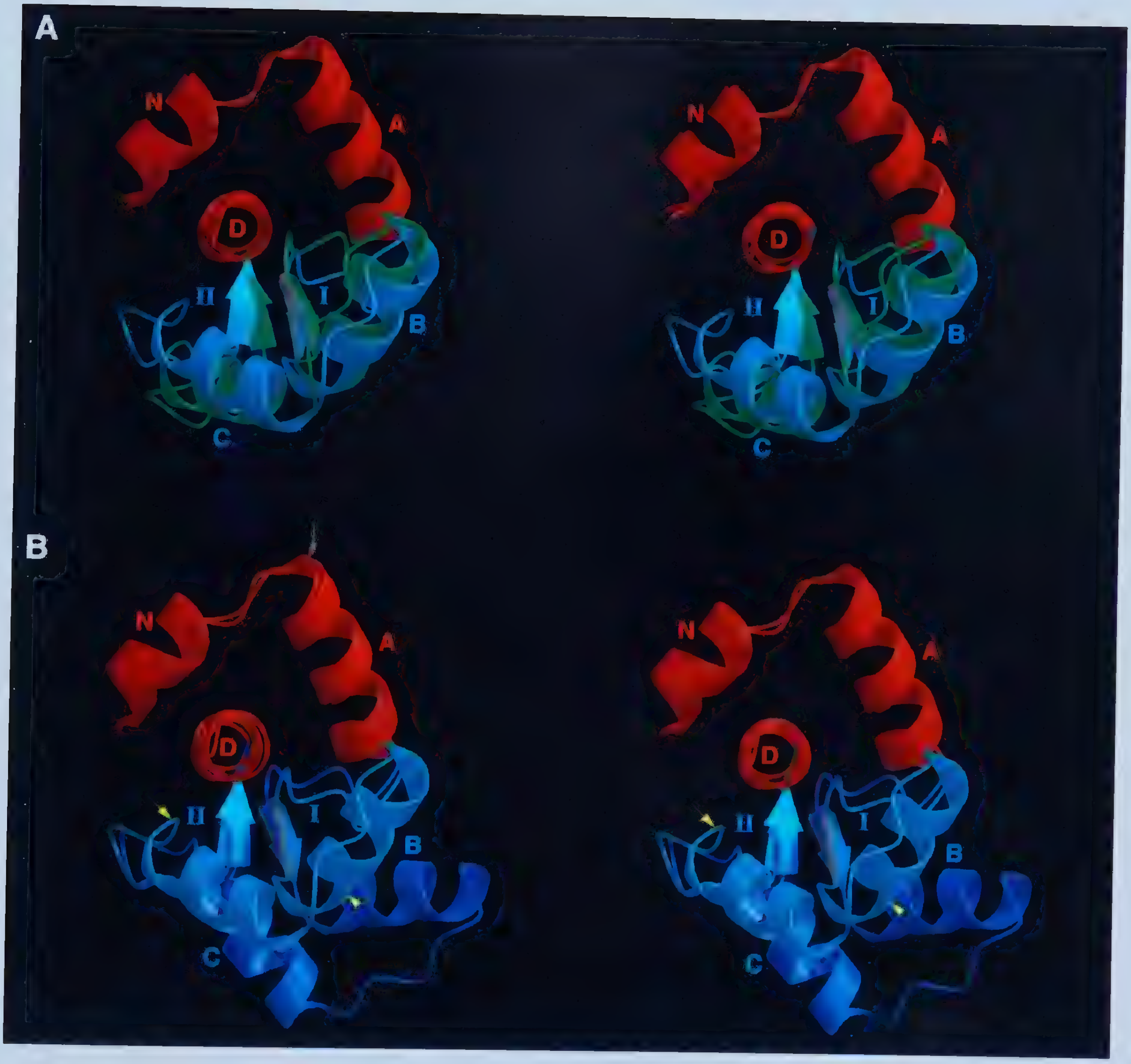

Figure 44. (*a*) Comparison of the E41A-sNTnC•Ca$_2$ structure with sNTnC•apo. The superimposed region (helices N, A, and D) is shown in [red]. The helix B/helix C unit is shown in [green] and [cyan] for sNTnC•apo and E41A-sNTnC•Ca$_2$, respectively. (*b*) Comparison of the E41A-sNTnC•Ca$_2$ structure with sNTnC•Ca$_2$. The helix B/helix C unit of sNTnC•Ca$_2$ is shown in [blue], and the other colors are as in (*a*). The positions of the two hinges for the opening of the structure (see text) are indicated by arrows,

As expected, site II adopts a conformation very close to that in sNTnC•Ca_2 (NAD: rmsd of 0.99Å). When site II is superimposed (residues 66-77), the calcium position in E41A-sNTnC•Ca_2 is only 0.26Å away from the one in sNTnC•Ca_2. Similarly, site I has a conformation similar to that in sNTnC•Ca_2 as far as residues 30-38 are concerned (figure 45). As pointed out previously [66] it is important that the mutation does not change the way calcium sits in the binding site.

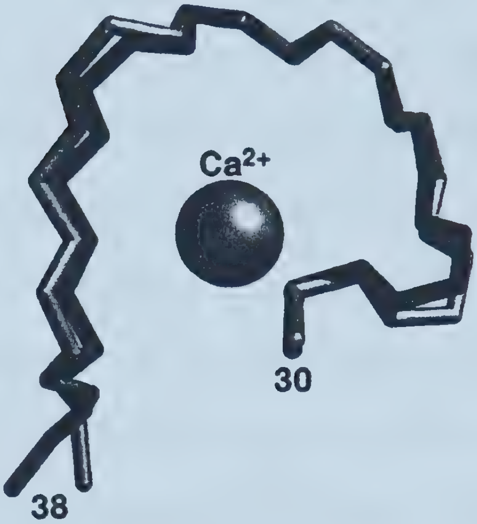

Figure 45. Superimposition of site I (residues 30-38) in sNTnC•Ca_2 (light gray) and E41A-sNTnC-Ca_2 (dark gray). The good overlap indicates that the mutational change did not affect the way calcium sits in the binding pocket. Note that the calcium ion was not included in site I for the structure calculations.

Experimental procedures

Sample preparation

Cloning, expression, and labeling with either ^{15}N or $^{15}N/^{13}C$ of E41A-sNTnC was performed by M. Li, J. Pearlstone and L. Smillie [64]. The experimental data were obtained under near-physiological conditions (30 °C, pH 6.7, 100mM KCl) at a protein concentration of 1.5-2.0 mM and a calcium concentration of about 5 equivalents.

NMR experiments

Chemical shift assignments (^{1}H, ^{15}N, and ^{13}C) were performed using multidimensional heteronuclear NMR experiments acquired on a Unity-600MHz spectrometer equipped with a triple resonance probe head and Z-pulsed field gradient. The following experiments were used for assignments: HNCACB [67], CBCA(CO)NNH [67], 75 and 150 ms ^{15}N-edited-NOESY [68], 57 ms ^{15}N-edited-TOCSY [68], 17 ms HCCHTOCSY [69], 75 and 150 ms ^{13}C-edited-NOESY [55], 2D-COSY in D_2O [70], and 150 ms 2D-NOESY [52, 53] in D_2O. Valine and leucine methyl groups were stereo specifically assigned using a ^{13}C-HSQC of a 30% ^{13}C-labeled sample [71]. Coupling constants were obtained using an HNHA experiment [72]. Spectra were processed using the software package NMRPipe [73] and analyzed using the program PIPP [74].

Structure determination

Inter-proton distance information was derived from the NOESY experiments listed above. The 2D-NOESY was calibrated based on NOE corresponding to known distance (Phe Hδ–Hε = 2.48Å). The 75 ms 3D-NOESYs were calibrated using an NOE corresponding to a known distance, located on the same ^{15}N or ^{13}C trace, and an error of 50% was assumed on each NOE intensity. The following distances were used to calibrate the 3D spectra: $HN_i–H\alpha_i$ = 2.70 - 3.05 Å (for residues with negative φ), $HN_i–H\alpha_{i-1}$ = 1.7 - 3.6 Å, H–C–C–H = 2.2 - 3.1 Å, H–C–CH_3 = 2.5-2.7 Å, H–C–H = 1.7-1.8 Å. In cases where direct calibration was not possible, the distance constraints were overestimated. For NOEs found only in the 150 ms NOESYs, the upper bound was set to 6Å. For all proton-proton restraints,

the lower bound was set to 1.7Å. The calcium-ligand distance restraints were set to 2.4±0.4Å between the calcium ion and the oxygens involved in coordinating calcium [15]. Dihedral restraints for the φ angle were obtained from the HNHA experiment, using a correction factor of 1.055. A 25% errors on the peak intensities was assumed, and the minimum φ dihedral restraint range was set to ±10°. The initial set of restraints included only a portion of the NOEs found in table 7, no dihedral restraints, and no calcium restraints. From this initial set of restraints and starting from an extended structure, 101 structures were generated with the simulated annealing protocol (sa.inp) implemented in XPLOR [75], using 12000 high temperature steps (60ps at 1000K) and 6000 cooling steps (30ps, final temperature of 100K). Out of those 101 structures, 50 folded properly (i.e. had significant lower total energy than the rest) and were kept as starting structures for further rounds of refinements. The refinement rounds were also done with the simulated annealing protocol, but using 6000 high temperature step (30ps) and 4000 cooling steps (20ps). The set of structures presented in this paper includes the 40 structures with the lowest total energy selected from the 50 structures obtained in the last round of refinement.

7. MECHANISM OF THE CALCIUM-INDUCED STRUCTURAL CHANGE IN SNTNC

Muscle contraction is triggered by the calcium-induced conformational change that occurs in the regulatory domain of TnC. Upon binding of two calcium ions, the N-domain of sTnC 'opens' and exposes a large hydrophobic patch [48,59,63]. A similar structural change occurs in CaM upon calcium-binding [76-78]. Although the calcium-induced structural change found in these proteins is now well characterized (chapter 5), the mechanism by which calcium causes the 'opening' is not known. The structure of E41A-sNTnC•Ca_2 (previous chapter) provides a unique tool to understand how proteins like sTnC and CaM operate, as it is a snapshot of sNTnC just prior to the calcium-induced opening. As shown above, binding of calcium to site II does not trigger the opening of the skeletal N-domain. Only minor structural changes occur upon calcium-binding in E41A-sNTnC. Binding of calcium to site II, which has been shown to be important [79, 80], requires minor rearrangement of the ligands and the loop which can be accommodated without opening the domain. Similarly, binding of calcium to site I (Glu41 not coordinated) does not open the N-domain. This demonstrates that the ligands in site I, with the exception of Glu41, can coordinate calcium with only minor rearrangements, as was originally proposed [15]. Exposure of the hydrophobic patch is an unfavorable event, and therefore the opening will not occur unless it is necessary and energetically favorable. As shown in figure 46, the two oxygens of Glu41 in sNTnC•apo are 10.8Å away from the calcium position. These oxygens must approach the calcium ion to 2.4Å [15] in order for site I to bind calcium properly. Unlike the other ligands

in site I and II, Glu41 cannot coordinate the calcium ion when the domain is in the closed form. To reach the calcium, Glu41 causes changes in the backbone dihedral angle at the base of helix B, which result in a reorientation of the helix B/helix C unit. I therefore conclude that it is the coordination of Glu41 to the calcium ion that ultimately leads to the opening of the domain, and that the other ligands play a role in positioning the calcium and setting the stage for Glu41. Glu41 literally ‘locks’ the domain in the open form.

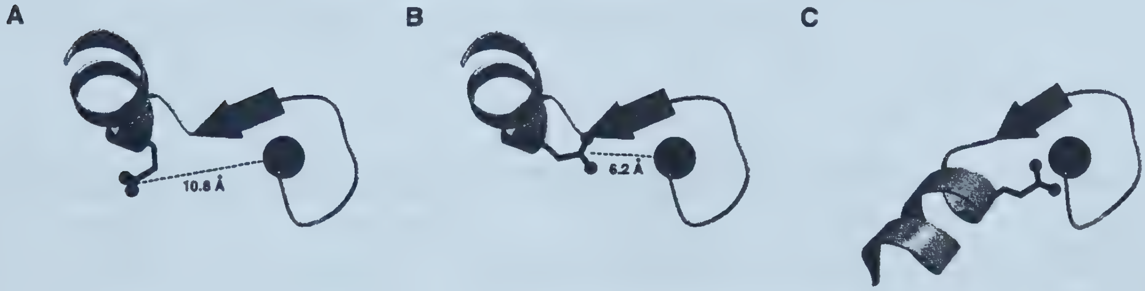

Figure 46. Glu41 cannot coordinate calcium when the domain is in the closed form. The backbone of loop I and helix B are shown in light gray, the side chain of Glu41 is shown in the dark gray stick representation, the position of the calcium ion is shown by the large sphere, and the coordination oxygens of Glu41 are shown by small spheres. The indicated distance is between the calcium ion and the center of the two coordinating oxygens. (a) Glu41 in closed form (sNTnC•apo). The kink at residue Glu41 is clearly visible. (b) Same as in (a) but with the side-chain χ_1 and $\chi_2$angles of Glu41 modified in order to minimize the distance of the ligands to the calcium ion. The coordinating oxygens are still 6.2 Å away from the calcium ion; this is 3.8 Å short of the coordinating distance (2.4 Å). (c) Glu41 in sNTnC-Ca_2.

The two hinges in the calcium-induced structural reorientation of sNTnC occur at the beginning of helix B (primarily at residue Glu41) and at the end of helix-C (primarily at residue Val65) (indicated by arrows in figure 44). The identification of Val65 as the hinge at the C-terminal end of the helix B/helix C unit is based on the observation that the change that occurs at Val65 when sNTnC binds two calcium is not found in E41A-sNTnC•Ca_2 (table 9). The backbone dihedral angles of Val65 in E41A-sNTnC•Ca_2 are identical, within

experimental error, to those of sNTnC•apo (table 9). The best experimental measure of the φ dihedral angle in solution is the backbone coupling constant, $^3J_{HN\text{-}H\alpha}$. The coupling constant measured for Val65 in E41A-sNTnC•Ca_2 (7.5Hz) is similar to the one observed in the NMR data of sNTnC•apo (7.4Hz [47]) and to the one expected from the crystal structure of the apo N-domain of sTnC•Ca_2 ($\varphi = -84° \Rightarrow 7.3$Hz), but significantly different from the one expected for the crystal structure of sNTnC•Ca_2 ($\varphi = -115° \Rightarrow 9.8$Hz) ($^3J_{HN\text{-}H\alpha}$ was not obtained in the NMR data of sNTnC•Ca_2 [47]). It is interesting to note that the dihedral changes that occur at the two hinges are similar, but opposite in direction (table 9).

Table 9. Backbone dihedral angle at the hinge positions as a function of calcium.

Dihedral angle	sNTnC•apo [a]	sNTnC•Ca_2 (X-ray) [b]	sNTnC•Ca_2 (NMR) [c]	E41A-sNTnC•Ca_2
Glu41, φ	-96	-65	-66 ± 10	-83 ± 7
Glu41, ψ	-7	-43	-47 ± 9	-13 ± 8
Val65, φ	-84	-115	N/A [d]	-89 ± 7
Val65, ψ	-37	-1	N/A [d]	-34 ± 8

[a] PDB accession code 5TNC. [b] PDB accession code 1AVS. [c] PDB accession code 1TNQ. [d] The backbone dihedral angles of Val65 are not defined in the NMR structure, due to a lack of restraints.

To investigate the mechanism further, I have performed the following experiment. I looked at an E77A mutant of sNTnC, Glu77 being the site II equivalent of Glu41. Preliminary results showed that this mutant was unable to bind any calcium strongly. Similar calcium binding properties were observed for comparable mutants (Glu→Gln) of calmodulin [81]. This inability of site I to bind calcium strongly when site II is perturbed shows that

although complete calcium binding to site I causes the opening, calcium binding to site II is first required. We previously determined the two different calcium-binding constants of the N-domain [25], but we were unable to unambiguously associate them to their corresponding sites. The results presented here clearly indicate that the strongest calcium-binding occurs in site II. The calcium binding scenario for sNTnC is therefore the following: the first calcium binds to site II, causing only minor conformational changes but setting the stage for the second calcium binding to site I, causing the structural change required to trigger skeletal muscle contraction.

As mentioned earlier, the structure of this skeletal mutant can potentially be used as a model for cardiac TnC (cTnC) which is unable to bind calcium in site I. cTnC is 70% homologous to sTnC, and the majority of the differences occur in the first 40 residues. The results presented here strongly suggest that the calcium induced structural change in cTnC does not involve an extensive opening of the structure as was found for sTnC, as there is no calcium in site I. Since cTnC and sTnC are nearly identical in the second HLH (site II), it is very likely that the calcium saturated structure of cNTnC resembles more E41A-sNTnC•Ca_2 than sNTnC•Ca_2. As will be shown in the next chapter, this has recently been verified with the determination of the calcium-bound cTnC and cNTnC structures.

The mechanism of the direct coupling between calcium-binding and induced structural change can be summarized as follows. First, the opening of the structure exposes a large hydrophobic patch, an event which is energetically unfavorable in water ($\Delta G \approx 2.0$ kcal $mole^{-1}$ [82]). This exposure can only occur if the favorable interactions associated with calcium-binding compensate for it, and if the binding of calcium cannot be accommodated

in the closed form. Second, the structural change is defined as a hinge motion between two units, one including the N-, A-, and D-helices, and the other the B- and C- helices. Finally, the movement of the BC unit relative to the NAD unit, which involves the displacement of several residues by more than 15Å, is driven by a single amino acid, Glu41.

Clearly, several factors contribute to the regulation of muscle contraction. However, I have shown that the 'muscular work' (i.e., opening of the regulatory domain of skeletal TnC to trigger contraction) was accomplished by Glu41 reaching for the calcium ion, and one could look at it as 'flexing muscle with one amino acid'.

8. CARDIAC TNC

The paradigm for calcium regulation has been that calcium-binding leads to a transition from a ‘closed’ to an ‘open’ state with resulting exposure of a large hydrophobic surface for interaction with target proteins such as TnI. The NMR structures of skeletal TnC in its various states have served to support this view and define the changes induced. However, the NMR structures of cardiac TnC have brought into focus the question of whether such large conformational changes are always involved in calcium regulation.

This chapter presents a summary of the NMR structural studies of cTnC•Ca_3, cNTnC•apo, and cNTnC•Ca_2. I want to emphasize here that Leo Spyracopoulos, Monica Li and Sam Sia were the ones who did all the hard work in the cardiac TnC studies, although I was actively involved in the acquisition and processing of the NMR spectra, in the chemical shift and NOE assignments, and in the structure calculations and analysis.

NMR structure of cardiac TnC in the Ca_3 state

The three dimensional structure of chicken recombinant cTnC (C35S, C84S mutant) in calcium-saturated state was solved by NMR [83], and the structural statistics are shown in table 10. The overall structure of cTnC•Ca_3 consists of two separate N- and C- globular domains, connected by a flexible linker, like the calcium-saturated structures of sTnC and calmodulin. The most striking feature of cTnC•Ca_3 is that the calcium-bound N-terminal regulatory domain is partially closed (figure 47), resulting in significantly less exposed hydrophobic surface than found in calcium-bound sTnC, a direct consequence of the defunct

calcium-binding site I in cTnC. The helix packing in the calcium-bound N-domain of cTnC•Ca_3 is similar to that in the apo N-domain of sTnC. With no calcium bound in site I, the A/B helices run almost antiparallel to each other, exhibiting the typical A/B interhelical angle found in the apo state of sTnC (table 11). On the other hand, with calcium bound at site II, helix C is in fact in a partially open conformation, but does not open up to the extent seen in sTnC (table 11). These observations demonstrate that the inability of site I to bind calcium results in a more compact conformation of helix B and helix C than is observed in sTnC. The structure of the C-domain of cTnC•Ca_3 is similar to the one in sTnC as indicated by the comparable interhelical angle of the two EF hands (table 11).

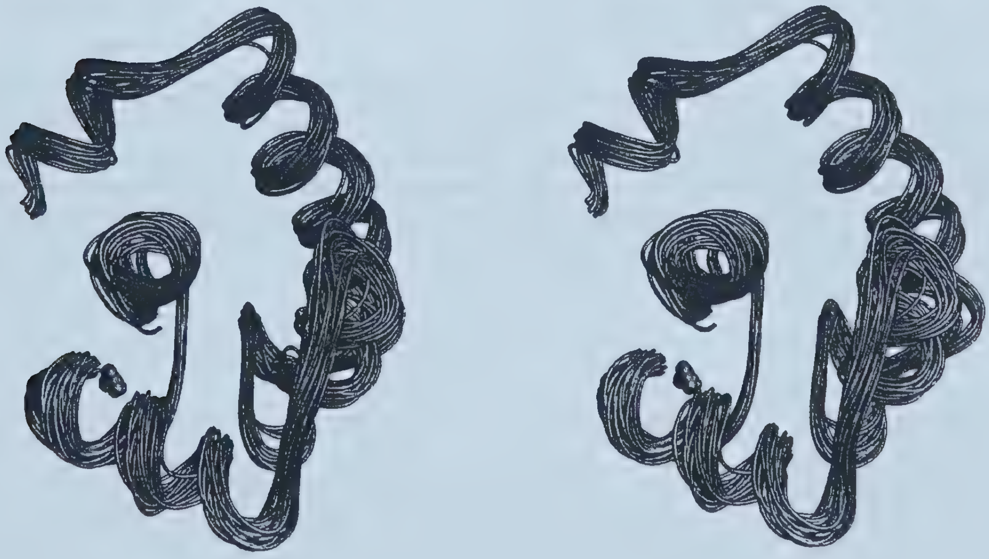

Figure 47. Structure of calcium-saturated cTnC. Stereo views of the superimposition of 30 structures for the regulatory N-domain (a) and the structural C-domain (b). Only residues 5-84 and 95-158 are shown for the N-domain and C-domain, respectively. Positions of the calcium ions are indicated by gray spheres.

Table 10. Structural statistics of the 40 structures of cTnC [a]

	N-domain (2-89)	C-domain (90-161)
NOE distance restraints (Å)		
Total	1239	1080
inter-residue sequential ($\lvert i-j \rvert = 1$)	285	267
inter-residue medium range ($1 < \lvert i-j \rvert \leq 5$)	315	222
inter-residue long range ($\lvert i-j \rvert > 5$)	162	170
intra-residue	477	421
experimental dihedral restraints (°)	$49\ \varphi$, $37\ \psi$, $18\ \chi_1$	$41\ \varphi$, $26\ \psi$, $20\ \chi_1$
calcium coordination restraints (Å) [b]	6	12
rmsd from idealized covalent geometry		
bonds (Å)	0.0012 ± 0.0001	0.0011 ± 0.0001
angles (°)	0.47 ± 0.01	0.44 ± 0.01
impropers (°)	0.35 ± 0.01	0.33 ± 0.01
energies (kcal mol^{-1})		
F_{NOE} [c]	2 ± 1	4 ± 1
F_{cdih} [c]	0.03 ± 0.03	0.03 ± 0.05
F_{total}	105 ± 4	84 ± 2
rmsd from the average structure (Å) [d]		
backbone atoms	0.54 ± 0.09	0.46 ± 0.07
heavy atoms	0.97 ± 0.09	0.94 ± 0.10
φ/ψ in most favored or additionally allowed region (%) [e]	98	99

[a] There are no distance violations over 0.2 Å for the N-domain, and only 1 distance violation over 0.2 Å for the C-domain. [b] No restraints involving the calcium ions were used in the initial stages of structure calculations, and were added only in the final stages of refinement. [c] The final force constants were $F_{NOE} = 50\ \text{kcal mol}^{-1}$ and $F_{cdih} = 200\ \text{kcal mol}^{-1}\ \text{rad}^{-2}$. [d] Residues 5-29, 34-48, 56-65, and 69-84 for the N-domain; residues 97-124 and 130-158 for the C-domain. [e] As determined by the program PROCHECK.

Table 11. Interhelical angles in cTnC compared to sTnC and CaM

	Inter-helical angle (°) [a]	
	first site [b]	second site [b]
avg of apo forms [c]	135 ± 5	134 ± 9
avg of Ca_2 forms [d]	95 ± 9	91 ± 11
cTnC•Ca_3 (N-dom.)	144 ± 3	110 ± 4
cTnC•Ca_3 (C-dom.)	111 ± 4	115 ± 3
cNTnC•Ca_1	135 ± 4	118 ± 3
cNTnC•apo	139 ± 3	128 ± 5

[a] Calculated using the program IHA. [b] First site corresponds to the A-B helix pair for N-domains and to the E-F helix pair for C-domains. Similarly, second site corresponds to the C-D and G-H helix pair for N-domains and C-domains, respectively. [c] Average of nine apo domains found in the PDB data bank. PDB accession codes: 1TNP, 5TNC, 4TNC, 1TOP, 1DMO, 1CFC, and 1CMF. [d] Average of 27 calcium saturated domains found in the PDB data bank. PDB accession codes: 1TNQ, 1TNW, 1OSA, 1CLL, 3CLN, 4CLN, 1LIN, 1CTR, 1CDM, 1CDL, 2BBN, 5TNC, 4TNC, 1TOP, 1PON, 1CMG, and 1AVS.

NMR structure of cNTnC in the apo and Ca_1 state

We also solved the structures of the N-domain of human recombinant cTnC in both the apo and calcium-saturated [84] (figure 48), and the structural statistics are shown in table 12. This pair of structures defines the calcium-induced structural transition in the regulatory domain of cTnC. The B/C structural unit in cNTnC moves only slightly away from the NAD structural unit (figure 49). This movement is only a small fraction of the analogous change in the skeletal isoform. The global fold of cNTnC•apo is very similar to that of sNTnC•apo. The interhelical angles of cNTnC•apo are comparable to those of sNTnC•apo (table 11), indicative of a closed conformation for the apo state of the regulatory domain in both isoforms. The structure of cNTnC•Ca_1 differs significantly from that of sNTnC•Ca_2, but displays similar interhelical angles to those in cTnC•Ca_3, indicating that both cNTnC and

cTnC remain in a predominantly closed conformation upon calcium-binding. This evidence demonstrates that separation of the two domains in cTnC has little structural effect on the regulatory domain.

Table 12. Structural statistics for the 40 structures of cNTnC•apo and cNTnC•Ca_1

	cNTnC•apo	cNTnC•Ca_1
NOE distance restraints (Å)		
Total	1213	1344
inter-residue sequential ($\|i-j\| = 1$)	297	307
inter-residue medium range ($1 < \|i-j\| \leq 5$)	255	305
inter-residue long range ($\|i-j\| > 5$)	167	171
intra-residue	494	561
experimental dihedral restraints (°)	48 φ, 23 ψ, 11 χ_1	53 φ, 21 ψ, 23 χ_1
calcium coordination restraints (Å) [b]	0	6
rmsd from idealized covalent geometry		
bonds (Å)	0.00107 ± 0.00005	0.00105 ± 0.00004
angles (°)	0.457 ± 0.004	0.450 ± 0.002
impropers (°)	0.340 ± 0.002	0.340 ± 0.002
energies (kcal mol^{-1})		
F_{NOE} [c]	2.0 ± 1.4	1.5 ± 0.4
F_{cdih} [c]	0.02 ± 0.02	0.02 ± 0.02
F_{total}	97 ± 3	95 ± 2
rmsd from the average structure (Å) [d]		
backbone atoms	0.61 ± 0.11	0.61 ± 0.09
heavy atoms	1.10 ± 0.09	1.02 ± 0.07
φ/ψ in most favored or additionally allowed region (%) [e]	[x]	[x]

[a] There are 7 (0.18/structure) distance violations over 0.2 Å for cNTnC•apo, and no distance violation over 0.2 Å for the cNTnC•Ca_2. [b] No restraints involving the calcium ions were used in the initial stages of structure calculations, and were added only in the final stages of refinement. [c] The final force constants were F_{NOE} = 50 kcal mol^{-1} and F_{cdih} = 200 kcal mol^{-1} rad^{-2}. [d] Residues 5-29, 34-48, 56-65, and 69-84 for the N-domain; residues 97-124 and 130-158 for the C-domain. [e] As determined by the program PROCHECK.

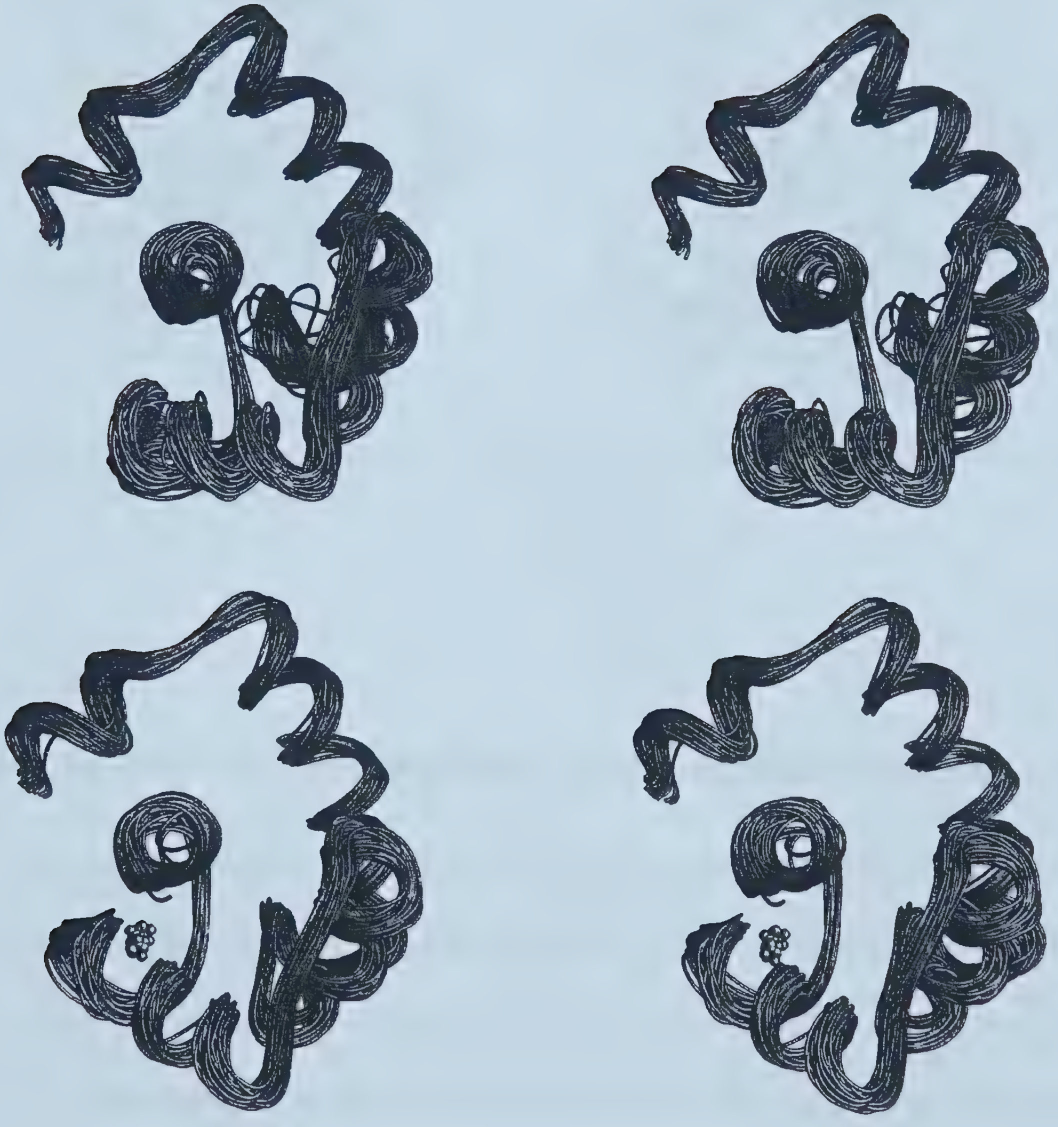

Figure 48. Structure of the regulatory domain of cNTnC in apo and calcium-saturated states. (a) Backbone superimposition of the 40 structures of cNTnC•apo (residues 5-84). (b) backbone superimposition of the 40 structures of cNTnC•Ca_1 (residues 5-84).

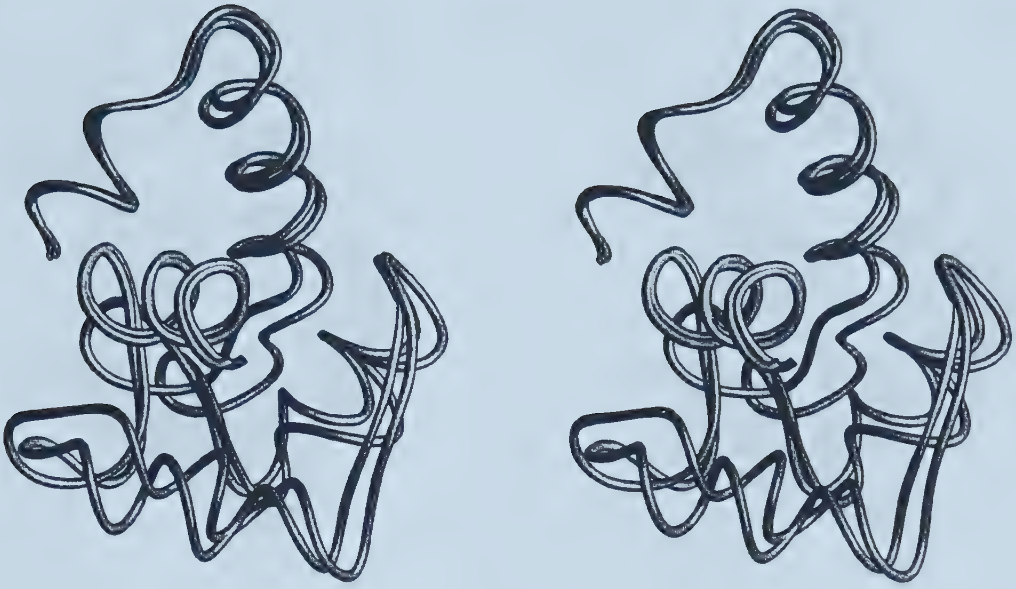

Figure 49. Calcium-induced structural change in cNTnC. The structure of cNTnC•apo and cNTnC•Ca_1 were superimposed using helices N, A and D.

Implications for the regulation of cardiac muscle

The structural differences between cardiac and skeletal TnC [83, 84] can be explained by what is in fact the most striking functional differences between the two proteins, namely that site I in cTnC is inactive due to an insertion and substitutions of key ligands. The above structures confirm what was originally proposed based on the structure of E41A-sNTnC•Ca_2; in cTnC there is no calcium at site I to pull the Glu40 (cTnC equivalent of Glu41 in sTnC), and opening of the structure is not observed upon calcium binding. This is emphasized in figure 50, where the structures of cNTnC•Ca_1 and E41A-sNTnC•Ca_2 are superimposed.

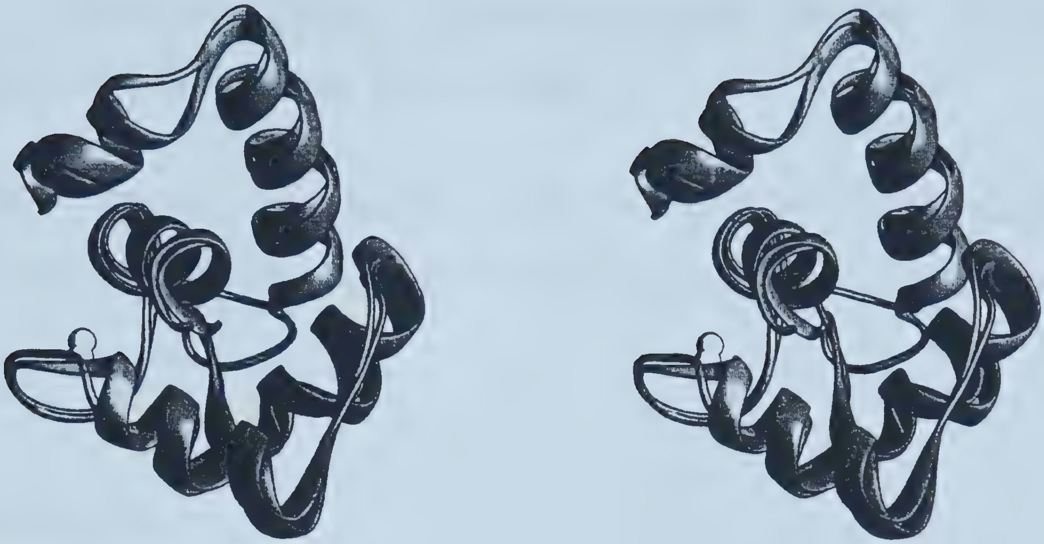

Figure 50. Comparison of the cNTnC•Ca$_1$ structure with the E41A-sNTnC•Ca$_2$ structures. All residues but helix N and site I were used for the backbone superimposition (rmsd 1.4 Å).

The substantially reduced hydrophobic surface exposure of calcium-saturated cTnC has important implications for the binding of cardiac TnI with cTnC. It is possible that the mode of interaction between TnI and TnC in cardiac muscle is in fact different from that in skeletal muscle. On the other hand, it is possible that the calcium dependent binding of cardiac TnI forces open the regulatory domain of cTnC, with the end result being that the cardiac TnI-TnC complex binds in a similar fashion to skeletal TnC-TnI. At present, there is no compelling evidence to either favor or discount either model for cardiac TnC-TnI interaction.

9. STRUCTURAL COMPARISON WITH OTHER CALCIUM BINDING PROTEINS

This chapter presents a comparison of the structures of NTnC with three other proteins: calmodulin (CaM), calbindin-D_{9k}, and S100B. The sequence and function of these proteins are also summarized.

Calmodulin

Function and sequence

Calmodulin (CaM) is found in all eukaryotic organisms, and several bacterial species also produce CaM homologues. CaM has several known regulatory functions which include intermediary metabolism, secretion, motility, signal transduction, and cell growth and division [1]. Similar to sTnC, CaM consists of 2 pairs of EF-hand motifs, and can bind four calcium ions. The C-domain contains two high affinity sites, ($K_d < 10^{-5}$ M), and the N-domain contains two lower affinity sites (K_d is 10^{-4} to 10^{-5} M). CaM has been shown to interact with well over 100 different proteins [1]. Typically, CaM interacts with its target upon calcium-binding.

The CaM sequence is highly homologous to the sTnC sequence. The largest homology is found in the N-domain where CaM is 64 % identical to sTnC. The two major differences are the absence of helix N in CaM and a shorter sequence connecting the two domains (see figure 51).

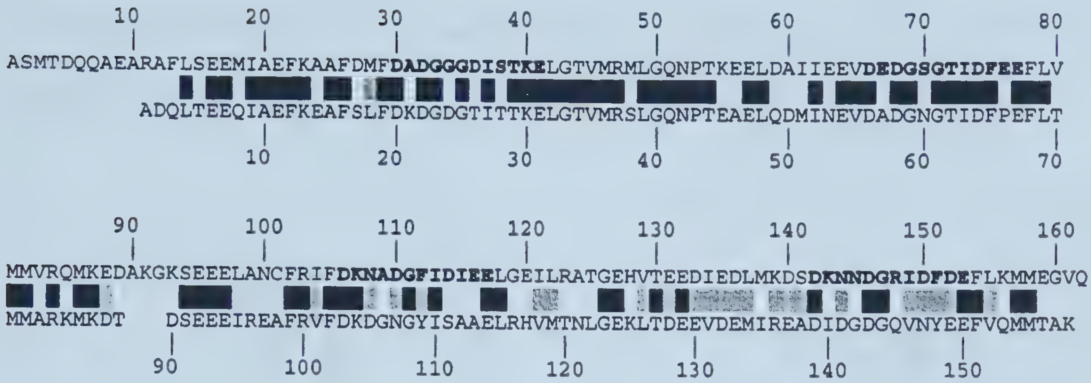
10 20 30 40 50 60 70 80
ASMTDQQAEARAFLSEEMIAEFKAAFDMF**DADGGGDISTKE**LGTVMRMLGQNPTKEELDAIIEEV**DEDGSGTIDFEE**FLV
ADQLTEEQIAEFKEAFSLFDKDGDGTITTKELGTVMRSLGQNPTEAELQDMINEVDADGNGTIDFPEFLT
10 20 30 40 50 60 70
90 100 110 120 130 140 150 160
MMVRQMKEDAKGKSEEELANCFRIF**DKNADGFIDIEE**LGEILRATGEHVTEEDIEDLMKDS**DKNNDGRIDFDE**FLKMMEGVQ
MMARKMKDT DSEEEIREAFRVFDKDGNGYISAAELRHVMTNLGEKLTDEEVDEMIREADIDGDGQVNYEEFVQMMTAK
90 100 110 120 130 140 150

Figure 51. Sequence comparison between chicken sTnC (top) and human CaM (bottom). The sTnC calcium binding sites are shown in bold. (■) and (▒) indicates sequence identity and sequence similarity, respectively.

Structures of calmodulin

The first X-ray structure of CaM was solved around the same time as the first X-ray structure of TnC. Unlike TnC which was solved in the Ca_2 state, the structure of CaM was in the fully saturated Ca_4 state. The structure of CaM has the same general appearance as TnC, with two domains linked by a long helical linker. The C-terminal domains are very similar, whereas the N-domain is significantly more open in CaM. The difference in the global fold of the N-domains of CaM and TnC was associated with their different state (apo in TnC, Ca_2 in CaM). At the time, this was probably the best experimental result in support of the HMJ model.

More recently, the NMR structure of apo-CaM was solved [76-78]. These structures have defined the calcium-induced structural change in CaM. Both the N- and C-domain of CaM undergo an opening upon the binding of calcium, which results in the exposure of a

large hydrophobic patch. This calcium-induced structural change is illustrated in figure 52 for the N-domain.

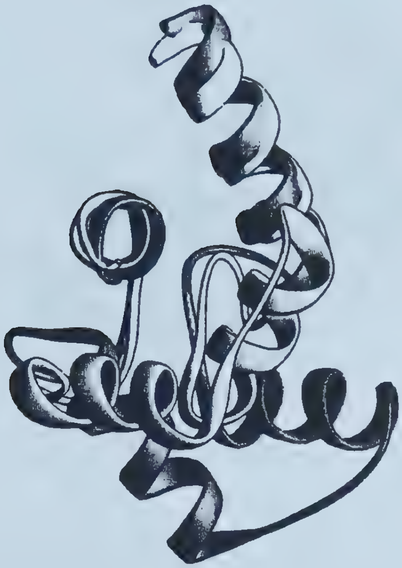

Figure 52. Calcium-induced structural change in the N-domain of CaM. Helices A and D were superimposed, clearly showing the calcium-induce movement of the B-C unit. The calcium saturated structure is shown as darker gray. The orientation is similar to the one used in previous figures of TnC, i.e. looking down helix D.

This hydrophobic patch is involved in the interaction of CaM with its targets. This was clearly demonstrated by the NMR structure of CaM bound to the cognate peptide of smooth muscle myosin light chain kinase [85]. In the presence of the target peptide, the linker between the two heads is bent, partially unwound and wrapped around the target peptide (figure 53). With respect to the TnC-TnI complex, it is not known if the conformation is

similar to the CaM-MLCK$_{peptide}$ complex; there is actually data suggesting that TnC is in the extended conformation in the TnC-TnI complex [86].

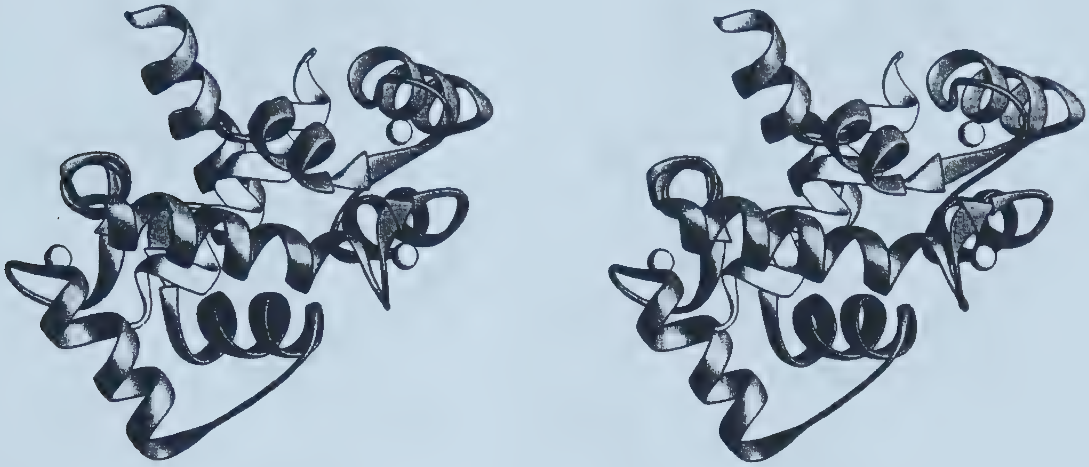

Figure 53. Structure of CaM bound to MLCK peptide. The N-domain of CaM is shown in the same orientation as the previous figure. The MLCK peptide is shown in white.

As illustrated above, the calcium-induced structural change in the N-domain of CaM is very similar to the one observed in sNTnC. The calcium-bound form of CaM and sNTnC are compared in figure 54 and show a good similarity.

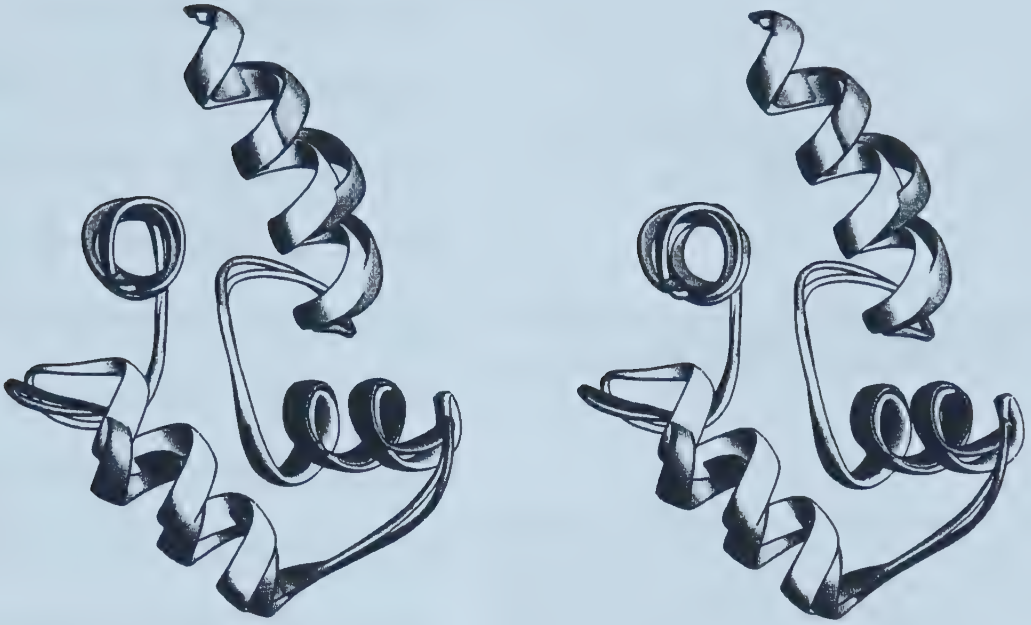

Figure 54. Superimposition of the N-domains of CaM and sNTnC•Ca_2 (NMR structure) in the calcium-bound form. Residues 6-75 (CaM) and 16-85 (sNTnC•Ca_2) were superimposed (backbone rmsd of 1.4 Å). CaM is shown in white.

Calbindin-D_{9k}

Function and sequence

Calbindin-D_{9k}, a member of the S100 calcium-binding family, is a cytosolic calcium-binding protein characteristic of mammals and present in several tissues. It is thought to increase calcium absorption by buffering cytoplasmic calcium. Calbindin-D_{9k} is smaller than TnC, has only one domain which consists of one pair of EF-hands, and can bind two calcium with high affinity ($K_{Ca} = 10^6$ M^{-1}).

The 79 amino acid sequence of calbindin-D_{9k} is only 47% homologous (28% identical) to the N-domain of sTnC. The homology is even less with the C-domain of sTnC. As can be seen from the superposition on figure 55, site I of calbindin-D_{9k} differs significantly from site I of sTnC. In particular, site I of calbindin-D_{9k} consists of 14 residues, and differs from the typical 12 residue length seen in EF-hand sites.

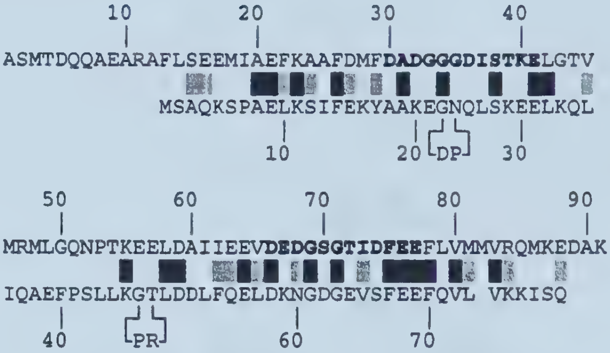
10
20
30
40
ASMTDQQAEARAFLSEEMIAEFKAAFDMFDADGGGDISTKELGTV
MSAQKSPAELKSIFEKYAAKEGNQLSKEELKQL
10
20
DP
30
50
60
70
80
90
MRMLGQNPTKEELDAIIEEVDEDGSGTIDFEEFLVMMVRQMKEDAK
IQAEFPSLLKGTLDDLFQELDKNGDGEVSFEEFQVL VKKISQ
40
PR
60
70

Figure 55. Comparison of the calbindin-D_{9k} sequence (bottom) with the sequence of the N-domain of sTnC (top). The sTnC calcium binding sites are shown in bold. (■) and (▒) indicates sequence identity and sequence similarity, respectively.

Structures of calbindin-D_{9k}

Structures of calbindin-D_{9k} have been solved in the apo, Cd_1 and Ca_2 form [87-89]. All three structures have the same general fold, and the binding of calcium does not induce a dramatic conformational change as observed for sTnC and CaM. The calcium-induced structural changes consist of subtle reorganization of some residues in the hydrophobic core. The global fold of calbindin-D_{9k}, in all three states, resembles most the apo state of the N-domain of TnC (figure 56). It should be noted that calbindin-D_{9k} has not been shown to interact with any target in a calcium-dependent manner. The primary role of calbindin-D_{9k} is as a buffer of the cytosolic calcium concentration. Therefore the calcium-induced

exposure of an hydrophobic patch observed for CaM and TnC is not necessary for the function of calbindin-D_{9k}.

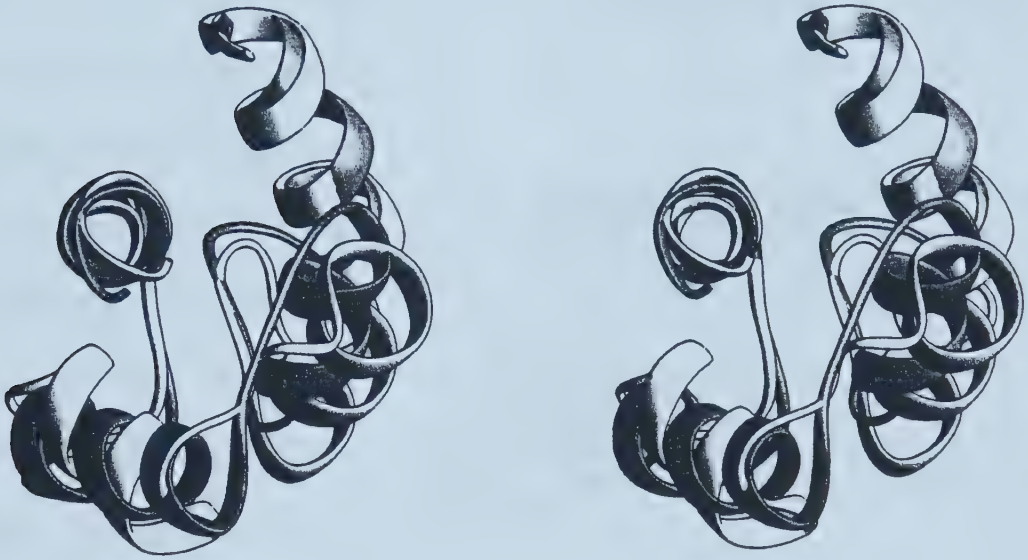

Figure 56. Structure of calcium saturated calbindin-D_{9k} compared to the apo structure of the N-domain of sTnC. Helices A and D were used in the superimposition. Calbindin-D_{9k} is shown in white.

S100B

Function and sequence

Another member of the S100 family is S100B, a homodimeric protein secreted in the central nervous system. S100B plays a role in cell differentiation and growth, and in

cytoskeletal structure and function. The effects of S100B are mediated via its interaction with target proteins.

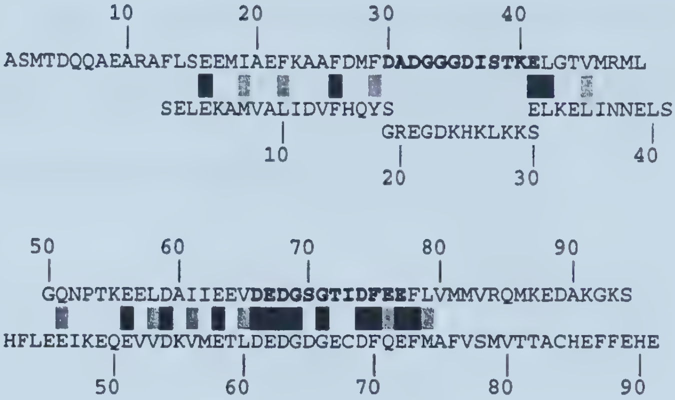
10
20
30
40
ASMTDQQAEARAFLSEEMIAEFKAAFDMFDADGGGDISTKELGTVMRML
SELEKAMVALIDVFHQYS
ELKELINNELS
GREGDKHKLKKS
10
20
30
40
50
60
70
80
90
GQNPTKEELDAIIEEVDEDGSGTIDFEEFLVMMVRQMKEDAKGKS
HFLEEIKEQEVVDKVMETLDEDGDGECDFQEFMAFVSMVTTACHEFFEHE
50
60
70
80
90

Figure 57. Comparison of the S100β sequence (bottom) with the sequence of the N-domain of sTnC (top). The sTnC calcium binding sites are shown in bold. (█) and (▒) indicates sequence identity and sequence similarity, respectively.

S100B consists of two S100β monomers. The S100β monomer has 91 residues and is highly homologous to calbindin-D_{9k}; the homology is significantly less relative to sTnC, especially for the first EF-hand (figure 57). Although the length of the S100β sequence is similar to the N-domain of TnC, it does not actually have the initial non-EF-hand helix found in TnC (helix N). Instead, the first helix in the first EF-hand is extended to nearly 20 residues. Like calbindin-D_{9k} and other S100 proteins, the first EF-hand of each S100β subunit has two more amino acid residues than typical EF-hand domains. Finally, the B-C linker is five residues longer in S100β compared to TnC.

Structures of S100B

Recently, several structures for S100B have been solved. There exists one apo structure which was solved by NMR and recently refined [90], two calcium-bound structures solved by NMR [91, 92], and one calcium-bound structure solved by X-ray [93]. Additionally there is one calcium-bound structure of calcyclin, which is highly homologous to S100B,

solved by NMR [94]. The calcium-induced conformational change involves an opening for the second EF-hand only. Unlike TnC and CaM, the conformation of the first EF-hand is not significantly affected by the binding of calcium. Figure 58 shows a comparison of the calcium-bound structure of S100β with E41A-sNTnC•Ca_2 and sNTnC•Ca_2; helix C of S100β is located between helix C of E41A-sNTnC•Ca_2 and sNTnC•Ca_2.

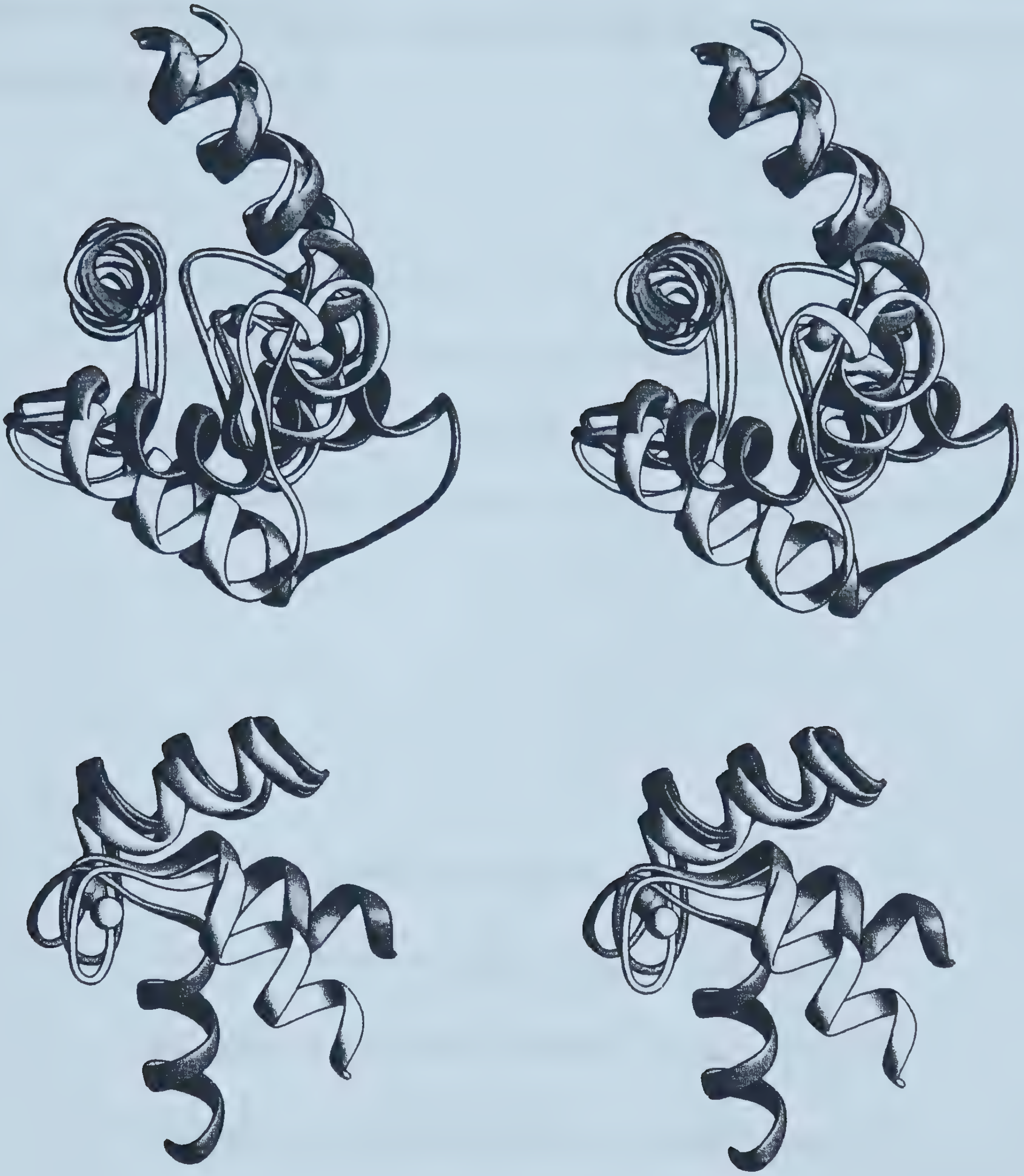

Figure 58. Comparison of the calcium saturated S100β structure (white) with the structure of E41A-sNTnC•Ca_2 (gray, most closed structure) and sNTnC•Ca_2 (gray, most opened structure). (top) Whole domain in the usual orientation. (bottom) Only helices C and D, clearly showing the position of helix C of S100β relative to E41A-sNTnC•Ca_2 and sNTnC•Ca_2. Helix A and D were used for the superimposition.

SECTION THREE: DYNAMICS AND THERMODYNAMICS ASPECTS OF TNC

10. Backbone analysis of sNTnC•apo 107
11. Methyl group dynamics analysis of sNTnC•apo 144
12. Contribution of dynamics to the function of sNTnC 153
13. Dynamics and thermodynamics of cNTnC•apo and cNTnC•Ca_1 164

The characterization of protein dynamics provides unique insights which are not obtainable from structure alone. It is important to study protein dynamics and thermodynamics in order to truly understand function.

10. BACKBONE DYNAMICS ANALYSIS OF SNTNC•APO

As shown in Section Two of this thesis, a large amount of structural information on TnC is now available. However, the dynamic properties of TnC have not yet been characterized. This chapter reports a study of the backbone dynamics of sNTnC in the apo form. The dynamic information is based on ^{15}N relaxation parameter measurements at two fields, 500 and 600 MHz. I determined the overall correlation time and the order parameters of the N-H bond vectors for sNTnC•apo. Several motional models were considered in order to appropriately interpret the data. I first analyzed the data using three different isotropic models described previously [95]: the simple S^2-τ_e model, the S^2-τ_e-R_{ex} model where the additional term takes into account potential chemical or conformational exchange, and the two-time-scale model. The data were also fitted with a model which included anisotropic rotational diffusion [96].

Theory

T_1, T_2 and NOE

Theoretical expressions for the T_1, T_2 and NOE relaxation parameters of an amide ^{15}N nucleus are well established [95, 97].

$$\frac{1}{T_1}=d^2[J(\omega_H-\omega_N)+3J(\omega_N)+6J(\omega_H+\omega_N)]+c^2J(\omega_N) \tag{1}$$

$$\begin{aligned}\frac{1}{T_2}=&0.5d^2[4J(0)+J(\omega_H-\omega_N)+3J(\omega_N)+6J(\omega_H)+6J(\omega_H+\omega_N)]+\\&\tfrac{1}{6}c^2[3J(\omega_N+4J(0)]\end{aligned} \tag{2}$$

$$\mathrm{NOE}=1+\frac{\gamma_H}{\gamma_N}d^2[6J(\omega_H+\omega_N)-J(\omega_H-\omega_N)T_1 \tag{3}$$

The constants d^2 and c^2 are defined as

$$d^2=\frac{0.1\gamma_H^2\gamma_N^2h^2}{4\pi^2}\left\langle\frac{1}{r_{NH}^3}\right\rangle^2 \tag{4}$$

$$c^2=\left(\tfrac{2}{15}\right)\gamma_N^2H_0^2(\sigma_\parallel-\sigma_\perp)^2 \tag{5}$$

where γ_H and γ_N are the gyromagnetic ratios of the ^1H and ^{15}N nuclei, respectively, ω_H and ω_N are the ^1H and ^{15}N Larmor frequencies, r_{NH} is the internuclear ^1H-^{15}N distance (1.02Å), H_0

is the magnetic field strength, $\sigma_{\parallel}$ and $\sigma_{\perp}$ are the principal components of the ^{15}N chemical shift anisotropy (CSA) tensor.

Isotropic models

S^2-τ_e model

Analysis of experimental ^{15}N relaxation data with the assumption of isotropic rotational diffusion is often done using the 'model-free' approach where the spectral density function is [98, 99]

$$J(\omega)=\frac{S^2\tau_m}{1+\omega^2\tau_m^2}+\frac{(1-S^2)\tau}{1+\omega^2\tau^2} \tag{6}$$

where $1/\tau=1/\tau_m+1/\tau_e$, S^2 is the order parameter, τ_m is the overall correlation time and τ_e is the effective correlation time representing fast internal motions. For the S^2-τ_e model, equation 6 is used as the spectral density (J) in the T_1, T_2 and NOE expressions (equations 1, 2, and 3).

S^2-τ_e-R_{ex} model

Conformational exchange can be accounted for by incorporating an exchange rate term, R_{ex}, in the T_2 equation:

$$\frac{1}{T_2}=\frac{1}{T_{2,DD}}+\frac{1}{T_{2,CSA}}+R_{ex} \tag{7}$$

where $T_{2,DD}$ and $T_{2,CSA}$ represent the dipole-dipole and CSA contributions to the calculated T_2. This is referred in the text as the S^2-τ_e-R_{ex} model analysis, and uses the spectral density function defined in equation 6.

Two-time-scale model

The third model which is considered under the assumption of isotropic tumbling is the two-time-scale model [100, 101] which accounts for internal motions occurring on two distinct time scales. This extended form of the model-free spectral density is given by the following expression:

$$J(\omega)=\frac{S^2\tau_m}{1+\omega^2\tau_m^2}+\frac{(S_f^2-S^2)\tau}{1+\omega^2\tau^2} \qquad (8)$$

where $S^2=S_f^2S_s^2$ and $1/\tau=1/\tau_m+1/\tau_s$. S_f^2 and S_s^2 are the order parameters characterizing the fast and slow internal motions, respectively, and τ_s is the effective correlation time for the slow internal motions. Equation 8 is obtained with the assumption that the term containing the correlation time describing the faster internal motion contributes a negligible amount to the relaxation [101].

Determination of the parameters

Determination of the parameters in the spectral density function was done by optimizing a χ^2 function given by [95]:

$$\chi^2 = \left(\frac{T_{1.c} - T_{1.e}}{\sigma_{T_1}}\right)^2 + \left(\frac{T_{2.c} - T_{2.e}}{\sigma_{T_2}}\right)^2 + \left(\frac{NOE_c - NOE_e}{\sigma_{NOE}}\right)^2 \tag{9}$$

where the subscript c and e represent calculated and experimental parameters, and $\sigma_{T_1,T_2,NOE}$ are estimates of the error on the experimentally determined parameters. Relaxation analysis assuming isotropic rotational diffusion was performed using programs provided by Farrow et al. [95].

Anisotropic models

Fully anisotropic model

The theory used in the analysis of the relaxation data where anisotropic rotational diffusion is taken into account is as described by Tjandra et al. [96]. For the general case of anisotropic rotational diffusion and $\tau_e \ll (6D)^{-1}$, the spectral density function is approximated by:

$$J(\omega) = S^2 \sum_{k=1,2,3,4,5} A_k \left[\frac{\tau_k}{1+\omega^2\tau_k^2}\right] + (1-S^2)\left[\frac{\tau}{1+\omega^2\tau^2}\right] \tag{10}$$

with the following definitions:

$A_1 = 6m^2n^2 \qquad A_2 = 6l^2n^2 \qquad A_3 = 6l^2m^2 \qquad A_4 = d - e \qquad A_5 = d + e$

l, m, and n are the direction cosines of the NH vector with respect to the diffusion axes x, y, and z, respectively

$$d = \tfrac{1}{2}\left[3\left(l^4 + m^4 + n^4\right) - 1\right]$$

$$e = \tfrac{1}{6}\left[\delta_x(3l^4 + 6m^2n^2 - 1) + \delta_y(3m^4 + 6l^2n^2 - 1) + \delta_z(3n^4 + 6l^2m^2 - 1)\right]$$

$$\delta_i = \frac{D_i - D}{\sqrt{D^2 - L^2}}$$

D is defined as ⅓ the trace of the diffusion tensor: $D = \tfrac{1}{3}\left(D_x + D_y + D_z\right)$

$$L^2 = \tfrac{1}{3}\left(D_xD_y + D_xD_z + D_yD_z\right)$$

$$\tau_1 = \frac{1}{4D_x + D_y + D_z} \qquad \tau_2 = \frac{1}{4D_y + D_x + D_z} \qquad \tau_3 = \frac{1}{4D_z + D_x + D_y}$$

$$\tau_4 = \frac{1}{6\left(D + \sqrt{D^2 - L^2}\right)} \qquad \tau_5 = \frac{1}{6\left(D - \sqrt{D^2 - L^2}\right)}$$

$$\frac{1}{\tau} = 6D + \frac{1}{\tau_e}$$

Axially symmetric model

In the case of the axially symmetric diffusion model ($D_x = D_y = D_\perp$; $D_z = D_\parallel$), $J(\omega)$ is approximated by

$$J(\omega) = S^2 \sum_{k=1,2,3} A_k\left[\frac{\tau_k}{1 + \omega^2\tau_k^2}\right] + (1 - S^2)\left[\frac{\tau}{1 + \omega^2\tau^2}\right] \qquad (11)$$

with the following definitions:

$$A_1 = \left(1.5\cos^2\alpha - 0.5\right)^2$$

$$A_2 = 3\sin^2\alpha\cos^2\alpha$$

$$A_3 = 0.75\sin^4\alpha$$

where α is the angle between the N–H bond vector and the cylinder axis. The time constants are:

$$\tau_1 = \frac{1}{6D_\perp} \qquad \tau_2 = \frac{1}{D_\parallel + 5D_\perp} \qquad \tau_3 = \frac{1}{4D_\parallel + 2D_\perp}$$

Determination of the parameters

The error function which is optimized to obtain the anisotropic diffusion parameters is given by

$$E = \sum_n \frac{\left(\frac{T_{1,e}}{T_{2,e}} - \frac{T_{1,c}}{T_{2,c}}\right)^2}{\sigma^2_{T_1/T_2}} \qquad (12)$$

where σ_{T_1/T_2} is the estimated error in the experimental T_1/T_2 ratio, and the summation extends over all residues, N, used in the fit. The calculated T_1/T_2 ratio is given by the ratio of equations 1 and 2, and the spectral density function is defined by equation 10.

Optimization of equation 12 was performed using in-house programs (ANIS, written by S. M. Gagné). Evaluation of the statistical significance of a reduction in the E function when increasing the number of adjustable parameters was performed using the statistical F test [102]. The reduced error function is defined as:

$$E_v = \frac{E}{N-m} \tag{13}$$

where m is the number of variables used in the fitting procedure. A test for the validity of adding x variables is done with the following ratio

$$F_x = \frac{E_m - E_{m+x}}{x \cdot E_{v,m+x}} \tag{14}$$

where E_m and E_{m+x} are the error functions, E, from the fitting which uses m and m+x variables, respectively. A large F_x value justifies the addition of x variables in the fitting. The probability that the observed improvement in the (m+x)-parameter fit over the m-parameter fit is obtained by chance is calculated from the normalized integral of the probability density function $P(F_x; x; N\text{-}m\text{-}x)$. The numerical evaluation of $P(F_x; x; N\text{-}m\text{-}x)$ was done with the *Mathematica 3.0* package [103] using the following *Mathematica* definition:

$$P(F_x; x; N-m-x) = 1 - \mathrm{CDF}[\mathrm{FRatioDistribution}[x, N-m-x], F_x] \tag{15}$$

Results

The primary goal of this work is to relate the dynamic properties of sNTnC to its function. However, several technical details need to be presented first in order to establish the validity of the dynamic parameters which are obtained. In a first step, I outline my approach to obtain accurate ^{15}N-T_2 measurements which are not affected by sample heating. Following the acquisition of the experimental ^{15}N relaxation parameters, I determined the overall rotational correlation time under the assumption of isotropic rotational diffusion and using the simple S^2-τ_e spectral density. Under this same assumption, I fitted the ^{15}N relaxation parameters to three different models as described in the Theory section. As will be shown, the isotropic fits suggest the presence of conformational exchange for a portion of the molecule. Anisotropic rotational diffusion can however be mistaken for conformational exchange, and I included anisotropy in the final fitting.

Influence of sample heating on ^{15}N-T_2 measurements

Measurement of ^{15}N-T_2 relaxation data for proteins in solution requires the application of a large number of ^{15}N pulses for various relaxation decay time periods [95]. Depending on various factors such as decay time duration, power level used, delay between scans, and sample conditions, T_2 experiments are prone to sample heating. In particular, ionic strength, solvent, and γB_2 magnitude can have profound effects on sample heating [104]. Sample heating can lead to inaccurate data in two ways. First, it can directly affect the dynamic properties of the protein which are temperature dependent. Second, since each data

point requires a different spin-lock period, the amount of sample heating will vary between data points and adversely affect the observed exponential decay. Care must therefore be taken to avoid or minimize sample heating.

A simple way to reduce heating is to increase the relaxation delay between scans, and I looked at the dependence of the observed T_2 on the relaxation delay. T_2 data was obtained using five different relaxation delays : 1.0, 1.5, 2.0, 2.5 and 3.0s. The precision of each of the T_2 values was estimated as described in the Methods. The accuracy of the different T_2 measurements was estimated by assuming that the data obtained with the longest relaxation delay (3.0s) gave the 'correct' T_2 ($T_{2,c}$):

$$\text{accuracy} = \frac{1}{N} \sum_{n} \frac{\Delta_{T_2}}{T_{2,c}} \tag{16}$$

where Δ_{T_2} is the absolute difference between the T_2 at a given relaxation delay and $T_{2,c}$. The average is over all 74 characterized residues (N). The relation between accuracy of the observed T_2 and the relaxation delay is shown in figure 59. Although the precision of the various T_2 is nearly constant at ~1%, the accuracy of those values is very poor when using short relaxation delays. For this sample and the experimental conditions described in Methods, a relaxation delay of 2.5s was necessary to obtain an accuracy of the order of ~1%. The 1.5s experiment was repeated twice, two weeks apart, and showed that the inaccuracy of 4.5% was reproducible ('precise') to 1%. These data clearly demonstrate that one can obtain inaccurate T_2, although very precise, if care is not taken to minimize sample heating. In our experience, dielectric heating of the NMR samples due to the electric component of

the r.f. field is an insidious problem which is easily avoided by either choosing a long relaxation delay (~3 s) or ensuring that the relaxation delay is optimized for the conditions. A relaxation delay of 3s was used in the present study. Note that a longer relaxation delay also reduces potential problems related to partial water saturation.

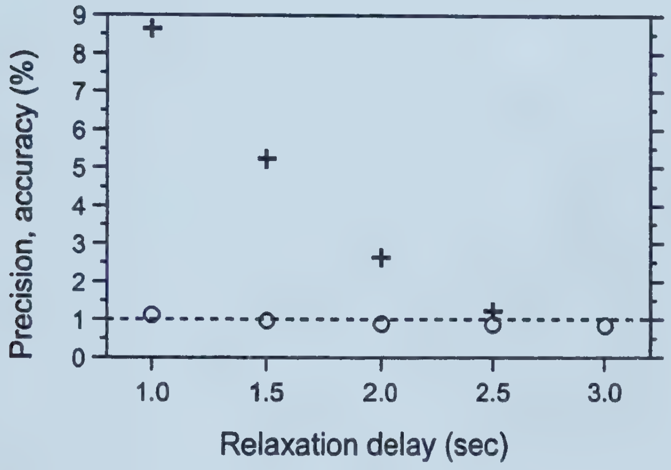

Figure 59. Effect of sample heating and length of the relaxation delay on the precision (O) and accuracy (+) of the measured $^{15}N-T_2$. For each delay, the average of all 74 measured T_2 is used. Precision and accuracy evaluated as described in the text.

$^{15}N-T_1$, $-T_2$, and -NOE data.

^{15}N relaxation parameters were obtained using 2D $^1H-^{15}N$ correlation NMR spectra. A total of 74 well resolved N–H correlation could be unambiguously characterized and are shown in figure 60. ^1H and ^{15}N assignments were published previously [2, 47]. Overlapped resonances were not considered. T_1, T_2 and NOE data were obtained at ^1H frequencies of 500 and 600 MHz, and temperature of 29.6°C. The acquisition of the various data occurred over a period of 4 months using a single sample. Characteristic fits for the T_1 and T_2 data are shown in figure 61. The ^{15}N T_1, T_2 and NOE at both frequencies are displayed graphically in figure 62a, 62b and 62c, respectively.

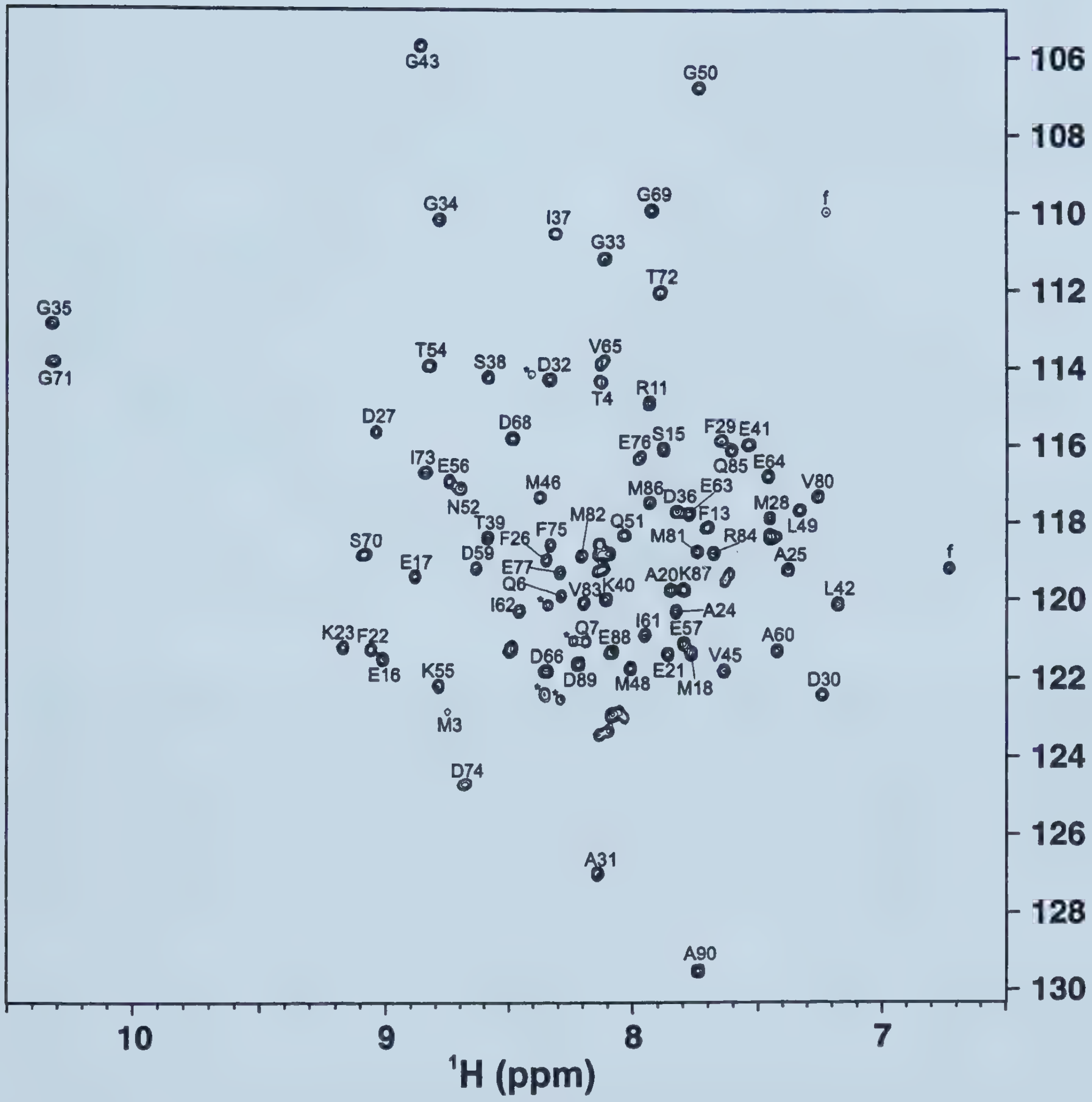

Figure 60. 2D ^{1}H–^{15}N HSQC correlation spectra of sNTnC•apo. The 74 residues for which relaxation data were characterized are labeled with their residue name and number. Folded peaks from upfield arginine side-chains are labeled (f), and impurity peaks labeled (*).

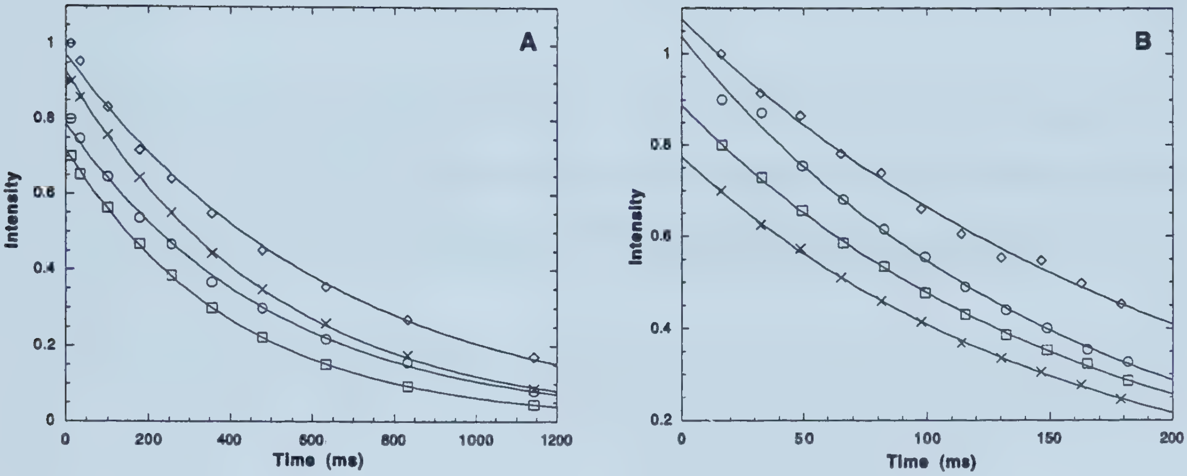

Figure 61. Representative ^{15}N-T_1 (a) and ^{15}N-T_2 (b) relaxation decays obtained in the present study. The following typical decays with errors of approximately 1% are shown: T_1^{500} (Met 28, 410.2 ± 4.1 ms, □), T_1^{600} (Glu76, 496.5 ± 5.0 ms, ×), T_2^{500} (Val65, 160.2 ± 1.6 ms, □), T_2^{600} (Ile37, 156.0 ± 1.6 ms, ×). Additionally, the worst fit for each experiments is shown: T_1^{500} (Thr4, 477.1 ± 10.8 ms, O), T_1^{600} (Asn52, 630.5 ± 15.3 ms, ◇), T_2^{500} (Gly43, 157.4 ± 4.2 ms, O), T_2^{600} (Thr4, 204.8 ± 5.0 ms, ◇).

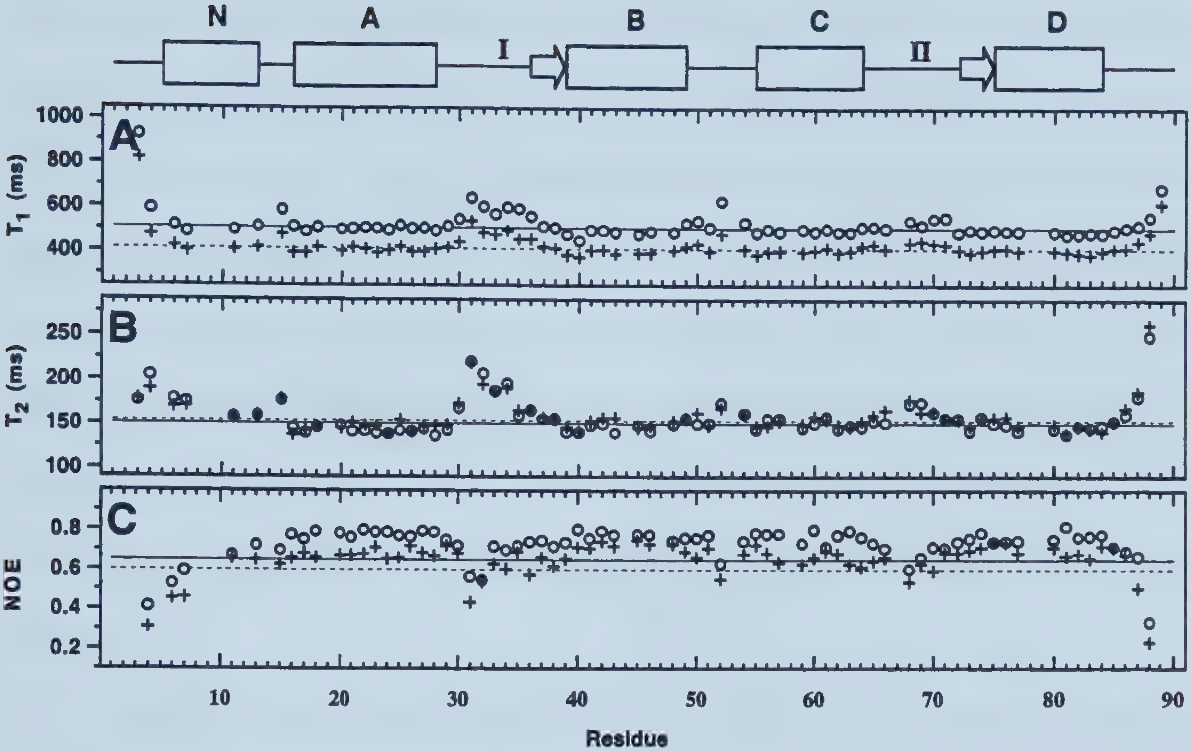

Figure 62. Sequential plots of the measured ^{15}N-T_1 (a), ^{15}N-T_2 (b), and {^{1}H}-^{15}N-NOE at 500 (+) and 600 (O) MHz. The horizontal lines in (a) and (b) indicate the average values for residues with $NOE^{500} > 0.60$ at 500 (- - - -) and 600 (——) MHz. In plot (c), the lines indicate NOE=0.60 (- - - -) and NOE=0.65 (——). The secondary structure elements of sNTnC•apo are shown above plot (a), where the helices are labeled N, A, B, C, and D, and the two calcium binding loops are labeled I and II.

The T_1^{500}, T_2^{500}, and T_2^{600} parameters were measured once, and the corresponding average error estimated from the fits were 0.8%, 0.8% and 0.9%, respectively. The T_1^{600} experiment was repeated twice using slightly different parameters, and the average is reported. The two T_1^{600} data sets indicated an average error of 0.9%, when estimated from the fit. The average difference between the two T_1^{600} data sets and their average was 0.7%. On the basis of the various errors estimated here, the minimum error on the T_1 and T_2

parameters was set to 1%. For residues where the estimated error from the fitting was larger than 1%, this larger value was used. Usually, the error associated with the NOE parameters is larger than that for the T_1 and T_2, primarily due to the lower signal-to-noise of the NOE experiment. The NOE^{500} and NOE^{600} experiments were repeated three and four times, respectively. Estimates of the error based on noise rms were 1.5% and 1.0% for NOE^{500} and NOE^{600}, respectively. Estimates of the error based on the standard deviation between the repeated experiments was 2.2% and 1.3% for the NOE^{500} and NOE^{600}, respectively. The average errors estimated from the standard deviations were used as minimum errors for the NOE data.

Typically, residues with an $NOE^{500} > 0.60$ or $NOE^{600} > 0.65$ satisfy the condition $\tau_e \ll (1/\omega_H)$ and, for an isotropically tumbling protein, very fast internal motions on a time scale te do not affect the T_1/T_2 ratio. In sNTnC-apo, 60 residues have an $NOE^{500} > 0.60$, and 63 residues have an $NOE^{600} > 0.65$. For the 60 residues with $NOE^{500} > 0.60$, the average T_1^{500}, T_1^{600}, T_2^{500}, T_2^{600}, NOE^{500} and NOE^{600} are 413 ± 22 ms, 508 ± 27 ms, 154 ± 11 ms, 151 ± 11 ms, 0.68 ± 0.04 and 0.76 ± 0.04, respectively.

As expected, T_1^{600} is larger than T_1^{500}, but the pattern of the T_1 data is similar at both fields (figure 62a). This is emphasized in the T_1^{600} / T_1^{500} ratio shown in figure 63a. With the exception of the N- and C-terminal residues, the T_1^{600} / T_1^{500} ratio is relatively constant with an average ratio of 1.23 ± 0.03 for the 60 residues having an $NOE^{500} > 0.60$. Figure 62b and 63b clearly indicate that T_2^{500} and T_2^{600} are nearly equivalent for the majority of residues.

The T_2^{600} / T_2^{500} ratio is slightly smaller than 1 with an average ratio of 0.98 ± 0.04 for residues with $NOE^{500} > 0.60$. It should be noted that the contribution from dipole-dipole relaxation to T_2 ($T_{2,DD}$) is expected to be, for all purpose, identical at both fields. On the other hand, the contribution from chemical shift anisotropy relaxation to T_2 ($T_{2,CSA}$) is proportional to $1/\omega_N^2$. Thus, the difference between the $T_{2,CSA}$ at the two fields predicts $T_2^{500} > T_2^{600}$. The T_1/T_2 ratio, which can be used to determine the overall correlation time [95], is plotted in figure 63c for both fields. The average T_1^{500} / T_2^{500} and T_1^{600} / T_2^{600} ratios are 2.69 ± 0.09 and 3.37 ± 0.17, respectively. Theory predicts that $NOE^{600} > NOE^{500}$, as is observed in the data presented here (figure 62c and 63d). The average NOE^{600}/NOE^{500} ratio is 1.11 ± 0.06 for residues with $NOE^{500} > 0.60$.

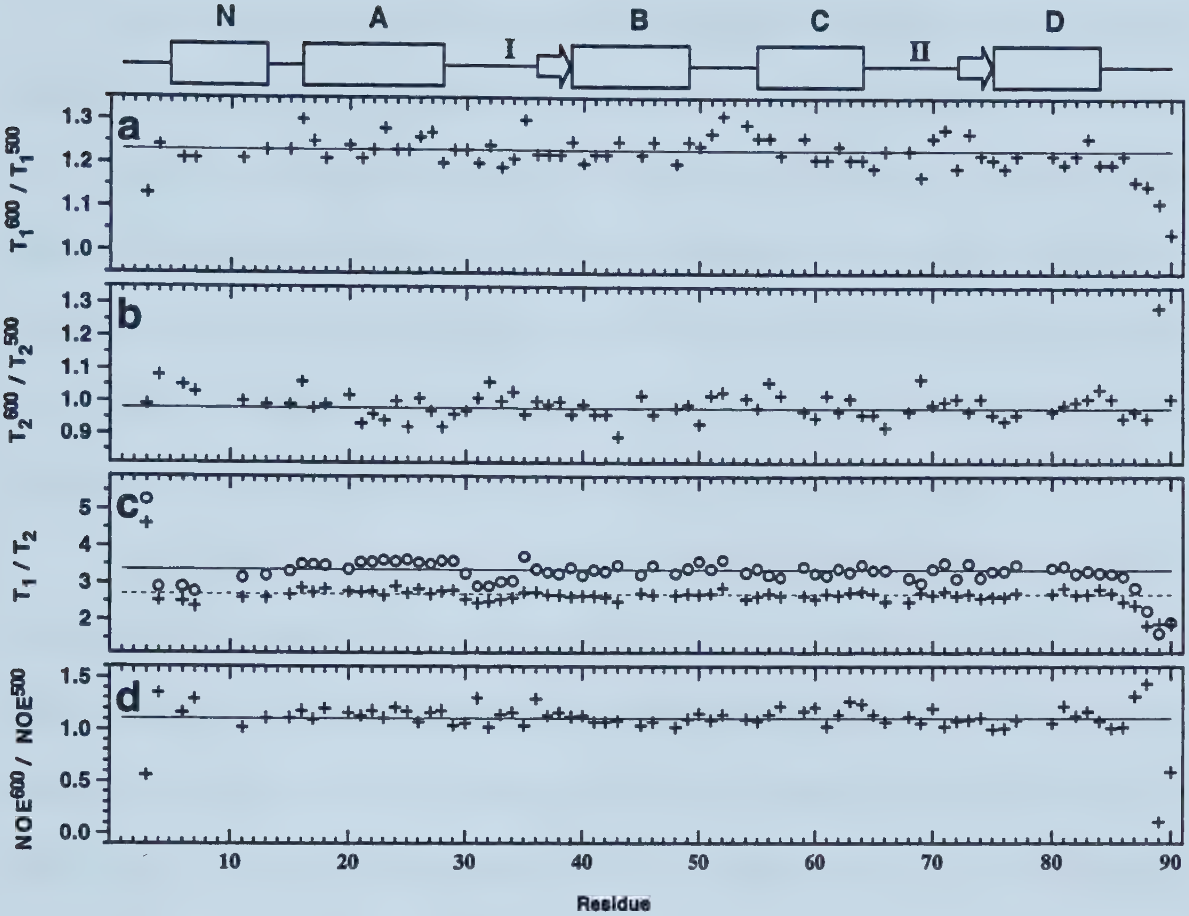

Figure 63. Sequential plots of the T_1^{600} / T_1^{500} ratio (a), T_2^{600} / T_2^{500} ratio (b), T_1/T_2 ratio (c) at 500 (+, - - - -) and 600 (○, ——) MHz, and NOE^{600}/NOE^{500} ratio (d). The horizontal lines in all plots indicate the average values for residues with $NOE^{500} > 0.60$. The secondary structure elements of sNTnC•apo are shown above plot (a) as in figure 62.

Determination of the overall correlation time (τ_m).

Although it is possible to simultaneously fit the data at both fields to characterize the molecular motion of sNTnC•apo, I chose to treat the 500 and 600 MHz data separately. The advantage of this approach is that each parameter (τ_m, S^2, τ_e, R_{ex}, ...) is independently determined twice.

The first step in the dynamics analysis is the determination of the overall correlation time (τ_m) of sNTnC•apo. We first used an approach similar to the one presented by Farrow et al. [95] which assumes that the overall tumbling motion of sNTnC•apo is isotropic. The validity of this assumption can be verified by examining the known structure of sNTnC•apo. The relative lengths of the principal axes of the inertia tensor of sNTnC•apo were determined to be 1.00:0.91:0.85, calculated using residues 2-90 of the X-ray structure of sTnC•Ca_2. The assumption of isotropic motion is therefore, to a first approximation, valid.

A grid search in which the order parameter (S^2) and the effective correlation time (τ_e) were optimized in equation 9 was used to determine a τ_m for each residue. The S^2-τ_e spectral density model (equation 6) was used for the calculated values in equation 9. Table 13 reports the average optimum τ_m and the global optimum τ_m for residues with $NOE^{500} > 0.60$ or $NOE^{600} > 0.65$. Although the estimated error from the standard deviation of the average τ_m is 0.15 (500 MHz) and 0.18 ns (600 MHz), the consistency between the 500 and 600 data could suggest that τ_m is accurate to ~0.03 ns. However, even if the experimental data used to obtain the τ_m at both fields are independent, there are several possible common sources of error, such as the choice of the spectral density model, the assumption of isotropic motion, the value of r_{NH} used (1.02Å) and the value of ($\sigma_{\parallel} - \sigma_{\perp}$) used (-160ppm). I therefore do not believe the τ_m reported here to be accurate to ~0.03 ns, although it appears I can determine it to that precision. Of course, several independent measurements would be necessary to estimate the real precision of the τ_m reported here. Despite this, the standard deviation of the averages can be used for a conservative estimate of the precision. Thus, the overall correlation time of sNTnC•apo is 4.86 ± 0.15 ns at 29.6°C.

Table 13. Summary of overall correlation time (τ_m) determination with the isotropic model

Data set	$\langle\tau_m\rangle$ [a]		Global τ_m [b]	$\langle\chi^2\rangle$ [c]
500 MHz	4.87 ± 0.15	(60)	4.88	1.66
600 MHz	4.84 ± 0.18	(63)	4.84	3.77

[a] Average τ_m obtained from individual fit for residues with $NOE^{500} > 0.60$ or $NOE^{600} > 0.65$. Number of residues used is shown in parentheses. [b] τ_m which best fit all residues. [c] Average χ^2 for the optimum τ_m. $\langle\chi^2\rangle = (1/kN)\sum_N \chi^2$, where χ^2 is as defined in equation 9, N is the number of residues and k is the number of measured variables. In the present case, k is equal to 3, and N is equal to 60 and 63 for the 500 and 600 MHz data, respectively.

Backbone analysis under the assumption of isotropic rotational diffusion.

S^2-τ_e model

Relaxation data is most commonly interpreted with the model-free formalism for internal motion [98, 99], where the spectral density is represented as a function of the overall correlation time τ_m, the order parameter S^2, and the effective correlation time for internal motions τ_e (equation 6). Isotropic motion is assumed. The results from this analysis were obtained during the evaluation of τ_m; they are plotted in figure 64a and 64b for both fields. The order parameters at 500 and 600 MHz have an rms of 0.02 over all residues except Asp89. The average S^2 for residues with $NOE^{500} > 0.60$ is 0.85 ± 0.05 and 0.84 ± 0.05 for the 500 and 600 data, respectively. Not surprisingly, the N- and C-terminal regions are flexible. Additionally, the calcium binding loops have lower order parameters, with site I being more flexible than site II. The Gly-Gly-Gly sequence which is found in site I, but not in site II, likely contributes to this greater flexibility. The B-C linker, which is exposed in the sNTnC•apo structure, also has lower order parameters. Finally, helix N also appears to

be somewhat more flexible than the other helices. Unfortunately, there are several amides from helix N which could not be characterized due to partial overlap.

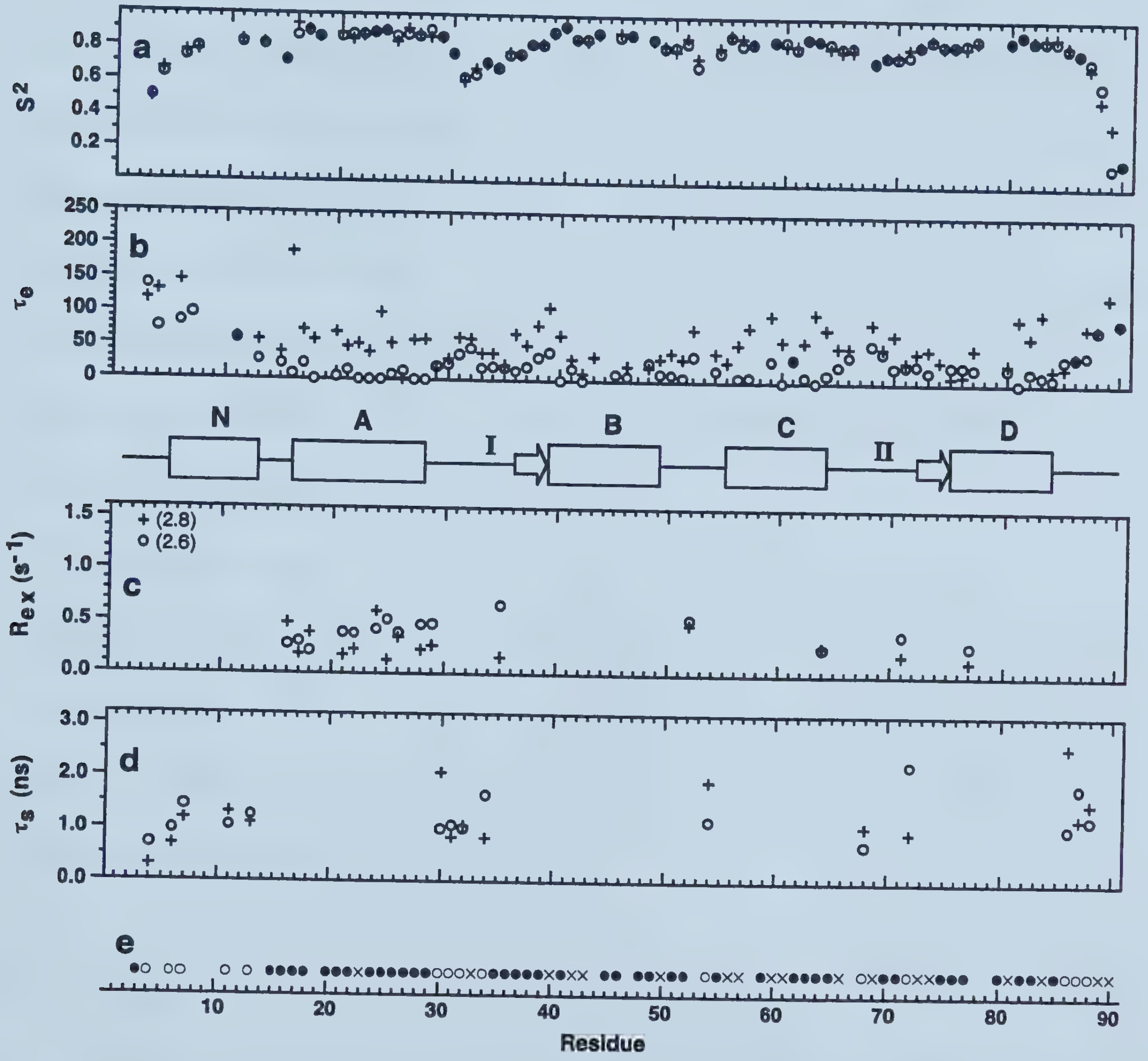

Figure 64. Sequential plots summarizing the various fits made under the assumption of isotropic tumbling. Results for all residues from the S^2-τ_e spectral density are in (a) and (b) for both 500 (+) and 600 (O) MHz data. Residues which require inclusion of an R_{ex} term in the T_2 or use the two-time-scale spectral density are shown in (c) and (d), respectively. The optimum R_{ex} value is shown in (c), and the optimum slower effective correlation time (τ_s) is shown in (d). The model which was selected for each residue is illustrated in (e), where S^2-τ_e is indicated by (●), S^2-τ_e-R_{ex} by (◉), two-time-scale by (O), not well-fit with any models by (×), and not characterized by ( ). Secondary structure elements illustrated as in figure 62.

Although the data presented is consistent between the two data sets, the τ_e^{500} and τ_e^{600} are systematically different with average values of 62 and 33 ps, respectively. While interpretation of τ_e values is often not attempted due to the large uncertainty associated with this parameter, we tried to find an explanation for this difference. The discrepancy is due to a larger than expected NOE^{600}/NOE^{500} ratio. Using the spectral density described in equation 6, and values of 4.86 ns and 0.85 for τ_m and S^2, respectively, a NOE^{600}/NOE^{500} ratio in the 1.05-1.02 range is predicted, corresponding to τ_e ranging from 0-100 ps. As noted above, the observed ratio is actually 1.11 ± 0.06. There is evidently at least one NOE data set which contains a systematic error.

For several residues, the S^2-τ_e spectral density did not provide a good fit, i.e. the relaxation parameters (T_1, T_2 and NOE) were not fit within 95% confidence limits. For those residues which did not fit well with the S^2-τ_e model, two alternative isotropic models were tested: one which include an exchange term in the T_2 equation, and another which corresponds to a two-time-scale model [100, 101].

S^2-τ_e-R_{ex} model

The relaxation parameters were therefore fitted with a S^2-τ_e-R_{ex} model (equation 6 and equation 7). As before, the 500 and 600 MHz data was treated separately. The inclusion of an R_{ex} parameter in the analysis of a residue was considered valid if it satisfied the following two conditions. First, all three relaxation parameters must be fit within 95% confidence limits. Second, the fitted R_{ex} must be significant, i.e. its value must be greater than its associated error. Further, these two conditions must also be satisfied for both the 500

and 600 MHz data; therefore the R_{ex} term is considered appropriate only if data at both fields independently validate its use. The 16 residues which fulfilled these requirements are shown with their R_{ex} values in figure 64c. With the exception of Met3, the other 15 residues were fit with an average R_{ex}^{500} and R_{ex}^{600} of 0.26 ± 0.14 s^{-1} and 0.39 ± 0.12 s^{-1}, respectively. Interestingly, 10 of the 16 residues which require a R_{ex} parameter are located in helix A. The other residues are somewhat scattered and not located within spatial proximity in the structure. As was shown in other studies [96, 105, 106], conformational exchange can sometimes be a misinterpretation of the experimental data when anisotropic rotational diffusion is present. The presence of conformational exchange needs to be validated and one can look at the $R_{ex}^{600} / R_{ex}^{500}$ ratio which should theoretically be equal to $600^2/500^2$, or 1.44. The ratio for helix A is scattered with an average of 1.84 ± 1.28. One third of helix A residues which are better fit with an R_{ex} term actually have an R_{ex}^{500} greater than R_{ex}^{600} ($R_{ex}^{600} / R_{ex}^{500}$ of 0.57 ± 0.40, 0.55 ± 0.28, 0.72 ± 0.22 for residues 16, 18, and 24, respectively). This suggests that conformational exchange is not an appropriate interpretation of the experimental data for helix A.

Two-time-scale model

The third isotropic fit we have used is the two-time-scale approach proposed by Clore et al. [100, 101] and described by equation 8. Selection of this model for a residue was as described above for the S^2-τ_e-R_{ex} model. A total of 15 residues localized in three distinct regions were best fit with the two-time-scale model, as illustrated in figure 64d. The first

two regions are the calcium binding loops (residues 30, 31, 32, 34, 68 and 72) and the C-terminal end (residues 86, 87, 88). This is not surprising, since loops and terminal ends are likely to have additional motion on the nanosecond time scale. The third region which is best fit with this model is helix N (residues 4, 6, 7, 11, and 13). It should be noted that there is a gradient in the correlation time for the slower internal motion: τ_s gradually increases from the free N-terminal end to C-terminal end of helix N. This strongly suggests that helix N is partially unstructured.

Summary of isotropic fits

Figure 64e summarizes the results from the different fits which were made under the assumption of isotropic rotational diffusion. Of the 74 residues for which relaxation data was analyzed, 25 are best fit with the S^2-τ_e model, 16 required an exchange term (R_{ex}), and 15 needed the two-time-scale model. 18 residues did not give a satisfactory fit by the criteria listed above.

Rotational diffusion anisotropy.

As pointed out by Tjandra et al. [96], the presence of rotational diffusion anisotropy could, under certain circumstances, be misidentified as conformational exchange. That a whole helix requires a R_{ex} term in order to have a good fit is actually compatible with diffusion anisotropy. Conformational exchange leads to a reduction of the T_2 and does not affect the T_1. Helix A shows the shortest average T_2, but also has a slightly longer average

T_1 value compared to the other three well structured helices (B, C, and D). In other words, the T_1/T_2 ratio of helix A is significantly larger suggesting rotational diffusion anisotropy. As noted previously, the principal components of the inertia tensor, with a relative ratio of 1.00:0.91:0.85, suggest very little anisotropy. However, a recent study of the rotational diffusion anisotropy of ubiquitin has shown that even slight anisotropic diffusion can be reflected in the relaxation data [96]. A study from Luginbühl et al. [105] also showed that in some cases the two-time-scale model can provided a misleading view of the internal motions when anisotropic global rotation is present. I therefore considered the anisotropy of sNTnC•apo in my analysis in a manner similar to Tjandra et al. [96]

Residues with $NOE^{500} > 0.60$ or $NOE^{600} > 0.65$ which did not indicate conformational exchange [96] were selected to explore the anisotropy of sNTnC•apo. The following condition was used to identify conformational exchange:

$$\frac{\langle T_2\rangle - T_{2,n}}{\langle T_2\rangle} - \frac{\langle T_1\rangle - T_{1,n}}{\langle T_1\rangle} > 1.5\sigma \qquad (17)$$

where $T_{2,n}$ is the T_2 of residue n, and $\langle T_2\rangle$ is the average T_2. σ is equal to 0.035 (500 data) and 0.054 (600 data) and is the standard deviation of $(\langle T_2\rangle - T_{2,n})/\langle T_2\rangle - (\langle T_1\rangle - T_{1,n})/\langle T_1\rangle$. Note that residues from helix A are not excluded by this condition, since these residues have opposite fractional changes in T_1 and T_2. Also, only residues which were located in helices and β-sheets were considered since loop residues are usually less well defined, and a single H–N vector orientation might not be representative. Using these conditions, 41 and 47 residues were selected from the 500 and 600 MHz data, respectively, to determine if rotational

anisotropy was present in sNTnC•apo. The data was fit to three models for the diffusion tensor [96]: isotropic, axially symmetric and fully anisotropic. The parameters which characterize the anisotropic models are as defined in Tjandra et al. [96]: the diffusion anisotropy is given by $D_{\parallel}/D_{\perp}$ which is equivalent to $2D_z/(D_x+D_y)$, the orientation of D_z is a function of θ and φ (spherical polar coordinates), and the orientations of D_x and D_y are defined by a third angle, ψ. D_x, D_y and D_z represent the magnitudes of the principal components of the diffusion tensor. The correlation time $\tau_{m,eff}$ is calculated from $(6D)^{-1}$ where $D = (D_x + D_y + D_z)/3$. Coordinates from the crystal structure of sNTnC•apo were used for the analysis (PDB accession code 5TNC).

I have characterized the diffusion anisotropy of sNTnC•apo and the results are shown in table 14. As evident by the decrease in the error function, the fit is better with an axially symmetric diffusion tensor than with an isotropic diffusion tensor. As presented in Theory, the significance of the decrease in the error function was evaluated using the statistical F-test [102]. The probability that the improvement observed with the inclusion of additional parameters occurred by chance is obtained from $P(F_x; x; N\text{-}m\text{-}x)$ (see Theory). For the axially symmetric model, these probabilities are 8×10^{-3} and 8×10^{-6} for the 500 and 600 MHz data, respectively, therefore justifying the inclusion of the additional terms in the fit, relative to the isotropic model. The fully asymmetric model provides a more modest improvement, relative to the axially symmetric model, as shown by the smaller average Fx. The corresponding $P(F_x; x; N\text{-}m\text{-}x)$ are 0.19 and 0.17 for the 500 and 600 MHz data, respectively. The D_x/D_y ratio and ψ obtained for the fully asymmetric model are therefore not considered statistically significant, and the axially symmetric diffusion tensor model is

chosen to best represent the motion of sNTnC•apo. Note that for the axially symmetric model I have considered both the oblate ($D_{\parallel} < D_{\perp}$) and the prolate model ($D_{\parallel} > D_{\perp}$), and figure 65 shows that sNTnC•apo is best represented by a prolate model.

Table 14. Experimental diffusion parameters for sNTnC•apo

Model		$\tau_{m,eff}$ [a] (ns)	$D_{\parallel}/D_{\perp}$ [b]	D_x/D_y	θ [c] (°)	φ [c] (°)	ψ [c] (°)	E [d]	E_v [e]	F_x [f]
Isotropic	500	4.82	1	1				102	2.5	
	600	4.83	1	1				379	8.2	
	Avg.	4.82	1	1				241	5.4	
Ax. Symm.	500	4.82	1.07	1	5	-171		74	2.0	4.6
	600	4.81	1.13	1	12	-66		205	4.8	12.2
	Avg.	4.82	1.10	1	8	-118		140	3.4	8.4
Asymm.	500	4.80	1.10	1.07	8	-152	73	68	1.9	1.7
	600	4.83	1.13	1.07	13	-13	65	188	4.6	1.9
	Avg.	4.81	1.11	1.07	11	-83	69	128	3.3	1.8

[a] Effective correlation time, defined as $(6D)^{-1}$. [b] Defined as $2D_z/(D_x+D_y)$. [c] Euler angles describing the orientation of the diffusion tensor in the PDB coordinate frame (accession code 5TNC). [d] Error function (equation 12). [e] Reduced error function (equation 13). [f] A test for the validity of adding x variables to the fitting procedure (equation 14).

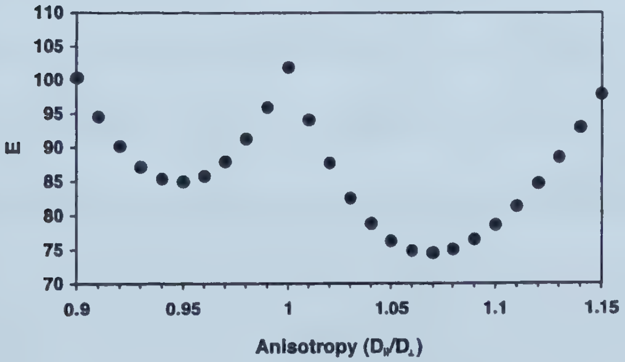

Figure 65. Comparison between oblate ($D_{\parallel} < D_{\perp}$) and prolate ($D_{\parallel} > D_{\perp}$) for the axially symmetric anisotropic fitting of the 500 MHz data. For each point, the anisotropy and the correlation time (4.82 ns) were kept constant, while the orientation of $D_{\parallel}$ was optimized.

The $\tau_{m,eff}$, $D_{\parallel}/D_{\perp}$ and θ obtained from the axially symmetric model are consistent for the 500 and 600 MHz data, whereas the φ angle is less well determined. Note that it is not surprising that the φ angle is poorly defined, given that φ is near $0°$. The $\tau_{m,eff}$ obtained here is, for all purpose, identical to the one obtained above using the isotropic diffusion model. The small difference in the isotropic τ_m in tables 13 and 14 is due to the different approach and residues used in the evaluations. The average $D_{\parallel}/D_{\perp}$ ratio of 1.10 is small, as expected from the near symmetric inertia tensor of sNTnC•apo. In fact, it is smaller than the $D_{\parallel}/D_{\perp}$ ratio of 1.17 obtained for ubiquitin [96].

Using the θ and φ angles determined above, I calculated the orientation of the various helices with respect to the unique axis of the diffusion tensor. Table 15 summarizes the relaxation parameters and orientations of the helices of sNTnC•apo. As expected from the consistency of the experimental data, both the 500 and 600 data indicate a similar orientation for the helices. Based on helix orientation, and the average backbone amide H–N vector orientation, helices N, B, C and D are nearly perpendicular to the $D_{\parallel}$ axis of the diffusion tensor. Helix A, on the other hand, is nearly parallel to $D_{\parallel}$. This is represented graphically in figure 66. The peculiar orientation of helix A relative to the diffusion tensor can therefore explain the larger T_1/T_2 ratio observed for this helix. The anisotropy of the molecular tumbling, although small, provides an explanation for the relaxation parameters of helix A.

Table 15. T_1/T_2 ratio of the five helices of sNTnC•apo and orientation of N–H vectors relative to the axially symmetric diffusion tensor

Parameter	Helix [a] N	 A	 B	 C	 D
T_1^{500}/T_2^{500}	2.51 ± 0.11	2.78 ± 0.07	2.64 ± 0.09	2.67 ± 0.07	2.72 ± 0.09
T_1^{600}/T_2^{600}	3.00 ± 0.21	3.54 ± 0.07	3.36 ± 0.10	3.32 ± 0.12	3.36 ± 0.08
Angle (°) [b]	75 ± 14	19 ± 9	63 ± 11	79 ± 8	67 ± 11

[a] Helices defined using the following residue ranges: N (5 to 13), A (16 to 28), B (39 to 48), C (55 to 64), and D (75 to 85). [b] Average angle between the N–H vectors of the helix and the principal axis of the diffusion tensor ($D_{\parallel}$).

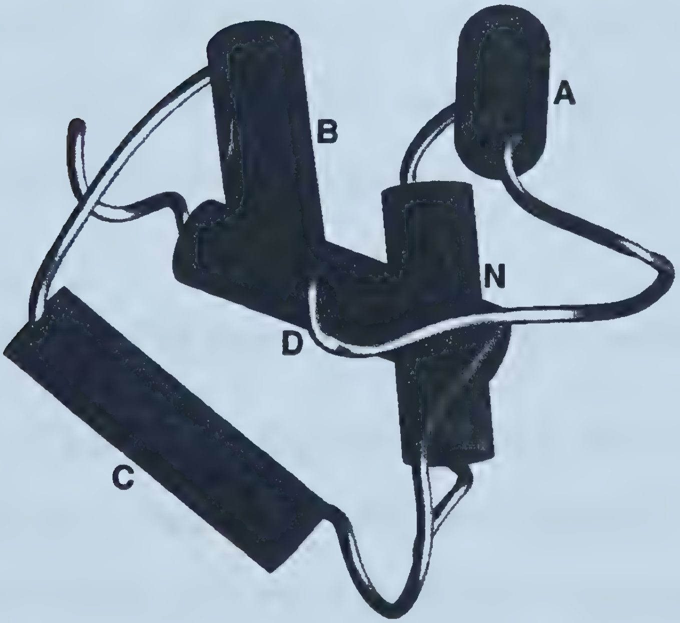

Figure 66. Representation of the structure of sNTnC•apo relative to the axially symmetric diffusion tensor. Helices are shown as cylinders. In this orientation $D_{\parallel}$ is perpendicular to the page, clearly showing that it is nearly parallel to helix A and more perpendicular to the other four helices.

The order parameters were evaluated by taking into account the rotational anisotropic diffusion of sNTnC•apo. Using a spectral density function which takes into account rotational anisotropic diffusion (equation 10), we evaluated S^2 and τ_e in the same manner as for the isotropic S^2-τ_e model. The average anisotropic tumbling parameters obtained for the

axially symmetric model were used for the fit (table 14). Comparison of the results from the S^2-τ_e isotropic and anisotropic analysis does not show any significant differences. The rms difference between isotropic and anisotropic fits is 0.003 for S^2, and 5 ps for τ_e. These differences are well within experimental error and indicate that inclusion of anisotropy is not necessary into the evaluation of the backbone order parameters for sNTnC•apo, a result which is consistent with other studies [96]. The inclusion of anisotropy is however necessary for the selection of the appropriate model. Of the 10 residues from helix A which required the inclusion of an exchange term under assumption of isotropic tumbling, 8 are well fit using the S^2-τ_e model when anisotropic tumbling is taken into account. For those 8 residues, the average χ^2 for the S^2-τ_e model is reduced from 9.4 ± 3.9 to 3.3 ± 2.6 upon inclusion of anisotropic tumbling in the analysis.

Summary of the ^{15}N relaxation results

The quality of the relaxation data presented in this paper is high, as highlighted by the consistency between the 500 and 600 MHz data sets. The analysis was first carried out with the assumption of isotropic tumbling, but the presence of slight anisotropy leads to misinterpretation of the experimental data. Anisotropic tumbling was therefore included in the analysis.

Consistency between the 500 and 600 MHz data

I chose to analyze the 500 and 600 MHz data separately, in order to obtain two independent characterizations of the dynamic properties of sNTnC•apo. First, the experimental relaxation is consistent between the two data sets. Using $\tau_m = 4.86$ ns, $S^2 = 0.85$ and $\tau_e = 0$ in equation 6, one predicts a T_1^{600} / T_1^{500} ratio of 1.22 and a T_2^{600} / T_2^{500} ratio of 0.97. The observed 600/500 ratios agree well with the theoretical ones, with average values of 1.23 ± 0.03 and 0.98 ± 0.04 for T_1^{600} / T_1^{500} and T_2^{600} / T_2^{500}, respectively. The T_1^{600} / T_1^{500} ratio should agree well with the theory, except in special cases such as apo-calmodulin where large amplitude motions on a nanosecond time scale significantly shorten the observed T_1s. The agreement between the measured and theoretical T_1^{600} / T_1^{500} ratio is an indication of the absence of such motions in sNTnC•apo.

As previously noted, the NOE^{600}/NOE^{500} ratio is larger than expected with an average of 1.11 ± 0.06, and a theoretical ratio of 1.05-1.02 for τ_e in the 0 to 100 ps range. This larger than expected ratio is most likely due to experimental error. Closer inspection of the data indicates that the NOE^{600} is larger than expected. Using $\tau_m = 4.86$ ns and $\tau_e = 0$ ps, one predicts the maximum NOE^{500} and NOE^{600} to be 0.751 and 0.788, respectively. The 500 MHz data does not contain any NOE larger than the maximum value; Val45 has the largest NOE at 0.748 ± 0.030. The 600 MHz data contains nine residues with $NOE^{600} > NOE_{max}$, ranging from 0.790 ± 0.010 to 0.818 ± 0.011. Of these nine residues, three have NOE larger than the maximum value within experimental error, i.e. $(NOE^{600} - \sigma_{NOE}) > NOE_{max}$. The error present in the 600 MHz data will be corrected in future studies but was not in the data

presented here. We believe the discrepancy is most likely due to water saturation. The systematic error present in the NOE data has been used herein to determine its effect on the analysis of the dynamics.

The overall correlation time, order parameters, and the anisotropic analysis are all consistent between the two fields. This not only supports a high level of confidence in the determined values, but also clearly indicates which relaxation parameters are critical to the analysis. Despite the error present in one of the NOE data sets, both analysis gave the same results, with the exception of the τ_e values. This observation is reassuring, since NOE values are usually the most imprecise relaxation measurements and, at least in the present study, the most inaccurate ones. I conclude that, unless one wishes to obtain accurate τ_e values, the precision and accuracy of the experimental NOE data are not critical to the analysis. In the present study, where we do not interpret the τ_e data, the only role of the NOE data was to select residues where very fast internal motions on a time scale τ_e do not affect the T_1/T_2 ratio, expressed as residues with $NOE^{500} > 0.60$ or $NOE^{600} > 0.65$.

Although both data could have been fit together, and the goodness of the fit used to evaluate the confidence level on the determined parameters, treating the data separately has several advantages. First, consistency between two data sets is more easily appreciated than, for example, a low χ^2. Second, fitting of the data on some computers is significantly faster since doubling the number of parameters in a fitting procedure more than doubles the necessary computing time, whether a minimization or a grid search is performed. I believe that obtaining relaxation parameters at two or more different field strengths and treating them

independently is an excellent approach to validate the results obtained from the analysis. Other studies published recently have also used a similar approach [107, 108].

Rotational correlation time and rotational diffusion anisotropy.

I have determined the overall correlation time (τ_m) of sNTnC•apo to be 4.86 ± 0.15 ns at 29.6 °C, under sample conditions listed in the Methods. This value was obtained using the model-free analysis with the spectral density defined as a function of τ_m, S^2 and τ_e (equation 6), and the assumption that the rotational motion is isotropic. With the assumption of isotropic motion, 16 residues required the inclusion of a conformational exchange term (R_{ex}) in the T_2 expression. In particular, the entire helix A required R_{ex} terms in order to obtain a good fit. Although it is possible for an entire helix to undergo conformational exchange, it is not likely in the present case. If conformational exchange did occur in helix A, one would expect to observe conformational exchange for residues in helix B and helix D which are packed on helix A, especially since three Phe residues are located in helix A. This was not observed.

Analysis of the relaxation parameters while considering rotational anisotropy indicated a significantly better fit for an axially symmetric diffusion tensor with $\tau_{m,eff}$, $D_{\parallel}/D_{\perp}$, θ and ψ equal to 4.82, 1.10, 8° and -118°, respectively. Anisotropic motion is a more plausible explanation for the relaxation parameters observed in helix A than conformational exchange. The $\tau_{m,eff}$ determined while accounting for motional anisotropy is identical to the τ_m determined with the assumption of isotropic motion. This therefore justifies the assumption of isotropic motion for determination of the overall correlation time. The

anisotropic diffusion of sNTnC•apo is very small with $D_{\parallel}/D_{\perp} = 1.10$ and is consistent with the inertia tensor (1.00:0.91:0.85) calculated from the structure coordinates. Tjandra et al. [96] showed that slight anisotropy ($D_{\parallel}/D_{\perp} = 1.17$) could be reflected in the observed relaxation parameters of ubiquitin. The present study shows that even smaller anisotropy can affect relaxation parameters.

Motional anisotropy should be considered, especially if incorporation and interpretation of conformational exchange is attempted in the analysis. Although the molecule studied here is nearly spherical, slight motional anisotropy affects the observed relaxation parameters and anisotropy has to be considered. As suggested by recent studies [96,105,107,108], motional anisotropy should always be carefully considered in the analysis of ^{15}N relaxation data.

Materials and Methods

Sample preparation.

Cloning, expression, and labeling of chicken [U-^{15}N]-sNTnC is as previously described [47]. [U-^{13}C; U-^{15}N; U-40% ^{2}H]-sNTnC was obtain in a similar manner, except that expression was performed in a 50% D_2O aqueous media. The level of deuteration was determined from mass spectrometry, assuming a minimum level of 95% for ^{15}N and ^{13}C. To obtain metal-free sNTnC, 14mg of protein was dissolved in 0.5ml of 100mM EDTA, applied to a 1.5 cm × 90 cm G-25 gel filtration column equilibrated and eluted with 25mM

NH_4HCO_3, and monitored at λ=254 nm. The pooled fractions were lyophilized, twice redissolved in water, and lyophilized again to ensure removal of NH_4HCO_3. Milli-Q deionized water was used in all steps. The NMR sample was prepared by dissolving 10mg of metal-free sNTnC in 0.5 ml of 100 mM KCl in 90% H_2O/10% D_2O. To the sample was added 5 mL of 100 mM DSS and 5 mL of 1.3% NaN_3. EDTA was also added to a concentration of 10 mM to ensure that the sample was completely in the apo form. The pH was adjusted to 6.7 with HCl and/or NaOH prior to transfer to the NMR tube.

Data acquisition: ^{15}N relaxation experiments.

^{15}N relaxation experiments were performed at a temperature of 29.6°C on Varian UNITY Inova 500 and Varian UNITY 600 spectrometers both equipped with z-axis pulsed field gradient, triple resonance probes. The ^{15}N-T_1, ^{15}N-T_2 and ^{15}N-{^{1}H}-NOE experiments were performed using the pulse sequences from Farrow et al. [95]

The T_1^{500}, T_2^{500} and T_2^{600} were acquired once, using ^{15}N relaxation delays of [11, 33, 100, 178, 255, 355, 477, 633, 833, and 1143 ms], [17, 33, 50, 66, 83, 99, 116, 132, 149, 165, and 182 ms], and [16, 33, 49, 65, 81, 98, 114, 130, 146, 163, and 179 ms], respectively. The T_1^{600} was acquired twice, using ^{15}N relaxation delays of [33, 100, 178, 255, 355, 477, 633, 833, and 1143 ms] and [11, 33, 100, 178, 255, 355, 477, 633, 833, and 1143]. Field strengths of 6.5, 3.8, 5.3 and 4.3 kHz were used for the ^{15}N hard pulses in the T_1^{500}, T_2^{500}, T_1^{600}, and T_2^{600} experiments, respectively. WALTZ-16 decoupling [109] of ^{15}N during acquisition was performed using field strengths of 1.2 and 0.8 kHz for the 500 and 600 MHz data,

respectively. The relaxation delay between transients was 3 s for the T_2^{500} and T_2^{600} experiments, and 1 s for the T_1^{500} experiment. The two T_1^{600} data sets were acquired using different relaxation delays of 1 and 1.5 s. The number of transients per complex t1 point was 8 or 16.

^{15}N-{^{1}H} steady-state NOEs were obtained by acquiring spectra with and without ^{1}H saturation applied before the start of the experiment. ^{1}H saturation was achieved with the use of 120° ^{1}H pulses applied every 5 ms [110]. A saturation time of 3 s was used in all NOE experiments. The NOE^{500} experiment was repeated three times, with slightly different parameters. The first NOE^{500} data set used a field of 6.5 kHz for ^{15}N hard pulses, 1.1 kHz for WALTZ-16 decoupling, and 10.6 kHz for ^{1}H saturation. The other two data sets used a field of 5.1 kHz for hard pulses, 1.0 kHz for WALTZ-16 decoupling, and 10.7 kHz for ^{1}H saturation. The first and third data sets were obtained with 64 transients per complex t1 point, and relaxation delays of 1 and 4 s for the spectra with and without saturation. The second data set used 48 transients per complex t1 point and relaxation delays of 2 and 5 s for the spectra with and without saturation. The NOE^{600} experiment was repeated four times. All four data sets were obtained with a field of 5.3 kHz for ^{15}N hard pulses and 0.8 kHz for WALTZ-16 decoupling, and with 64 transients per complex t1 point. The first NOE^{600} data set used relaxation delays of 1 and 4 s for the experiment with and without saturation, respectively, whereas the other three data sets used 2 and 5 s for the same corresponding delays. ^{1}H saturation was accomplished with a field of 10.4 kHz for the first NOE^{600} data set, and a field of 10.7 kHz for the other three data sets.

The spectral widths used for all 500 MHz experiments were 7000 and 1300 Hz for ^{1}H and ^{15}N, respectively. The corresponding spectral widths for the 600 MHz experiments were 8000 and 1560 Hz. The acquisition times in t1 (^{15}N) and t2 (^{1}H) were 74 and 73 ms, respectively, for all experiments. Other various delays and gradient strengths were as described in Farrow et al. [95]

Data processing

All spectra were processed using the *NMRPipe* software [73]. The *ranceY.M* macro from the *NMRPipe* package was used to generate pure absorptive 2D line shapes from the sensitivity-enhanced data (^{15}N experiments only). Although not mandatory, removal of the residual water signal was performed through the use of time domain polynomial subtraction (*NMRPipe* function *POLY -time*). ^{1}H-^{15}N spectra were processed using a 90° shifted sine apodization function in F2 (^{1}H) and a 90° shifted sine-squared function in F1 (^{15}N). The time-domain data in t1 was extended through complex linear prediction by 32 and 45 complex points for the 500 and 600 ^{1}H-^{15}N spectra, respectively. Both dimensions were baseline corrected using the *POLY -auto* function in *NMRPipe*.

The first 2D spectra of the ^{15}N- T_1^{500} experiment was manually peak-picked using *PIPP* [74], and all other ^{1}H-^{15}N 2D's were automatically peak-picked using the *STAPP* program [74]. Peak intensities were used in all cases. T_1, and T_2 decay curves were fitted to a two-parameters function of the form

$$I(t)=I_0 \exp\left(\frac{-t}{T_1}\right) \text{ and } I(t)=I_0 \exp\left(\frac{-t}{T_2}\right) \tag{18}$$

where I(t) is the intensity after a delay time t and I_0 is the intensity at time t = 0. Fitting was accomplished with the *xcrvfit* program (R. Boyko, executable available at the following address: http://www.pence.ualberta.ca). The uncertainty in the T_1 and T_2 values were approximated from the nonlinear least-squares fit. Uncertainties obtained using this approach were found to be slightly larger than those obtained from a Monte Carlo simulation. Steady-state NOE values were obtained from the ratio of the intensities of experiments recorded with and without proton saturation. The uncertainty in the NOE value was approximated from the baseline noise levels as described previously [95].

11. ANALYSIS OF METHYL GROUP DYNAMICS FOR sNTnC•apo

This chapter reports the analysis of the side-chain dynamics of sNTnC in the apo form. Side-chain methyl group dynamics were obtained from ^{2}H relaxation measurements of CH_2D groups in a partially deuterated sample. The dynamic properties of the methyl groups provide information on hydrophobic residues which contribute to the energetics of calcium binding and induced structural change.

Theory

The method used here makes use of a uniformly ^{13}C-labeled and partially ^{2}H-labeled sample. The pulse sequence selects specifically for $^{13}CH_2D$ methyl groups [111]. The relaxation of pure deuterium magnetization is derived using the following relations [111]:

$$\frac{1}{T_1^D} = \frac{1}{T_1^{I_zC_zD_z}} - \frac{1}{T_1^{I_zC_z}} \qquad (19)$$

$$\frac{1}{T_{1\rho}^D} = \frac{1}{T_1^{I_zC_zD_y}} - \frac{1}{T_1^{I_zC_z}} \qquad (20)$$

where T_1^D and $T_{1\rho}^D$ denote pure deuterium relaxation. $T_1^{I_zC_zD_z}$, $T_1^{I_zC_zD_y}$ and $T_1^{I_zD_z}$ are the relaxation parameters which are measured, where I_z, C_z, and D_z denote the z magnetization components of the methyl proton, carbon, and deuteron spins respectively, and D_y is the y

component of deuterium magnetization. It has been established that, under the conditions used here, $1/T_{1\rho}^{D} = 1/T_{2}^{D}$ [111]. The spectral density function used in the T_{1}^{D} and $T_{1\rho}^{D}$ equations is the same as that for the ^{15}N analysis (equation 6). However, S^2 represents the order parameter for a methyl group, and describes the spatial motion of the ^{13}C-^{2}H vector on the ns-ps time scale, and is given by $S^2 = S_{axis}^{2}\left[\left(3\cos^2\theta - 1\right)/2\right]^2$. The factor $\left(3\cos^2\theta - 1\right)/2$ relates to the rapid rotation of the ^{13}C-^{2}H vector about the averaging axis. Assuming tetrahedral geometry ($\theta = 109.5°$), $S^2 = 0.111 S_{axis}^{2}$. S_{axis}^{2} therefore corresponds to the order parameter describing the motion of the averaging axis. Motional parameters were obtained by minimizing the function

$$\chi^2 = \frac{\left(T_{1,c} - T_{1,e}\right)^2}{\sigma_{T_1}^{2}} + \frac{\left(T_{1\rho,c} - T_{1\rho,e}\right)^2}{\sigma_{T_{1\rho}}^{2}} \tag{21}$$

where the parameters are as described for equation 9.

Results

I have studied the side-chain dynamics of sNTnC•apo using the approach of Muhandiram et al. [111] where the T_{1}^{D} and $T_{1\rho}^{D}$ relaxation times are measured in uniformly ^{13}C-labeled and fractionally ^{2}H-labeled samples. The quality of the data can be appreciated

from the correlation spectra and decay curves which are shown in figure 67 and 68. Relaxation data were obtained for 44 methyl groups of sNTnC•apo. The T_1^D and $T_{1\rho}^D$ data are represented graphically in figure 69a and 69b, and the derived S^2_{axis} are shown in figure 69c. The data are presented on the basis of methyl group type in order to compare the motion of a particular methyl with methyl groups of the same nature.

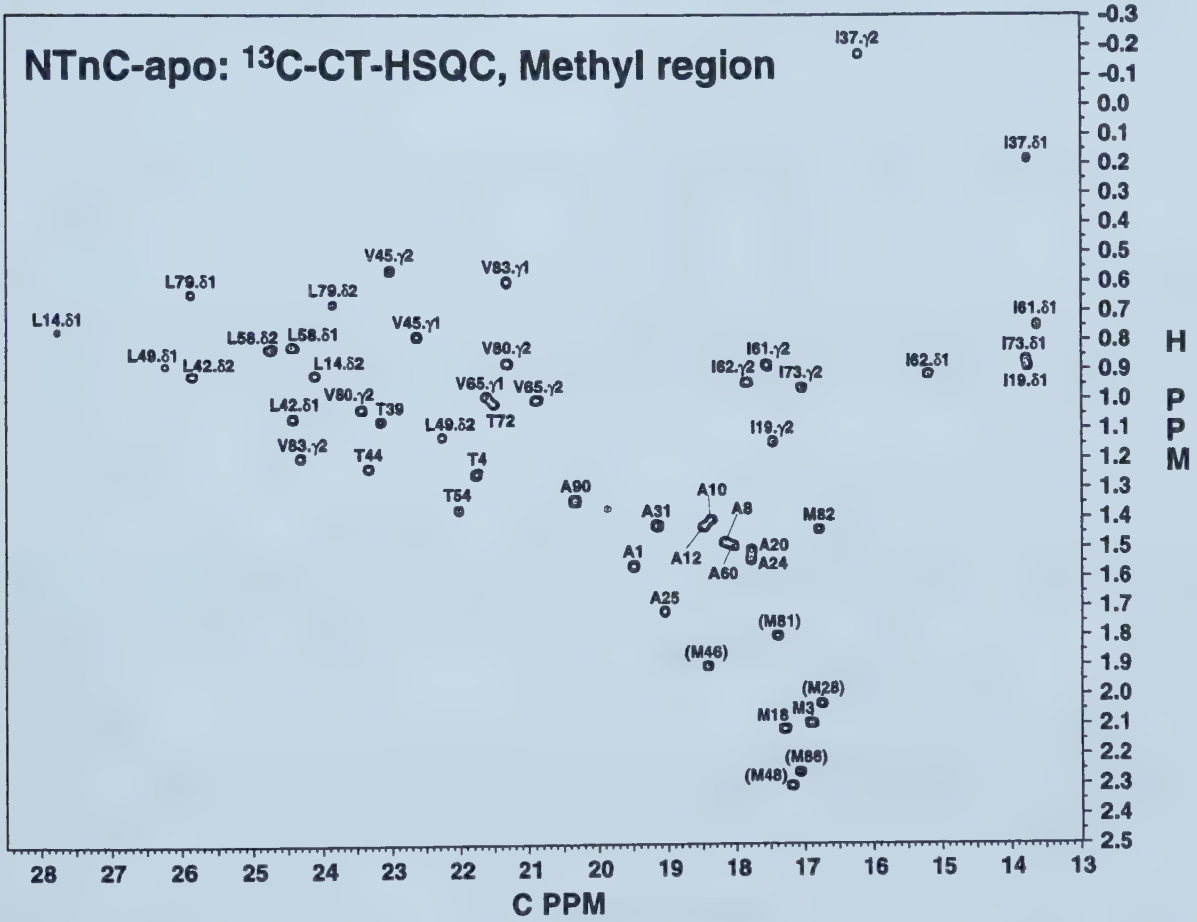

Figure 67. ^1H-^{13}C constant-time HSQC spectra of sNTnC-apo. The good dispersion allows for a characterization of most methyl groups. The assignments in parenthesis indicate negative peaks in the spectra.

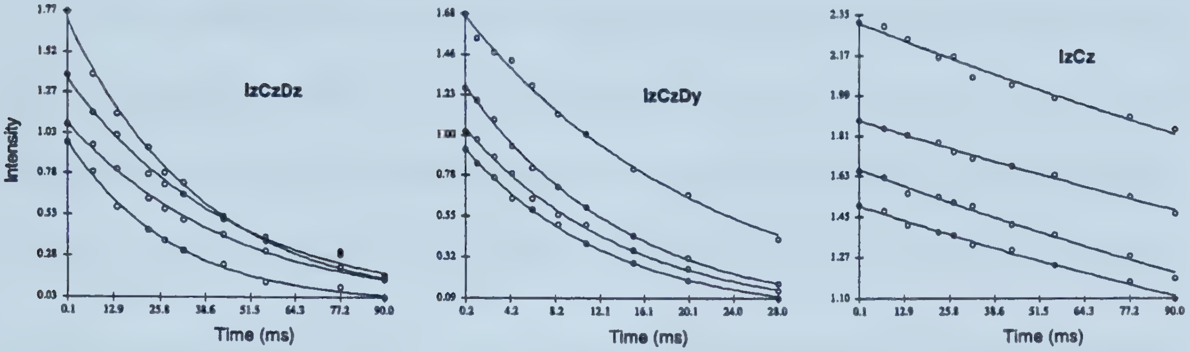

Figure 68. $I_zC_zD_z$, $I_zC_zD_y$, and I_zC_z decay curves for methyl groups of residues Thr4, Thr39, Thr44, and Thr54

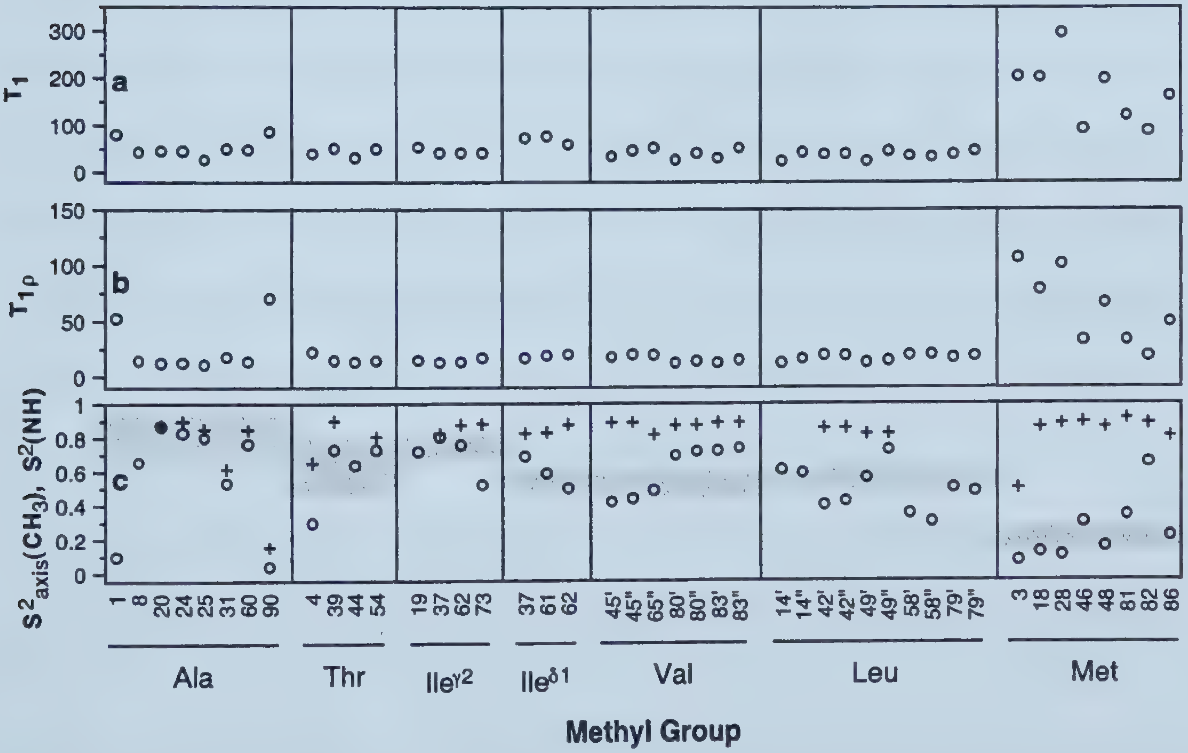

Figure 69. Plots of the measured methyl CH_2D ^2H-T_1 (a) and ^2H-$T_{1\rho}$ (b) at 600 MHz on a per-residue type basis. The derived order parameter of the averaging axis of the methyl groups (O) are shown in (c) along with the corresponding backbone ^{15}N order parameter (+). The shaded areas in (c) represent the average (± 1σ) for each residue type. The average was obtained from this work and other published data.

The backbone order parameters are also shown in figure 69c to indicate the motion of a methyl group relative to its backbone motion. For alanine residues, the methyl order parameters are similar to those of the backbone since the C^{α}-C^{β} bond is part of the backbone structure. For all other residue types, the S^2_{axis} of methyl groups is significantly smaller than the S^2 of the H–N vector because of additional degrees of freedom. The difference between the S^2 of the backbone amide and the S^2_{axis} of the methyl group is primarily function, though not exclusively, of flexibility of the dihedral angles between the methyl group and the backbone. For example, the large difference for Thr4 indicates a poorly defined χ_1 dihedral angle, whereas Thr54 appears to have a well-defined χ_1. Using this relation, the isoleucine$^{\gamma 2}$ and valine data indicate that Ile37, Ile62, Val80 and Val83 have relatively well-defined χ_1 angles compared to Ile73, Val45 and Val65. The larger difference observed for Ile62$^{\delta 1}$ compared to Ile62$^{\gamma 2}$ indicates that although the χ_1 of this residue shows little variability, the χ_2 angle is less restricted. All but one of the methionine residues have a very disordered methyl group. Met82 is the only restricted methionine methyl group.

Figure 69c also shows the 'normal' distribution of S^2_{axis} for each methyl type. The distribution was calculated from all S^2_{axis} obtained using the ^{2}H relaxation approach and published to date. As expected, the distribution of S^2_{axis} for alanine residues is similar to the S^2 of H–N vectors, with an average of 0.83 ± 0.11. The relative position of the average of the other methyl types is in agreement with the nature of the particular side-chain. With the exception of terminal residues Ala1, Met3, Thr4 and Ala90, the other methyl groups which

significantly fall outside of the expected distribution are of interest. Therefore Ala8, Ala31, Ile73$^{\gamma2}$ and Leu58 can be looked as having larger motion than usually observed. Using the same analogy, the S^2_{axis} of Ile37$^{\delta1}$, Val80, Val83, and Met82 indicate that those residues have reduced motion, most likely due to tight packing of the methyl group on other hydrophobic residues.

When comparing S^2_{axis} to the solvent ASA of the side-chains, one finds that there is not always a direct correlation between these two parameters, as pointed out previously [112], although generally more exposed residues will have lower order parameters. Of the six non-terminal methionines in sNTnC•apo, three are exposed and three are buried. Met18, Met28, and Met48 are exposed in the NMR structure [63] with side-chain solvent ASA of 94 ± 11 Å^2, 129 ± 16 Å^2, and 124 ± 17 Å^2, respectively (the corresponding values in the crystal structure [12] are 70 Å^2, 137 Å^2, and 85 Å^2). Met46, Met81, and Met82 are more buried in the NMR structure with solvent ASA of 11 ± 9 Å^2, 20 ± 9 Å^2, and 27 ± 11 Å^2, respectively (the corresponding values in the crystal structure are 0 Å^2, 4 Å^2, and 0 Å^2). Although the three exposed methionines have lower order parameters than the three buried ones (figure 69c), one cannot quantitatively relate solvent ASA to order parameters when comparing the three buried methionines. For example, Met46, Met81, and Met82 have similar solvent ASA, but the order parameter of Met82 is significantly larger than the other two (figure 69c). Therefore one should be cautious when attempting to correlate solvent ASA and flexibility.

Materials and Methods

Sample preparation.

Cloning, expression, and labeling of chicken [U-^{13}C; U-^{15}N; U-40% ^{2}H]-sNTnC was obtain in a similar manner as for the [U-^{15}N]-sNTnC sample, except that expression was performed in a 50% D_2O aqueous media. The level of deuteration was determined from mass spectrometry, assuming a minimum level of 95% for ^{15}N and ^{13}C. The NMR sample was prepared by dissolving 10mg of metal-free sNTnC in 0.5 ml of 100 mM KCl in 90% H_2O/10% D_2O. To the sample was added 5 mL of 100 mM DSS and 5 mL of 1.3% NaN_3. EDTA was also added to a concentration of 10 mM to ensure that the sample was completely in the apo form. The pH was adjusted to 6.7 with HCl and/or NaOH prior to transfer to the NMR tube.

Data acquisition: ^{2}H relaxation experiments.

The ^{2}H relaxation experiments were performed at 30.9°C on a Varian UNITY+ 600 spectrometer equipped with z-axis pulsed field gradient and triple resonance probe. The ^{2}H-T_1 and ^{2}H-$T_{1\rho}$ were obtained using the approach described by Muhandiram et al. [111] with a [U-^{13}C; U-^{15}N; U-40% ^{2}H]-sNTnC sample.

Measurement of $T_1^{I_zC_zD_z}$, $T_1^{I_zC_zD_y}$ and $T_1^{I_zC_z}$ were made once with relaxation delays of [0.05, 7, 14, 23, 27, 32, 44, 56, 77, and 90 ms], [0.25, 1.3, 2.8, 4.4, 6.2, 8.4, 10.9, 15.1, 20, and 28 ms], and [0.05, 7, 14, 23, 27, 32, 44, 56, 71, and 90 ms], respectively. The spectral widths were 9000.9 and 5494.5 Hz for ^{1}H and ^{13}C, respectively. All data sets were recorded

as 152 × 576 complex matrices, with 32 transients per t1 increment for the $T_1^{I_zC_zD_z}$ and $T_1^{I_zC_zD_y}$ experiments, and 16 transients per t1 increment for the $T_1^{I_zC_z}$ experiment. The relaxation delay between transients was 1.7 s for all experiments. Field strengths, gradients and delays were as described elsewhere [111].

Data processing

All spectra were processed using the *NMRPipe* software [73]. Although not mandatory, removal of the residual water signal was performed through the use of time domain polynomial subtraction (*NMRPipe* function *POLY -time*). ^{1}H-^{13}C spectra were processed using a 60° shifted sine-squared apodization function in both dimensions. The time-domain data in t1 was extended through complex linear prediction by 104 points for the ^{1}H-^{13}C spectra. Both dimensions were baseline corrected using the *POLY -auto* function in *NMRPipe*.

Peak-picking of the ^{1}H-^{13}C 2D's was also automated in a similar way as for the ^{15}N relaxation data (chapter 10). Peak intensities were used in all cases. Decay curves were fitted to a two-parameters function of the form

$$I(t) = I_0 \exp\left(\frac{-t}{T_1}\right) \tag{22}$$

where I(t) is the intensity after a delay time t and I_0 is the intensity at time t = 0. Fitting was accomplished with the *xcrvfit* program (R. Boyko, executable available at the following

address: http://www.pence.ualberta.ca). The uncertainty in the relaxation parameters were approximated from the nonlinear least-squares fit.

12. CONTRIBUTION OF DYNAMICS TO THE FUNCTION OF sNTNC

The main goal of this study was to relate relaxation parameters of both backbone amides and side-chain methyls to the structure and function of sNTnC•apo. It will be shown that the side-chain methyl group dynamics play an important role in the energetics of the calcium induced structural change. Finally, the backbone order parameters of binding loop residues are used to calculate conformational entropy, and a quantitative contribution of entropy to binding affinity is obtained.

Comparison with structural data

Backbone dynamics

This study is the first to report experimental data on the backbone dynamics of sTnC. Although the crystallographic B-factors and NMR rmsd reported with the X-ray and NMR structures are not direct measures of dynamics, a qualitative comparison of these values with the order parameters can be made. The per residue rmsd obtained from a family of NMR structures has no direct relation with the determined S^2; it is simply a reflection of the restraints used to generate the structures. Although per residue rmsd should not be interpreted in terms of flexibility, regions with small S^2 values should usually correspond to a higher rmsd in the ensemble of calculated structures. Comparison of the S^2 values determined here with the per residue backbone rmsd from the NMR structures of sNTnC•apo [63] is illustrated in figure 70. This comparison indicates that the lack of definition in the

NMR structure for the N- and C-terminal residues and in both calcium binding loops is largely due to flexibility. The correlation is however not perfect on a per residue basis in the calcium binding loops. This could be due to an 'over-constraining' of the first residues in the loops, or a small lack of restraints for some later residues. Overall, the correlation between the backbone rmsd of the NMR structure and the S^2 is good, and there is no indication of a lack of restraints in the NMR structure. There is however a possibility of 'over-constraining' around helix N which is well-defined in the NMR structure from residue 7 and up. Despite the fact that several residues from helix N could not be characterized in the present study, all of the determined ones have an S^2 lower than the rest of the helices. Additionally, the S^2_{axis} of the Ala8 methyl group is lower than for most alanines (figure 69c).

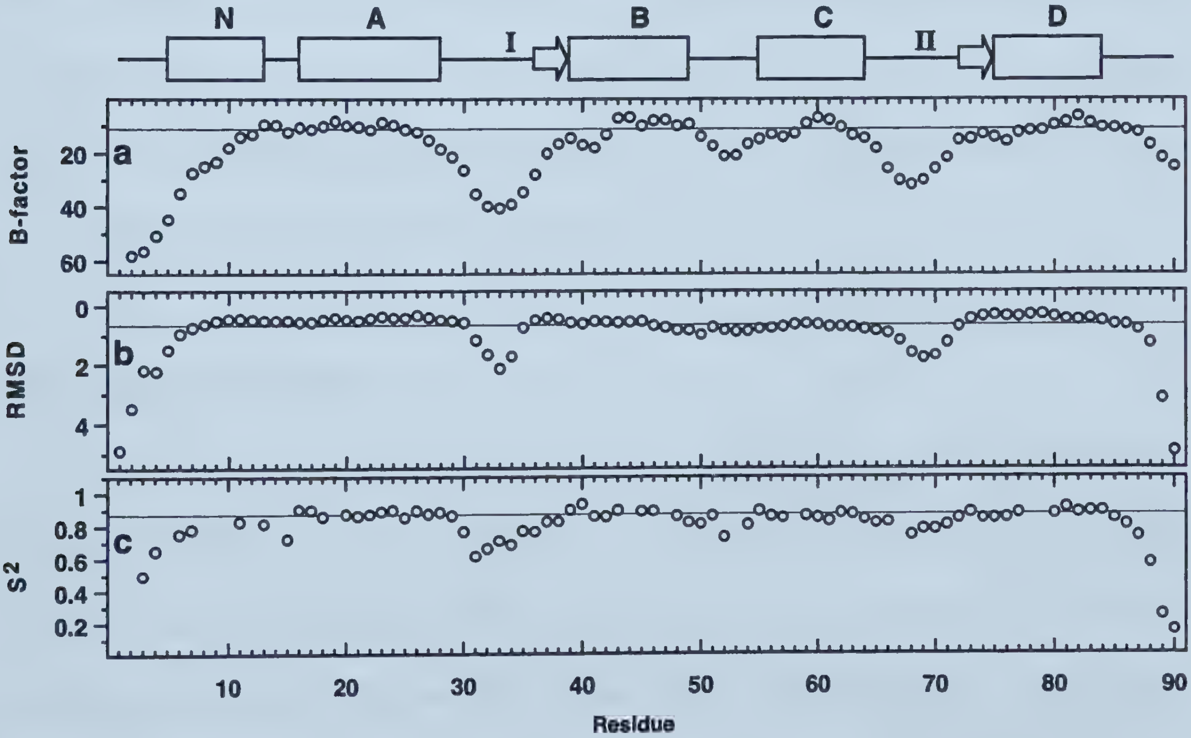

Figure 70. Comparison between the nitrogen B-factor (a) of the X-ray structure, the backbone RMSD (b) of the NMR structure, and the backbone order parameter (c) of the present study. The line in each plot represents the average value for helical residues. The secondary structure elements are shown on top as in figure 62.

The value of the crystallographic B-factor is affected by several factors, but since internal motion is one of its major contributors, tendencies in the order parameter are usually, but not always, reflected in the value of the B-factor. Previous reports have shown that there is no quantitative correlation between B-factors and order parameters, but that a qualitative correlation usually exists [113, 114]. A qualitative comparison of S^2 values from this study and B-factors from the crystal structure of sTnC•Ca_2 is shown in figure 70. The flexible regions of sNTnC, as determined by the S^2 values, have large B-factors in the crystal structure. Interestingly, the disorder in helix N, as suggested by the relaxation data, is in agreement with the X-ray data where helix N residues have larger B-factors compared to the other helices. This terminal helix is packed on only one other helix, helix D, and is therefore likely less stable than the other helices. Because of its location in space, helix N could be partially unfolded without affecting the environment of the functional regions of sNTnC, such as the calcium binding loops and the hydrophobic pocket.

Methyl group dynamics

Inspection of the order parameters of the methyl groups in relation to the calcium induced structural change reveals some interesting features. As noted above, Met82 has an unusually high order parameter. Met82 is also the methionine residue which gets the most exposed upon calcium binding: an ASA increase of 63 Å^2 based on the NMR structures, and 51 Å^2 based on the X-ray structures. Note that the larger calcium-induced exposure of Met82 relative to other methionines is due to the open form (calcium-saturated) and not to the apo

structure since all three buried methionines have essentially the same ASA in the apo structure. Since exposing hydrophobic residues is energetically expensive, one could think that the larger exposure of Met82 would contribute more to the cost of opening the structure. When the dynamics are taken into account, one sees a different picture. Assuming that the order parameter of Met82 will be more 'normal' in the open form, i.e. around 0.2 (figure 70c), this would correspond to a large gain in conformational entropy. Therefore the overall cost of exposing Met82 will be significantly smaller than the exposure of the other methionines, since those will not gain as much entropy upon the calcium induced structural change.

In both the NMR and the crystal structures of sNTnC•apo, the side-chain of Leu49 is significantly more exposed than all other leucine side-chains. Despite this, Leu49 is less flexible than other leucine residues, as shown by its large order parameter (figure 70c). When looking at the calcium-saturated structures, one finds that Leu49 is the only leucine side-chain that is exposed upon the structural change (73 $Å^2$ for the NMR structures, and 94 $Å^2$ for the X-ray structures). Again, a residue which gets significantly exposed is rigid in the apo form, and the energetic cost associated with exposing a hydrophobic side-chain can be reduced by a gain in conformational entropy. It is therefore clear that the dynamics of the methyl groups play a role in the energetics of calcium binding, and ultimately to the energetics of the calcium induced structural change. Since the dynamics of the calcium saturated form have not been determined yet, I cannot provide a quantitative description of these energetics. It is however evident that future studies of methyl dynamics of calcium

saturated sNTnC will provide valuable understanding of the fine tuning which occurs in order for this protein to adequately perform its function.

Correlation between flexibility and calcium-binding affinity

The order parameters which were determined for the backbone amides of sNTnC•apo show a value of ~0.85 for secondary structural elements, and lower values for loops and terminal regions, as is typical for many proteins. Although these measurements can be used to validate the apparent flexibility in the calculated NMR structure, interpretations of the backbone order parameters are often limited. Following earlier work of Akke et al. [115], Yang and Kay [116] recently presented an approach where contributions to conformational entropy arising from bond vector fluctuations measured from NMR-derived order parameters could be evaluated. I have used this approach to correlate flexibility and calcium-binding affinity.

There is a conformational entropic change associated with the binding of calcium to sites I and II of sNTnC. This entropic change is defined as : $\Delta S_p = S_p^{Ca} - S_p^{apo}$, where S_p^{Ca} is the conformational entropy of the calcium bound state and S_p^{apo} is the conformational entropy of the calcium free state. Note that ΔS_p is the conformational entropy change of the protein only, and does not include any entropic contribution from solvent or calcium ions. One would therefore expect ΔS_p to be negative; this notion is supported by the calcium-saturated

crystal structure data where the B-factors of the calcium binding loops are among the lowest (figure 71a). The difference in calcium-induced ΔS_p between site I and site II is :

$$\Delta\Delta S_p = \left(S_p^{I,Ca} - S_p^{I,apo}\right) - \left(S_p^{II,Ca} - S_p^{II,apo}\right) \tag{23}$$

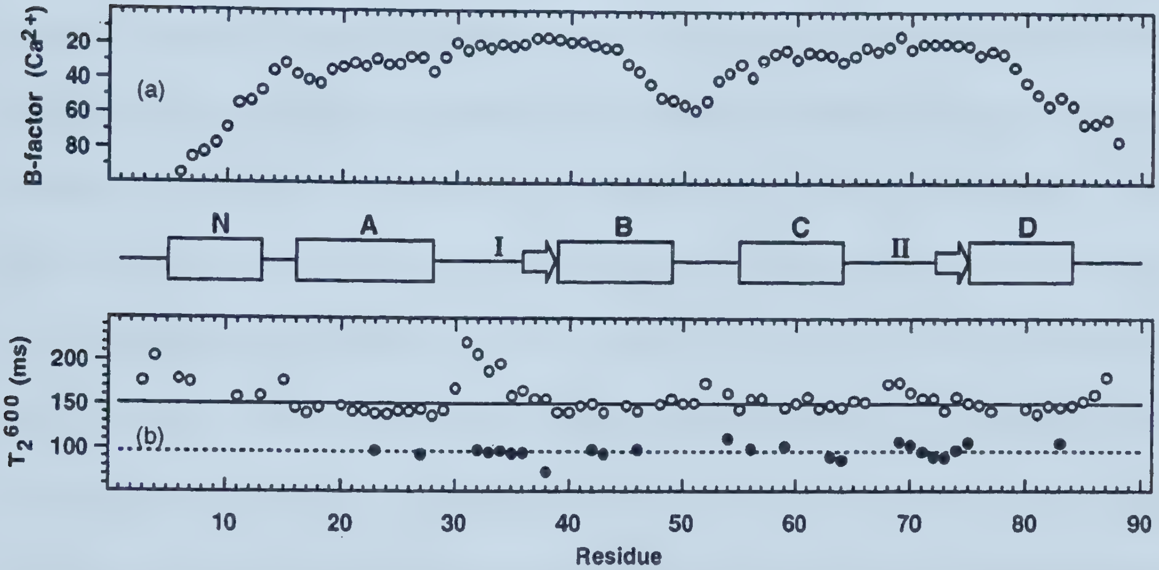

Figure 71. Crystallographic (a) and NMR (b) data showing the lack of flexibility in the calcium binding loops when calcium is bound. (a) The crystallographic B-factors are from the X-ray structure of sNTnC•Ca$_2$. (b) The ^{15}N-T$_2$ of sNTnC•Ca$_2$ at 600 MHz (●) are compared with the ^{15}N-T$_2$ of sNTnC•apo (○) at the same field strength. The apo data are the same as shown in figure 62a. The calcium data were acquired on a 1.5mM sample under the same conditions as for the apo data. The smaller number of characterized residues for sNTnC•Ca$_2$ is due to overlap and to poor spectral quality of the partially dimerized protein.

Ideally, dynamics data for both the apo and the calcium-saturated forms would be used to estimate $\Delta\Delta S_p$. Although relaxation data is readily available for the apo form, it was not possible to obtain the relevant NMR relaxation data for the calcium form. As pointed out previously [49, 63] sNTnC dimerizes upon calcium binding with a K_d of ~0.8 mM. Due to the value of K_d, the concentration required to obtain relaxation data for a 95% monomeric

sample is too low (~20 μM) for NMR relaxation experiments. It might be possible to make a sample which is predominantly dimeric, however the dimeric state has no physiological relevance, and the dynamic properties of the dimer would likely be different from the monomer; thus, relaxation data for the dimer is not acceptable for the present study. One could take the monomer/dimer equilibrium into account in the analysis, but the larger number of variables that would be involved (one set for each state) would exceed the number of experimental parameters. Although relaxation data for the calcium form cannot be used quantitatively, we can extract qualitative information from it. Figure 71b shows the ^{15}N-T_2 relaxation data for the calcium saturated form of sNTnC at a concentration of 1.5 mM where sNTnC is approximately 40% monomeric. As mentioned previously [63], the spectral quality of sNTnC•Ca_2 is significantly inferior to that of sNTnC•apo because of broadening and overlap, and therefore only 24 residues can be characterized with confidence. The average T_2 of the calcium form is smaller due to increased average molecular weight of the partial dimer. However, when compared with the T_2's in the calcium form, the relaxation data indicates that the calcium binding sites have lost their flexibility upon calcium binding; this is best illustrated by residues 32-34. That the calcium binding loops lose their flexibility similarly upon calcium binding is further supported by the X-ray B-factors of sNTnC•Ca_2 (figure 71A).

Although detailed information about the dynamics of the calcium form is not readily available, the partial information shown in figure 71 allows us to determine that $S_p^{I,Ca} \approx S_p^{II,Ca}$.

The difference, $\Delta\Delta S_p$, between site I and II is then reduced to:

$$\Delta\Delta S_p = S_p^{II,apo} - S_p^{I,apo} \tag{24}$$

As proposed by Yang and Kay [116], we can approximate the contribution to the difference in conformational entropy arising from differences in ps-ns timescale bond vector fluctuations, by using the following relation:

$$\Delta\Delta S_p = k\sum_{n} \ln \frac{3-\sqrt{1+8S_{LZ,II}}}{3-\sqrt{1+8S_{LZ,I}}} \tag{25}$$

where k is Boltzmann's constant, $S_{LZ,I}$ and $S_{LZ,II}$ are order parameters determined by NMR for site I and II, respectively, and $\Delta\Delta S_p$ is the difference in conformational entropic loss associated with calcium binding to site II and calcium binding to site I.

The difference in flexibility between sites I and II is highlighted in figure 72. Residues in site I are substantially more disordered than residues in site II, with the exception of Thr39 and Lys40, which are more ordered than their homologous residues. This difference in order parameters can be translated into entropic differences using equation 25, and results of this calculation are shown in table 16. The total difference in conformational entropy ($\Delta\Delta S_p$) between sites I and II in the apo state is 3.23 ± 0.06 cal mol^{-1} K^{-1}. At the temperature used in this study, this means that in the apo state site I is about 0.98 ± 0.02 kcal mol^{-1} more stable than site II in terms of conformational entropic free energy. As note above, this difference is also an approximation of the difference in conformational entropic loss due

to calcium binding. It has been shown previously that the two sites have different calcium binding affinity [25], and that the higher affinity is associated with site II [117].

Clearly, other entropic contributions from the solvent and calcium contribute significantly to the free energy of binding. Strynadka et al. [61] have indicated that the structural nature of the calcium coordination in site I is a possible explanation for a weaker calcium affinity. Based on the NMR structure, they also proposed that conformational flexibility in site I may create an energetic cost in ordering this site for optimal calcium binding [61]. Based on the experimental data presented here, I show that the larger conformational entropic cost associated with calcium binding to site I to be approximately 1 kcal mol^{-1} at 30°C. It should be noted that this value is related to ps-ns timescale motions only, and that contribution from slower motions are not accounted for. However, the value of 1 kcal mol^{-1} is consistent with the dissociation constants previously measured [25] for sites I and II of 16μM and 1.7μM, respectively. Therefore, conformational entropy is a major factor for the fine tuning of the calcium affinity in sNTnC, and likely in other similar calcium binding proteins.

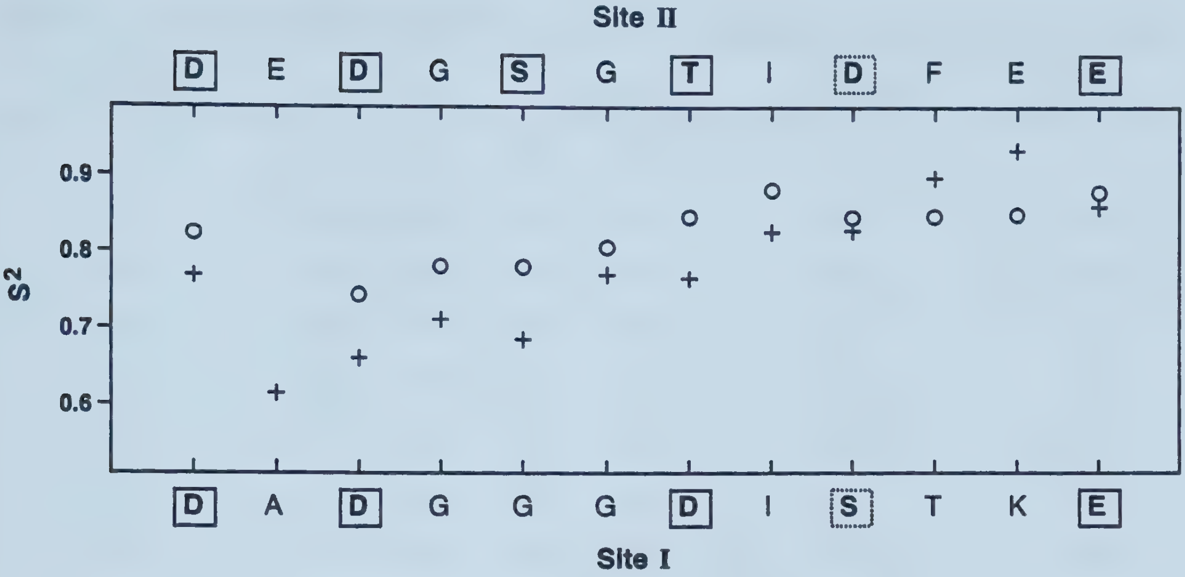

Figure 72. Comparison of the backbone order parameters between calcium binding site I (+) and II (O). The average of the 500 and 600 MHz determination is used. The sequences of site I and II are shown below and above the graph, respectively.

Table 16. Conformational entropy difference between site I and site II

Residue (site I-site II)	S^2 Site I [a]	S^2 Site II [a]	ΔS_p [b] (cal mol^{-1} K^{-1})	$-T\Delta S_p$ [c] (kcal mol^{-1})
30-66	0.768 ± 0.006	0.824 ± 0.007	-0.60	+0.18
31-67	0.614 ± 0.005	0.684 ± 0.008 [d]	-0.47	+0.14
32-68	0.660 ± 0.006	0.744 ± 0.006	-0.64	+0.20
33-69	0.710 ± 0.006	0.780 ± 0.007	-0.61	+0.19
34-70	0.685 ± 0.005	0.780 ± 0.007	-0.80	+0.24
35-71	0.770 ± 0.006	0.805 ± 0.008	-0.36	+0.11
36-72	0.765 ± 0.006	0.846 ± 0.006	-0.91	+0.28
37-73	0.825 ± 0.006	0.881 ± 0.006	-0.81	+0.25
38-74	0.827 ± 0.006	0.845 ± 0.008	-0.23	+0.07
39-75	0.897 ± 0.007	0.847 ± 0.006	+0.83	-0.25
40-76	0.933 ± 0.007	0.849 ± 0.007	+1.68	-0.51
41-77	0.859 ± 0.006	0.878 ± 0.007	-0.30	+0.09
Sum			-3.23	+0.98 ± 0.02

[a] Average of the S^2 determined at 500 and 600 MHz. Errors are estimated from Monte Carlo analysis. [b] Calculated using equation 25. [c] Using a temperature of 302.75 K (29.6°C). Error estimated from Monte Carlo analysis. [d] Relaxation parameters for residue 67 were not determined due to overlap in the HSQC spectra. Value extrapolated from neighboring residues (66 and 68) to reflect the tendency of homologous residue 31 relative to its own neighboring residues (30 and 32).

13. DYNAMICS AND THERMODYNAMICS OF cNTnC•APO AND cNTnC•CA$_1$

In the previous chapter, I have shown that the contribution to the conformational entropy derived from motions sensed by ^{15}N NMR relaxation measurements differs by approximately 1 kcal mol^{-1} between sites I and II of sNTnC; this is close to the difference in free energy of binding between the two sites. In this chapter, I present the backbone amide ^{15}N NMR relaxation measurements of apo and calcium-saturated cNTnC to directly determine the contribution of conformational entropy changes of sites I and II to the free energy of calcium-binding to cNTnC. These results provide insight into the entropic differences between the skeletal and cardiac TnC which respond so differently in a structural fashion to calcium-binding.

Before I continue, it should be noted that Leo Spyracopoulos and I worked as a team on this cNTnC relaxation study, and that Leo is the principal contributor.

Results

^{15}N-T$_1$, T$_2$, and NOE data.

cNTnC•apo

For cNTnC•apo, ^{15}N NMR relaxation data for 59 of 89 residues were obtained at 300 MHz, and 72 of 89 at 500 and 600 MHz. Of the seventeen uncharacterized residues at 500 and 600 MHz, Met1 and Asp2 were not observed due to rapid exchange with water, Pro52 and Pro54 do not have amide protons, and the remaining residues were overlapped in the 2D

{^{1}H-^{15}N}-HSQC spectra. For the 300 MHz relaxation data, additional residues were excluded due to overlap and poor signal to noise in the 2D {^{1}H-^{15}N}-HSQC spectra. Relaxation data for cNTnC•apo are shown in figure 73. The average T_1^{300} for all residues was 252 ± 41 ms with an average error of 26 ms, the average T_1^{500} for all residues was 444 ± 22 ms with an average error of 7 ms, and the average T_1^{600} was 548 ± 22 ms with an average error of 5 ms (figure 73a). The pattern of T_1 values is similar at the three fields. Residues for which internal motion affects the measured T_1 value were identified by an NOE less than 0.49, 0.60, or 0.65 at 300, 500, and 600 MHz, respectively. These included residues 5, 7, 10, 20, 30, 33, 34, 41, 43, 56, 62, 66, 67 at 300 MHz, residues 3-5, 7, 8, 30-34, 66, and 67 at 500 MHz, and residues 3-5, 30-34, 51, and 65-67 at 600 MHz. Most of these residues are located within the N-terminus, calcium-binding sites, and the BC linker. Excluding these residues gives T_1^{600}/T_1^{300}, T_1^{500}/T_1^{300}, and T_1^{600}/T_1^{500} ratios of 2.2 ± 0.4, 1.8 ± 0.3, and 1.25 ± 0.07, respectively. The average T_2^{300} for all residues is 145 ± 16 ms with an average error of 7 ms , the average T_2^{500} is 145 ± 18 ms with an average error of 1 ms, and the average T_2^{600} for all residues is 140 ± 20 ms with an average error of 1 ms. Excluding those residues with $NOE^{300} < 0.49$, $NOE^{500} < 0.6$, and $NOE^{600} < 0.65$ gives T_2^{600}/T_2^{300}, T_2^{500}/T_2^{300}, and T_2^{600}/T_2^{500} ratios of 0.9 ± 0.1, 1.0 ± 0.1, and 0.96 ± 0.09, respectively. The pattern of T_2 values is similar for all three fields. The average NOE^{300} for all residues is 0.55 ± 0.11 with

an average error of 0.06, the average NOE^{500} for all residues is 0.65 ± 0.11 with an average error of 0.01, and the average NOE^{600} for all residues is 0.73 ± 0.10 with an average error of 0.01 (figure 73c). The average NOE^{600}/NOE^{300}, NOE^{500}/NOE^{300}, and NOE^{600}/NOE^{500} ratios excluding those residues with NOE^{300} < 0.49, NOE^{500} < 0.60 and NOE^{600} < 0.65 are 1.2 ± 0.2, 1.2 ± 0.2, and 1.03 ± 0.08. The average T_1^{600} / T_2^{600}, T_1^{500} / T_2^{500}, T_1^{300} / T_2^{300} and ratios were 4.1 ± 0.3 , 3.2 ± 0.2, and 1.8 ± 0.3, using residues not affected by internal motions.

cNTnC•Ca$_1$

For cNTnC•Ca$_1$, relaxation data were collected only at one field, 500 MHz. As will be discussed later, there is a small amount of calcium-induced aggregation for cNTnC, and relaxation data were acquired on a dilute sample in an 8mm NMR tube. Unfortunately, larger probe size was only available on our 500 MHz spectrometer. Chemical shift assignments of the dilute sample were checked using a 3D HNHA experiment. The average T_1 was 440 ± 106 ms with an average error of 12 ms for 71 of 89 residues (figure 74a). The average T_2 for all characterized residues was 166 ± 82 ms with an average error of 5 ms (figure 74b). The average NOE was 0.57 ± 0.27 with an average error of 0.04 (figure 74c). The average NOE value for cNTnC•Ca$_1$ is somewhat lower than expected from theory (NOE maximum is 0.76 for $\tau_m = 5.02$ ns, $S^2 = 0.85$ and $\tau_e = 0$ ps). We feel that this may be related to spectrometer drift, given the long acquisition times required to collect spectra with and without NOE (~ 46 hours per spectrum), also the spectrum with NOE was acquired after the spectrum without NOE. Thus, residues with an NOE < 0.566 were selected as those with significant internal motions and are 3, 4, 5, 12, 29, 32, 37, 51, 57, 64, 66, 84, 85, 86, 88, 89.

These residues are in the N- and C-termini, and the defunct calcium-binding site. Excluding these residues, the average T_1/T_2 ratio is 2.8 ± 0.3.

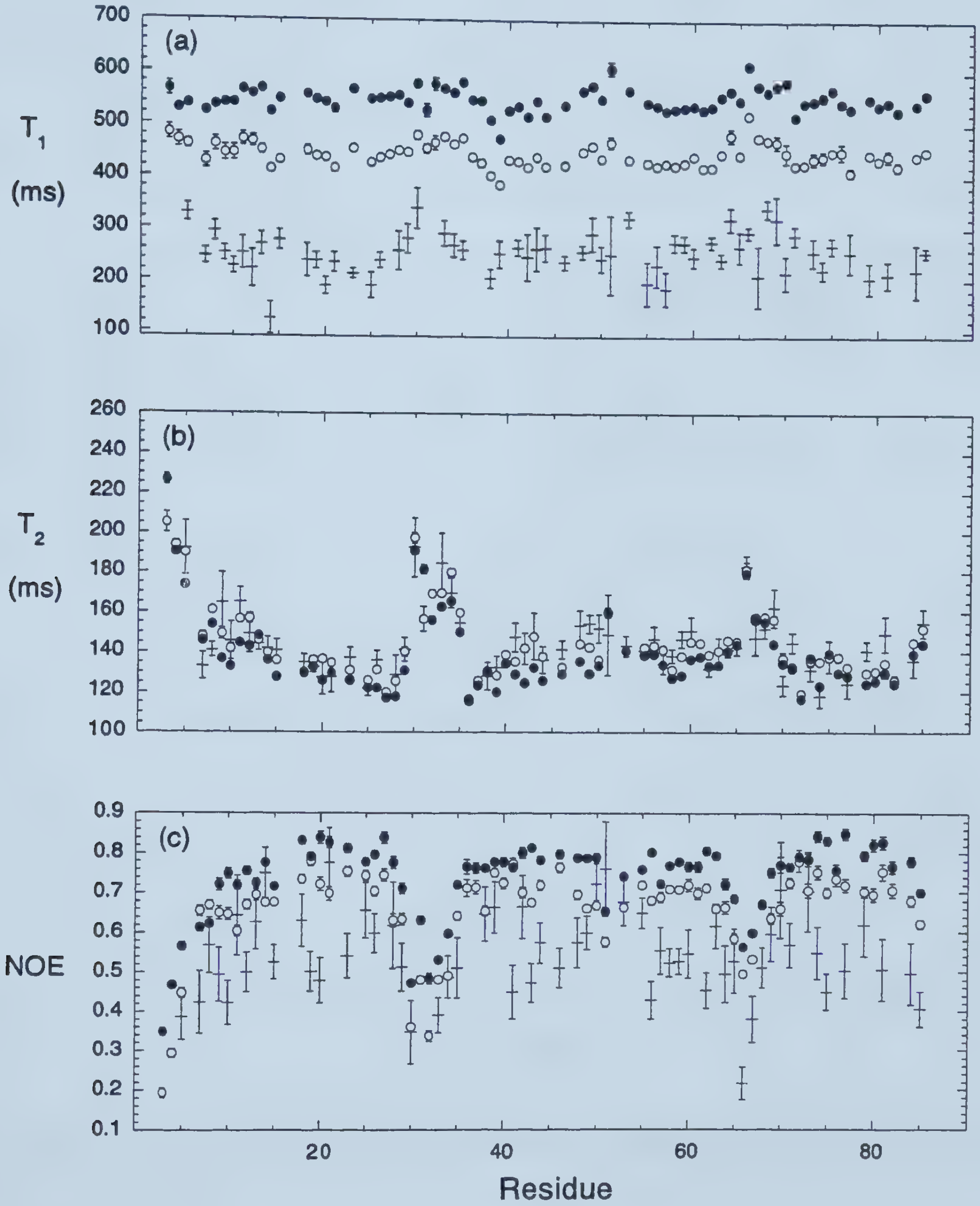

Figure 73. Plots of ^{15}N-T_1 (a), ^{15}N-T_2 (b), and {^{1}H}^{15}N NOE (c) at 300 (+), 500 (○), and 600 (●) MHz for cNTnC•apo. The elements of secondary structure are helix N (5-11), helix A (14-26), helix B (38-48), helix C (54-64), helix D (74-84), β-strand (35-37, 71-73), site I (28-40), site II (65-76), and the BC linker (49-53).

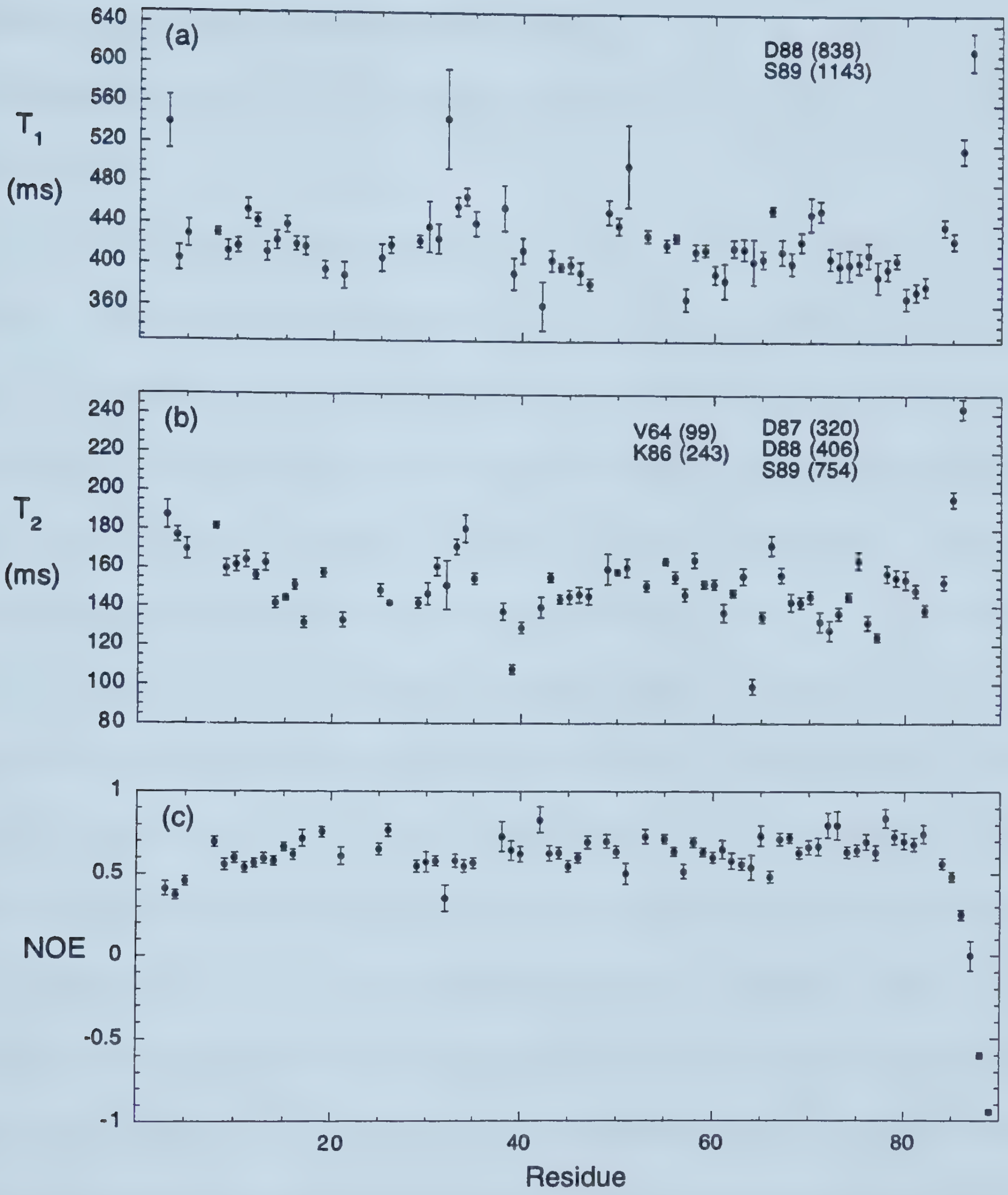

Figure 74. Plots of ^{15}N-T$_1$ (a), ^{15}N-T$_2$ (b), and {^{1}H}^{15}N NOE (c) at 500 MHz for cNTnC•Ca$_1$. The elements of secondary structure are as for figure 73.

Determination of the overall correlation time

The analysis of the data was done using the same approach as for sNTnC•apo (chapter 10).

cNTnC•apo

For cNTnC•apo, relaxation data acquired at 300, 500, and 600 MHz were treated separately. The τ_m was determined with the assumption that the rotational tumbling of the molecule is isotropic. The average values of the principal axes of the inertia tensor are 1.00:0.91:0.76 using residues 1-89 of the ensemble of forty solution structures (chapter 8), indicating that rotational tumbling is isotropic to a first approximation. The overall correlation time was determined from the average obtained from per residue fits of the relaxation data to the S^2-τ_m-τ_e model (isotropic rotational tumbling), and using only relaxation data for residues with an $NOE^{300} > 0.49$, $NOE^{500} > 0.60$, and $NOE^{600} > 0.65$, as previously described [118]. The correlation time for cNTnC•apo was determined to be 5.48, 5.53, and 5.55 ns based on 300, 500, and 600 MHz relaxation parameters, respectively.

Recently, it has been shown that a small degree of anisotropy in the rotational tumbling of a protein can be reflected in the relaxation data (chapter 10). Using an approach similar to that for sNTnC•apo (chapter 10), the $D_\parallel/D_\perp$ ratio for an axially symmetric diffusion tensor was determined to be 1.12 from an analysis of the T_1/T_2 ratios at 500 and 600 MHz for residues in the α-helices of cNTnC•apo (table 17), indicating that the degree of anisotropy in the rotational tumbling of cNTnC•apo is small. Relaxation data at 300 MHz was not used in the analysis of rotational tumbling anisotropy because the 500 and 600 MHz relaxation data were of significantly superior quality. Values of $D_\parallel/D_\perp$ close to 1 will not affect the determination of S^2 and τ_m when assuming the rotational tumbling is isotropic. The

coordinates used for the calculation of the rotational diffusion anisotropy were from the ensemble of 40 solution NMR structures (chapter 8).

Table 17. Rotational diffusion anisotropy of cNTnC [a]

	cNTnC•apo (500 MHz)	cNTnC•apo (600 MHz)	cNTnC•Ca$_1$ (500 MHz)
θ	53 ± 7	55 ± 5	84 ± 8
φ	-18 ± 10	-32 ± 7	-19 ± 7
$D_{\parallel}/D_{\perp}$	1.13 ± 0.03	1.11 ± 0.02	1.30 ± 0.03
E	241 ± 23	322 ± 34	230 ± 18
E_v	6.5 ± 0.6	8.7 ± 0.9	7.4 ± 0.6
F_x	3.8 ± 1.5	5.7 ± 1.9	5.0 ± 1.2

[a] Values in the table are the averages and standard deviations from the ensembles of forty solution NMR structures for cNTnC•apo and cNTnC•Ca$_1$. Parameters are as defined in chapter 10.

cNTnC•Ca$_1$

The τ_m for cNTnC•Ca$_1$ is dependent upon protein concentration. For example, at a protein concentration of about 0.37 mM, τ_m was determined to be 6 ns. This value is reduced to 5 ns at a protein concentration of 0.15 mM. The concentration dependence of τ_m are most likely due to calcium-induced protein dimerization. The average values of the principal components of the inertia tensor were determined to be 1.00:0.89:0.71 using residues 1-89 in the ensemble of 40 solution structures, justifying the assumption of isotropic rotational tumbling for the calcium-saturated protein. In addition, the anisotropy of diffusion $D_{\parallel}/D_{\perp}$ for an axially symmetric diffusion tensor was determined to be 1.30 for cNTnC•Ca$_1$ (table 17), using coordinates for the ensemble of 40 solution NMR structures (chapter 8). For a protein concentration of 0.15 mM, τ_m was determined from relaxation data with $NOE^{500} > 0.566$.

Analysis of backbone dynamics

One of the primary goals of this study is to extract reliable values of S^2 for apo and calcium-saturated cNTnC in order to calculate the conformational entropy change for this two-state transition. The model-independent analysis for cNTnC was carried out under the assumption of isotropic rotational tumbling. For each residue, relaxation data were fitted to three spectral density models, as in chapter 10. These included an S^2-τ_e, S^2-τ_e-R_{ex}, and a two-time-scale model. S^2 values from the S^2-τ_e model are usually reliable for the calculation of the conformational entropy changes associated with calcium binding, even in the presence of a small degree of rotational tumbling anisotropy. However, for some residues in sites I and II, S^2 values from the S^2-τ_e-R_{ex} model were used due to significant improvements in the fit over the S^2-τ_e model for cNTnC•apo and cNTnC•Ca$_1$ (table 18). In addition, the lower than expected average NOE for cNTnC•Ca$_1$ has no effect on the determined τ_m and S^2 values, but increases τ_e values. Thus, S^2 values will be reliable for the calculation of conformational entropy changes, even in the presence of systematic error for the NOE data, as previously noted (chapter 10).

Table 18. Calcium-induced conformational entropy changes in sites I and II of cNTnC

residue	S^2		$-T\Delta S_p$ [b] (kcal mol^{-1})	residue	S^2		$-T\Delta S_p$ [b] (kcal mol^{-1})
	apo [a]	Ca$_1$			apo [a]	Ca$_1$	
29	.843 ± .007	.844 ± .011	.00 ± .05	65	.808 ± .008	.920 ± .014	.56 ± .11
30	.647 ± .009	.840 ± .028	.53 ± .11	66	.681 ± .006	.743 ± .009	.15 ± .03
31	.688 ± .008	.796 ± .018	.29 ± .06	67	.757 ± .006	.835 ± .016	.25 ± .06
32	.708 ± .011	.736 ± .041	.07 ± .11	68	.771 ± .006	.889 ± .021	.47 ± .12
33	.717 ± .009	.752 ± .012	.09 ± .04	69	.780 ± .010	.886 ± .016	.42 ± .09
34	.722 ± .007	.732 ± .015	.02 ± .04	70	.831 ± .016 [c]	.797 ± .031 [c]	-.12 ± .12
35	.767 ± .005	.807 ± .014	.13 ± .05	71	.889 ± .006 [c]	.792 ± .019 [c]	-.40 ± .07
36	.861 ± .014 [c]	ND [d]		72	.877 ± .014 [c]	.884 ± .026 [c]	.04 ± .16
37	.874 ± .017 [c]	.803 ± .030 [c]	-.29 ± .13	73	.860 ± .014	.927 ± .020	.41 ± .18
38	.910 ± .007	.894 ± .024	-.10 ± .15	74	.863 ± .014	.873 ± .014	.05 ± .10
39	.965 ± .017 [e]	.919 ± .028 [c]	-.30 ± .30	75	.831 ± .009	.829 ± .016	-.01 ± .07
40	.858 ± .007	.869 ± .025 [c]	.05 ± .13	76	.866 ± .013	.923 ± .017	.35 ± .15
			0.5 ± 0.4				2.2 ± 0.4

[a] S^2 values for cNTnC•apo are the averages of the 500 and 600 MHz relaxation data. However, the ^{15}N-T_2 value for Ala31 at 500 MHz was found to be biased and gives rise to a large S^2. Thus, the value of S^2 for Ala31 is from the 600 MHz data. [b] Measurement uncertainties for S^2 were propagated in the standard manner. [c] S^2 values for these residues were taken from the S^2-τ_e-R_{ex} model. [d] Not determined. [e] The value of S^2 for Lys39 is at the upper limit ($S^2 \sim 0.95$) of the applicability of eq 1, where the classical description of conformational entropy breaks down, and the value for $-T\Delta S_p$ was calculated by assuming $S^2 = 0.95$ for this residue.

The average S^2 is 0.84 ± 0.06, 0.85 ± 0.05, and 0.86 ± 0.04 at 300, 500, and 600 MHz using residues with $NOE^{300} > 0.49$, $NOE^{500} > 0.60$ and $NOE^{600} > 0.65$ for apo-cNTnC, and the S^2-τ_e model (figure 75a). For cNTnC•Ca$_1$, the average S^2 was 0.86 ± 0.06 for residues with $NOE^{500} > 0.566$, and the S^2-τ_e model (figure 76a). The S^2 values indicate that for cNTnC•apo, the N-terminal residues, both calcium-binding sites, and the BC-linker region are flexible (figure 75a). While the C-terminal residues are also expected to be flexible, dynamics data for these residues are not included due to spectral overlap. For cNTnC•Ca$_1$,

the S^2 values indicate that the N- and C-terminal residues, site I, and the BC-linker are flexible. Site II becomes more rigid upon calcium-binding, as well as defunct site I (figure 76a).

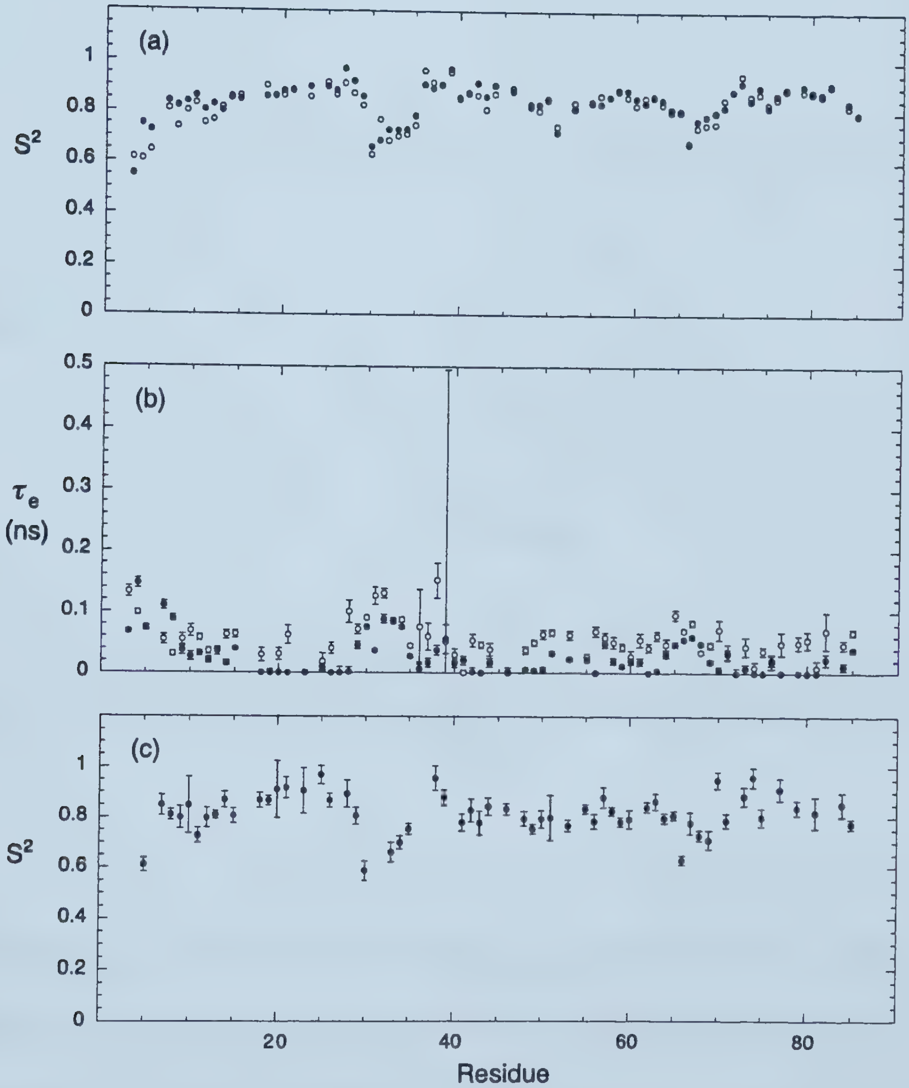

Figure 75. Order parameters (S^2) and internal correlation times (τ_e) for cNTnC•apo derived from the S^2-τ_e model. (a) S^2 at 500 (○) and 600 (●) MHz. (b) S^2 at 300 MHz. (c) τ_e at 500 (○) and 600 (●) MHz. Elements of secondary structure are as in figure 73. The error bars for S^2 in (a) are smaller than the symbols used and are not shown. Sites I and II, residues in the N-helix, and residue Asn51 in the BC-linker show S^2 values well below 0.85, indicating an increase in the amplitude of internal motion compared to the helices and β-sheet. Values of τ_e are extremely sensitive to the measured NOE, and the systematically elevated NOE^{600} leads to smaller τ_e values obtained from the 600 MHz (compared to the 500 MHz τ_e)

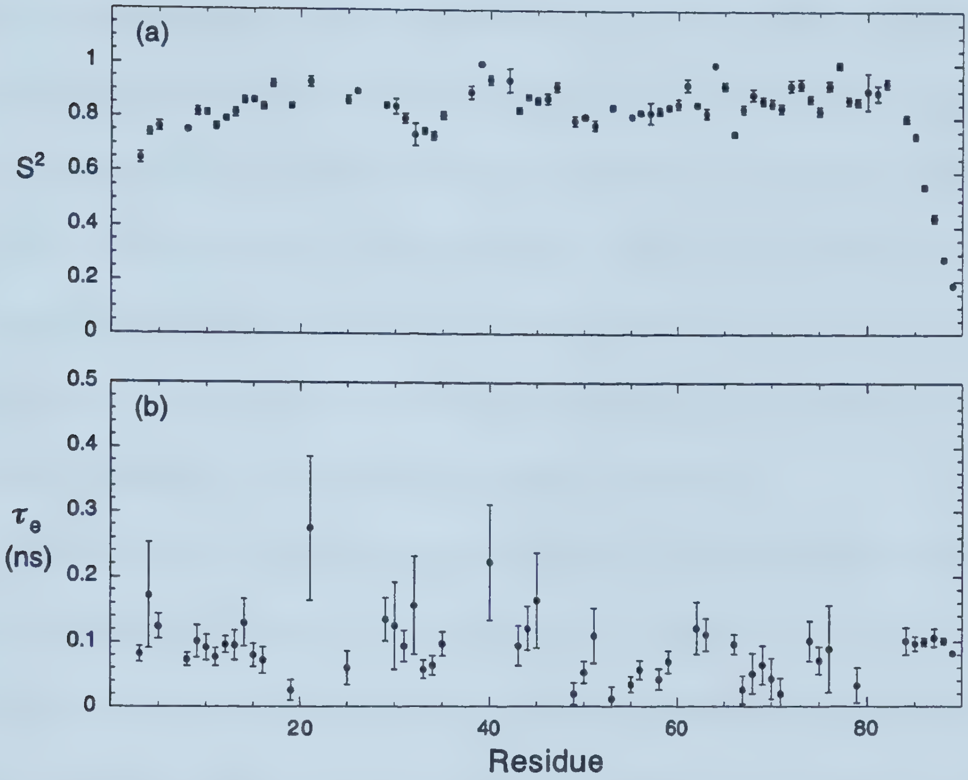

Figure 76. S^2 (a) and τ_e (b) for cNTnC•Ca$_1$ derived from the S^2-τ_e model at 500 MHz. Elements of secondary structure are as in figure 73. Residues Lys39 at the beginning of helix B, Val64 at the hinge of helix C, and Phe77 in helix D have significantly decreased T_2's; thus the S^2-τ_e model is not appropriate and gives rise to unusually large order parameters ($S^2 = 1$) for these residues.

An analysis of rotational tumbling anisotropy requires high quality relaxation data, and for cNTnC•apo, we did not use 300 MHz data, as the 500 and 600 MHz data contained more characterized residues and were of superior quality. Seven residues required an R_{ex} term to fit the T_2 data to within 95% confidence limits for cNTnC•apo at 500 and 600 MHz. Of these seven residues, five are in helix A. As in the case of sNTnC•apo, this is due to the unique orientation of helix A with respect to the principal axis of the rotational diffusion

tensor, and not a conformational exchange phenomenon (chapter 10). On the other hand, the observed line broadening for some residues in sites I and II reflects a conformational exchange phenomenon, and not rotational tumbling anisotropy, as identified using the criteria of Tjandra and Bax [96]. These include residues 36 and 72 for cNTnC•apo at 500 and 600 MHz. Nine residues required a two time scale model to fit the relaxation data for cNTnC•apo to within 95% confidence limits at 500 and 600 MHz. These include residues at the beginning of the N-helix, and the calcium-binding loops. One residue was not fit by any model at 500 MHz, and six residues were not fit at 600 MHz.

For cNTnC•Ca$_1$, 15 residues required an R_{ex} term to fit the relaxation data to within 95% confidence limits. Of these 15, four are in helix A, three in the β-sheet, four in site I, one in site II, one in helix C, one in helix D, and one in the BC-linker. It should be noted however, that unlike cNTnC•apo, we do not have the benefit of an independent analysis at 600 MHz to further validate the inclusion of an R_{ex} term for a given residue due to the lack of an 8 mm triple resonance probe for our Unity 600 spectrometer. Using the criteria of Tjandra and Bax [96], residues 37-39, and 71 were identified as residues undergoing conformational exchange phenomena. Eight residues required a two time scale model to fit the relaxation data to within 95% confidence limits. These residues included two in the N-helix, two at the end of helix D, one at the beginning of helix D, one at the end of helix B, and two in helix C. As in the case of the R_{ex} term, we do not have the benefit of an independent data set at 600 MHz to further justify the use of the two-timescale model. Seven residues were not fit by any model for cNTnC•Ca$_1$ at 500 MHz.

Summary

The dynamics data presented above show the calcium-induced changes in the backbone dynamics and thermodynamics in cNTnC as determined by ^{15}N NMR relaxation measurements. The apo- and calcium-saturated solution structures of cNTnC reveal that helices N, A and D form a structural unit which remains invariant to calcium binding, and that helices B and C move slightly away from the NAD unit upon calcium-binding (chapter 8). The interhelical reorientations that occur upon calcium-binding are reflected in the relaxation data as a difference in the rotational diffusion anisotropy of the apo and Ca^{2+} saturated states, as cNTnC•Ca$_1$ is somewhat less compact than cNTnC•apo. The differences in flexibility between sites I and II in sNTnC•apo show that site II is more rigid than site I by about 1 kcal mol^{-1} (chapter 12). In contrast, sites I and II in cNTnC•apo are similar in flexibility, this is due in part to site I sequence differences in cNTnC compared to sNTnC which abolish calcium binding in this site. The entropic difference between sites I and II in cNTnC•apo determined from changes in picosecond to nanosecond timescale fluctuations is small, with a value of 0.3 ± 0.3 kcal mol^{-1}. Upon calcium-binding to site II, residues within the flexible loops of the binding site (positions 2 - 6 of 12 positions) become more rigid as some of the side-chains of the loop residues take up specific conformations in order to ligate calcium. Surprisingly, flexible loop residues within site I of cNTnC also become more rigid upon calcium-binding to site II. The data show that sites I and II are structurally and thermodynamically coupled.

Rotational correlation time and rotational diffusion anisotropy

The rotational correlation time for cNTnC•apo was determined to be 5.48 ± 0.12, 5.53 ± 0.11, and 5.55 ± 0.10 ns using 300, 500, and 600 MHz relaxation data, respectively, at 30 °C and with the sample conditions described in the Methods. These correlation times are the averages obtained from per residue fits of the relaxation data to the S^2-τ_e model, excluding residues with $NOE^{300} > 0.49$, $NOE^{500} > 0.60$ and $NOE^{600} > 0.65$. The agreement between the three fields for τ_m is excellent, and the average is 5.52 ± 0.06 ns. This correlation time is somewhat longer than that found for sNTnC•apo at 30 °C (4.86 ± 0.15 ns). However, it should be noted that the solvent composition differs for the two isoforms. Specifically, cNTnC•apo contains 15 mM DTT which may increase the solution viscosity compared to sNTnC•apo. Additionally, cNTnC•apo may be slightly aggregated, which could give rise to an increased correlation time. While aggregated proteins show unusually large correlation times, and increased S^2 values, the average S^2 value for cNTnC•apo excluding flexible residues is 0.85, which corresponds well to the S^2 value expected for regions of well-defined secondary structure in proteins [119]. Thus, if aggregation is present for cNTnC•apo, it does not appear to affect the S^2 values significantly. The correlation time determined for cNTnC•Ca$_1$ is 5.02 ± 0.22 ns at 30 °C and is the average obtained from per residue fits of the relaxation data to the S^2-τ_e model, excluding residues with NOE > 0.566. This correlation time is shorter than that for cNTnC•apo, perhaps due to aggregation of cNTnC•apo, or may be due to solution viscosity effects upon dilution of cNTnC•Ca$_1$, and the presence of calcium in the sample.

For cNTnC•apo, the average $D_{\parallel}/D_{\perp}$ ratio (1.12) determined from 500 and 600 MHz relaxation parameters for an axially symmetric anisotropic rotational diffusion tensor is comparable to the value of 1.10 for sNTnC•apo, indicating that the rotational tumbling of both isoforms in the apo states is nearly isotropic. It should be noted that the probabilities that the improvement in the fits arose by chance when using an anisotropic rotational diffusion model are 0.019 and 0.0028 at 500 and 600 MHz, respectively. As noted previously (chapter 10), such a small degree of anisotropy in the tumbling of cNTnC•apo has little effect on S^2 when assuming the tumbling is isotropic. However, the R_{ex} terms required to fit the relaxation data for certain residues in helix A are due to its unique orientation with respect to the long axis of the rotational diffusion tensor in comparison to helices N, B, C, and D (figure 77).

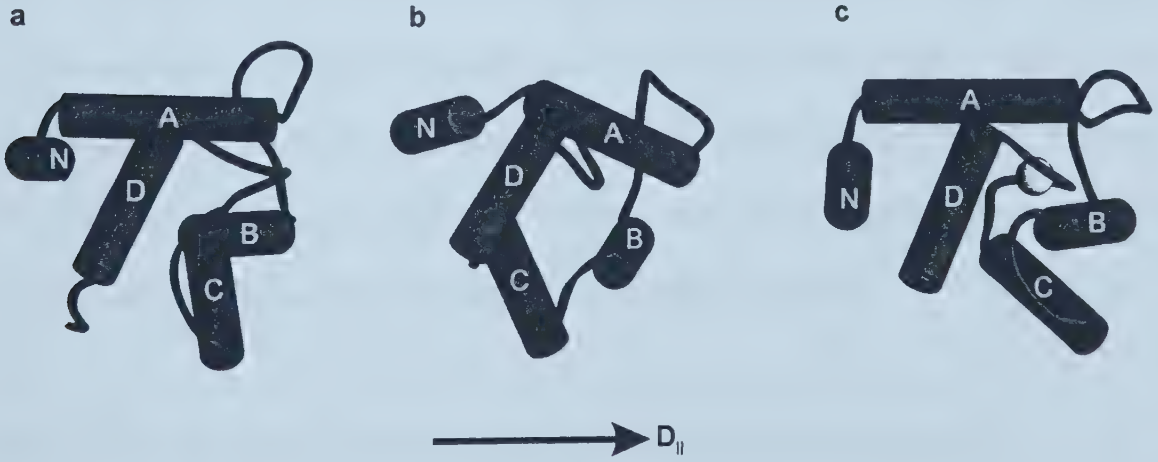

Figure 77. NMR solution structures of apo (a) and calcium-saturated (b) cNTnC oriented with respect to the long axis of the rotational diffusion tensor ($D_{\parallel}$) which lies along the plane of the page. This figure clearly shows that cNTnC•Ca$_1$ is more elongated along $D_{\parallel}$, accounting for the larger $D_{\parallel}/D_{\perp}$ ratio compared to cNTnC•apo. The X-ray structure of sNTnC•apo is also shown in (c) for comparison with cNTnC; the similar orientation of both isoforms relative to $D_{\parallel}$ is remarkable.

For cNTnC•Ca$_1$, the relaxation data is more adequately described by axially symmetric anisotropic diffusion with a $D_\parallel/D_\perp$ ratio of 1.30. The structure of cNTnC•apo is slightly more spherical and compact than cNTnC•Ca$_1$ with respect to the long axis of the rotational diffusion tensor. The probability that the improvement in the fit for anisotropic above isotropic rotational tumbling arose by chance is 0.0067, justifying the use of an axially symmetric anisotropic rotational tumbling model. The larger anisotropy for the rotational diffusion tensor of cNTnC•Ca$_1$ is not surprising, given the different orientations of the helices B and C with respect to helices N, A and D compared to cNTnC•apo [84] (figure 77). It should be noted that helices N, A and D are structurally invariant to calcium-binding [84]. As in the case of cNTnC•apo, helix A adopts a unique orientation with respect to the long axis of the anisotropic rotational diffusion tensor, and therefore, the R_{ex} terms required to fit the relaxation data for five residues in this helix are due to anisotropic tumbling. Figure 77 shows the minimized average structures of apo- and calcium-saturated cNTnC oriented with respect to the long axis of the rotational diffusion tensor. This figure also show the orientation of sNTnC•apo relative to its own long axis, and the clearly indicates that both cNTnC and sNTnC share the same anisotropic tumbling properties.

Relevance of backbone amide dynamics to solution structures

The ensemble of solution structures for cNTnC•apo show regions of disorder (larger than average backbone rmsd) at the N- and C-termini, sites I and II, and the BC-linker [84]. The backbone amide S^2 show that sites I and II are more flexible on the picosecond to nanosecond timescale, as well as the BC-linker, compared to regions of well-defined

secondary structure. Interestingly, although helix N is well-defined in the ensemble of solution structures, the relaxation data show that it is more flexible than helices A, B, C, and D (figure 75a). This is likely due to the fact that it is a terminal helix that is not as highly packed as helices A, B, C, and D that pack against each other and contribute to the main hydrophobic core of cNTnC•apo. The ensemble of solution structures for cNTnC•Ca$_1$ reveals disordered regions at the N and C-termini, and sites I and II [84]. Although the backbone rmsd's are larger for sites I and II compared to the well-defined regions, they are not as large as those for sites I and II in cNTnC•apo. The S^2 values indicate that the flexible loop region of site II (positions 2 - 6 of the 12 residue site) becomes significantly less flexible upon calcium-binding. For example, the average S^2 of 0.76 ± 0.05 for the flexible loop of site II in the apo-state (using 500 and 600 MHz data) increases to 0.83 ± 0.06 in the calcium-saturated state. The flexible loop region of site I also becomes more rigid compared to the apo-state, with an average S^2 value for positions 2 - 6 of 0.70 ± 0.03 that increases to 0.77 ± 0.04 (figure 76a and table 18). Helix N is also more flexible than the other helices, as observed for sNTnC•apo.

Comparison of site I and site II dynamics in apo-cNTnC

Sites I and II are coupled *via* the anti-parallel β-sheet in cNTnC and sNTnC. The twelve residue E-F-hand sites in cNTnC•apo are rigid at one end (positions 10 - 12) and become progressively more flexible at the opposite end (positions 2 - 4, figure 78). A comparison of the crystal structures of helix-loop-helix calcium binding proteins led to the suggestion that the carboxylate side-chain at position 1 hydrogen bonds with the backbone

amide proton at position 6 in the Ca^{2+}-saturated state [15], and that this interaction is also important in stabilizing site II in the apo state for sNTnC [61]. The S^2 values for Asp65 and Gly70 in cNTnC•apo are 0.81 and 0.83, respectively. At the end of the β-sheet closest to Gly70, residues 37 and 71 are rigid, and help stabilize Gly70, supporting the suggestion that positions 1 and 6 are involved in a hydrogen bonding interaction which is important in stabilizing site II in the apo state. In the ensemble of forty NMR solution structures for cNTnC•apo, the hydrogen bond between the amide proton of Gly70 and the carboxylate oxygens (either O$^{\delta 1}$ or O$^{\delta 2}$) of Asp65 has an occupancy of 60% with an average distance (HN–O) of 2.5 ± 0.4 Å [84] (see figure 79). In comparison, the Asp to Leu mutation in position 1 of site I of cNTnC removes the hydrogen bond between positions 1 and 6 which stabilizes site II in the apo state. From the dynamics data presented here, the hydrogen bond formed between the side-chain of Asp65 and the main-chain amide of Gly70 is a more important factor in determining the calcium binding affinity of site II in cNTnC than proposed hydrogen bonds involving the backbone amides of position 5 and 6 and the carboxylate side-chain of position 3 in sNTnC due to the greater flexibility at these residues (Asp67, S^2 = 0.76; Ser69, S^2 = 0.78) [61].

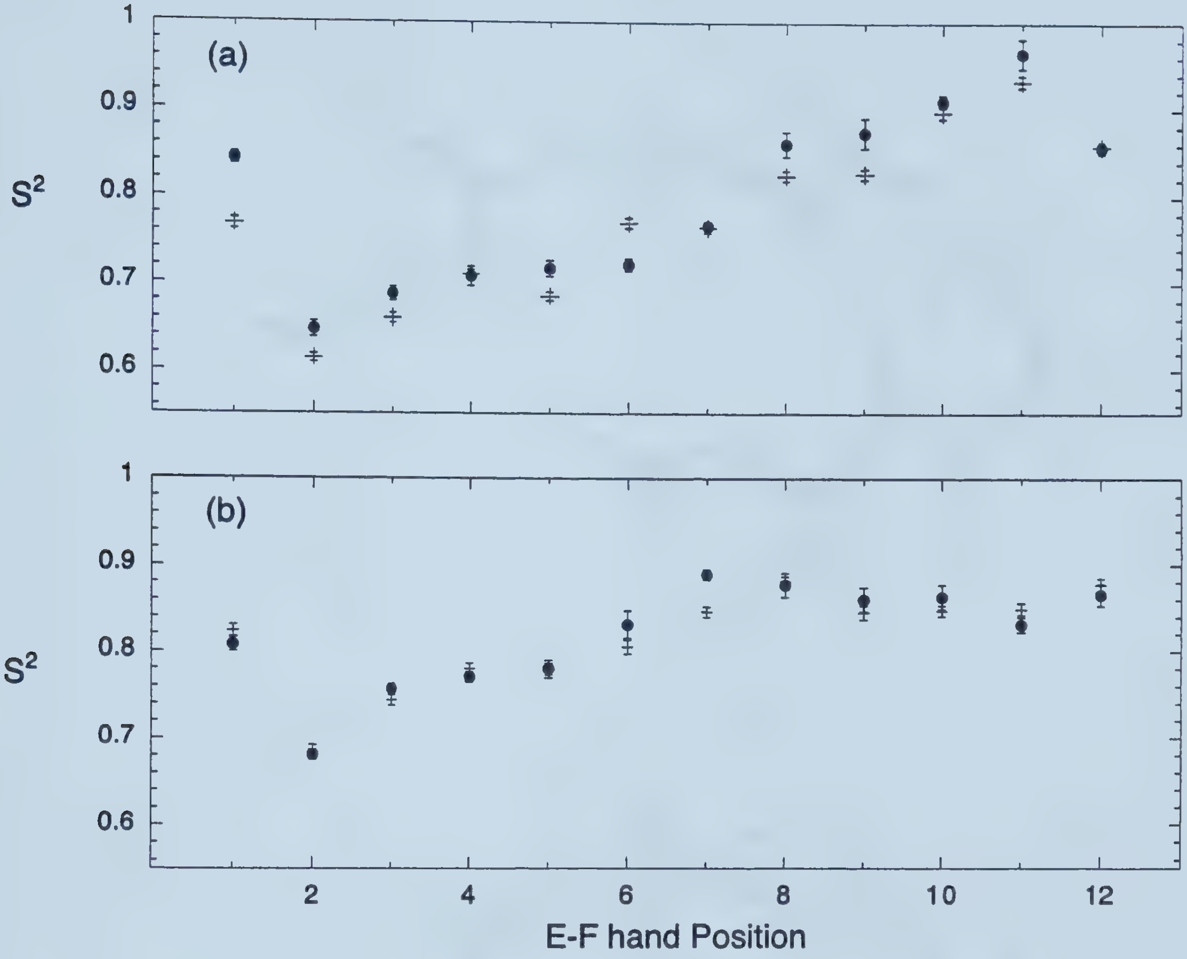

Figure 78. Comparison of the S^2 for site I (a) and site II (b) in sNTnC•apo (+) and cNTnC•apo (O). The averages of the 500 and 600 MHz data have been used for both isoforms. S^2 values for site II are similar for sNTnC and cNTnC, indicating that the flexibility of site II is similar in the two isoforms of NTnC. The first three positions of site I in cNTnC•apo are more rigid than their counterparts in sNTnC on account of hydrophobic interactions arising from D29L, D31A sequence differences and the Val28 insertion in CNTnC compared to sNTnC.

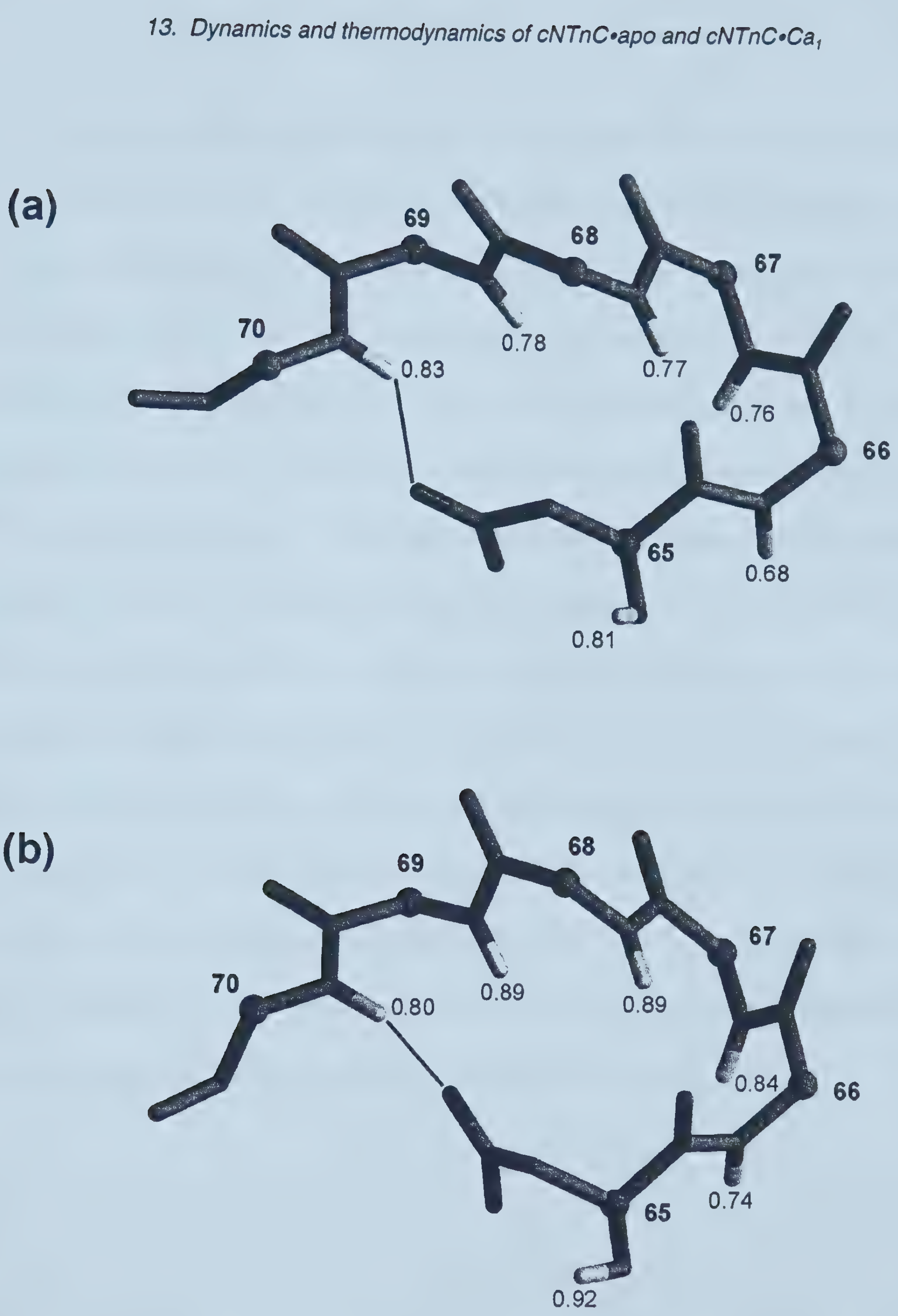
(a)
69
68
67
70
0.78
0.83
0.77
0.76
66
65
0.68
0.81
(b)
69
68
67
70
0.89
0.80
0.89
0.84
66
65
0.74
0.92

Figure 79. Backbone atoms (C^{α}, C, N, O, HN) for site II in cNTnC•apo (a) and cNTnC•Ca$_I$ (b). The non-hydrogen side-chain atoms for Asp65 are also shown. S^2 values for the backbone amide nitrogens are indicated. The hydrogen bond between the backbone amide proton of Gly70 and the carboxylate oxygen of Asp65 is indicated by a line.

The calcium-binding sites are coupled *via* the anti-parallel β-sheet in cNTnC, and there are differences in dynamics of the individual strands which each site contributes to the sheet. Residue Asp73 for the β-strand in site II (residues 71 - 73) is more rigid ($S^2 = 0.86$) than its partner (Cys35, $S^2 = 0.77$) for the β-strand in site I (residues 35 - 37), with Cys35 being the most flexible in the β-sheet. The central pair of residues in the β-sheet (Ile36 and Val72) are connected by two hydrogen bonds: one between the backbone carbonyl of Ile36 and the backbone amide proton of Val72 which shows 100% occupancy in the ensemble of forty solution NMR structures, and an average O–HN distance of 2.3 ± 0.1 Å, and another between the backbone carbonyl of Val72 and the backbone amide proton of Ile36 which shows 100% occupancy and an average O–HN distance of 2.1 ± 0.2 Å [84]. One end of the β-sheet is stabilized by a hydrogen bond between the backbone carbonyl of Gly70 and the amide proton of Thr38 (100% occupancy, average O–HN distance: 2.1 ± 0.3 Å), while at the other end, the hydrogen bond between the backbone carbonyl of Gly34 and the amide proton of Phe74 is weaker (20% occupancy, average O–HN distance: 3.2 ± 0.1 Å) and accounts, in part, for the greater flexibility observed for Cys35 (see figure 80).

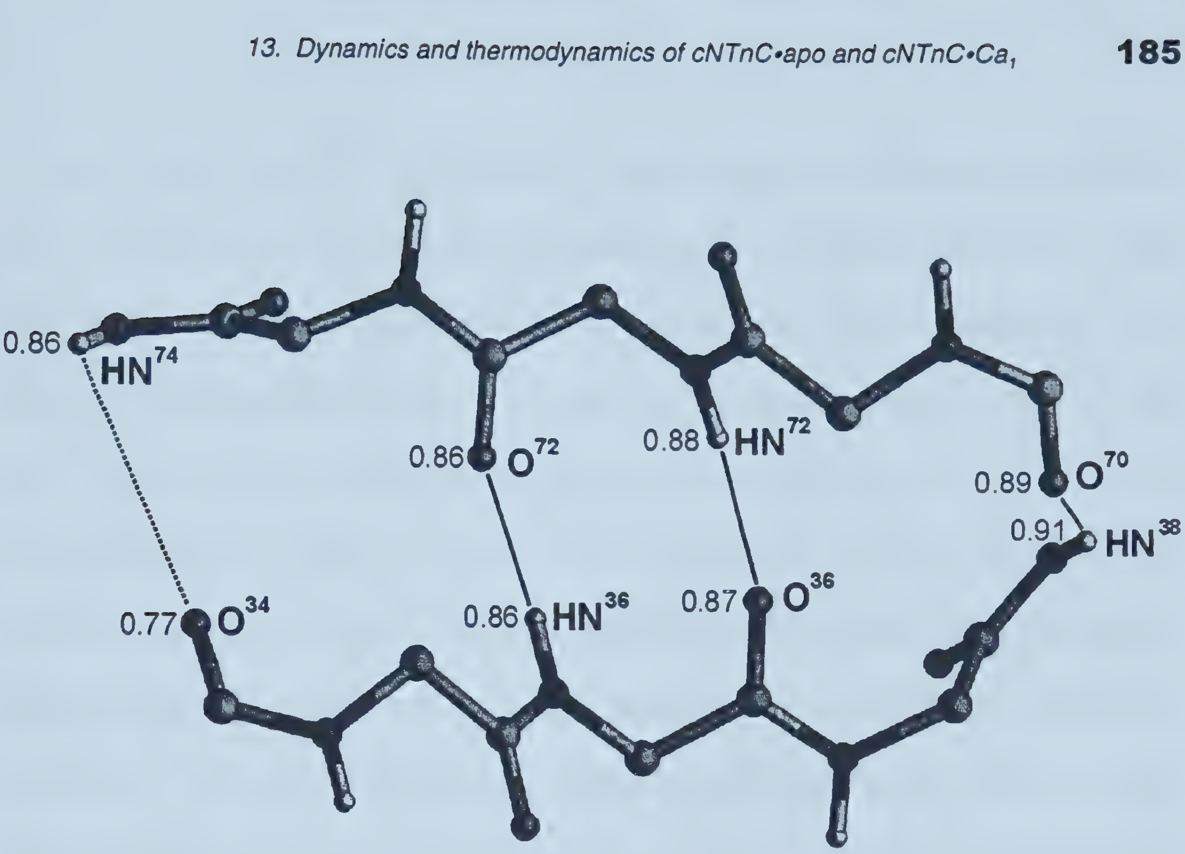

Figure 80. Backbone atoms (C^{α}, C, O, N, HN) of the central β-sheet in cNTnC•apo. Strong hydrogen bonds are indicated by solid lines, and weaker hydrogen bonds by dashed lines. The two central hydrogen bonds between the backbone amide protons and carbonyl oxygens of Ile36 and Val72 form the pivot point for the calcium-induced transition in cNTnC. S^2 values across hydrogen bonded pairs are indicated. Note that for the carbonyl oxygens, the S^2 values are from the backbone amide nitrogen of the following residue (i + 1) within the same peptide plane. The S^2 values across the central hydrogen bonds are well matched.

Comparison to site I and site II dynamics and thermodynamics in apo-sNTnC

The site II amino acid sequence in cNTnC and sNTnC is highly conserved, whereas site I is sufficiently mutated in cNTnC to abolish calcium-binding entirely. Figure 78 shows that S^2 for site II in sNTnC•apo and cNTnC•apo are similar, whereas for site I, positions 1 - 3 are more rigid for cNTnC•apo compared to sNTnC•apo. A comparison of site I and site II thermodynamics of sNTnC•apo and cNTnC•apo reveal a decrease in conformational

entropy for site I of -0.9 ± 0.3 kcal mol^{-1} and no significant difference for site II of cNTnC•apo compared to the skeletal isoform. The conformational entropy differences were calculated using all residues in sites I and II for both isoforms of NTnC. Positions 1 - 3 of site I in cNTnC•apo contribute 0.37 ± 0.04 kcal mol^{-1} to a total decrease of 0.9 ± 0.3 kcal mol^{-1} in conformational entropy for this site compared to sNTnC•apo. Site I in cNTnC contains an insertion (Val28) and might be expected to be more flexible than site I in sNTnC due to an increase in loop length. However, Val28 and Leu29 at the end of helix A serve to stabilize position 1 of site I in cNTnC•apo compared to site I in sNTnC•apo. Val28 and Leu29 show S^2 values of 0.83 and 0.84, respectively, indicating that these residues are not flexible on the picosecond to nanosecond timescale. Val28 is also highly packed, exposing only 20 ± 7 Å^2 of side-chain accessible surface area, and makes several hydrophobic contacts to residues at position 3 (Ala31) and positions 6 - 8 (Gly34, Cys35, and Ile36) of site I [84]. Leu29 makes hydrophobic contacts to Ile36 and Ser37 within the β-sheet of site I. The Gly-Gly-Gly sequence at positions 4 - 6 in site I of sNTnC is not appreciably more flexible compared to the Glu-Asp-Gly sequence in cNTnC (figure 78). In fact, the flexible binding loop of site I in cNTnC•apo and sNTnC•apo are similar in flexibility, each with an average S^2 of 0.76 ± 0.05.

The results give insight into the binding affinities for site II in cNTnC and sNTnC. For sNTnC, mutation of a single ligand at position 12 of site I (E41A) diminishes the calcium affinity of this site significantly and concomitantly causes a 10-fold reduction in the calcium affinity for site II (chapter 6). In contrast, although cNTnC has an inactive site I, site

II has a binding affinity similar to site II in native sNTnC. We attribute this difference between sNTnC and cNTnC in part to the 'stiffer' site I in cNTnC.

Calcium induced changes in dynamics and thermodynamics

Picosecond and nanosecond timescale fluctuations of the backbone amide nitrogens in the calcium-binding sites of cNTnC contribute +2.7 ± 0.6 kcal mol^{-1} to the free energy of calcium-binding to site II. As shown in table 18, there is a decrease in conformational entropy in the calcium-binding loops of both sites I and II (residues 30 - 34, and 66 - 70, respectively, *i.e.* positions 2 - 6 of the 12 residue sites) upon calcium-binding. Calcium-binding to site II in cNTnC leads to a significant increase in S^2 for the flexible loop residues, as observed for calcium-binding to the archetypal site II in calbindin D_{9k} [120]. In the apo-state, positions 2 - 6 in site II of cNTnC show S^2 values of 0.68, 0.76, 0.77, 0.78, and 0.83, and these values change to 0.74, 0.84, 0.89, 0.89, and 0.80 upon calcium-binding, as shown in figure 81. In the apo-state, positions 2 - 6 in site I show S^2 values of 0.65, 0.69, 0.71, 0.72, and 0.72 that increase to 0.84, 0.80, 0.74, 0.75, and 0.73 upon Ca^{2+} binding (figure 81). The changes in the binding loops account for +1.0 ± 0.2 and +1.2 ± 0.2 kcal mol^{-1} from sites I and II respectively, of the conformational entropy contribution to the free energy of calcium-binding to site II of cNTnC. These results are consistent with the initial observation that the dominant contribution to the free energy of cooperative calcium-binding to sites I and II in calbindin-D_{9k} arises from stiffening of backbone residues within the flexible loop of calcium-binding site II [115]. Within the β-sheet, the paired residues, Ser37 and Thr71, become more flexible upon calcium-binding. Residues Cys35 and Val72 at the other end of the β-sheet,

on the other hand, become more rigid compared to the apo-state. Thus, entropic changes at one end of the β-sheet cancel those at the other end (Ser37/Thr71 -0.7 ± 0.2 kcal mol^{-1}; Cys35/Asp73 +0.5 ± 0.2 kcal mol^{-1}) upon calcium-binding.

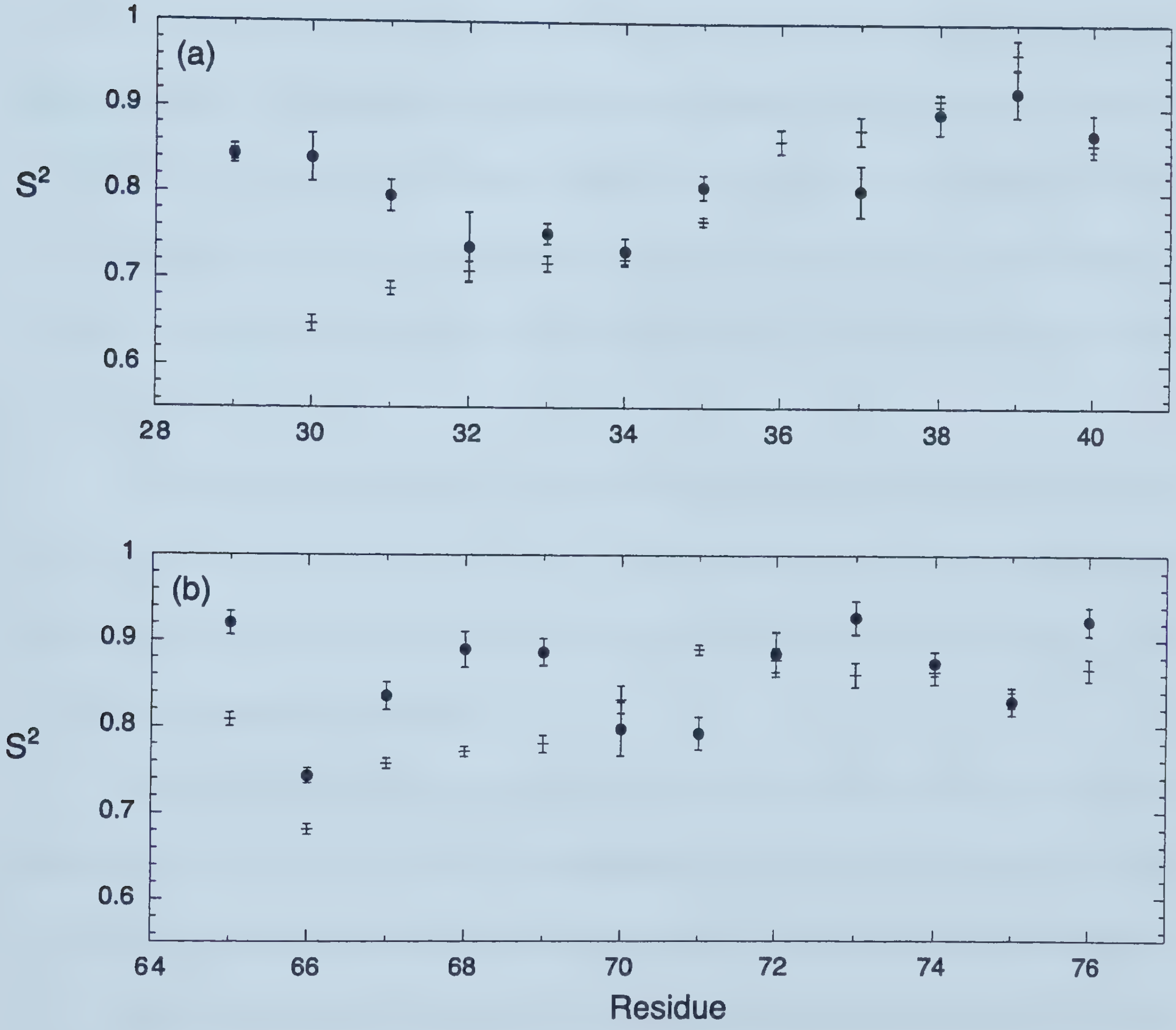

Figure 81. Comparison of S^2 for site I (a) and site II (b) in cNTnC•apo (+) and cNTnC•Ca_2 (●). The average of the 500 and 600 MHz data have been used for cNTnC•apo. The first five positions in site II of cNTnC become more rigid upon calcium binding. Positions 1, 3, and 5 of site II coordinate calcium via side-chain carbonyls.

For the central pair of residues in the β-sheet, relaxation data are available only for Val72, and the S^2 values in the apo and calcium states are similar, indicating that there is no change in flexibility for Val72 upon calcium-binding. The changes in S^2 for the β-sheet upon calcium-binding suggest that the pivot point for the calcium-induced transition in cNTnC occurs at residues Ile36 and Val72 in the β-sheet, and that while the β-sheet was more flexible at Cys35 in the apo-state, it becomes more flexible at the opposite end (residues Ser37 and Thr71) upon calcium-binding. While relaxation data is not available for Ile36 in the calcium-saturated state, we can estimate that the total entropic change for site I does not change if we assume that the changes in S^2 for Ile36 upon Ca^{2+} binding are similar to those for Val72 (Table 18).

The stiffening of the β-sheet at Cys35 is a consequence of stabilizing hydrophobic interactions between Cys35 and Val28/Ala31. This mechanism is an important factor in the coupling of the two calcium-binding sites and allows for the stiffening of positions 1 - 3 in site I when calcium binds in site II.

Another notable change upon calcium-binding is that position 12 in site II becomes significantly more rigid in the calcium-saturated state. Glu76 in site II coordinates calcium *via* its bidentate side-chain and is therefore expected to be more rigid in the calcium state.

Interestingly, position 2 in the active calcium binding site II is observed to be flexible in the calcium-saturated state. This is somewhat surprising considering that the side-chains of residues at positions 1 and 3 are involved in calcium ligation. However, as pointed out by Baldellon et al. [121], position 2 in the second site of calcium-saturated parvalbumin, and the corresponding residue in the C-terminal domain of calcium-saturated calmodulin are also

flexible for these paired E-F hand proteins. It has been proposed that position 2 in the second E-F hand site is a flexible hinge between the helix at the N-terminal end of the calcium-binding site and the remainder of the site [121].

Materials and methods

Sample Preparation

The expression vector for cNTnC (1-89) was engineered as described previously [122]. ^{15}N-labeled protein was expressed in *Escherichia coli* as previously described [25,47]. Purification of the protein was achieved using previously described protocols employed for cleaved sTnC [123]. cNTnC was obtained in the apo-state as previously described for sNTnC [25]. NMR samples contained 500 μL of 9:1 H_2O/D_2O (pH 6.7), 100 mM KCl, 15 mM DTT, 5 mM EDTA, and 1.78 mM protein for cNTnC•apo. Calcium-saturated samples of cNTnC contained 1.3 mL of 9:1 H_2O/D_2O (pH 6.7), 100 mM KCl, 15 mM DTT, 1 mM Ca^{2+}, and ~0.15 mM protein. All NMR samples contained 0.03% NaN_3.

NMR Spectroscopy

NMR spectra were acquired using Varian Unity INOVA 500 MHz or Unity 600 MHz spectrometers equipped with 5 mm triple resonance probes and *z*-axis pulsed field gradients and a Varian Unity 300 MHz spectrometer with a 5 mm inverse broadband probe for cNTnC•apo. For the calcium-saturated protein, NMR spectra were acquired on a Unity

INOVA 500 MHz spectrometer equipped with an 8 mm triple resonance probe with *z*-axis pulsed field gradients. ^{15}N-T$_1$, ^{15}N-T$_2$, and {^{1}H}^{15}N NOE experiments were conducted at 30°C using sensitivity-enhanced gradient pulse sequences developed by Farrow et al. [95] at 500 and 600 MHz and sensitivity-enhanced non-gradient pulse sequences at 300 MHz written in-house (L. Spyracopoulos) that are modified versions of sequences developed by Kördel et al. [124]. For the apo-protein, T$_1$ data were acquired once at 300, 500, and 600 MHz using relaxation delays of 11.1, 55.5, 122.1, 199.8, 277.5, 388.5, 499.5, 666.0, 888.0, and 1254.3 ms. Pulse sequence details are similar to the sNTnC study (chapter 10). ^{15}N-T$_2$ data was acquired once at 300 MHz using delays of 16.6, 33.2, 49.7, 66.3, 82.9, 99.5, 116.1, 132.6 ms, once at 500 MHz using delays of 16.6, 33.2, 49.8, 66.4, 83.0, 99.7, 116.3, 132.9, 149.5, 166.1 ms, and once at 600 MHz using delays of 16.3, 32.6, 48.9, 65.2, 81.4, 97.7, 114.0, 130.3, 146.6, 162.9 ms. For the T$_2$ pulse sequence, the delay between transients was 3 s at 500 MHz and 2.5 s at 300 and 600 MHz, which in conjunction with the field strength of nitrogen pulses and decoupling, drastically reduces the effect of dielectric sample heating due to the radio frequency field, as noted previously (chapter 10). {^{1}H}^{15}N NOE's were measured by recording spectra in the presence and absence of proton saturation. The spectrum recorded without proton saturation was acquired with a delay between transients of 8 s at 300 MHz and 5 s at 500 and 600 MHz. The spectrum recorded in the presence of proton saturation incorporated a relaxation delay of 4.5 s, followed by 3.5 s of proton saturation for a total delay between transients of 8 s at 300 MHz. The 500 and 600 MHz spectra recorded in the presence of proton saturation incorporated a relaxation delay of 2 s, followed by 3 s of proton saturation for a total delay between transients of 5 s.

For the calcium-saturated protein, T_1 data were acquired with relaxation delays of 11.1, 55.5, 122.1, 199.8, 277.5, 388.5, 499.5, 666.0, and 888.0 ms. T_2 data were acquired with relaxation delays of 16.5, 33.03, 49.54, 66.05, 82.57, 99.08, 115.60, 132.11 ms, and a delay between transients of 2.5 s. $\{^1H\}^{15}N$ NOE's were recorded in the same fashion as for cNTnC•apo.

Data processing and analysis

All spectra were processed with the program *NMRPipe* [73]. The superposed orthogonal components of the sensitivity-enhanced two-dimensional free induction decays were sorted and processed with the *ranceY.M* macro within the *NMRPipe* software. As noted previously, post-acquisition processing of the t_2 interferograms for removal of residual water was not necessary, except for the ^{15}N-T_2 spectra measured at 300 MHz. For cNTnC•apo, 90°-shifted sine and sine-squared window functions were applied in t_2 and t_1, respectively. Linear prediction was employed to extend the t_1 domain by half the number of experimental points. The t_2 and t_1 domains were extended to twice the number of points with zero-filling. Baseline correction was performed with an automatic polynomial subtraction in the F_2 and F_1 domains, and the region upfield of 6.5 ppm in the F_2 dimension was discarded. Peak-picking was done in the same fashion as for sNTnC•apo (chapter 10). T_1 and T_2 values were obtained by non-linear least squares fits of the amide crosspeak intensities to a two-parameter exponential decay using software provided by Lewis E. Kay, except for T_1^{300} values, which were obtained from non-linear least squares fits of the amide crosspeak intensities to three-

parameter exponential decays using the *xcrvfit* program (R. Boyko, executable available at the following address: http://www.pence.ualbetra.ca). Uncertainties in the measured T_1 and T_2 data were obtained from the non-linear least squares fits. Uncertainties in the NOE values were estimated from the baseline noise in the 2D {^{1}H-^{15}N}-HSQC spectra recorded with and without proton saturation.

SECTION FOUR: DISCUSSION

14. To open or not to open? That was the question! 195

15. To be flexible or not to be flexible? That is the question! 201

16. Future studies 205

17. And the morale of this tale is... 210

14. TO OPEN OR NOT TO OPEN? THAT WAS THE QUESTION!

Transient increases in intracellular calcium concentration in striated muscle cells are recognized by the thin filament proteins to regulate muscle contraction. This cascade of events is initiated by calcium binding to TnC. The resultant signal is transmitted to the other members of the thin filament (troponin I, troponin T, tropomyosin, and actin), which in turn modifies the interaction between the thick and thin filaments, leading to muscle contraction (chapters 2 and 3).

TnC is an 18 kD protein and is a member of the family of EF-hand calcium binding proteins (chapter 4). Two isoforms of TnC exist in striated muscle, skeletal muscle TnC (sTnC) and cardiac muscle TnC (cTnC). Both molecules comprise four putative EF-hand helix-loop-helix motifs as potential calcium binding sites (I-IV), except that site I in cTnC is inactive. Sites I and II are paired as a unit in the N-terminal half and sites III and IV form another pair in the C-terminal half of the molecule. Sites III and IV bind calcium ($K_{Ca} \sim 10^7$ M^{-1}) with high affinity and are believed to be always occupied by either calcium or magnesium ($K_{Mg} \sim 10^3$ M^{-1}) under physiological conditions for a structural role, whereas calcium binds to sites I and II with lower affinity ($K_{Ca} \sim 10^5$ M^{-1}) and regulates muscle contraction.

The first three dimensional structure of TnC was solved by X-ray crystallography in 1985 [26, 27]. In this structure the regulatory calcium-binding sites were unoccupied, and no calcium bound X-ray structure was solved for another dozen years. During this time, it

became feasible to determine the three dimensional structures of proteins in solution using NMR techniques [125, 126]. Several factors expedited the rapid growth and success of NMR into structural studies of TnC. Firstly, the recognition that individual synthetic helix-loop-helix calcium-binding peptides spontaneously folded into paired calcium binding sites opened the door to the study of homo- and hetero-dimeric TnC peptides. Secondly, the availability of separate N- and C-terminal domains obtained by proteolytic digestion and molecular biology provided functional proteins of ideal size for 2D NMR methods. Thirdly, the advent of multidimensional multinuclear NMR methods in concert with isotope labeling with ^{13}C, ^{15}N, and ^{2}H using expression in *E. coli* extended the upper molecular weight limit accessible to NMR to include molecules as big as TnC. In the intervening dozen years since the first X-ray structure, a large number of TnC solution NMR structures in different states have been solved. In addition to the III-III homodimer, the IV-IV homodimer, the III-IV heterodimer, and the TR_1C fragment (chapter 4), these include the NMR solution structures of intact sTnC in the calcium-saturated state and of the N-terminal domain of sTnC in both apo and calcium-saturated states (chapter 5), of the E41A mutant of sNTnC in the calcium saturated state (chapter 6), of cTnC in its calcium-saturated state and the N-terminal regulatory domain of cTnC in both apo and calcium-saturated states (chapter 8). These structures have defined the calcium-induced structural changes in TnC, elucidated the mechanism of the linkage between calcium-binding and the concomitant conformational changes, and delineated the important structural differences between skeletal and cardiac TnC's.

The HMJ model (1986) was the first to propose that the calcium-induced structural change in the regulatory domain of TnC involved an opening of the structure (chapter 4). This structural change involves movement of the B/C helices away from the A/D helices. The opening of the structure exposes a large hydrophobic patch which is believed to interact with another muscle protein, TnI, and trigger muscle contraction. The NMR data on avian skeletal TnC (1995) supports the central paradigm of the close-to-open transition, but indicated that the calcium-induced opening is larger than first expected (chapter 5). This large opening is in agreement with the recent X-ray data of Strynadka et al. (chapter 5). Other X-ray structures of the N-domain of sTnC have also been recently solved, and displayed an open conformation. The extent of the calcium-induced opening of sTnC is best characterized by the A/B and C/D interhelical angles which change by ~50° and ~70°, respectively, upon calcium-binding.

In order to obtain insight into the mechanism of regulation within sTnC, that is, the coupling between calcium binding and subsequent structural change, I studied the structure of a calcium-bound mutant of sNTnC, E41A-sNTnC•Ca_2 (chapter 6). In this mutant, the bidentate ligand to the calcium in site I (E41) was removed. The initial goal was to explore the contribution of site I into the calcium induced structural change by making site I defunct. The calcium titration of E41A-sNTnC revealed that despite removal of the bidentate ligand, site I was still able to bind calcium although with a diminished affinity (K_d = 1-2 mM) (chapter 6).

The structure of E41A-sNTnC•Ca_2 remains closed upon calcium binding, indicating that the linkage between calcium-binding and the induced conformational change has been

broken. This provides a snapshot of sTnC between the off and the on state. Comparison of the helix packing in E41A-sNTnC•Ca_2 with sNTnC•apo and sNTnC•Ca_2 reveals valuable information. The interhelical angles of E41A-NTnC•Ca_2 are like the apo forms rather than the Ca_2 form. Therefore, the hydrophobic patch is not exposed upon calcium-binding unless the bidentate ligand in site I (E41) is involved into calcium-coordination. Although several factors contribute to the triggering mechanism, the opening of the sNTnC structure is ultimately dependent, in a temporal and energy balance sense, on one amino acid; Glu41 (chapter 7).

The structural study of calcium-bound E41A-sNTnC also provided a first model for the possible calcium-induced structural change in cTnC because of its similar calcium-binding properties (i.e. only site II was a fully active calcium-binding site). The speculation that cNTnC might behave like E41A-sNTnC were soon confirmed by the solution structures of cTnC and cNTnC (chapter 8). Unlike sTnC, the calcium-induced structural change in the N-domain of cTnC did not involve an opening of the structure and concomitant exposure of the hydrophobic patch.

The substantially reduced hydrophobic surface exposure of calcium-saturated cTnC has important implications for the binding of cardiac TnI with cTnC. It is possible that the mode of interaction between TnI and TnC in cardiac muscle is in fact different from that in skeletal muscle. On the other hand, it is possible that the calcium dependent binding of cardiac TnI forces open the regulatory domain of cTnC, with the end result being that the cardiac TnI-TnC complex binds in a similar fashion to skeletal TnC-TnI. At present, there

is no compelling evidence to either favor or discount either model for cardiac TnC-TnI interaction.

The compact structure of cNTnC•Ca_1 provides a structural precedent for a calcium-binding regulatory protein in which one of the two sites in the paired set of EF-hands is inactive. This unique structural feature sets cTnC apart from other 'calcium sensor' EF-hand calcium-binding proteins, such as sTnC and calmodulin, as well as 'calcium buffer' EF-hand proteins such as parvalbumin and calbindin. It has been generally believed that calcium binding to calcium sensor proteins involves large conformational changes accompanying an exposure of a large hydrophobic surface, allowing the protein to interact with targets to accomplish regulatory functions, whereas the capture of calcium ions by calcium buffer proteins is accompanied by only minor conformational changes. cTnC is the first example of isolated calcium sensor proteins which does not undergo major calcium-induced structural changes. Very recently, the structures of calpain small domain [127, 128], calcyclin [94], and S100B [91-93] proteins in calcium-saturated states have been shown to be in the 'closed' conformations.

One question has to be asked. Are all those structures giving us the complete story? The answer is NON!

I have shown that all four structures which have been solved for the regulatory domain of sTnC in the calcium-bound state have a different level of opening. Clearly, this indicates that a single fixed structure does not provide an accurate representation. I will expand on this in the next chapter.

I have shown closed conformation for E41A-sNTnC•Ca_2 and cNTnC•Ca_1. There is still the question of whether an open state is involved for those proteins. The correlation time for those proteins was found to increase from about 5 ns in the apo state to between 6 and 7 ns in the calcium-bound state. The correlation time for this calcium-bound proteins was also found to be concentration dependent. This suggest partial dimerization, which has traditionally been associated with an open state. Also, the recent work of Leo Spyracopoulos an Monica Li on a cNTnC•Ca_1:cTnI$_{147\text{-}163}$ complex has revealed an open conformation. Therefore I think that the open state is populated for both E41A-sNTnC•Ca_2 and cNTnC•Ca_1, but because of limitations to the technique used for structural determinations, we have failed to observed that.

15. TO BE FLEXIBLE OR NOT TO BE FLEXIBLE? THAT IS THE QUESTION!

NMR and X-ray crystallography are powerful structural techniques, and the number of protein structures solved by these methods increases every years. Although structures provide a generous amount of information on a particular system, an important aspect is often neglected: dynamics. Even in a family of NMR structures, true flexibility information can rarely be extracted. It is however important to characterize the dynamics of a system, as this can provide information on energetics and on populated conformations which might not be seen in a static structure. There are several aspects of dynamics which can be of interest for function.

Backbone and side-chain dynamics

Chapters 10 to 12 presented a characterization of the backbone and side-chain dynamics properties of sNTnC•apo, and chapter 13 presented the backbone dynamics of cNTnC•apo and cNTnC•Ca_2. Based on the dynamic characteristics of sNTnC•apo, two different levels of 'fine tuning' of the calcium affinity were extracted. First, the affinity is directly adjusted by the amount of flexibility present in the calcium binding loops of the apo form. Significantly lower backbone order parameters (S^2) were observed for calcium binding site I relative to site II, and the contribution of the bond vector fluctuations to the conformational entropy of sites I and II was calculated. The conformational entropy loss due to calcium binding ($\Delta\Delta S_p$) differs by 1 kcal mol^{-1} between sites I and II. This is consistent

with the different dissociation constants previously measured for sites I and II of 16 μM and 1.7 μM, respectively. This difference in conformational entropy between the two sites has therefore a major contribution to the difference in calcium affinity between the two sites.

Since the binding of calcium triggers a large conformational change, a second and indirect level of 'fine tuning' occurs in the apo state through the degree of flexibility of hydrophobic residues which are exposed upon calcium binding. My results show that in sNTnC it is not necessarily the side-chains which are more buried in the apo state which have reduced motion, but often the ones which will be exposed upon calcium binding. It is clear from this work that a complete determination of the dynamic characteristic is necessary in order to fully understand how sTnC and other proteins are 'fine tuned' to appropriately carry their function.

A flexible open state?

A general feature emerges when we compare the sTnC structures obtained by NMR and X-ray; the average NMR structure is often more open than the X-ray structures. First, the average NMR structure is more open than the X-ray structures. Second, the X-ray structures cover a range of interhelical angles. In the following, I explore the causes and possible implications related to this finding..

First of all, I must say that defining the interhelical orientation in the open form is difficult using NMR, at least when using standard NMR structure determination approaches. The reason for this is that the open structure has a very limited number of interhelical

contacts shorter than 5Å, and therefore the number of observed long range interhelical NOEs is modest. This is the principal reason why the interhelical angles cover a range of 15-20° in most NMR structures of TnC. Despite the fact that the opening is not well defined in the NMR structures, this does not necessarily mean they are inconsistent with the X-ray structure. When comparing the range of interhelical angles which is observed in the NMR structures with the crystal structure, one finds that the X-ray structure is in the range covered by the NMR family of structures, usually at the most closed extremity. This is best illustrated for the C/D interhelical angle of the calcium bound N-domain of sTnC. Figure 82 compares the distribution of this interhelical angle in the NMR structures with the corresponding X-ray structures. This figure is consistent with a flexible open state where the crystal structures would correspond to the most compact open form.

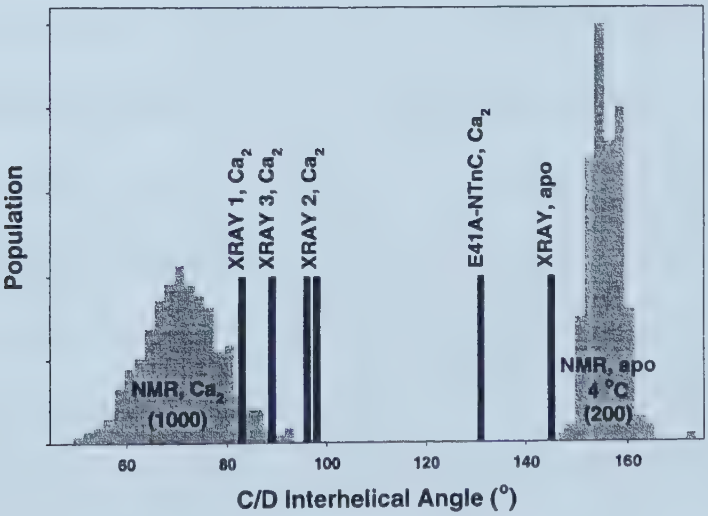

Figure 82. Distribution of the C-D inter-helical angle for the various structures of the N-domain of sTnC. 1000 structures were calculated for NMR-Ca_2, XRAY1 is the Strynadka et al. X-ray structure, XRAY2 are the Cohen et al. structure, XRAY3 is the Phillips et al. structure, NMR-apo-4°C is a low temperature NMR structure solved by Sakae Tsuda (personal communication), E41A-NTnC•Ca_2 is the structure of the sNTnC E41A mutant which will be presented in the next chapter.

Although we cannot directly interpret the lack of definition in the NMR structures as true flexibility, the question still exists; is the open form flexible in terms of interhelical arrangement? The NOE data would not be significantly different whether the open form is rigid or covers a range of 15-20° in interhelical angles. Thus NMR structural data has not yet provided an answer to the question in this case. Interestingly, experimental data which supports a flexible open form come from X-ray crystallography [61, 62]. As can be seen in figure 82, the C-D interhelical angle varies significantly amongst the crystal structures.

The notion of a flexible open state is actually not without sense. The major determinant which keeps helices packed together in globular proteins is the favorable interactions between the helices (usually involving hydrophobic amino acids). In the open form of the N-domain of sTnC, the A/B and C/D helices do not make favorable contacts for the most part. Therefore the limited number of interhelical interaction is likely too small to hold these helices together. Flexibility may also be desirable for function.

It is interesting to note that TnC was not really made to be in an open state with an empty hydrophobic patch. In fact, the population of the empty open state is most probably insignificant in muscle. TnI, being already located just a few angstroms away from the regulatory domain of TnC, is readily available for binding to the hydrophobic patch once the calcium induced conformation change occurs.

16. FUTURE STUDIES

As with most research studies, every answer brings new questions. There are still lots to learn about the troponin system.

Future structural studies

Regarding structural studies of TnC alone, the field is quite mature. The next step will be to tackle the troponin complex (figure 83).

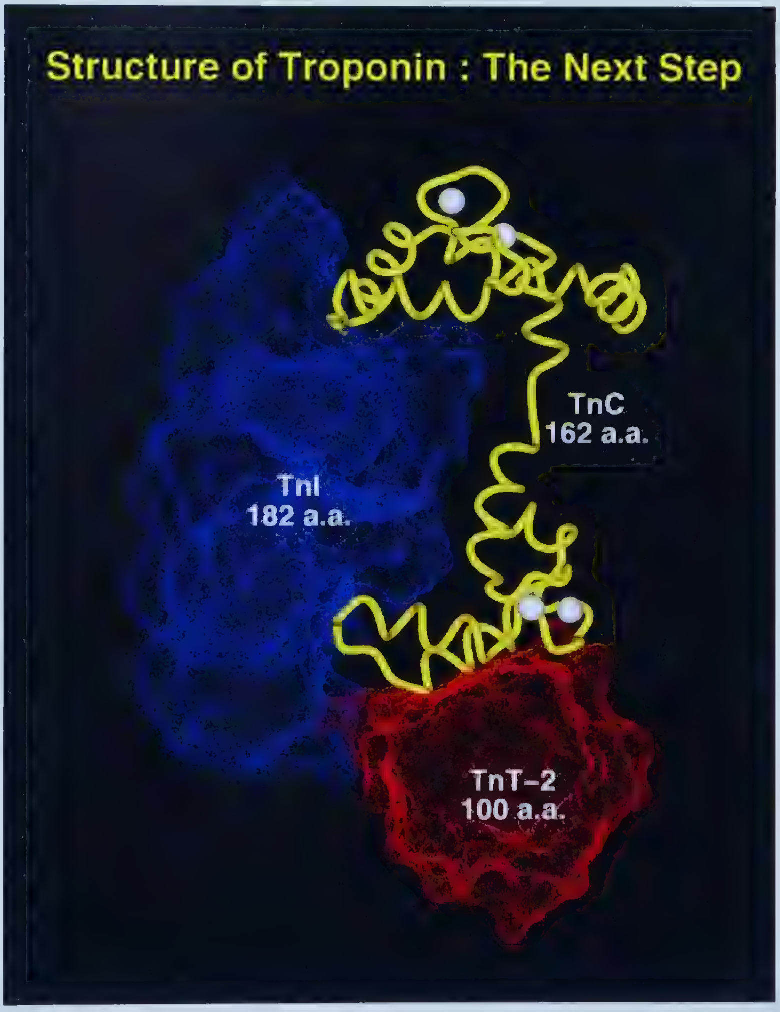

Figure 83. Representation of the troponin 'core' complex. Currently, only TnC and some small TnI fragments have had their structure solved.

A significant step toward this troponin complex goal was achieved by the Maéda group earlier this year when they published an X-ray structure of the sTnC:sTnI$_{1-47}$ complex (figure 84) [9]. Leo Spyracopoulos and Monica Li have recently solved the NMR structure of the cNTnC:cTnI$_{147-163}$ complex (figure 85).

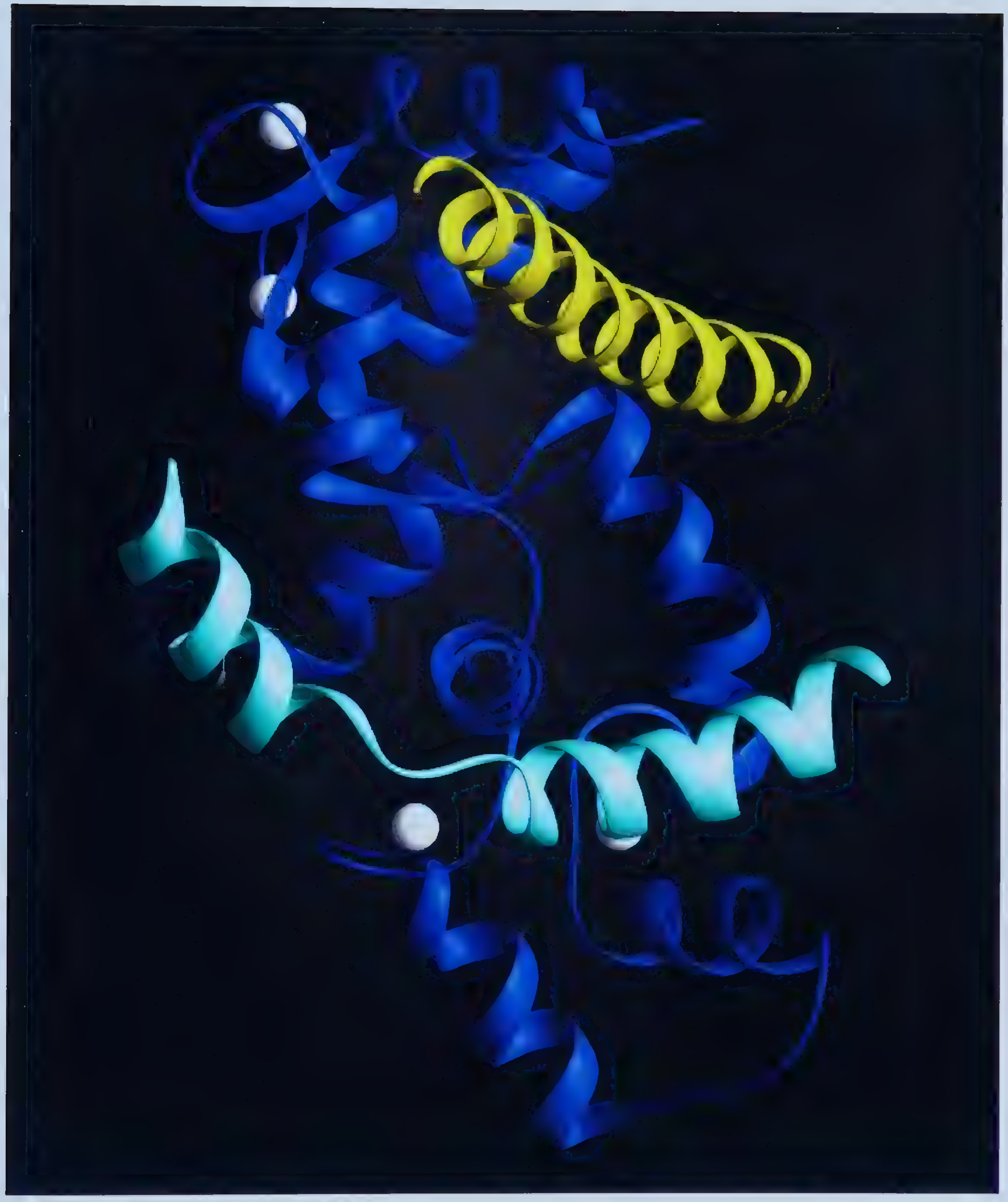

Figure 84. sTnC•Ca$_4$:sTnI$_{1\text{-}47,\mathrm{reg}}$ complex. The structure of sTnC•Ca$_2$:sTnI$_{1\text{-}47}$ was solved by X-ray. In that structure, the N-domain was in the apo form and therefore in the closed conformation. Shown here is a model of sTnC•Ca$_4$:sTnI$_{1\text{-}47,\mathrm{reg}}$ provided by the Maéda group. They have modeled the regulatory region of sTnI into an open structure of the regulatory domain of sTnC. Note that their model is based on my structure of sNTnC•Ca$_2$. Shown in blue is TnC with the N-domain in the lower part, in the same orientation used along the thesis. The TnI$_{1\text{-}47}$ and TnI$_{\mathrm{reg}}$ are shown in yellow and white, respectively.

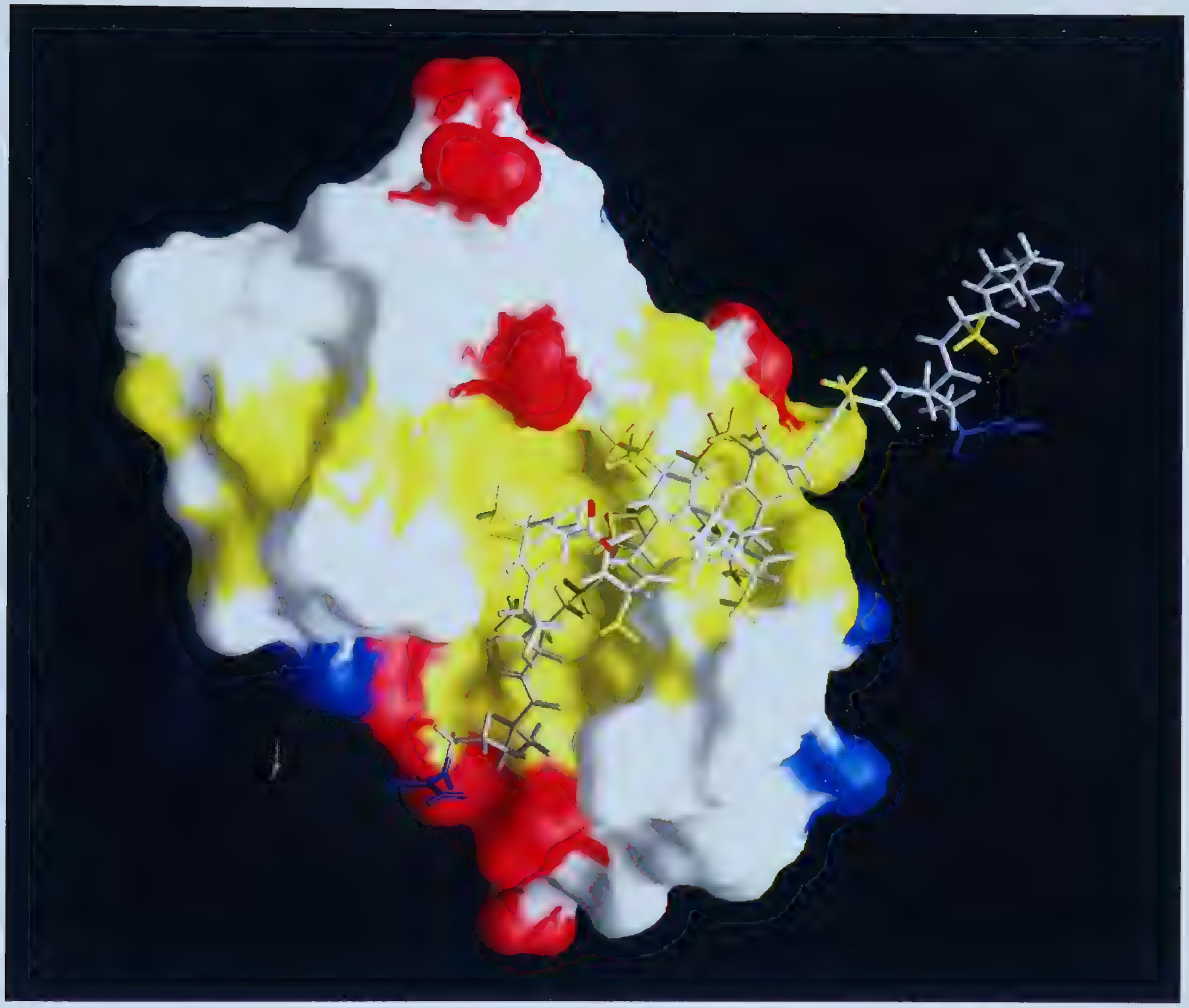

Figure 85. Structure of cNTnC•Ca$_1$ (GRASP surface) complexed with cTnI$_{147\text{-}163}$ (stick representation). cNTnC•Ca$_1$ is in the usual orientation, with helix D coming out of the page. The yellow surface indicates hydrophobic residues.

Earlier this year, I acquired preliminary spectra of a large sTnC:sTnI$_{1\text{-}116}$:sTnT$_{157\text{-}263}$ (figure 86). This is a 43kD complex. Trough a proper choice of labeling, it will be possible to study the structure of complexes like this. With triple labeled samples (^{2}H, ^{15}N, and ^{13}C) and some of the new NMR techniques available, it will be possible to study the structure of the whole troponin complex by NMR.

TnC:TnI$_{1-116}$:TnT$_{157-263}$
^{1}H-1D-NMR spectra as a function of temperature
Spectral region shown: Gly$_{HN}$ from each Ca^{++}-binding loops (TnC)

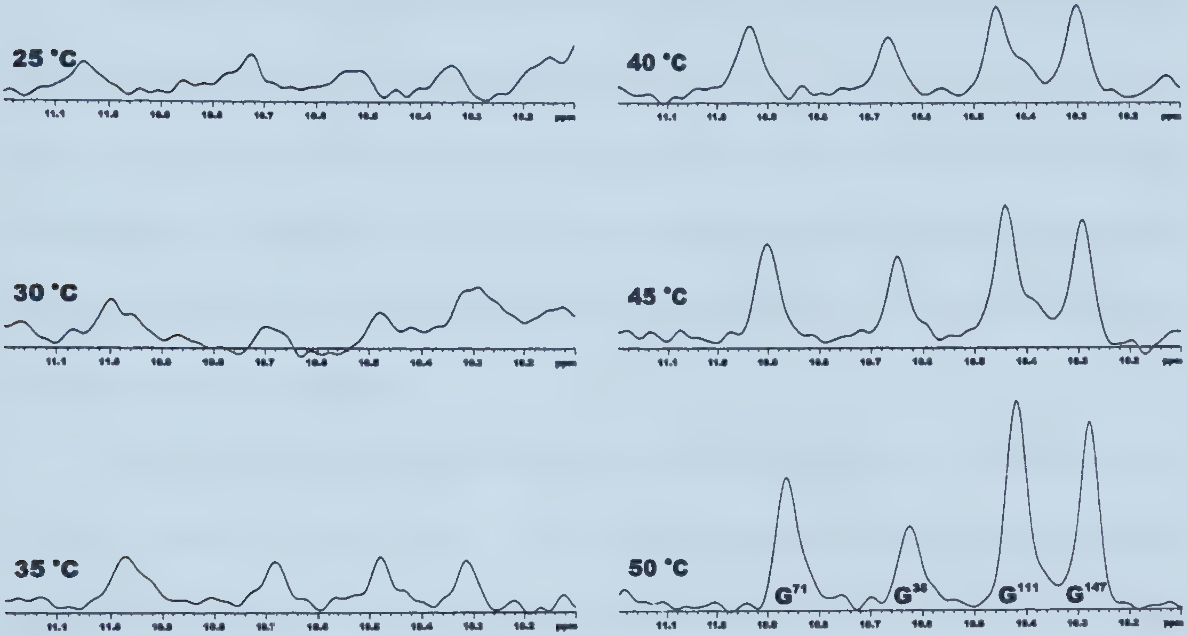

Figure 86.

Dynamics studies

There is still lots to learn about the dynamics of the TnC system. One element which is missing in this thesis is the relaxation data of sNTnC•Ca_2. This data will first allow the confirmation (or the refutation) of some of the conclusions I have made. It will also provide a more complete information on the relation between dynamics and function. Side-chain dynamics will also be very informative when available for sNTnC•Ca_2 and for sNTnC•Ca_2 in complex with TnI fragments.

Perhaps one of the most interesting aspect of the dynamics of TnC which deserves attention is the large scale motions. Could NMR characterize the flexible open state discussed in chapter 15? I believe so. Perhaps the new residual dipolar coupling technique would be the best approach for this. Recently, David Weber used this technique to define the orientation of helix C in S100β•apo, as this orientation of this helix could not be properly defined by traditional NMR approach (D. Weber, personal communication).

17. AND THE MORALE OF THIS TALE IS ...

The person who attempts to interpret or publish NMR structures without relaxation data does so at his own peril.

REFERENCES

1. Celio M.R., Pauls T.L. & Schwaller B.: *Guidebook to the calcium-binding proteins*, New York: Oxford University Press Inc.; 1996.
2. Gagné, Stéphane M.: **Calcium-induced structural changes in the regulation domain of troponin-C by multidimensional NMR spectroscopy**. *University of Alberta* 1994. Ref Type: Thesis/Dissertation
3. Rayment I., Rypniewski W.R., Schmidt-Base K., Smith R., Tomchick D.R., Benning M.M., Winkelmann D.A., Wesenberg G. & Holden H.M.: **Three-dimensional structure of myosin subfragment-1: a molecular motor**. *Science* 1993, **261**:50-58.
4. Kabsch W., Mannherz H.G., Suck D., Pai E.F. & Holmes K.C.: **Atomic structure of the actin:DNase I complex**. *Nature* 1990, **347**:37-44.
5. Flicker P.F., Phillips G.N.J. & Cohen C.: **Troponin and its interactions with tropomyosin. An electron microscope study**. *J.Mol.Biol.* 1982, **162**:495-501.
6. Mak A.S. & Smillie L.B.: **Structural interpretation of the two-site binding of troponin on the muscle thin filament**. *J.Mol.Biol.* 1981, **149**:541-550.
7. White S.P., Cohen C. & Phillips G.N., Jr.: **Structure of co-crystals of tropomyosin and troponin**. *Nature* 1987, **325**:826-828.
8. Pearlstone J.R. & Smillie L.B.: **Troponin T fragments: physical properties and binding to troponin C**. *Can.J.Biochem.* 1978, **56**:521-527.
9. Vassylyev D.G., Takeda S., Wakatsuki S., Maeda K. & Maeda Y.: **Crystal structure of troponin C in complex with troponin I fragment at 2.3-Å resolution**. *Proc.Natl.Acad.Sci.U.S.A.* 1998, **95**:4847-4852.
10. Farah C.S. & Reinach F.C.: **The troponin complex and regulation of muscle contraction**. *FASEB J.* 1995, **9**:755-767.
11. van Eerd J.P. & Takahashi K.: **The amino acid sequence of bovine cardiac tamponin-C. Comparison with rabbit skeletal troponin-C.** *Biochem.Biophys.Res.Commun.* 1975, **64**:122-127.
12. Herzberg O. & James M.N.: **Refined crystal structure of troponin C from turkey skeletal muscle at 2.0 Å resolution**. *J.Mol.Biol.* 1988, **203**:761-779.

13. Satyshur K.A., Pyzalska D., Greaser M., Rao S.T. & Sundaralingam M.: **Structure of chicken skeletal muscle troponin C at 1.78 Å resolution**. *Acta Crystallographica Section D* 1994, **D50**:40-49.

14. Kretsinger R.H.: **Structure and evolution of calcium-modulated proteins**. *CRC Crit.Rev.Biochem.* 1980, **8**:119-174.

15. Strynadka N.C.J. & James M.N.G.: **Crystal structures of the helix-loop-helix calcium-binding proteins**. *Annu.Rev.Biochem.* 1989, **58**:951-998.

16. Ebashi S.: *Nature* 1963, **200**:1010

17. Ebashi S. & Ebashi F.: *J.Biochem.(Tokyo)* 1964, **55**:604-613.

18. Ebashi S. & Kodama A.: *J.Biochem.(Tokyo)* 1965, **58**:107-108.

19. Hartshorne D.J. & Mueller H.: **Fractionation of troponin into two distinct proteins**. *Biochem.Biophys.Res.Commun.* 1968, **31**:647-653.

20. Schaub M.C. & Perry S.V.: **The relaxing protein system of striated muscle. Resolution of the troponin complex into inhibitory and calcium ion-sensitizing factors and their relationship to tropomyosin**. *Biochem.J.* 1969, **115**:993-1004.

21. Schaub M.C., Perry S.V. & Hacker W.: **The regulatory proteins of the myofibril. Characterization and biological activity of the calcium-sensitizing factor (troponin A)**. *Biochem.J.* 1972, **126**:237-249.

22. Greaser M.L. & Gergely J.: **Purification and properties of the components from troponin**. *J.Biol.Chem.* 1973, **248**:2125-2133.

23. Greaser M.L. & Gergely J.: **Reconstitution of troponin activity from three protein components**. *J.Biol.Chem.* 1971, **246**:4226-4233.

24. Murray A.C. & Kay C.M.: **Hydrodynamic and optical properties of troponin A. Demonstration of a conformational change upon binding calcium ion**. *Biochemistry* 1972, **11**:2622-2627.

25. Li M.X., Gagné S.M., Tsuda S., Kay C.M., Smillie L.B. & Sykes B.D.: **Calcium binding to the regulatory N-domain of skeletal muscle troponin C occurs in a stepwise manner**. *Biochemistry* 1995, **34**:8330-8340.

26. Herzberg O. & James M.N.: **Structure of the calcium regulatory muscle protein troponin-C at 2.8 Å resolution** . *Nature* 1985, **313**:653-659.

27. Sundaralingam M., Bergstrom R., Strasburg G., Rao S.T., Roychowdhury P., Greaser M. & Wang B.C.: **Molecular structure of troponin C from chicken skeletal muscle at 3-angstrom resolution**. *Science* 1985, **227**:945-948.

28. Satyshur K.A., Rao S.T., Pyzalska D., Drendel W., Greaser M. & Sundaralingam: **Refined structure of chicken skeletal muscle troponin C in the two-calcium state at 2-Å resolution**. *J.Biol.Chem.* 1988, **263**:1628-1647.

29. Shaw G.S., Hodges R.S. & Sykes B.D.: **Calcium-induced peptide association to form an intact protein domain: ^{1}H NMR structural evidence**. *Science* 1990, **249**:280-283.

30. Kay L.E., Forman-Kay J.D., McCubbin W.D. & Kay C.M.: **Solution structure of a polypeptide dimer comprising the fourth Ca^{2+}-binding site of troponin C by nuclear magnetic resonance spectroscopy**. *Biochemistry* 1991, **30**:4323-4333.

31. Shaw G.S., Hodges R.S. & Sykes B.D.: **Determination of the solution structure of a synthetic two-site calcium-binding homodimeric protein domain by NMR spectroscopy**. *Biochemistry* 1992, **31**:9572-9580.

32. Shaw G.S. & Sykes B.D.: **NMR solution structure of a synthetic troponin C heterodimeric domain**. *Biochemistry* 1996, **35**:7429-7438.

33. Findlay W.A., Sönnichsen F.D. & Sykes B.D.: **Solution structure of the TR_1C fragment of skeletal muscle troponin-C**. *J.Biol.Chem.* 1994, **269**:6773-6778.

34. Evans J.S., Levine B.A., Leavis P.C., Gergely J., Grabarek Z. & Drabikowski W.: **Proton magnetic resonance studies on proteolytic fragments of troponin-C. Structural homology with the native molecule**. *Biochim.Biophys.Acta* 1980, **623**:10-20.

35. Levine B.A., Coffman D.M. & Thornton J.M.: **Calcium binding by troponin-C. A proton magnetic resonance study**. *J.Mol.Biol.* 1977, **115**:743-760.

36. Levine B.A., Thornton J.M., Fernandes R., Kelly C.M. & Mercola D.: **Comparison of the calcium- and magnesium-induced structural changes of troponin-C. A proton magnetic resonance study**. *Biochim.Biophys.Acta* 1978, **535**:11-24.

37. Seamon K.B., Hartshorne D.J. & Bothner-By A.A.: **Ca^{2+} and Mg^{2+} dependent conformations of troponin C as determined by ^{1}H and ^{19}F nuclear magnetic resonance**. *Biochemistry* 1977, **16**:4039-4046.

38. Tsuda S., Hasegawa Y., Yoshida M., Yagi K. & Hikichi K.: **Nuclear magnetic resonance study on rabbit skeletal troponin C: calcium-induced conformational change**. *Biochemistry* 1988, **27**:4120-4126.

39. Tsuda S., Ogura K., Hasegawa Y., Yagi K. & Hikichi K.: **^{1}H NMR study of rabbit skeletal muscle troponin C: Mg^{2+}-induced conformational change**. *Biochemistry* 1990, **29**:4951-4958.

40. Carew E.B., Leavis P.C., Stanley H.E. & Gergely J.: **A laser Raman spectroscopic study of Ca^{2+} binding to troponin C**. *Biophys.J.* 1980, **30**:351-358.

41. Nagy B. & Gergely J.: **Extent and localization of conformational changes in troponin C caused by calcium binding. Spectral studies in the presence and absence of 6 M urea**. *J.Biol.Chem.* 1979, **254**:12732-12737.

42. Leavis P.C., Nagy B., Lehrer S.S., Bialkowska H. & Gergely J.: **Terbium binding to troponin C: binding stoichiometry and structural changes induced in the protein**. *Arch.Biochem.Biophys.* 1980, **200**:17-21.

43. Leavis P.C., Rosenfeld S.S., Gergely J., Grabarek Z. & Drabikowski W.: **Proteolytic fragments of troponin C. Localization of high and low affinity Ca^{2+} binding sites and interactions with troponin I and troponin T**. *J.Biol.Chem.* 1978, **253**:5452-5459.

44. Johnson J.D. & Potter J.D.: **Detection of two classes of Ca^{2+} binding sites in troponin C with circular dichroism and tyrosine fluorescence**. *J.Biol.Chem.* 1978, **253**:3775-3777.

45. Hincke M.T., McCubbin W.D. & Kay C.M.: **Calcium-binding properties of cardiac and skeletal troponin C as determined by circular dichroism and ultraviolet difference spectroscopy**. *Can.J.Biochem.* 1978, **56**:384-395.

46. Li M.X., Chandra M., Pearlstone J.R., Racher K.I., Trigo-Gonzalez G., Borgford T., Kay C.M. & Smillie L.B.: **Properties of isolated recombinant N and C domains of chicken troponin C**. *Biochemistry* 1994, **33**:917-925.

47. Gagné S.M., Tsuda S., Li M.X., Chandra M., Smillie L.B. & Sykes B.D.: **Quantification of the calcium-induced secondary structural changes in the regulatory domain of troponin-C**. *Protein Sci.* 1994, **3**:1961-1974.

48. Herzberg O., Moult J. & James M.N.: **A model for the Ca^{2+}-induced conformational transition of troponin C. A trigger for muscle contraction**. *J.Biol.Chem.* 1986, **261**:2638-2644.

49. Slupsky C.M., Kay C.M., Reinach F.C., Smillie L.B. & Sykes B.D.: **Calcium-induced dimerization of troponin C: mode of interaction and use of trifluoroethanol as a denaturant of quaternary structure**. *Biochemistry* 1995, **34**:7365-7375.

50. Burgering M.J.M., Boelens R., Caffrey M., Breg J.N. & Kaptein R.: **Observation of inter-subunit nuclear Overhauser effects in a dimeric protein**. *FEBS Lett.* 1993, **330**:105-109.

51. Laskowski R.A., MacArthur M.W., Moss D.S. & Thornton J.M.: **PROCHECK: A program to check the stereochemical quality of protein structures**. *J.appl.Crystallogr.* 1993, **26**:283-290.

52. Jeener J., Meier B.H., Bachmann P. & Ernst R.R.: **Investigation of exchange processes by two dimensional NMR spectroscopy**. *J.Chem.Phys.* 1979, **71**:4546-4553.

53. Macura S. & Ernst R.R.: **Elucidation of cross relaxation in liquids by two-dimensional NMR spectroscopy**. *Molec.Phys.* 1980, **41**:95-117.

54. Kay L.E., Marion D. & Bax A.: **Practical aspects of 3D heteronuclear NMR of proteins**. *J.Magn.Res.* 1989, **84**:72-84.

55. Ikura M., Kay L.E., Tschudin R. & Bax A.: **Three-dimensional NOESY-HMQC spectroscopy of a ^{13}C-labeled protein**. *J.Magn.Res.* 1990, **86**:204-209.

56. Kay L.E. & Bax A.: **New methods for the measurement of NH-C_αH coupling constants in ^{15}N-labeled proteins**. *J.Magn.Res.* 1990, **86**:110-126.

57. Sykes B.D., Slupsky C.M., Wishart D.S., Sönnichsen F.D. & Gagné S.M.: **On the use of NMR in complex biological systems: NMR studies of calcium sensitive interactions amongst muscle proteins.** In *NMR as a structural tool for macromolecules: current status and future directions*, Edited by Nageswara BD, Kemple MD. New York: Plenum Press; 1996:275-284.

58. Havel T.F.: **An evaluation of computational strategies for use in the determination of protein structure from distance constraints obtained by nuclear magnetic resonance**. *Prog.Biophys.Mol.Biol.* 1991, **56**:45-78.

59. Slupsky C.M. & Sykes B.D.: **NMR solution structure of calcium-saturated skeletal muscle troponin C**. *Biochemistry* 1995, **34**:15953-15964.

60. Barbato G., Ikura M., Kay L.E., Pastor R.W. & Bax A.: **Backbone dynamics of calmodulin studied by ^{15}N relaxation using inverse detected two-dimensional NMR spectroscopy: the central helix is flexible**. *Biochemistry* 1992, **31**:5269-5278.

61. Strynadka N.C.J., Cherney M., Sielecki A.R., Li M.X., Smillie L.B. & James M.N.G.: **Structural details of a calcium-induced molecular switch: X-ray crystallographic analysis of the calcium-saturated N-terminal domain of troponin C at 1.75 Å resolution**. *J.Mol.Biol.* 1997, **273**:238-255.

62. Houdusse A., Love M.L., Dominguez R., Grabarek Z. & Cohen C.: **Structures of four Ca^{2+}-bound troponin C at 2.0 Å resolution: further insights into the Ca^{2+}-switch in the calmodulin superfamily**. *Structure* 1997, **5**:1695-1711.

63. Gagné S.M., Tsuda S., Li M.X., Smillie L.B. & Sykes B.D.: **Structures of the troponin C regulatory domains in the apo and calcium-saturated states.** *Nat.Struct.Biol.* 1995, **2**:784-789.

64. Li M.X., Gagné S.M., Spyracopoulos L., Kloks C.P., Audette G., Chandra M., Solaro R.J., Smillie L.B. & Sykes B.D.: **NMR studies of Ca^{2+} binding to the**

regulatory domains of cardiac and E41A skeletal muscle troponin C reveal the importance of site I to energetics of the induced structural changes. *Biochemistry* 1997, **36**:12519-12525.

65. Shrake A. & Rupley J.A.: **Environment and exposure to solvent of protein atoms. Lysozyme and insulin**. *J.Mol.Biol.* 1973, **79**:351-371.

66. Service R.F.: **Flexing muscle with just one amino acid**. *Science* 1996, **271**:31

67. Muhandiram D.R. & Kay L.E.: **Gradient-enhanced triple-resonance three-dimensional NMR experiments with improved sensitivity.** *Journal of Magnetic Resonance* 1994, **B103**:203-216.

68. Zhang O., Kay L.E., Olivier J.P. & Forman-Kay J.D.: **Backbone ^{1}H and ^{15}N resonance assignments of the N-terminal SH3 domain of drk in folded and unfolded states using enhanced-sensitivity pulsed field gradient NMR techniques.** *J.Biomol.NMR* 1994, **4**:845-858.

69. Kay L.E., Xu G.Y., Singer A.U., Muhandiram D.R. & Forman-Kay J.D.: **A gradient-enhanced HCCH-TOCSY experiment for recording side-chain ^{1}H and ^{13}C correlations in H_20 samples of proteins.** *Journal of Magnetic Resonance* 1993, **B101**:333-337.

70. Rance M., Søcrensen O.W., Bodenhaussen G., Wagner G. & Ernst R.R.: *Biochem.Biophys.Res.Commun.* 1988, **117**:479

71. Neri D., Szyperski T., Otting G., Senn H. & Wuthrich K.: **Stereospecific nuclear magnetic resonance assignments of the methyl groups of valine and leucine in the DNA-binding domain of the 434 repressor by biosynthetically directed fractional ^{13}C labeling**. *Biochemistry* 1989, **28**:7510-7516.

72. Kuboniwa H., Grzesiek S., Delaglio F. & Bax A.: **Measurement of HN-H_α J couplings in calcium-free calmodulin using new 2D and 3D water-flip-back methods**. *J.Biomol.NMR* 1994, **4**:871-878.

73. Delaglio F., Grzesiek S., Vuister G.W., Zhu G., Pfeifer J. & Bax A.: **NMRPipe: a multidimensional spectral processing system based on UNIX pipes.** *J.Biomol.NMR* 1995, **6**:277-293.

74. Garrett D.S., Powers R., Gronenborn A.M. & Clore G.M.: **A common sense approach to peak picking in two-, three-, and four-dimensional spectra using automatic computer analysis of contour diagrams.** *Journal of Magnetic Resonance* 1991, **95**:214-220.

75. Brunger A.T.: *X-PLOR Version 3.1: A System for X-ray Crystallography and NMR.*, New Haven: Yale University; 1992.

76. Zhang M., Tanaka T. & Ikura M.: **Calcium-induced conformational transition revealed by the solution structure of apo calmodulin**. *Nat.Struct.Biol.* 1995, **2**:758-767.

77. Kuboniwa H., Tjandra N., Grzesiek S., Ren H., Klee C.B. & Bax A.: **Solution structure of calcium-free calmodulin**. *Nat.Struct.Biol.* 1995, **2**:768-776.

78. Finn B.E., Evenas J., Drakenberg T., Waltho J.P., Thulin E. & Forsén S.: **Calcium-induced structural changes and domain autonomy in calmodulin**. *Nat.Struct.Biol.* 1995, **2**:777-783.

79. Sheng Z., Strauss W.L., Francois J.M. & Potter J.D.: **Evidence that both Ca^{2+}-specific sites of skeletal muscle TnC are required for full activity**. *J.Biol.Chem.* 1990, **265**:21554-21560.

80. Sorenson M.M., da Silva A.C., Gouveia C.S., Sousa V.P., Oshima W., Ferro J.A. & Reinach F.C.: **Concerted action of the high affinity calcium binding sites in skeletal muscle troponin C**. *J.Biol.Chem.* 1995, **270**:9770-9777.

81. Maune J.F., Klee C.B. & Beckingham K.: **Ca^{2+} binding and conformational change in two series of point mutations to the individual Ca^{2+}-binding sites of calmodulin**. *J.Biol.Chem.* 1992, **267**:5286-5295.

82. Foguel D., Suarez M.C., Barbosa C., Rodrigues J.J.J., Sorenson M.M., Smillie L.B. & Silva J.L.: **Mimicry of the calcium-induced conformational state of troponin C by low temperature under pressure**. *Proc.Natl.Acad.Sci.U.S.A.* 1996, **93**:10642-10646.

83. Sia S.K., Li M.X., Spyracopoulos L., Gagné S.M., Liu W., Putkey J.A. & Sykes B.D.: **Structure of cardiac muscle troponin C unexpectedly reveals a closed regulatory domain**. *J.Biol.Chem.* 1997, **272**:18216-18221.

84. Spyracopoulos L., Li M.X., Sia S.K., Gagné S.M., Chandra M., Solaro R.J. & Sykes B.D.: **Calcium-induced structural transition in the regulatory domain of human cardiac troponin C**. *Biochemistry* 1997, **36**:12138-12146.

85. Ikura M., Clore G.M., Gronenborn A.M., Zhu G., Klee C.B. & Bax A.: **Solution structure of a calmodulin-target peptide complex by multidimensional NMR**. *Science* 1992, **256**:632-638.

86. Olah G.A., Rokop S.E., Wang C.L., Blechner S.L. & Trewhella J.: **Troponin I encompasses an extended troponin C in the Ca^{2+}-bound complex: a small-angle X-ray and neutron scattering study**. *Biochemistry* 1994, **33**:8233-8239.

87. Akke M., Forsén S. & Chazin W.J.: **Solution structure of $(Cd^{2+})_1$-calbindin D_{9k} reveals details of the stepwise structural changes along the Apo-->$(Ca^{2+})_{II}$-->$(Ca^{2+})_{I,II}$ binding pathway**. *J.Mol.Biol.* 1995, **252**:102-121.

88. Kördel J., Skelton N.J., Akke M. & Chazin W.J.: **High-resolution structure of calcium-loaded calbindin D_{9k}**. *J.Mol.Biol.* 1993, **231**:711-734.

89. Skelton N.J., Kördel J. & Chazin W.J.: **Determination of the solution structure of Apo calbindin D_{9k} by NMR spectroscopy**. *J.Mol.Biol.* 1995, **249**:441-462.

90. Drohat A.C., Amburgey J.C., Abildgaard F., Starich M.R., Baldisseri D. & Weber D.J.: **Solution structure of rat apo-S100B(ββ) as determined by NMR spectroscopy**. *Biochemistry* 1996, **35**:11577-11588.

91. Drohat A.C., Baldisseri D.M., Rustandi R.R. & Weber D.J.: **Solution structure of calcium-bound rat S100B(ββ) as determined by nuclear magnetic resonance spectroscopy**. *Biochemistry* 1998, **37**:2729-2740.

92. Smith S.P. & Shaw G.S.: **A novel calcium-sensitive switch revealed by the structure of human S100B in the calcium-bound form**. *Structure* 1998, **6**:211-222.

93. Matsumura H., Shiba T., Inoue T., Harada S. & Kai Y.: **A novel mode of target recognition suggested by the 2.0 Å structure of holo S100B from bovine brain**. *Structure* 1998, **6**:233-241.

94. Sastry M., Ketchem R.R., Crescenzi O., Weber C., Lubienski M.J., Hidaka H. & Chazin W.J.: **The three-dimensional structure of Ca^{2+}-bound calcyclin: implications for Ca^{2+}-signal transduction by S100 proteins**. *Structure* 1998, **6**:223-231.

95. Farrow N.A., Muhandiram R., Singer A.U., Pascal S.M., Kay C.M., Gish G., Shoelson S.E., Pawson T., Forman-Kay J.D. & Kay L.E.: **Backbone dynamics of a free and phosphopeptide-complexed Src homology 2 domain studied by ^{15}N NMR relaxation**. *Biochemistry* 1994, **33**:5984-6003.

96. Tjandra N., Feller S.E., Pastor R.W. & Bax A.: **Rotational diffusion anisotropy of human ubiquitin from ^{15}N NMR relaxation.** *J.A.C.S.* 1995, **117**:12562-12566.

97. Abragam A.: *Principles of Nuclear Magnetism*, Oxford: Clarendon Press; 1961.

98. Lipari G. & Szabo A.: **Model-free approach to the interpretation of nuclear magnetic resonance relaxation in macromolecules. 1. Theory and range of validity**. *J.A.C.S.* 1982, **104**:4546-4559.

99. Lipari G. & Szabo A.: **Model-free approach to the interpretation of nuclear magnetic resonance relaxation in macromolecules. 2. Theory and range of validity**. *J.A.C.S.* 1982, **104**:4559-4570.

100. Clore G.M., Driscoll P.C., Wingfield P.T. & Gronenborn A.M.: **Analysis of the backbone dynamics of interleukin-1 beta using two-dimensional inverse**

detected heteronuclear ^{15}N-^{1}H NMR spectroscopy. *Biochemistry* 1990, **29**:7387-7401.

101. Clore G.M., Szabo A., Bax A., Kay L.E., Driscoll P.C. & Gronenborn A.M.: **Deviations from the simple two-parameter model-free approach to the interpretation of ^{15}N nuclear magnetic relaxation of proteins**. *J.A.C.S.* 1990, **112**:4989-4991.

102. Bevington P.R. & Robinson D.K.: *Data reduction and error analysis for the physical sciences*, 2nd edn. New York: McGraw-Hill; 1992.

103. Wolfram S.: *The mathematica book*, 3rd edn. Wolfram Media and Cambridge University Press; 1996.

104. Wang A.C. & Bax A.: **Minimizing the effects of radio-frequency heating in multidimensional NMR experiments**. *J.Biomol.NMR* 1993, **3**:715-720.

105. Luginbühl P., Pervushin K.V., Iwai H. & Wüthrich K.: **Anisotropic molecular rotational diffusion in ^{15}N spin relaxation studies of protein mobility**. *Biochemistry* 1997, **36**:7305-7312.

106. Lee L.K., Rance M., Chazin W.J. & Palmer A.G.: **Rotational diffusion anisotropy of proteins from simultaneous analysis of ^{15}N and ^{13}C alpha nuclear spin relaxation**. *J.Biomol.NMR* 1997, **9**:287-298.

107. Tjandra N., Wingfield P., Stahl S. & Bax A.: **Anisotropic rotational diffusion of perdeuterated HIV protease from ^{15}N NMR relaxation measurements at two magnetic fields**. *J.Biomol.NMR* 1996, **8**:273-284.

108. Phan I.Q.H., Boyd J. & Campbell I.D.: **Dynamic studies of a fibronectin type I module pair at three frequencies: anisotropic modelling and direct determination of conformational exchange**. *J.Biomol.NMR* 1996, **8**:369-378.

109. Shaka A.J., Keeler J., Frenkiel T. & Freeman R.: **An Improved Sequence for Broadband Decoupling: WALTZ-16**. *Journal of Magnetic Resonance* 1983, **52**:335-338.

110. Markley J.L., Horsley W.J. & Klein M.P.: **Spin-lattice relaxation measurements in slowly relaxing complex spectra**. *J.Chem.Phys.* 1971, **55**:3604-3605.

111. Muhandiram D.R., Yamazaki T., Sykes B.D. & Kay L.E.: **Measurements of ^{2}H T_1 and $T_{1\rho}$ relaxation times in uniformly ^{13}C-labeled and fractionnally ^{2}H-lebeled proteins in solution**. *J.A.C.S.* 1995, **117**:11536-11544.

112. Kay L.E., Muhandiram D.R., Farrow N.A., Aubin Y. & Forman-Kay J.D.: **Correlation between dynamics and high affinity binding in an SH2 domain interaction**. *Biochemistry* 1996, **35**:361-368.

113. Mandel A.M., Akke M. & Palmer A.G.: **Backbone dynamics of Escherichia coli ribonuclease HI: correlations with structure and function in an active enzyme**. *J.Mol.Biol.* 1995, **246**:144-163.

114. Powers R., Clore G.M., Garrett D.S. & Gronenborn A.M.: **Relationships between the precision of high-resolution protein NMR structures, solution order parameters, and crystallographic B factors**. *J.Magn.Res.* 1993, **101**:325-327.

115. Akke M., Bruschweiler R. & Palmer A.G.: **NMR order parameters and free energy: an analytical approach and application to cooperative calcium binding by calbindin D_{9k}**. *J.A.C.S.* 1993, **115**:9832-9833.

116. Yang D. & Kay L.E.: **Contributions to conformational entropy arising from bond vector fluctuations measured from NMR-derived order parameters: Application to protein folding.** *J.Mol.Biol.* 1996, **263**:369-382.

117. Gagné S.M., Li M.X. & Sykes B.D.: **Mechanism of direct coupling between binding and induced structural change in regulatory calcium binding proteins**. *Biochemistry* 1997, **36**:4386-4392.

118. Gagné S.M., Tsuda S., Spyracopoulos L., Kay L.E. & Sykes B.D.: **Backbone and methyl dynamics of the regulatory domain of troponin C: anisotropic rotational diffusion and contribution of conformational entropy to calcium affinity**. *J.Mol.Biol.* 1998, **278**:667-686.

119. Tjandra N., Kuboniwa H., Ren H. & Bax A.: **Rotational dynamics of calcium-free calmodulin studied by ^{15}N-NMR relaxation measurements**. *Eur.J.Biochem.* 1995, **230**:1014-1024.

120. Akke M., Skelton N.J., Kördel J., Palmer A.G. & Chazin W.J.: **Effects of ion binding on the backbone dynamics of calbindin D_{9k} determined by ^{15}N NMR relaxation.** *Biochemistry* 1993, **32**:9832-9844.

121. Baldellon C., Alattia J.R., Strub M.P., Pauls T., Berchtold M.W., Cave A. & Padilla A.: **^{15}N NMR relaxation studies of calcium-loaded parvalbumin show tight dynamics compared to those of other EF-hand proteins**. *Biochemistry* 1998, **37**:9964-9975.

122. Chandra M., Dong W.J., Pan B.S., Cheung H.C. & Solaro R.J.: **Effects of protein kinase A phosphorylation on signaling between cardiac troponin I and the N-terminal domain of cardiac troponin C**. *Biochemistry* 1997, **36**:13305-13311.

123. Golosinska K., Pearlstone J.R., Borgford T., Oikawa K., Kay C.M., Carpenter M.R. & Smillie L.B.: **Determination of and corrections to sequences of turkey and chicken troponins-C. Effects of Thr-130 to Ile mutation on Ca^{2+} affinity**. *J.Biol.Chem.* 1991, **266**:15797-15809.

124. Kördel J., Skelton N.J., Akke M., Palmer A.G. & Chazin W.J.: **Backbone dynamics of calcium-loaded calbindin D_{9k} studied by two-dimensional proton-detected ^{15}N NMR spectroscopy**. *Biochemistry* 1992, **31**:4856-4866.

125. Wüthrich K.: *NMR of proteins and nucleic acids.*, New York: John Wiley & Sons; 1986.

126. Ernst R.R., Bodenhaussen G. & Wokaun A.: *Principles of magnetic resonance in one and two dimensions*, Oxford: Clarendon Pres; 1987.

127. Blanchard H., Grochulski P., Li Y., Arthur J.S., Davies P.L., Elce J.S. & Cygler M.: **Structure of a calpain Ca^{2+}-binding domain reveals a novel EF-hand and Ca^{2+}-induced conformational changes**. *Nat.Struct.Biol.* 1997, **4**:532-538.

128. Lin G.D., Chattopadhyay D., Maki M., Wang K.K., Carson M., Jin L., Yuen P.W., Takano E., Hatanaka M., DeLucas L.J. & Narayana S.V.: **Crystal structure of calcium bound domain VI of calpain at 1.9 Å resolution and its role in enzyme assembly, regulation, and inhibitor binding**. *Nat.Struct.Biol.* 1997, **4**:539-547.

CURRICULUM VITAE

QUALIFICATIONS

- **9 years of research** experience using NMR to study proteins, polysaccharides and small organic molecules.
- **Extensive computer skills.**
- **Bilingual**. Fluent in both French and English.

NMR RELATED SKILLS and ACCOMPLISHMENTS

- 2 years of experience on Bruker spectrometers (WM-250, AM-300, AMX-500 and AMX-600).
- 7 years of experience on Varian spectrometers (UNITY-300, VXR-500, INOVA-500 and UNITY-600).
- Spectral acquisition, processing, and analysis of modern NMR experiments, especially of multidimensional multinuclear experiment (1D-3D, ^{1}H/^{2}H/^{15}N/^{13}C).
- Pulse sequence programming of 1D, 2D, and 3D NMR experiments.
- Initial setup of multidimensional multinuclear NMR experiments for general group usage.
- Experience with the following software packages: nmrPipe, PIPP, xplor, InsightII, Quanta, DGII.
- Evaluation and configuration decisions for the purchase of new NMR spectrometers.
- Troubleshooting of spectrometer or pulse sequence malfunction.
- Structure determination based on NMR data. Principal author of three sets of PDB coordinates (1TNP, 1TNQ, 1SMG) and secondary author of five others (1AJ4, 1AP4, 1SPY, 1MFD, 1SKT).
- Relaxation analysis: backbone dynamics (^{15}N), side-chain dynamics (^{2}H), diffusion anisotropy and entropy analysis.

COMPUTER SKILLS and ACCOMPLISHMENTS

- Extensive use (9 years) of UNIX systems : **SGI**, **SUN** and PC (**Linux**).
- Extensive use of the following personal computer systems: **Mac**, **Windows-95** and **WindowsNT**.
- **System administration** of UNIX (Solaris 2.6 and Linux) and WindowsNT systems.
- **Programming skills** include Awk, C, Fortran, and shell scripts.
- Author of the following programs:
  - CAL_3D_N15 and CAL_3D_C13 (NOE calibration of 3D spectra for structure calculation)
  - IHA (interhelical angle in proteins)
  - ANIS (analysis of relaxation data with the incorporation of anisotropic tumbling)
  - Author of several macros allowing an easier and more efficient use of spectrometers
  - Author of several scripts which facilitate the steps involved in the analysis of NMR data
  - All of the above have been use both inside and outside of the Sykes NMR group.

RELEVANT EMPLOYMENT

- **2 years** (09/94-09/96) in the laboratory of **Dr. Brian D. Sykes. Biochemistry, Univ. of Alberta**.

  In addition to my own research projects, responsibilities included:
  - training of graduate students and post-doctoral researchers regarding the theory, acquisition, processing and analysis of multidimensional multinuclear NMR experiments
  - configuration decisions for purchase of new 500 MHz spectrometer, including a visit at Varian (Palo Alto, CA) for evaluation
- **1 year** (05/90-09/90 and 01/91-09/91) in the laboratory of **Dr. Jean-Robert Brisson and Dr. David R. Bundle. Biological Science, NRC, Ottawa**.

  Research projects:
  - structural characterization of polysaccharides using NMR and simulations
  - structural characterization of trisaccharide-antibody complex using simulations
  - incorporation of the exo-anomeric effect into the CHARMM force field
  - writing of a FORTRAN program which does full relaxation matrix calculations
- **8 months** (01/89-05/89 and 09/89-01/90) in the laboratory of **Dr. Michael Bernstein. Merck Frosst Canada, Montréal**.
- **8 months** (05/88-09/88 and 09/90-01/91) in the laboratory of **Dr. Serge Lacelle. Université de Sherbrooke, Sherbrooke, QC**.

TEACHING EXPERIENCE

- Training of several graduate students and post-doctoral researchers for the theory, acquisition, processing and analysis of multidimensional multinuclear spectra.
- Teaching assistant in an undergraduate biochemistry laboratory course
- More than 10 group seminars.

EDUCATION

Ph.D. Biochemistry (1996-1999)	University of Alberta
M.Sc. Biochemistry (1991-1994)	University of Alberta
B.Sc. Chemistry (1987-1990)	Université de Shebrooke.

AWARDS

- Second prize for presentation at *Le 2^e^ Colloque Annuel de Chimie de l'Univ. de Sherbrooke* (1990)
- FCAR graduate studies scholarship (1991-1993)
- MERCK FROSST travel award for CFBS meeting (1997)
- MRC graduate studies scholarship (1996-1998)

ACTIVITIES

- Playing with my two children.
- Riding my motorcycle and doing mechanics on it.
- Golf, downhill skiing, billiards, curling, and softball.

PUBLICATIONS (1992-1998)

- **25 publications** (peer-reviewed journals and book chapters).
- **54 communications** (oral presentaions and posters at scientific conferences).
- 5 lectures.
- 3 technical contributions to *The NMR Newsletter*.

PUBLICATION LIST (peer-reviewed journals and book chapters)

1. E. Altman, J.-R. Brisson, S.M. Gagné and M.B. Perry. Structure of the capsular polysaccharide of *Actinobacillus Pleuropneumoniae* serotype 5b. *Eur. J. Biochem.* **204**: 225-230 (1992).

2. E. Altman, J.-R. Brisson, S.M. Gagné, J. Kolbe, P. Messner and U.B. Sleytr. Structure of the glycan chain from the surface layer glycoprotein *of Clostridium Thermohydrosulfuricum* L77-66. *Biochimica et Biophysica Acta* **1117**: 71-77 (1992).

3. T.L. Pauls, I. Durussel, J.A. Cox, I.D. Clark, A.G. Szabo, S.M. Gagné, B.D. Sykes and M.W. Berchtold. Metal binding properties of recombinant rat parvalbumin wildtype and F102W mutant. *J. Biol. Chem.* **268**: 20897-20903 (1993).

4. D.R. Bundle, H. Baumann, J.-R. Brisson, S.M. Gagné, A. Zdanov and M. Cygler. Solution structure of a trisaccharide-antibody complex: comparison of NMR measurements with a crystal structure. *Biochemistry* **33**: 5183-5192 (1994).

5. S.M. Gagné, S. Tsuda, M.X. Li, M. Chandra, L.B. Smillie and B.D. Sykes. Quantification of the calcium-induced secondary structural changes in the regulatory domain of troponin-C. *Protein Science* **3**: 1961-1974 (1994).

6. M.X. Li, S.M. Gagné, S. Tsuda, C.M. Kay, L.B. Smillie and B.D. Sykes. Calcium binding to the regulatory N-domain of skeletal muscle troponin C occurs in a stepwise manner. *Biochemistry* **34**: 8330-8340 (1995).

7. S.M. Gagné, S. Tsuda, M.X. Li, L.B. Smillie and B.D. Sykes. Structures of the troponin-C regulatory domains in the apo- and calcium-saturated states. *Nature Structural Biology* **2**: 784-789 (1995).

8. B.D. Sykes, C.M. Slupky, D.S. Wishart, F.D. Sönnichsen and S.M. Gagné. On the use of NMR in complex biological systems: NMR studies of calcium sensitive interactions amongst muscle proteins. In *NMR as a structural tool for macromolecules: current status and future directions* (ed B.D. Nageswara-Rao and M.D. Kemple) Plenum Press, New York, NY, USA, pps 275-284 (1996).

9. S. Tsuda, S.M. Gagné, B.D. Sykes and K. Hikichi. Multi-dimensional NMR analysis. In *The new protein engineering* (ed M. Hatano) Fuji Techno-System Co. Ltd., Tokyo, Japan, Chapter 3, pps 75-78 (1996).

10. B.D. Sykes, G. Audette, S.M. Gagné, M.X. Li, C.M. Slupsky, and S. Tsuda. NMR studies of the calcium-induced structural changes that trigger muscle contraction. In *Biomacromolecules: from 3-D to applications.* 34th Hanford symposium on health and the environment (ed R.L. Ornstein) Batelle Press, Columbus, OH, USA, pps 11-19 (1996).

11. S.M. Gagné, M.X. Li and B.D. Sykes. Mechanism of direct coupling between binding and induced structural change in regulatory calcium binding proteins. *Biochemistry* **36**: 4386-4392 (1997).

12. J.J. Wang, D. Sahoo, D. Schieve, S.M. Gagné, B.D. Sykes and R.O. Ryan. Multidimensional NMR studies of an exchangeable apolipoprotein and its interaction with lipids. *Techniques in Protein Chemistry* **VIII**: 427-438 (1997).

13. P. Lavigne, M.P. Crump, S.M. Gagné, R.S. Hodges, B.D. Sykes and C.M. Kay. ^{1}H NMR evidence for two buried Asn side-chains in the c-myc-max heterodimeric α-helical coiled-coil. *Techniques in Protein Chemistry* **VIII**: 617-623 (1997).

14. S.K. Sia, M.X. Li, L. Spyracopoulos, S.M. Gagné, W. Liu, J.A. Putkey and B.D. Sykes. NMR structure of cardiac troponin-C reveals an unexpected closed regulatory domain. *J. Biol. Chem.* **272**: 18216-18221 (1997).

15. J.J. Wang, S.M. Gagné, B.D. Sykes and R.O. Ryan. Insight into lipid surface recognition and reversible conformational adaptations of an exchangeable apolipoprotein by multidimensional heteronuclear NMR techniques. *J. Biol. Chem.* **272**: 17912-17920 (1997).

16. L. Spyracopoulos, M.X. Li, S.K. Sia, S.M. Gagné, M. Chandra, R.J. Solaro and B.D. Sykes. Calcium-induced structural transition in the regulatory domain of human cardiac troponin C. *Biochemistry* **36**: 12138-12146 (1997).

17. M.X. Li, S.M. Gagné, L. Spyracopoulos, C.P.A.M. Kloks, G. Audette, M. Chandra, R.J. Solaro, L.B. Smillie and B.D. Sykes. NMR studies of Ca^{2+}-binding to the regulatory domains of cardiac and E41A skeletal muscle troponin C reveal importance of site I to energetics of the induced structural changes. *Biochemistry* **36**: 12519-12525 (1997).

18. L. Spyracopoulos, S.M. Gagné, W. Gronwald, L.E. Kay and B.D. Sykes. NMR studies of protein sidechain dynamics: examples from antifreeze and calcium-regulatory proteins. In *Proceedings for the international school of structural biology and magnetic resonance, 3rd course on protein dynamics, function, and design* (eds O. Jardetzky and F.J. Le Fèure), Plenum Press, New York, NY, USA, pps 147-162 (1998).

19. S.M. Gagné, S. Tsuda, L. Spyracopoulos, L.E. Kay and B.D. Sykes. Backbone and methyl dynamics of the regulatory domain of troponin C: anisotropic rotational diffusion and contribution of the conformational entropy to calcium affinity. *J. Mol. Biol.* **278**: 667-686 (1998).

20. P. Lavigne, M.P. Crump, S.M. Gagné, R.S. Hodges, C.M. Kay and B.D. Sykes. Mechanism of heterodimerization and ^{1}H-NMR solution structure of the c-myc-max heterodimeric leucine zipper. *J. Mol. Biol.* **281**: 165-181 (1998).

21. R.T. McKay, J.R. Pearlstone, D.C. Corson, S.M. Gagné, L.B. Smillie and B.D. Sykes. Structure and interaction site of the regulatory domain of troponin-C when complexed with the 96-148 region of troponin-I. *Biochemistry* **37**: 12419-12430 (1998).

22. S.M. Gagné, M.X. Li, R.T. McKay and B.D. Sykes. The NMR angle on troponin C. *Biochem. Cell Biol.* **76**: 1-12 (1998).

23. L. Spyracopoulos, S.M. Gagné, M.X. Li and B.D. Sykes. Dynamics and thermodynamics of the regulatory domain of human cardiac troponin C in the apo and calcium-saturated states. *Biochemistry* **00**: 000-000 (in press).

24. S.M. Gagné, M.T. Sykes and B.D. Sykes. The regulatory domain of troponin C: To be flexible or not to be flexible. *Journal of the Korean Magnetic Resonance Society* **00**: 000-000 (in press).

25. S. Tsuda, S.M. Gagné, L. Spyracopoulos and B.D. Sykes. Low temperature-induced change of the solution structure of apo regulatory domain of skeletal muscle troponin C. *J. Biol. Chem.* **00**: 000-000 (submitted).

COMMUNICATIONS (oral presentations and posters at scientific conferences)

1. S.M. Gagné and M.A. Bernstein. Analysis of exocyclic glycopyranoside moiety rotamer populations using NOE and molecular modeling. *2nd MOOT NMR Meeting*, Hamilton, Ontario, Canada. September 1989.

2. M.A. Bernstein and S.M. Gagné. Solution ^{1}H NMR and modeling studies of Lasalocid-A free acid and amine complex. *10th International Biophysics Congress*, Vancouver, Canada. August 1990.

3. S.M. Gagné and M.A. Bernstein. Solution ^{1}H NMR and modeling studies of Lasalocid-A free acid and amine complex. *3rd MOOT NMR Meeting*, Ottawa, Canada. September 1990.

4. E. Altman, J.-R. Brisson, S.M. Gagné, J. Kolbe, P. Messner and U.B. Sleytr. Structure of the glycan chain from the surface layer glycoprotein of *Clostridium Thermohydrosulfuricum. 11th International Symposium on Glycoconjugates*. 1991.

5. S.M. Gagné, J.P. MacManus and B.D. Sykes. ^{1}H and ^{15}N resonance assignments and secondary structure of oncomodulin in solution by heteronuclear 3D NMR spectroscopy. *75th Canadian Institute of Chemistry Meeting*, Edmonton, Canada. June 1992.

6. S.M. Gagné, J.P. MacManus and B.D. Sykes. Oncomodulin: ^{1}H-^{15}N assignments and secondary structure by heteronuclear 3D NMR. *Sixth Symposium of the Protein Society*, San Diego, California. July 1992.

7. G.S. Shaw, C.M. Slupsky, A.P. Campbell, W.A. Findlay, S.M. Gagné and B.D. Sykes. Ternary peptide complexes mimic calcium sensitive interaction in muscle. *Keystone Symposium on Frontiers of NMR in Molecular Biology*, Taos, New Mexico. March 1993.

8. S.M. Gagné, M.X. Li, W.A. Findlay and B.D. Sykes. Study of the N-domain of troponin-C by heteronuclear multidimensional NMR. *Keystone Symposium on Frontiers of NMR in Molecular Biology*, Taos, New Mexico. March 1993.

9. S.M. Gagné, S. Tsuda, and B.D. Sykes. Study of the N-domain of troponin-C by heteronuclear multidimensional NMR. *39th Canadian Spectroscopy Conference*, Laval, Canada. August 1993.

10. C.M. Slupsky, S.M. Gagné, S. Tsuda, L. Calhoun and B.D. Sykes. NMR studies of calcium sensitive interactions amongst muscle proteins. *19th Annual Lorne Conference on Protein Structure and Function*, Lorne, Australia. February 1994.

11. M.X. Li, S.M. Gagné, S. Tsuda, L.B. Smillie and B.D. Sykes. NMR studies of calcium binding to N-domain of chicken troponin-C. *Biophys. J.* **66**: A310, 1994.

12. S.M. Gagné, S. Tsuda, M.X. Li, L.B. Smillie and B.D. Sykes. N-domain of troponin-C: solution structures of the Ca^{++} free and Ca^{++} bound state. *37th Annual General Meeting of the Canadian Federation of Biological Societies*, Montreal, Canada. June 1994.

13. S.M. Gagné, S. Tsuda, M.X. Li, C.M. Slupsky, L.A. Calhoun, L.B. Smillie and B.D. Sykes. The calcium induced change that triggers muscle contraction. *XVIth International Conference on Magnetic Resonance in Biological Systems*, Veldhoven, The Netherlands. August 1994.

14. S.M. Gagné, F.D. Sönnichsen and B.D. Sykes. Calibration of ^{15}N-edited NOESY spectra using an NOE ratio. *IUPUI Symposium on NMR as a Structural Tool fo Macromolecules: Current Status and Future Directions*, Indianapolis, IN. October 1994.

15. S.M. Gagné, S. Tsuda, M.X. Li, C.M. Slupsky, L.A. Calhoun, L.B. Smillie and B.D. Sykes. The calcium induced change that triggers muscle contraction. *IUPUI Symposium on NMR as a Structural Tool for Macromolecules: Current Status and Future Directions*, Indianapolis, IN. October 1994.

16. S.M. Gagné, S. Tsuda, M.X. Li, C.M. Slupsky, L.A. Calhoun, L.B. Smillie and B.D. Sykes. Calcium-induced structural changes in troponin-C. *Biophys. J.* **68**: A57, 1995.

17. M. Yamada, S.M. Gagné, B.D. Sykes, M. Ikebe and S. Maruta. Analysis of conformational change on smooth muscle myosin associated with phosphorylation using ^{19}F NMR. *Biophys. J.* **68**: A161, 1995.

18. M.X. Li, S.M. Gagné, S. Tsuda, L.A. Calhoun, L.B. Smillie and B.D. Sykes. Investigations of the mechanisms of calcium binding to the isolated N- and C-domains of troponin-C. *Ninth International Symposium on Calcium-Binding Proteins and Calcium Function in Health and Disease*, Airlie, Virginia. April 1995.

19. S.M. Gagné, S. Tsuda, M.X. Li, C.M. Slupsky, L.A. Calhoun, L.B. Smillie and B.D. Sykes. The calcium-induced structural change that triggers muscle contraction. *Ninth International Symposium on Calcium-Binding Proteins and Calcium Function in Health and Disease*, Airlie, Virginia. April 1995.

20. B.D. Sykes, D.S. Wishart, S.M. Gagné, F.D. Sönnichsen and W. Gronwald. Use of NMR chemical shifts in biomolecular NMR. *Tsukuba '95 NMR Meeting*, Tsukuba, Japan. September 1995.

21. S.M. Gagné, S. Tsuda, M.X. Li, L.B. Smillie and B.D. Sykes. Regulatory domain of troponin-C: solution structures in the Ca^{++}-free, one Ca^{++}, and two Ca^{++} states. *Tsukuba '95 NMR Meeting,* Tsukuba, Japan. September 1995.

22. S.M. Gagné, S. Tsuda, M.X. Li, C.M. Slupsky, L.B. Smillie and B.D. Sykes. The calcium induced change that triggers muscle contraction. *Japan Biophysical Society*, Sapporo, Japan. September 1995.

23. S.M. Gagné, S. Tsuda, M.X. Li, L.B. Smillie and B.D. Sykes. Regulatory domain of troponin-C: solution structures in the Ca^{++}-free, one Ca^{++}, and two Ca^{++} states. *Japan Biophysical Society,* Sapporo, Japan. September 1995.

24. M.X. Li, S.M. Gagné, L.A. Calhoun, L.B. Smillie and B.D. Sykes. Investigations of the mechanisms of calcium binding to the isolated N and C domains of troponin C. *1995 International Chemical Congress of Pacific Basin Societies*, Honolulu, Hawaii. December 1995.

25. S. Maruta, N. Sacki, K. Banno, S.M. Gagné, M. Ikebe and B.D. Sykes. Analysis of conformational change of smooth muscle myosin regulatory light chain accompanied with phosphorylation using ^{19}F-NMR. *Biophys. J.* **70**: A267, 1996.

26. P. Lavigne, S.M. Gagné, B.D. Sykes, R.S. Hodges and C.M. Kay. ^{1}H NMR evidence for two buried Asn side-chains in the c-MYC-MAX heterodimeric α-helical coiled-coil. *PENCE Annual General Meeting*, Canada. May 1996.

27. S.M. Gagné, S. Tsuda, M.X. Li, C.M. Slupsky, L.A. Calhoun, L.B. Smillie and B.D. Sykes. The calcium induced change that triggers muscle contraction. *39th Annual General Meeting of the Canadian Federation of Biological Societies*, London, Canada. June 1996.

28. P. Lavigne, S.M. Gagné, B.D. Sykes, R.S. Hodges and C.M. Kay. ^{1}H NMR evidence for two buried Asn side-chains in the c-MYC-MAX hereodimeric α-helical coiled-coil. *39th Annual General Meeting of the Canadian Federation of Biological Societies*, London, Canada. June 1996.

29. J.J. Wang, S.M. Gagné, B.D. Sykes and R.O Ryan. Multidimensional NMR studies of an exchangeable apolipoprotein-apolipophorin III from *M. Sexta*. *39th Annual General Meeting of the Canadian Federation of Biological Societies*, London, Canada. June 1996.

30. S.M. Gagné, S. Tsuda, M.X. Li, C.M. Slupsky, L.A. Calhoun, L.B. Smillie and B.D. Sykes. The calcium induced structural change that triggers muscle contraction. *XVIIth International Conference on Magnetic Resonance in Biological Systems*, Keystone, CO. August 1996.

31. S. Tsuda, S.M. Gagné and B.D. Sykes. Low-temperature effect on the structure and dynamics of dcicken skeletal troponin C. *The 35th Annual Experimental NMR Meeting*, Kyoto, Japan, pps. 249-252, November 1996.

32. S.M. Gagné, M.X. Li, R.T. McKay, S.K. Sia, L. Spyracopoulos and B.D. Sykes. The calcium induced structural change that triggers muscle contraction. *1997 Keystone Symposia: Frontiers of NMR in Molecular Biology - V.* Taos, New Mexico. February 1997.

33. J.J. Wang, S.M. Gagné, B.D. Sykes and R.O. Ryan. NMR structure of an exchangeable apolipoprotein: identification of a possible new structural motif. *1997 Keystone Symposia: Frontiers of NMR in Molecular Biology - V.* Taos, New Mexico. February 1997.

34. S.M. Gagné, M.X. Li, R.T. McKay, S.K. Sia, L. Spyracopoulos, J.A. Putkey, M. Chandra, R.J. Solaro, L.B. Smillie and B.D. Sykes. The calcium induced structural change that triggers skeletal and cardiac muscle contraction. *Biophys. J.* **72**: A332, 1997.

35. S.K. Sia, M.X. Li, L. Spyracopoulos, S.M. Gagné, J.A. Putkey and B.D. Sykes. NMR solution structure of calcium-saturated cardiac muscle troponin C. *Biophys. J.* **72**: A282, 1997.

36. L. Spyracopoulos, M.X. Li, S.K. Sia, S.M. Gagné, M. Chandra, R.J. Solaro and B.D. Sykes. Calcium induced structural transition in cardiac troponin-C. *Biophys. J.* **72**: A283, 1997.

37. Q. Kleerekoper, W. Liu, S.K. Sia, M.X. Li, L. Spyracopoulos, S.M. Gagné, B.D. Sykes and J.A. Putkey. NMR studies of drug binding to cardiac TnC and the relationship to the solution structure of cardiac TnC. *Biophys. J.* **72**: A330, 1997.

38. S.M. Gagné, M.X. Li, S.K. Sia, L. Spyracopoulos, J.A. Putkey, R.J. Solaro, L.B. Smillie and B.D. Sykes. Elucidation of the mechanism of the coupling between calcium-binding and the induced conformational change in calcium regulatory proteins. *International Symposium on Protein Condensation*, Rio de Janeiro, Brazil. May 1997.

39. S.M. Gagné, M.X. Li, S.K. Sia, L. Spyracopoulos, J.A. Putkey, R.J. Solaro, L.B. Smillie and B.D. Sykes. Elucidation of the mechanism of the coupling between calcium-binding and the induced conformational change in calcium regulatory proteins. *10th International Symposium on Calcium Binding and Calcium Function in Health and Disease*, Lund, Sweden. June 1997.

40. Q. Kleerekoper, W. Lui, S.K. Sia, M.X. Li, L. Spyracopoulos, S.M. Gagné, B.D. Sykes and J.A. Putkey. NMR studies of cardiac troponin C: solution structure and calcium binding. *10th International Symposium on Calcium Binding and Calcium Function in Health and Disease*, Lund, Sweden. June 1997.

41. S.M. Gagné, L. Spyracopoulos, M.X. Li, J. Pearlstone, P. Lavigne, L.E. Kay and B.D. Sykes. Troponin C: structures, dynamics and thermodynamics. *40th Annual General Meeting of the Canadian Federation of Biological Societies*, Québec, Canada. June 1997.

42. S.M. Gagné, M.X. Li and B.D. Sykes. Mechanism of direct coupling between binding and induced structural change in regulatory calcium binding proteins. *40th Annual General Meeting of the Canadian Federation of Biological Societies*, Québec, Canada. June 1997.

43. P. Lavigne, M.P. Crump, S.M. Gagné, R.S. Hodges, B.D. Sykes and C.M. Kay. The ^{1}H-NMR solution structure of the c-myc-max heterodimeric leucine zipper, *Protein Society Meeting*, Boston. 1997.

44. S.M. Gagné, M.X. Li, S.K. Sia, L. Spyracopoulos, J.A. Putkey, R.J. Solaro, L.B. Smillie and B.D. Sykes. Troponin C structures reveal mechanism of calcium regulatory proteins. *Biophys. J.* **74**: A9, 1998.

45. L. Spyracopoulos, S.M. Gagné, M.X. Li and B.D. Sykes. Dynamics and energetics of the regulatory domain of human cardiac troponin C in the apo and calcium-saturated states. *41th Annual General Meeting of the Canadian Federation of Biological Societies*, Edmonton, Canada. June 1998.

46. L. Spyracopoulos, M.X. Li, R.T. McKay, S.M. Gagné and B.D. Sykes. Structures and sites of interaction of cardiac and skeletal troponin C bound to cardiac and skeletal troponin I peptides. *41th Annual General Meeting of the Canadian Federation of Biological Societies*. Edmonton, Canada. June 1998.

47. R.T. McKay, J.R. Pearlstone, D.C. Corson, S.M. Gagné, L.B. Smillie and B.D. Sykes. Structure and interactions sites of the regulatory domain of troponin C when complexed with the 96-148 region of troponin I. *41th Annual General Meeting of the Canadian Federation of Biological Societies*, Edmonton, Canada. June 1998.

48. P.L. Lavigne, M.P. Crump, S.M. Gagné, R.S. Hodges, C.M. Kay and B.D. Sykes. Mechanism of heterodimerization and ^{1}H-NMR solution structure of the c-myx-max heterodimeric leucine zipper. *41th Annual General Meeting of the Canadian Federation of Biological Societies*, Edmonton, Canada. June 1998.

49. S.M. Gagné, L. Spyracopoulos, R.T. McKay, M.T. Sykes, S. Tsuda, L.E. Kay and B.D. Sykes. The NMR angle on troponin C. *13th Symposium of the Korean Magnetic Resonance Society: International Symposium on Biological NMR*, Seoul, Korea. August 1998.

50. S.M. Gagné, L. Spyracopoulos, R.T. McKay, M.T. Sykes, S. Tsuda, L.E. Kay and B.D. Sykes. The NMR angle on troponin C. *XVIIth International Conference on Magnetic Resonance in Biological Systems*, Tokyo, Japan. August 1998.

51. S.M. Gagné, M.T. Sykes, L. Spyracopoulos and B.D. Sykes. A flexible open structure in calcium-binding proteins? *XVIIth International Conference on Magnetic Resonance in Biological Systems*, Tokyo, Japan. August 1998.

52. L. Spyracopoulos, S.M. Gagné, S. Tsuda and B.D. Sykes. Dynamics and thermodynamics of the regulatory domains of skeletal and cardiac troponin C. *XVIIth International Conference on Magnetic Resonance in Biological Systems*, Tokyo, Japan. August 1998.

53. S. Tsuda, S.M. Gagné, L. Spyracopoulos and B.D. Sykes. Low temperature effect on the solution structure of apo regulatory domain of skeletal muscle troponin C. *XVIIth International Conference on Magnetic Resonance in Biological Systems*, Tokyo, Japan. August 1998.

54. L. Spyracopoulos, M.X. Li, S.M. Gagné, R.T. McKay and B.D. Sykes. Understanding the differences between cardiac and skeletal troponin C. *43rd Biophysical Society Annual Meeting*, Baltimore, MD. February 1999.

LECTURES

1. S.M. Gagné. Evaluation d'une methode d'analyse conformationelle quantitative par RMN. *Le 1er Colloque Annuel de Chimie de l'Université de Sherbrooke*, Sherbrooke, Canada (October 1990).

2. S.M. Gagné. Lasalocide-A: Étude conformationnelles en solution. *Le 2e Colloque Annuel de Chimie de l'Université de Sherbrooke*, Sherbrooke, Canada (October 1991).

3. S.M. Gagné. Quantification of the calcium-induced secondary structural changes in the regulatory domain of troponin C. *University of Toronto*, Toronto, Canada (June 1993).

4. S.M. Gagné. The NMR angle on troponin C. *Departemental Retreat*, Edmonton, Canada (June 1998).

5. S.M. Gagné. Skeletal troponin C: Structures, dynamics, and thermodynamics. *Hokkaido National Industrial Research Institute (HNIRI)*, Sapporo, Japan (September 1998).

University of Alberta Library
0 1620 1043 2837

B45729